JRJC 2023 - Journées de Rencontres Jeunes Chercheurs. Book of Proceedings

Thomas Strebler, Antonio Uras, Olivier Davignon, Michel Aguena, Alexis Vallier, Sabrina Sacerdoti, Sami Caroff, Batoul Diab, Chiara Lastoria, Oceane Poncet, et al.

To cite this version:

Thomas Strebler, Antonio Uras, Olivier Davignon, Michel Aguena, Alexis Vallier, et al.. JRJC 2023 - Journées de Rencontres Jeunes Chercheurs. Book of Proceedings. Journées de Rencontres Jeunes Chercheurs (JRJC 2023), 2024. hal-04609124v1

HAL Id: hal-04609124

https://hal.science/hal-04609124v1

Submitted on 12 Jun 2024 (v1), last revised 24 Jun 2024 (v2)

150 ans

Société Française de Physique | 150 ANS D'ENGAGEMENT POUR LA PHYSIQUE

JRJC 2023 22-28 OCTOBRE

Journées de Rencontre des Jeunes Chercheurs

SAINT-JEAN-DE-MONTS
(85) France
LA RIVIÈRE
Village club Cap France

BOOK OF PROCEEDINGS

Comité d'organisation :

François Brun	(CEA Saclay)
Luca Cadamuro	(IJCLab)
Rachel Delorme	(LPSC)
Romain Gaior	(LPNHE)
Andreas Goudelis	(LPCA)
Maxime Guilbaud	(SUBATECH)
Julien Masbou	(SUBATECH)
Laure Massacrier	(IJCLab)
Sabrina Sacerdoti	(APC)
Thomas Strebler *	(CPPM)
Antonio Uras *	(IP2I)
Laura Zambelli	(LAPP)

* Editors of these proceedings

Secrétariat :

Isabelle Cossin	(LPNHE)

Contents

Part I

Standard Model

session chaired by Olivier DAVIGNON

Combined fit of the τ_h identification efficiency scale factor and energy scale in CMS

Océane Poncet

Institut Pluridisciplinaire Hubert Curien

Abstract — This paper presents a new method for the measurement of data-to-simulation scale factors for the identification efficiency and energy scale of hadronic tau leptons (τ_h) using the DeepTau identification discriminators [1]. The analysis is based on pp collision data at a center-of-mass energy of $\sqrt{s} = 13$ TeV collected in 2018 with the CMS detector. The data analyzed correspond to a total integrated luminosity of $L = 59.7$ fb^{-1}. The note outlines the measurement technique employed and provides an overview of the obtained results.

Introduction

Tau leptons, being the heaviest leptons, hold a crucial role in probing the properties of the Higgs boson discovered in 2012 by the ATLAS [2] and CMS [3] collaborations, due to the proportionality between scalar couplings and fermion squared mass. They are also prevalent in other physics analyses, such as Standard Model (SM) process studies or searches for Beyond Standard Model (BSM) particles like W', Z' bosons, and leptoquarks. The tau lepton is not stable at the CMS detector's scale, having a lifetime of $\tau_\tau = 2.9 \times 10^{-13}$ s [6]. This means that a 20 GeV tau lepton decays after traveling about 980 μm. Identifying a tau lepton requires reconstructing and combining its decay products. Tau leptons decay leptonically to a muon or an electron, plus two neutrinos, in about one third of the cases. The light leptons produced in the decays are reconstructed and identified with the usual techniques for muons and electrons [4, 5]. In the remaining cases, tau leptons decay hadronically, producing charged and neutral mesons and a neutrino. The first section of this study describes the reconstruction and identification of these τ_h, and details the correction factors associated with their energy scale and identification efficiency. The second section presents the method of the combined measurement of the τ_h energy scale and the identification efficiency factor. The last section provides results of the scale factor values for each τ_h decay mode (DM) and for different $p_T(\tau_h)$ bins.

Reconstruction, identification and calibration of τ_h

Hadron-Plus-Strip (HPS) Algorithm

Hadrons are reconstructed by the Particle Flow (PF) algorithm of CMS [7]. They are directly reconstructed as charged hadrons ($\pi^\pm, K^\pm$,p), as neutral ones (K^0_L, n) or as photons in the case of $\pi^0 \to \gamma\gamma$ decay. Charged hadrons are the starting point of the Hadron-Plus-Strips (HPS) [8] algorithm which aims to reconstruct the τ_h DMs and momenta.

First, the algorithm starts from PF jets, constituted of charged hadrons, as seeds for τ_h candidates. Charged particles forming the τ_h object must satisfy specific criteria: a minimum transverse momentum (p_T) of 0.5 GeV and a transverse impact parameter d_{xy} less than 0.1 cm from the primary vertex (PV).

Secondly, the algorithm focuses on reconstructing π^0 candidates, from constituents within the jet. As photons often convert into electron-positron pairs, the algorithm clusters both electron and photon constituents into narrow "strips" in the $\eta - \phi$ plane. For electrons and photons, the minimum p_T threshold is set at 1 GeV. These strips, initiated by the most energetic electron or photon candidate, iteratively expand by adding other compatible candidates within a defined window around the strip center. The strip momentum is continuously recalculated with each addition of constituents, optimizing the strip size and position for precise reconstruction.

Finally, τ_h candidates are reconstructed by considering combinations of the highest-energy charged hadrons and strips, limited to a maximum of six each within the seed region. The HPS algorithm assigns a DM to the τ_h decay based on the count of charged hadrons and strips within the signal cone. The τ_h are reconstructed in the following DMs:

- One charged hadron ($\tau_h \to h^\pm$)
- One charged hadron and one or two strips ($\tau_h \to h^\pm\pi^0$)
- Three charged hadrons ($\tau_h \to h^\pm h^\mp h^\pm$)
- Three charged hadrons and one strip ($\tau_h \to h^\pm h^\mp h^\pm\pi^0$)

DeepTau discriminator

During the τ_h reconstruction, there is a significant background of quark and gluon jets which are misidentified as hadron jets. Additionally, muons and electrons can be misidentified as τ_h. Especially they can form well-isolated single-track jets reconstructed in the $h^{\pm}$ DM. The electrons can produce bremsstrahlung radiation, whose experimental signature can resemble that of a neutral pion in the electromagnetic calorimeter and can be misidentified as the $h^{\pm}\pi^0$ mode. The DeepTau algorithm based on a Deep Neural Network (DNN) [1] is used for the τ_h identification. This algorithm relies on energy deposits of the tau decay products and other PF candidates, along with a series of kinematic variables, reconstructed track quality, HPS-DM of the τ_h and other properties to provide three discriminant for identification of jets, electrons, and muons. The DeepTau score is used as a discriminant variables to identify genuine τ_h an reject fake ones. The cuts applied on this output score are referred to as Working Points (WP). The WPs are defined to target different values of the identification efficiency, so the calibration procedure must be realised for several WPs.

Correction factors

The simulation involves several inaccuracies in modeling the data, encompassing differences in pileup, kinematic distributions, object identification efficiencies, but also in the detector (material response...). To correct for the differences between data and Monte Carlo (MC), correction factors are applied to the MC, adjusting both the identification efficiency and the energy scale. These correction factors are computed using the so called "tag-and-probe method" to measure the energy scale and the identification scale factor of τ_h in $Z \to \tau_\mu \tau_h$ events [9]. Isolated, well-identified muons are used as "tag" objects, while the τ_h are the "probe" objects for the correction factor measurements.

τ_h Energy scale (TES)

The τ_h energy scale factor (TES) is defined as the ratio of the τ_h reconstructed energy in data to that in simulation. The TES is obtained from a maximum likelihood fit to the distribution of m_{vis}, defined as:

$$m_{vis} = \sqrt{(E_{\tau_h} + E_\mu)^2 - \|\vec{p_{\tau_h}} + \vec{p_\mu}\|^2} \tag{1}$$

where E_{τ_h}, E_μ, $\vec{p_{\tau_h}}$, and $\vec{p_\mu}$ represent the reconstructed visible energy and momentum of the visible τ_h decay products and of the muon. The distribution is fitted independently for each DM to extract the TES. To account for difference in kinematic, measurement have also been carried independently for each DM and in different $p_T(\tau_h)$ regions.

Identification efficiency scale factor (ID SF)

Differences in τ_h identification efficiency exist between the data and the simulation. To correct for this, the τ_h identification efficiency scale factors (ID SF) are computed. This scale factor affects the normalization of the signal. Similar to the TES, the data-to-simulation scale factor for the identification efficiency is obtained through a maximum likelihood fit on the m_{vis} distribution. This distribution is separately fitted in various bins of the τ_h transverse momentum $p_T(\tau_h)$ and in different DMs to extract the scale factors.

Combined fit of the τ_h energy scale and the identification scale factor

Selection

In this section, the ID SF and TES are determined using the following working points of the muons, electrons and jets discriminator to reduce the τ_h fake rate: D_μ Tight, D_e VVLoose and D_{jet} Medium [1]. Additionally, a cut on the transverse mass of the missing transverse energy and of the muon $m_T(\text{MET}, \mu) < 65$ GeV is applied to enhance to enhance the signal-background separation. Common selection on trigger paths, p_T, η, isolation of muons and τ_h and opening angle ΔR are also required and followed the same recommendations as in the previous analysis [9].

Measurement technique

In the previous analysis [9], both the TES and ID SF were individually fitted to the m_{vis} distribution within the signal region, with either the TES or the ID SF serving as the parameter of interest (POI) for the maximum likelihood fit.

The approach presented in this section involves a simultaneous fitting of both the TES and the ID SF. This aims to conduct a single adjustment on the same distribution with the same systematic uncertainties while considering the correlation between these two scale factors. The TES and the ID SF are measured for different regions, as expressed by the likelihood function:

$$L_(TES, IDSF, \theta) \quad \propto \quad p(data|TES, IDSF, \theta) \tag{2}$$

With $\theta = \{\theta^n_{i=1}\}$ the ensemble of the n systematic uncertainties and statistical model $p(data|TES, IDSF, \theta)$ encodes the probability density for the observed data parameterized by the parameters of the fit. The likelihood is maximized independently for each region.

The ID SF is defined as one of the POI in a maximum likelihood fit performed within the signal region. It is a rate parameter that affects the normalisation of the $Z \to \mu\tau_h$ events (ZTT). It's variation is limited to 30% to stabilize the fit.

The TES is also defined as a POI in the maximum likelihood fit. It impacts the m_{vis} by shifting the energy of the τ_h and by changing the shape of the signal distribution. Shape templates are generated for ZTT events, encompassing discrete variation of 0.001 between 0.970 and 1.030 of the TES for the fit in DMs, and between 0.950 and 1.050 for the fit in DMs and $p_T(\tau_h)$. The templates are generated for different values of the TES and then split in the fitted region, which allows to take in account the bin migration during the TES fit. Horizontal integral morphing [10] is utilized for interpolation between each varied template of ZTT.

The W+Jets scale factors are defined as freely floating parameters (rate parameter) for each fitted region. Additionally, the DY cross section is also a free parameter and estimated with the $Z \to \mu\mu$ control region (CR). Events are selected with two muons, with $m_{\mu\mu}$ in the range of $[70, 110]$ GeV.

Systematic uncertainties

Systematic uncertainties are incorporated as constrained nuisance parameters. They may impact either the shape or the normalization of the m_{vis} distribution.

The Log-Normal uncertainty (LnN uncertainties) affects the normalization of a process, with the associated nuisance parameter following a log-normal distribution. For shape uncertainties, vertical morphing [10] is employed to interpolate between up and down variation of the templates, with the corresponding nuisance assigned as a Gaussian probability density function. The rate parameter are free parameters in the fit, affecting the normalization of the specified processes.

A summary table presenting the parameters of the fit is provided in Table 1.

Table 1: Summary table of fit parameters.

Parameter	Type	Variation	Applied to
Luminosity	lnN	±2.5%	all except QCD
Muon efficiency	lnN	±2%	all except QCD
$t\bar{t}$ cross section	lnN	±6%	TT
VV cross sections	lnN	±5%	VV
Single top cross sections	lnN	±5%	ST
QCD normalization	lnN	±10%	QCD
$j \to \tau_h$ fake	lnN	±15%	W, QCD, ZJ, TTJ, STJ
$j \to \tau_h$fake energy scale	shape	±5%	ZJ, W, TTJ
$l \to \tau_h$fake rate	shape	$\pm 1 s.d.$	ZL, TTL
$\mu \to \tau_h$ fake energy scale	shape	±2%	ZL, TTL
Z p_T reweighting	shape	±10%	DY
Bin-by-bin	shape	-	all
DY cross sections	rate param.	-	ZTT, ZL, ZJ
W + jets normalization	rate param.	-	W
ID SF	rate param.	±30%	ZTT
TES	shape	±5%	ZTT

Legend: DY: Drell-Yan MC (ZTT + ZL + ZJ); ZTT: $Z \to \tau_h\tau_\mu$, real τ_h; ZL: $Z \to ll$, $l \to \tau_h$ fake; ZJ: $Z \to llj$, $j \to \tau_h$ fake; TT : $t\bar{t}$ production (TTT, TTL, TTJ): TTT : $t\bar{t} \to \tau_h$ real; TTL : $t\bar{t} \to l, l \to \tau_h$ fake; TTJ : $t\bar{t} \to jet, jet \to \tau_h$ fake; ST: single top; VV: Di-boson; QCD : QCD multijet production.

Results

Combined fit of the energy scale and the identification efficiency by DMs

The TES and ID SF are measured separately for each τ_h DM. The pre-fit distribution of the invariant mass of the τ_h visible decay products 1 with all DMs included is shown in Figure 1. A summary plot of the results of the correction factors is given in Figure 2.

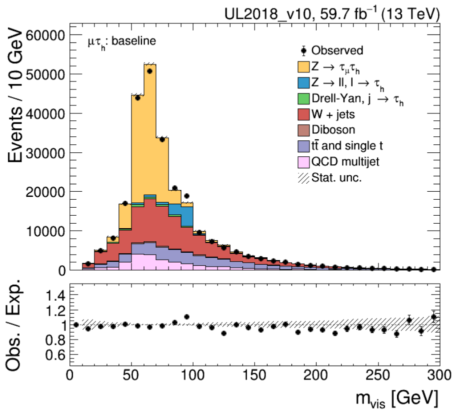

Figure 1: Pre-fit observed and expected distributions of m_{vis} for 2018 for the baseline containing all the DMs. The uncertainty band only includes statistical uncertainty in the expected events.

To ensure the stability of the measurement, several sanity checks were conducted in the $\mu\tau_h$ final state. Testing different binning widths and ranges displayed compatible results, with a maximum difference of 1%. Removing the DY control region and introducing a systematic uncertainty on the DY cross section resulted in a minimal variation (up to 0.3%) in the TES measurements. Employing a simultaneous fit across all DM regions by defining distinct TES and ID SF for each region allowed scanning the POI in one region while others were profiled. This allow to constrain the common nuisance parameters of all the regions. The results from this simultaneous fit method aligned well with other approaches.

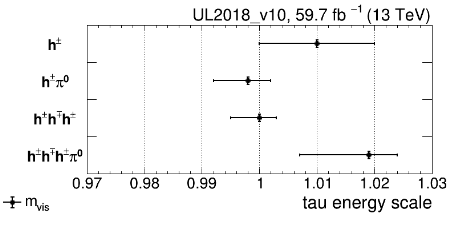

(a) Energy scale factor

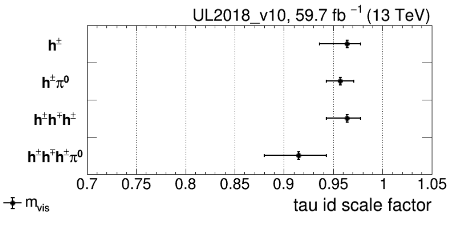

(b) Identification efficiency scale factor

Figure 2: The TES and the ID SF per τ_h DM for 2018 including systematic uncertainties.

Combined fit of the energy scale and the identification efficiency by DMs and $p_T(\tau_h)$

To accommodate the variations in the TES and iID SF across different DMS of the τ_h and its transverse momentum ($p_T(\tau_h)$), the fit was performed considering both DMs and the $p_T(\tau_h)$ by splitting the fit in DM-$p_T(\tau_h)$ bins. The division of $p_T(\tau_h)$ regions aims for sufficient statistics in the fit while minimizing fluctuations. Based on the $p_T(\tau_h)$ distribution in Figure 3, the range is divided into [20, 40] GeV and [40, 200] GeV. A more detailed division, was explored, but due to low statistics, only a two-region division of $p_T(\tau_h)$ is reported in this paper.

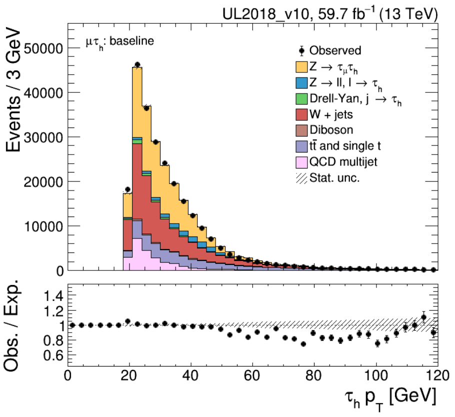

Figure 3: Pre-fit observed and expected distributions of $p_T(\tau_h)$ for 2018.

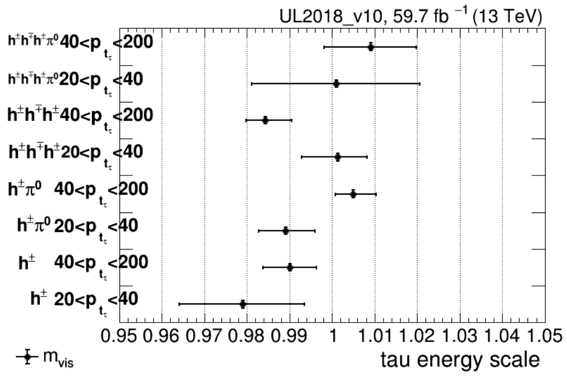

(a) Energy scale factor

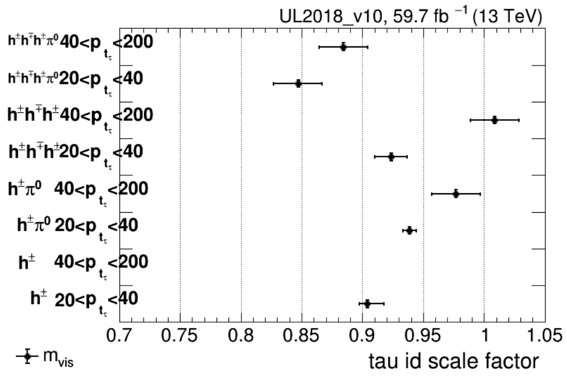

(b) Identification efficiency scale factor

Figure 4: The TES and ID SF per τ_h DM and $p_T(\tau_h)$ region for 2018. The ID SF for $h^\pm$ and 20 GeV $< p_T(\tau_h) <$ 200 GeV is out of the range but with a value of $1.0630^{+0.020}_{-0.020}$.

The TES and ID SF are fitted for each region and exhibit fluctuations in their negative log likelihood profile primarily due to Monte Carlo statistics limitations. These fluctuations might be mitigated in future analyses through increased statistics. Presently, the division into $p_T(\tau_h)$ regions is restricted to two per DM. Because of these fluctuations, asymmetric parabolae are fitted to the likelihood profiles values below 5.

The correlation between the ID SF and the TES exhibit low correlations for low $p_T(\tau_h)$ ($20 < p_T(\tau_h) < 40$ GeV) but are strongly correlated for high $p_T(\tau_h)$ ($40 < p_T(\tau_h) < 200$ GeV). This correlation results from bin migration between regions as TES varies, causing normalization changes and correlating TES with identification efficiency. This study underscores the importance of a simultaneous fit for both correction factors, though the limitation on $p_T(\tau_h)$ regions could be improved with enhanced statistics.

A summary plot of the results for the correction factors per DMs and $p_T(\tau_h)$ region is provided in Figure 4. The results for the DM and $p_T(\tau_h)$ regions are comparable with the results by DM only, but there is a significant dependency in $p_T(\tau_h)$ for the identification efficiency.

References

[1] CMS Collaboration, Performance of the DeepTau algorithm for the discrimination of taus against jets, electron, and muons, CMS-DP-2019-033 (2019), url:https://cds.cern.ch/record/2694158

[2] ATLAS Collaboration, Observation of a new particle in the search for the Standard Model Higgs boson with the ATLAS detector at the LHC, Phys. Lett. B 716 (2012), 1-29, url: https://doi.org/10.48550/arXiv.1207.7214

[3] CMS Collaboration, Observation of a New Boson at a Mass of 125 GeV with the CMS Experiment at the LHC, Phys. Lett. B 716 (2012), 30-61, url: https://doi.org/10.48550/arXiv.1207.7235

[4] CMS Collaboration, Performance of the CMS muon detector and muon reconstruction with proton-proton collisions at $\sqrt{s}$ = 13 TeV, JINST 13 (2018) P06015, url: https://doi.org/10.48550/arXiv.1804.04528

[5] CMS Collaboration, Electron and photon reconstruction and identification with the CMS experiment at the CERN LHC, JINST 16 (2021) P05014, url: https://doi.org/10.48550/arXiv.2012.06888

[6] Particle Data Group, Review of Particle Physics, PTEP (2020) no.8, 083C01 url: https://doi.org/10.1093/ptep/ptaa104

[7] CMS Collaboration, Particle-flow reconstruction and global event description with the CMS detector, JINST 12 (2017) P10003, url: https://doi.org/10.48550/arXiv.1706.04965

[8] CMS Collaboration, Performance of reconstruction and identification of τ leptons decaying to hadrons and ν_τ in pp collisions at $\sqrt{s} = 13$ TeV, JINST 13 (2018) P10005, P10005, url: https://doi.org/10.48550/arXiv.1809.02816

[9] CMS Collaboration, Identification of hadronic tau lepton decays using a deep neural network, JINST 17 (2022) P07023, url: https://doi.org/10.48550/arXiv.2201.08458

[10] M. Baak, S. Gadatsch, R. Harrington, W. Verkerke, Interpolation between multi-dimensional histograms using a new non-linear moment morphing method, Nucl. Instrum. Meth. A 771 (2015) 39-48, url: https://doi.org/10.48550/arXiv.1410.7388

Measurement of the CKM angle γ in $B^{\pm} \to D^0(\to K_s^0\pi^+\pi^-\pi^0)K^{\pm}$ decays at LHCb

Jessy Daniel

Université Clermont-Auvergne, CNRS/IN2P3, Laboratoire de Physique de Clermont-Ferrand (LPC)

Abstract — The observable Universe is mainly made up of matter, while almost all the antimatter disappeared in the very early times. One explanation is that the Universe obeys the Sakharov conditions [1], which means in particular the existence of a C (charge) and CP (charge - parity) symmetry violation. In Standard Model (SM), the main contribution to CP violation comes from the Cabibbo–Kobayashi–Maskawa (CKM) mechanism [2] [3]. In particular, the γ angle of the CKM matrix sets a benchmark for CP violation, to be compared with the SM predictions, leading to possible New Physics discovery. We present here the current status of one measurement of the γ angle at LHCb detector, using the decay channel $B^{\pm} \to D^0K^{\pm}$ with $D^0 \to K_s^0\pi^+\pi^-\pi^0$.

Introduction

In SM, the CKM matrix can be parameterized by four independent parameters experimentally measurable. One of the key goals of LHCb detector is to constrain those parameters and in particular the γ complex angle. Direct measurements of this angle, with tree-diagram decays, theoretically clean, set a "standard candle" for the SM. One can then test discrepancy wih loop-level measurements that could be sensible to new physics phenomenon. The CKMFitter group has notably proved that, with a 1° precision on direct measurements, one may test the Standard Model up to an energy scale of at least 17 TeV [4], currently not directly accessible.

The current direct measurement combination at LHCb is $\gamma = (63.8^{+3.5}_{-3.7})^{\circ}$ [5], while the world average for indirect measurement, more precise, is $\gamma = (65.5^{+1.1}_{-2.7})^{\circ}$ [6]. As no analysis currently dominates the measurement, each additional mode or method to deal with $B_{(s)} \to D^{(*)}X$ open-charm B decays, that occurs at tree level, may help to increase the precision. This is the case of the measurement presented here, with a binned model-independent analysis of the mode $B^{\pm} \to Dh^{\pm}$ with $D^0 \to K_s^0\pi^+\pi^-\pi^0$, which will be denoted as $D^0 \to f$. This is similar to the BPGGSZ method [7], the current most precise measurement at LHCb [8], with an additional π^0 meson in the final state.

CKM mechanism and γ angle

The CKM complex unitary matrix describes the coupling between up-type and down-type quarks through the weak interaction. It is giving the following equation :

$$\begin{pmatrix} d' \\ s' \\ b' \end{pmatrix} = \begin{pmatrix} V_{ud} & V_{us} & V_{ub} \\ V_{cd} & V_{cs} & V_{cb} \\ V_{td} & V_{ts} & V_{tb} \end{pmatrix} \begin{pmatrix} d \\ s \\ b \end{pmatrix} \tag{1}$$

where d',s' and b' are electro-weak eigenstates, while d,d and b are mass eigenstates. Then, each element describes the transition probability between quarks through $W^{\pm}$ boson exchange. This matrix can be reduced to four independent parameters, three mixing angles and one complex phase, leading to the Wolfenstein parameterization, described by :

$$V_{CKM} = \begin{pmatrix} 1-\frac{\lambda^2}{2} & \lambda & A\lambda^3(\rho-i\eta) \\ -\lambda & 1-\frac{\lambda^2}{2} & A\lambda^2 \\ A\lambda^3(1-\rho-i\eta) & -A\lambda^2 & 1 \end{pmatrix} + \mathcal{O}(\lambda^4) \tag{2}$$

In addition, the expected unitarity of V_{CKM} in the SM leads to 6 unitary equations :

$$\sum_{i=1}^{3} V_{ji}V_{ki}^{*} = \sum_{i=1}^{3} V_{ij}V_{ik}^{*} = 0 \tag{3}$$

Each equation gives a unitary triangle in the complex plane. In particular the "B_d" triangle, referred as "the" unitary triangle, is directly linked to CP violation in B mesons and is experimentally measurable. Notably, a precise direct measurement of the CKM matrix complex phase $\gamma \equiv arg(-V_{ud}V_{ub}^{*}/V_{cd}V_{cb}^{*}) \equiv arg(\bar{\rho}+i\bar{\eta})$ sets a strong constraint for SM. Discrepancy with indirect measurement would indeed lead to an "opening" of the triangle, meaning a violation of the unitary. A scheme of the unitary triangle, as it has been calculated by

CKMFitter in 2021, is shown in Fig. 1.

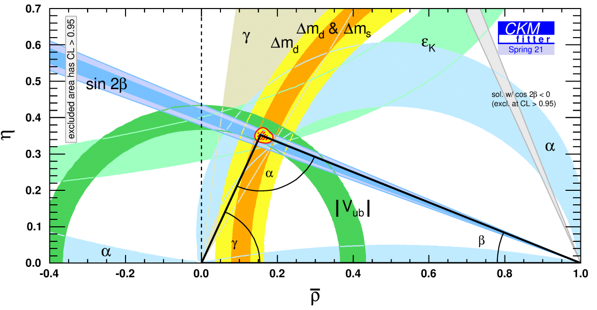

Figure 1: The CKM unitary triangle, calculated by CKMFitter as of Spring 2021.

Analysis formalism and strategy

The angle γ can be directly measured by amplitude modulation in the interference between the processes $b \to c\bar{u}s$ and $b \to u\bar{c}s$. This is the case in the $B^\pm \to D^0K^\pm$ decay, whose Feynman diagrams are shown in Fig. 2.

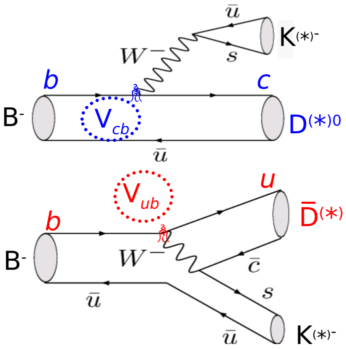

Figure 2: Feynman diagrams of the interference between $b \to c\bar{u}s$ and $b \to u\bar{c}s$ processes.

The amplitude A_B for the decay from B^+ to final state at a given point in the D^0 meson decay phase-space $\mathcal{D}$ is :

$$A_B = \bar{A} + r_B e^{i(\delta_B+\gamma)} A, \tag{4}$$

where δ_B is the strong phase difference between $B \to D^0K$ and $B \to \bar{D}^0K$, A (resp. $\bar{A}$) is the amplitude for $D^0 \to f$ (resp. $\bar{D}^0 \to f$), and r_B is the amplitude ratio between the suppressed and the favored B decay channel. The probability density for the whole decay can then be written as :

$$P_{B^+} = |\bar{A}|^2 + r_B^2|A|^2 + 2\sqrt{|A|^2|\bar{A}|^2}(x_+C - y_+S), \tag{5}$$

where $x_+ = r_B sin(\delta_B + \gamma)$, $y_+ = r_B cos(\delta_B + \gamma)$, $C = cos(\Delta\delta_D)$, and $S = sin(\Delta\delta_D)$, where $\Delta\delta_D$ is the strong phase difference between $D^0 \to f$ and $\bar{D}^0 \to f$. A similar equation can be written for B^- with $A \leftrightarrow \bar{A}$, $\gamma \leftrightarrow -\gamma$, $x_- \leftrightarrow x_+$, and $y_- \leftrightarrow y_+$. The information on γ then lies in the $x_\pm$ and $y_\pm$ observables, whose measurement depends on $\Delta\delta_D$, which varies over $\mathcal{D}$. To deal with this variation, in the the absence of an amplitude model for the D^0 decay, a model independent strategy is employed using a binned map of the D^0 decay phase space from Cleo-c study [10], similarly to what was done by Belle in [9]. One can then calculate the yield in each bin, for B^- and B^+ as :

$$\begin{aligned}\Gamma_i^- &= h^-(K_i + r_B^2\bar{K}_i + 2\sqrt{K_i\bar{K}_i}(c_ix_- + s_iy_-)),\\ \Gamma_i^+ &= h^+(\bar{K}_i + r_B^2K_i + 2\sqrt{K_i\bar{K}_i}(c_ix_+ - s_iy_+)),\end{aligned} \tag{6}$$

where K_i (resp. $\bar{K}_i$) are the fractions of D^0 (resp. $\bar{D}^0$) decaying in the bin i, $h^\pm$ are normalisation factors, and c_i (resp. s_i) are the average value of C (resp. S) in each bin.

The strategy will then be the following, from the raw data set to γ measurement : after a precise selection to extract signal from the data and a study of residual backgrounds, a "nominal" fit will be defined on the $B^\pm$ reconstructed mass to get the signal yields in each bin. A simultaneous fit will be processed to extract $x_\pm$ and $y_\pm$ thanks to Eq. 6 and inputs from Cleo-c [10]. K_i and $\bar{K}_i$ will be calculated from the corresponding $B^\pm \to D^0\pi^\pm$ decay at LHCb. Then, the γ angle can be extracted from the values of $x_\pm$ and $y_\pm$.

The LHCb detector and data set

The LHCb detector [11] is a single-arm forward spectrometer covering the pseudorapidity range $2 < \eta < 5$, designed for the study of particles containing b or c quarks. It includes a high-precision tracking system composed of a vertex detector surrounding the pp interaction region, and various tracking stations located upstream and downstream of a dipole magnet with a bending power of about 4 Tm. The tracking system gives an excellent impact parameter resolution of $(15 + 29/p_t)\,\mu$m and measures the momentum of charged particles with a relative uncertainty from 0.5 % at low momentum to 1 % at 200 GeV/c. Charged hadrons identification is performed thanks to two ring-imaging Cherenkov detectors. Photons, electrons and hadrons are identified, and their energy is measured by a calorimeter system including an electromagnetic and a hadronic calorimeter. Finally, muons are identified by the outer muon stations. The online event selection is performed by a trigger, which consists of a hardware stage followed by a software stage for full event reconstruction.

The data set considered in this analysis consists of the full Run 1 and 2 data taking periods, corresponding to an integrated luminosity of $9\,fb^{-1}$ recorded at LHCb with pp collisions at centre-of-mass energies of 7 TeV (2011), 8 TeV (2012) and 13 TeV (2015-2018).

Data selection and background analysis

Taking the "raw" data from LHCb, the first step is to extract the interesting signal. The goal of the selection is then to develop a discrimination tool maintaining the signal efficiency to the highest possible level, while rejecting the combinatorial and physical background as much as possible.

The selection is designed and optimized using the reference decay channel $B^\pm \to D^0(\to K_s^0\pi^+\pi^-\pi^0)\pi^\pm$, which is statistically favored compared to $B^\pm \to D^0K^\pm$ ($\mathcal{B}(B^\pm \to D^0\pi^\pm) = (12.67 \pm 0.43) \times \mathcal{B}(B^\pm \to D^0K^\pm)$), with a similar topology and less sensitivity to CP asymmetry. In order to optimize the selection for each step, we compare the expected signal from phase-space Monte-Carlo simulation with the background from data "side-bands", where only background is expected, for some well-defined discriminating variables. The selection is made in a bottom-up strategy, from the final particles to D^0 and $B^\pm$ mesons, each step being optimized using the output of the previous one. It consists on a three-step strategy: a first multivariate analysis (MVA) based on a MultiLayer Perceptron (MLP) on geometrical and topological variables from the D^0 decay; rectangular cuts on K_s^0, π^0 and D^0 mesons reconstructed masses; a second MVA using an MLP method on geometrical and topological variables from the $B^\pm$ decay.

Then, a particle identification (PID) selection is applied to remove most of the bachelor track mis-identification background. In particular, in the absence of such a selection, the $B^\pm \to D^0K^\pm$ signal would be flooded under mis-identified pions. Finally, a third MVA has been developed to choose the best candidate in case of multiplicity (several candidates for the same pp collision).

The optimization of this study leads to more than 35 % efficiency on the signal with a rejection factor on combinatorial background of around 10^3. Concerning the PID selection, one obtains 70.7 % efficiency on $B \to D^0K$ signal with only 2.6 % efficiency on misidentified events.

After the selection, a deep study of residual physical backgrounds has been performed. Physical background is described as the background coming from real decay channels, which can be mis-reconstructed or partially reconstructed, in opposition to combinatorial background, where particles from primary vertex or other decays are associated to reconstruct a non-real candidate. Studying an exhaustive set of physical background decay channels, using Monte-Carlo simulated samples for every possible one, on which the selection has been applied, it has been shown that no peaking background is seen. However, the shapes of the main backgrounds have been studied to include them in the nominal fit, in particular in order to take into account their possible tail under the signal.

Nominal fit and current results

In order to get the signal yields in each bin, a fit is needed to handle the different sources of background. A bin-integrated fit of the $B^\pm$ invariant mass distribution is then computed for both $B \to D\pi$ and $B \to DK$ channels on events surviving the whole selection. As previously, the strategy is to first fit parameters on the $B \to D\pi$ reference channel, which have more statistics, and then fix most of the fit parameters for $B \to DK$. We proceed with maximum likelihood fits on the mass window $m(B^\pm) \in [5.0, 5.66]\,\mathrm{GeV/c^2}$.

Note that the reconstructed mass has been processed through the DecayTreeFitter (DTF) tuple tool [12], which kinematically refit the signal decay chain with a number of geometrical and topological constraints, where in particular D^0, K_s^0, and π^0 mesons masses are constrained to their PDG values and the $B^\pm$ meson is constrained to originate from its assigned primary vertex. This DTF methods enables to improve the mass resolution by approximately 40 %.

Here is a list of the several components of the $B^\pm$ invariant mass fit :

- The signal : Signal shape is extracted from corrected simulation fit with a double-sided Crystal-Ball distribution. Mean and width, as well as the right tail, are free parameters for $B \to D\pi$ channel and are fixed accordingly for $B \to DK$ channel.
- The combinatorial background is fitted as a second order Chebychev polynomial. Note that other shapes will be tested and the difference will be included as a systematic.
- The Physical Background : we consider main contributors from the background study. The shapes are taken from the simulation corrected for the difference with data, and the ratio between each backgrounds is constrained according to their branching fraction and the efficiency of selection.
- The Cross-Feed : This is the component coming from the mis-identification of the hadron coming from the $B^\pm$ meson decay, when the mis-identified particle survives the PID selection. Due to the mass difference between a pion and a kaon, a mis-identified pion event leads to a higher reconstructed $B^\pm$ mass in $B \to DK$ analysis. This is the opposite for a mis-identified kaon in $B \to D\pi$ analysis. The shape is taken from simulated sample for $B \to D\pi$ and from $B \to D\pi$ data with mis-identification hypothesis for $B \to DK$. The yields are calculated according to the selection efficiency and branching fraction difference.

The integrated nominal fits are then shown in Fig. 3 and 4 for $B \to D\pi$ ad $B \to DK$ channels respectively. We obtain a yield of 1935 ± 66 events in $B^\pm \to D^0K^\pm$ channel, which is more than twice the statistics owned by the corresponding Belle analysis [9], with a similar purity at 2σ around the signal peak of 60.2 %. Also note that, as expected, the global asymmetry between B^+ and B^- is consistent with 0.

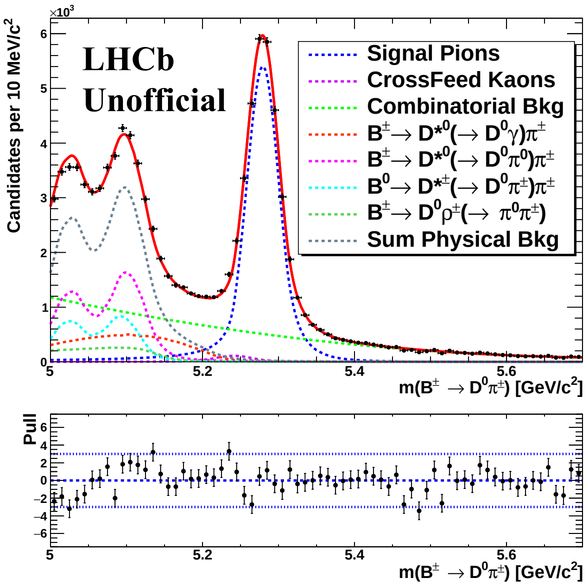

Figure 3: $m_{DTF}(B^{\pm})$ distribution fit in data for $B^{\pm} \to D^0\pi^{\pm}$ channel, with signal and background components.

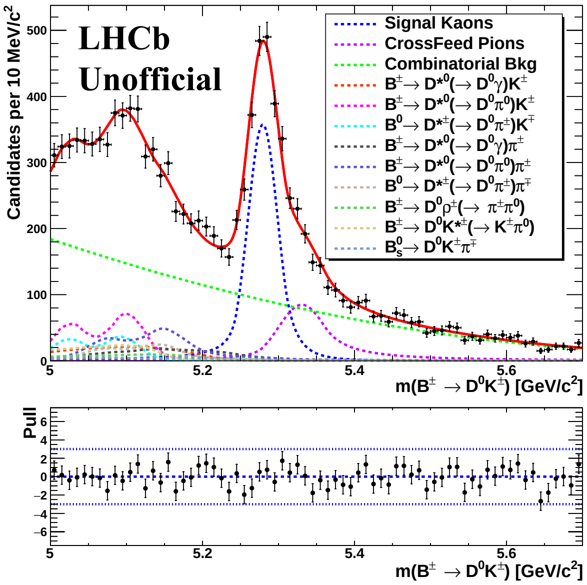

Figure 4: $m_{DTF}(B^{\pm})$ distribution fit in data for $B^{\pm} \to D^0K^{\pm}$ channel. This is the so-called nominal fit.

Prospects

After the selection, the background study and the parameterization of a nominal fit, the next step will be to extract the physical parameters from signal thanks to a simultaneous fit on the nine bins for B^+ and B^- categories and for $B \to DK$ and $B \to D\pi$ channels as this last one will be used to extract the K_i and $\bar{K}_i$ parameters. Then a final fit will be processed to measure the γ angle. In addition, a deep study of the systematic uncertainties is still to be done.

Considering that we have twice the Belle analysis statistics, and according to the current average value of r_B (which quantifies the sensitivity of a channel to γ), one can expect a statistical error of about $16-21°$.

Moreover, it is planned to work on an amplitude analysis of the D^0 decay leading to a continuous map of $\Delta\delta_D$ and then a more precise model-dependent γ angle measurement. In addition, as we expect the uncertainty to be statistically dominated, this measurement precision should benefit from the Run 3 data, which should give five times more statistics than the current Run 1+2 dataset.

References

[1] A. Sakharov, Violation of CP invariance, C asymmetry and baryon asymmetry of the universe, JETP Letters 5 (1967) 24.

[2] N. Cabibbo, Unitary symmetry and leptonic decays, Phys. Rev. Lett. 10 (1963) 531.

[3] M. Kobayashi and T. Maskawa, CP-violation in the renormalizable theory of weak interaction, Prog. Theor. Phys. 49 (1973) 652.

[4] CKMFitter group, J. Charles et al., Future sensitivity to new physics in B_d, B_s and K mixings, Phys. Rev. D 89 (2014) 033016.

[5] LHCb Collaboration, Simultaneous determination of the CKM angle γ and parameters related to mixing and CP violation in the charm sector, LHCb-CONF-2022-003, 2022.

[6] CKMFitter group, J. Charles et al., CKMFitter global fit results as of Spring 21, 2021.

[7] A. Giri, Y. Grossman, A. Soffer, and J. Zupan, Determining γ using $B^{\pm} \to DK^{\pm}$ with multibody D decays, Phys. Rev. D 68 (2003) 071301.

[8] LHCb Collaboration, R. Aaij et al., Measurement of the CKM angle γ in $B^{\pm} \to DK^{\pm}$ and $B^{\pm} \to D\pi^{\pm}$ decays with $D \to K^0_s h^+h^-$, JHEP 02 (2021) 0169.

[9] The Belle Collaboration, P. K. Resmi, J. Libby, K. Trabelsi et al., First measurement of the CKM angle ϕ_3 with $B^{\pm} \to D(K^0_s\pi^+\pi^-\pi^0)K^{\pm}$ decays, JHEP 10 (2019) 178.

[10] P. K. Resmi, J. Libby, S. Malde, and G. Wilkinson, Quantum-correlated measurements of $D^0 \to K^0_s\pi^+\pi^-\pi^0$ decays and consequences for the determination of the CKM angle γ, JHEP 01 (2018) 082.

[11] LHCb collaboration, A. A. Alves Jr. et al., Te LHCb detector at the LHC, JINST 3 (2008) S08005.

[12] W. D. Hulsbergen, Decay chain fitting with a Kalman filter, Nucl. Instrum. Meth. A552 (2005) 566.

Combined angular analysis of $B \to D^{*} e\nu_{e}$ and $B \to D^{*}\mu\nu_{\mu}$ at the LHCb detector

Bogdan Kutsenko

Aix Marseille Univ, CNRS/IN2P3, CPPM, Marseille, France

Abstract — Semileptonic b-hadron decays provide powerful probes for testing lepton flavor universality. In the standard model the interactions of electroweak bosons with leptons are independent of the lepton flavor, however, interference between the Standard Model charged weak interaction and hypothetical New Physics currents can result in violation of this universality. Fundamental couplings of potential New Physics currents can be extracted from experiments using angular analysis techniques. In particular for $B \to D^{*}\ell\nu_{\ell}$ decays theoretically clean angular observables can be constructed. Distributions of angular observables are well defined as a linear combination of angular functions. Angular coefficients of these terms depend on fundamental couplings and can be extracted from the fit. Therefore, measurements of angular coefficients are sensitive to a variety of New Physics contributions to the Lagrangian. However, the analysis suffers from heavy biases due to neutrino reconstruction and non-linear detector efficiencies. An MC feasibility study of the $B \to D^{*}e\nu_{e}$ and $B \to D^{*}\mu\nu_{\mu}$ angular analysis with the LHCb detector is performed. The sensitivity of such analysis to some New Physics currents is tested.

Introduction

Several intriguing hints on deviations from the Standard Model (SM) predictions have appeared in the studies of decays of B hadrons involving leptons [1, 2, 3]. The most striking deviation is the hint of violation of lepton flavor universality (LFU), which states that the interactions of the electroweak bosons with the leptons are independent of the lepton flavor. LFU can be tested with ratios of branching fractions to final states with different lepton flavors:

$$R(D^{*})_{e/\mu} = \frac{Br(B^{0} \to D^{*}e\nu_{e})}{Br(B^{0} \to D^{*}\mu\nu_{\mu})}$$

This value is a convenient probe of the SM because hadronic uncertainties are largely canceled in the ratio. To even further reduce the impact of the systematic uncertainties and understand in more details the underlying physics processes, angular analysis are commonly done. Theoretically clean angular observables can be constructed for $B^{0} \to D^{*}\ell\nu_{\ell}$. The observables are defined in the B^{0} rest frame and shown in Fig. 1.

Since the angular dependence is theoretically well-known [3], angular coefficients can be extracted from the fit of angular observables. Furthermore, New Physics (NP) can be characterized in this way because angular coefficients are directly proportional to Lagrangian couplings [4].

Such an angular analysis with $B^{0} \to D^{*}e\nu_{e}$ and $B^{0} \to D^{*}\mu\nu_{\mu}$ was conducted by the Belle collaboration by measuring the values of angular coefficients [3, 6]. Initially, in the untagged analysis of Belle data, some hints for LFU violation were observed, for example, $\sim 4\sigma$ discrepancy with the SM in the difference between electron and muon forward-backward asymmetry $\Delta A_{FB}^{\ell} = A_{FB}^{\mu} - A_{FB}^{e}$. The analysis of the Belle dataset was updated using B-tagged measurements and no significant discrepancies with the SM were observed. However, due to the additional B-tagging, the statistical uncertainty of the angular coefficients is substantially increased.

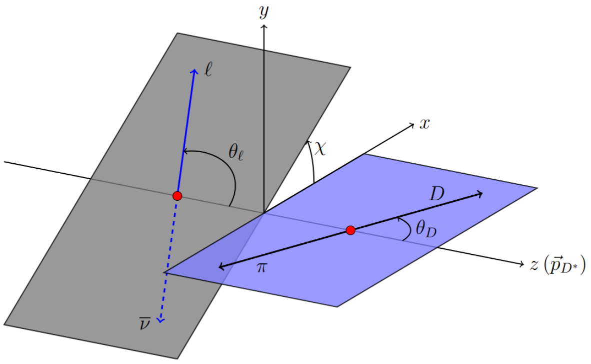

Figure 1: Definition of angular observables: $\cos\theta_{\ell}, \cos\theta_{D}, \chi$. Picture is taken from [8]

The Belle measurement can be cross-checked with the LHCb detector and one can obtain values of forward-backward lepton asymmetry and D* polarization from the fit. The analysis suffers from biases in angular distributions caused by non-uniform detector efficiencies and limited resolution of neutrino reconstruction. To resolve this bias, a model-independent template fit approach was implemented [8].

Angular analysis methodology

Differential distributions

Assuming a purely P-wave $D\pi$ final state, the four-dimensional differential distribution $\frac{d\hat{\Gamma}^{(\ell)}}{dq^2 d\cos\theta_\ell d\cos\theta_D d\chi}$ can be fully described by 12 q^2 dependant angular coefficients [8]. By integrating two angles out of three, the following one-dimensional differential distributions can be obtained:

$$\frac{1}{\hat{\Gamma}^{(\ell)}}\frac{d\hat{\Gamma}^{(\ell)}}{d\cos\theta_\ell} = \frac{1}{2}\cdot 1 + \langle A_{FB}^{(\ell)}\rangle\cos\theta_\ell + \frac{1}{4}(1-3\langle\tilde{F}_L^{(\ell)}\rangle)\frac{3\cos^2\theta_\ell - 1}{2} \tag{1}$$

$$\frac{1}{\hat{\Gamma}^{(\ell)}}\frac{d\hat{\Gamma}^{(\ell)}}{d\cos\theta_D} = \frac{3}{4}(1-\langle F_L^{(\ell)}\rangle)\sin^2\theta_D + \frac{3}{2}\langle F_L^{(\ell)}\rangle\cos^2\theta_D \tag{2}$$

$$\frac{1}{\hat{\Gamma}^{(\ell)}}\frac{d\hat{\Gamma}^{(\ell)}}{d\chi} = \frac{1}{2\pi}\cdot 1 + \frac{2}{3\pi}\langle S_3^{(\ell)}\rangle\cos 2\chi + \frac{2}{3\pi}\langle S_9^{(\ell)}\rangle\sin 2\chi \tag{3}$$

These projections depend on five q^2 integrated angular coefficients : $\langle A_{FB}^{(\ell)}\rangle$,$\langle\tilde{F}_L^{(\ell)}\rangle$, $\langle F_L^{(\ell)}\rangle$, $\langle S_3^{(\ell)}\rangle$ and $\langle S_9^{(\ell)}\rangle$. $\langle S_9^{(\ell)}\rangle$ vanishes in CP averaged measurements. Furthermore, angles are biased due to neutrino reconstruction effects [9] and non-linear detector efficiencies. Taking into account heavy biases, projections Eq. (1) to Eq. (3) cannot be used directly in the binned fit to extract angular coefficients.

To resolve the discrepancies between reconstructed and true angles, the model-independent fit approach from [8] was implemented. Angular functions from Eq. (1) to Eq. (3) were changed to the appropriate templates h_X that include the reconstruction and acceptance effects:

$$\begin{aligned}\frac{1}{\hat{\Gamma}^{(\ell)}}\frac{d\hat{\Gamma}^{(\ell)}}{d\cos\theta_\ell} = (\frac{1}{2} - \frac{1}{8}(1-3)\langle\tilde{F}_L^{(\ell)}\rangle)h_{const,\theta_\ell} + \\ +\langle A_{FB}^{(\ell)}\rangle h_{\cos\theta_\ell} + \frac{3}{8}(1-3\langle\tilde{F}_L^{(\ell)}\rangle)h_{\cos^2\theta_\ell}\end{aligned} \tag{4}$$

$$\frac{1}{\hat{\Gamma}^{(\ell)}}\frac{d\hat{\Gamma}^{(\ell)}}{d\cos\theta_D} = \frac{3}{4}((1-\langle F_L^{(\ell)}\rangle)h_{const,\theta_D} + (3\langle F_L^{(\ell)}\rangle - 1)h_{\cos^2\theta_D} \tag{5}$$

$$\frac{1}{\hat{\Gamma}^{(\ell)}}\frac{d\hat{\Gamma}^{(\ell)}}{d\chi} = (\frac{1}{2\pi} - \frac{2}{3\pi}\langle S_3^{(\ell)}\rangle)h_{const,\chi} + \frac{2}{3\pi}\langle S_3^{(\ell)}\rangle h_{(1+\cos 2\chi)} \tag{6}$$

Each template is obtained by reweighing the reconstructed angles with weights

$$\omega_X = \frac{f_X}{I_X\cdot f_X}, \tag{7}$$

where f_X is the appropriate angular function and I_X is the true angular coefficient generated in MC simulation.

Signal-only fit on MC

An example of the templates for each angular function in the $\cos\theta_\ell$ differential distribution for SM MC is presented in Fig. 2. The result of a template fit of Eq. (4) is shown in Fig. 3.

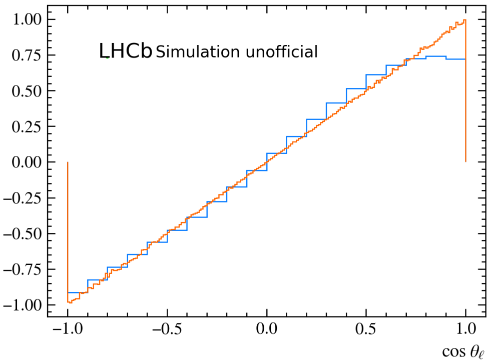

(a) $\cos\theta_\ell$

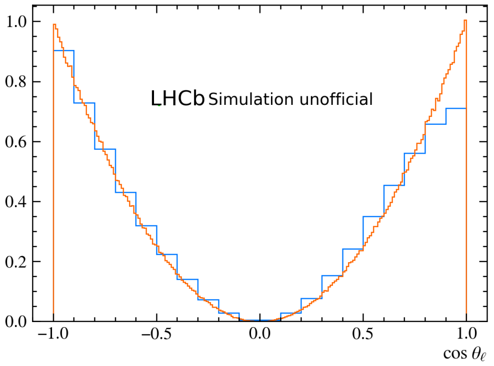

(b) $cos^2(\theta_\ell)$

Figure 2: Templates for different angular functions from $\cos\theta_\ell$

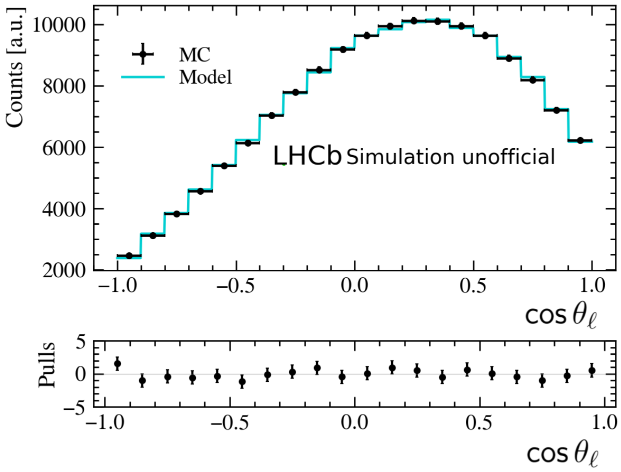

Figure 3: Results of a template fit to the SM MC

The comparison of the uncertainties we expect from a fit of data from LHCb Run 2 taken from 2016 to 2018 with integrated luminosity of 5.7 fb^{-1} and the statistical uncertainties of angular coefficients obtained from Belle data is presented in Fig. 4. Results are obtained from the SM MC template fit of the $\cos\theta_\ell$ differential distribution. The estimated statistical uncertainty is lower than the uncertainty in Belle's result by a factor of 15. However, the final results on data are expected to be dominated by systematical uncertainty, the main contributions to which are the $B \to D^{**}\ell\nu_\ell$ background decay model, MC corrections, and the limited size of the MC sample for the templates.

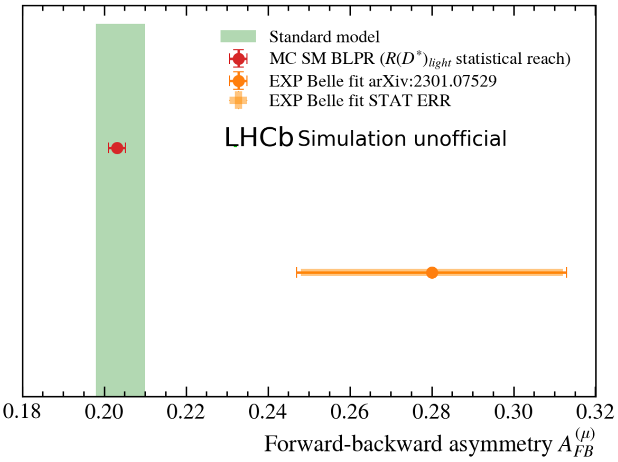

(a) $B \to D^*\mu\nu_{mu}$

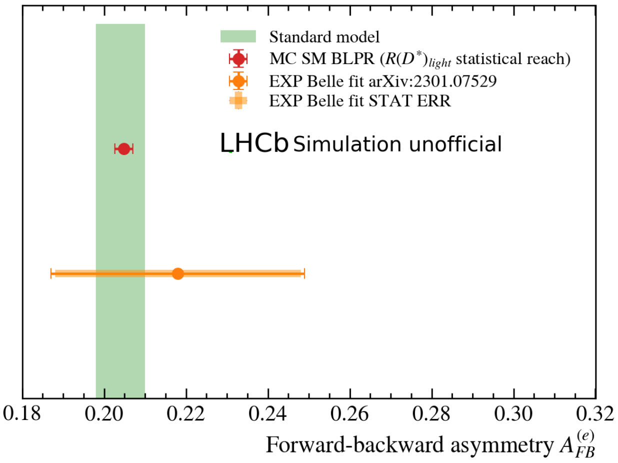

(b) $B \to D^*e\nu_e$

Figure 4: Comparison of expected statistical uncertainty for $\langle A_{FB}^{(\ell)} \rangle$ with Belle results [6]. Estimation is based on MC studies. SM MC was obtained using BLPR formfactor parametrisation [7]

Model independence

An essential part of the template fit is model independence. Since the weights are calculated as a ratio of an angular function to the true angular distribution and then applied to the reconstructed angles, most of the model dependence should be neglected in this ratio. This is accurate for a variety of NP contributions to a certain extent of coupling amplitude. The simplest way to check model independence is to reweigh the MC sample in all reasonable NP scenarios with different amplitudes and obtain templates separately for each reweighed sample. An example of such templates for $cos\theta_\ell$, obtained from a left-handed vector current addition to the Lagrangian [4] with different amplitudes is presented in Fig. 5. With increasing amplitude of left vector current NP coupling V_{qRIL}, discrepancies between templates become more apparent reaching up to 20 % at $cos\theta_\ell$ = -1.

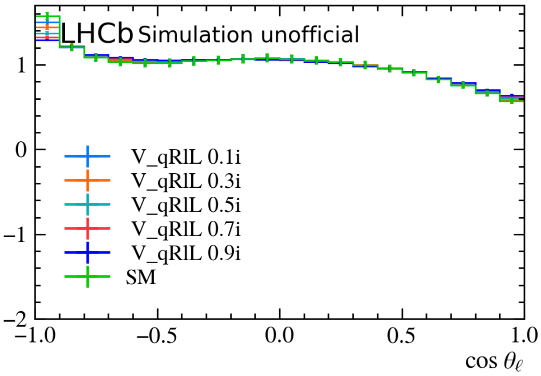

(a) Constant

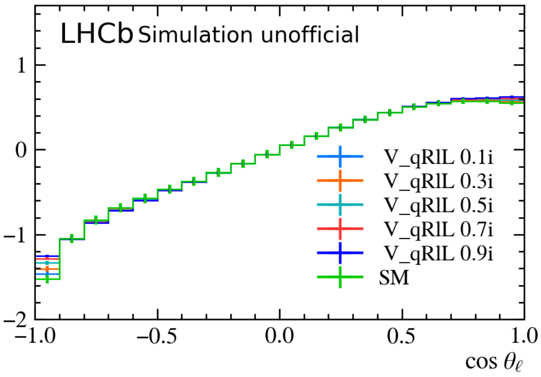

(b) $\cos\theta_\ell$

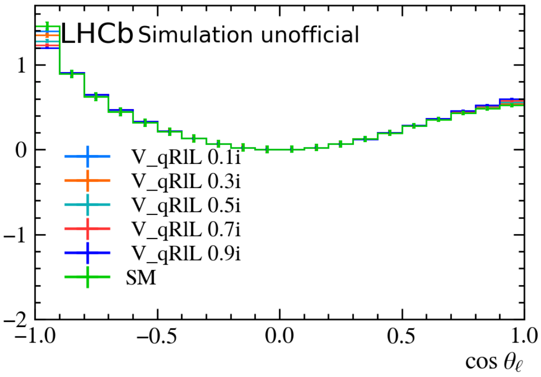

(c) $cos^2(\theta_\ell)$

Figure 5: Templates variation with different NP couplings amplitudes for $\cos\theta_\ell$ distribution

Sensitivity of the angular template fit to NP couplings

An essential property of the model-independent binned template fit approach is the sensitivity to different NP couplings. Each angular coefficient is proportional to a coupling or to the interference of couplings [4]. This sensitivity can be tested with reweighted MC. The example of an additional left vector current coupling with different amplitudes is presented for $B \to D^{*}\mu\nu_{\mu}$ in Fig. 6. Results in Fig. 7 show the value and statistical uncertainty of the angular coefficients.

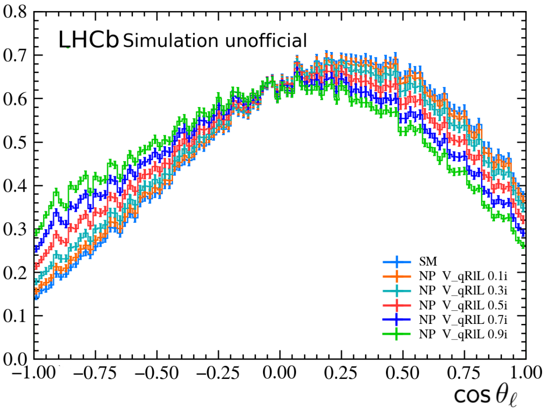

Figure 6: Distributions of $\cos\theta_\ell$ for left vector current NP contributions with different amplitudes

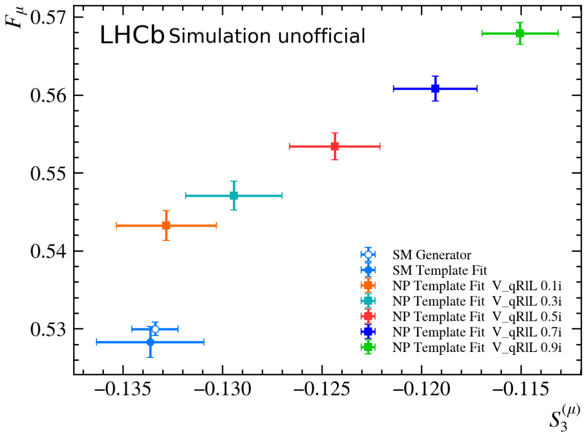

(a) Angular coefficients obtained from a template fit of $\cos\theta_D$ and χ 1D differential distributions

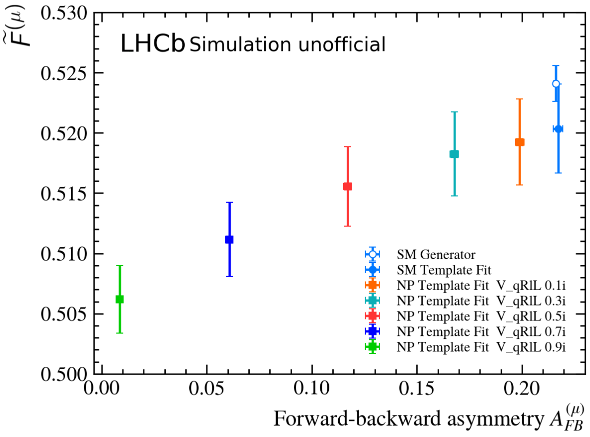

(b) Angular coefficients obtained from a template fit of $\cos\theta_\ell$ 1D differential distributions

Figure 7: Sensitivity test for a left vector current NP contribution with different amplitudes for $B \to D^{*}\mu\nu_{\mu}$

Conclusions

Precision measurements of angular observables provide an additional test of the SM which is complementary to the $R(D^{*})$ measurements since it has independent systematical uncertainties and allows to study the underlying physics processes. Feasibility studies of the angular analysis of $B \to D^{*}e\nu_{e}$ and $B \to D^{*}\mu\nu_{\mu}$ with the LHCb detector are performed using MC. The analysis is performed using a model-independent binned template fit of 1D angular differential distributions. The model independence of the approach and the sensitivity to NP effects are proven for a limited number of NP couplings. The expected statistical uncertainty for angular observables is estimated based on the statistical reach taken from data. The measurements can be competitive with the angular coefficients measurement from the Belle detector. It will be the first angular analysis at LHCb for $B \to D^{*}e\nu_{e}$.

References

[1] M. Bordone, N. Gubernari, D. van Dyk, and M. Jung, Eur. Phys. J. C 80, 347 (2020), arXiv:1912.09335 [hep-ph]

[2] HFLAV collaboration, Y. S. Amhis et al., Eur. Phys. J. C81 (2021) 226, arXiv:1909.12524, 1534 updated results and plots available at https://hflav.web.cern.ch/

[3] C. Bobeth, M.Bordone, and N. Gubernari et all, Phys. J. C81 (2021) 11, arXiv:2104.02094

[4] M. Duraisamy, P. Sharma, and A. Datta, Phys. Rev. D90, 074013 (2014), arXiv:1405.3719 [hep-ph].

[5] M. A. Ivanov, J. G. Korner, and C.-T. Tran, Phys. Rev. D 94, 094028 (2016), arXiv:1607.02932 [hep-ph].

[6] Belle Collaboration, M. T. Prim et al, arXiv:2301.07529

[7] F.U.Bernlochner, Z. Ligeti, M. Papucci, D.J. Robinson, Combined analysis of semileptonic B decay to D and $D^{\star}$: $R(D^{\star})$,|Vcb|, and new physics. Phys. Rev. D 95, 115008 (2017). arXiv:1703.05330

[8] D. Hill, M. John, W. Ke, and A. Poluektov, JHEP 11 (2019) 133, arXiv:1908.04643

[9] S. Dambach, U. Langenegger, and A. Starodumov, Nuclear Instruments and Methods in Physics Research Section A: Accelerators, Spectrometers, Detectors and Associated Equipment 569 (2006) 824

Improving Tracking Algorithms for ITk Detector at the HL-LHC

Jeremy Couthures

Laboratoire d'Annecy de Physique des Particules (LAPP)
CNRS, University Savoie Mont Blanc, France

Abstract — In anticipation of the High Luminosity phase of CERN's Large Hadron Collider, the ATLAS experiment is upgrading its core components with a new silicon tracker (ITk) to enhance track measurement accuracy and data processing speeds. However, this upgrade alone is insufficient to handle the expected luminosity increase and has to be coupled with significant improvements in the tracking software to maintain realistic computing requirements. This study is focused on the track seeds reconstruction for the ITk detector and explores the possibility to use hashing techniques to improve the seed reconstruction efficiency, manage the combinatorial challenges, and eventually reduce overall computational time. The code developments are done within the ACTS framework, an experiment-independent toolkit for charged particles track reconstruction.

Introduction

Motivation

To prepare for the High Luminosity phase of the Large Hadron Collider at CERN (HL-LHC), the ATLAS experiment is replacing its innermost components with a full-silicon tracker[1, 2], the Inner Tracker (ITk) detector, improving the spatial resolution of the tracks measurements and increasing the data readout rate. This upgrade of the tracker will extend its pseudorapidity coverage from $|\eta| \leq 2.7$ with the current Inner Detector to $|\eta| \leq 4.0$ for ITk. The tracker will then be able to detect particles in a region uncovered before, and the granularity of the detector will also be increased. The luminosity is linked to the number of collisions per seconds. Due to the current luminosity at the LHC, it is not possible to resolve each collision separately. Therefore the collisions pile-up in an event, and the corresponding hits are superimposed in the detector. The average number of collisions in an event, denoted μ, will increase from around 34 in Run 2, up to 200 for the HL-LHC. The complexity of the tracking problem will then significantly increase with the HL-LHC phase. The tracker upgrade alone will not be sufficient to cope with the tremendous increase of luminosity, and significant improvements have to be incorporated at every step of the existing software to keep the required computing resources at a realistic level.

Tracking chain

The standard track reconstruction chain is shown in Figure 1.
It starts by converting the hits in the detector into space points and clusters. The second step consists in finding triplets of space points compatible with a particle coming from the interaction point, forming a seed. Each seed is then expanded with the remaining space points using a Combinatorial Kalman Filter (CKF), forming the track candidates. To address the issue of overlapping track candidates, a final step is necessary to solve the ambiguities. This step also involves removing incorrect combinations of space points ("fake tracks") and duplicated tracks.

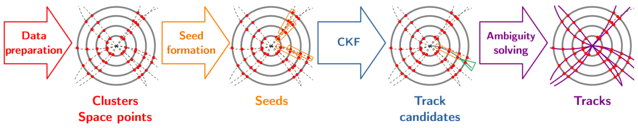

Figure 1: Steps of the track reconstruction chain. Credits: Noemi Calace

This work focuses on the track seeds reconstruction, exploring the possibility to use hashing techniques to improve the reconstruction efficiency, limit the combinatorics and eventually reduce the computing time.

ACTS Framework

The framework used is A Common Tracking Software[5] (ACTS). It is an experiment-independent toolkit for tracking. It includes a fast tracking detector simulation, Fatras, based on the ATLAS fast track simulation[7], but can also be combined with other common simulation softwares such as Geant4[6] or Pythia8[8].

ACTS Configuration

In this study, we use samples of 100 $t\bar{t}$ events generated with Pythia8 and propagated with ACTS Fatras. No secondary particles are included. The preselection applied to the particles are referenced in the Table 1. Those particles correspond to the reconstructible particles. Different samples are generated for the pile-up values $\mu = 50$, 100 and 150. The detector used is the generic detector from ACTS, a detector based on the TrackML[9] detector, this model represents only active detector elements, no other material is defined.

Variable	Value
$\lvert\eta\rvert$	≤ 4.0
p_T	> 1 GeV
number of hits	> 9

Table 1: Preselections applied on the particles.

The last step of the tracking chain, the ambiguity resolution step, is not used in this study.

Evaluation

The evaluation is performed at the level of the track, after the CKF algorithm. The quantities used to evaluate the performances are:

$$\text{efficiency} = \frac{\#\text{ tracks matched to a truth particle}}{\#\text{ reconstructible particles}}$$

$$\text{fake rate} = \frac{\#\text{ tracks not matched to truth particle}}{\#\text{ reconstructed tracks}}$$

$$\text{duplication rate} = \frac{\#\text{ reconstructible particles with} > 1\text{ track match}}{\#\text{ reconstructible particles}}$$

CPU time

Performances

In order to reduce the number of seeds to expand as track candidates, a maximum number of seeds sharing the same middle space point (maxSeedsPerSpM cut) is applied in ACTS, keeping only the ones with the best quality score. The quality score is linked to the number of compatible measurements with the seed and the estimated interaction point.

For this study, the value of the maximum number of seeds sharing the same middle space point is set to 1 to favour timing performance.

The impact of the maxSeedsPerSpM cut on the performance is shown on the Figure 2. The ratios of the tracking efficency, fake rate and duplication rate, of the tracking chain without the maxSeedsPerSpM cut and with the default configuration are shown as a function of the pseudorapidity η. A value higher than 1 means that the maxSeedsPerSpM cut has an impact on this pseudorapidity range.

In the transition regions between the barrel and the endcaps (around $|\eta| = 2$), as well as in the new forward region to be covered by the ITk detector ($|\eta| > 2.7$), the efficiency is negatively affected by the maxSeedsPerSpM cut. These regions exhibit a different behavior compared to the barrel region. The transition regions are mainly influenced by pile-up, indicated by increasing ratios with higher pile-up values. A high number of seeds in the transition regions leads to keeping fake tracks with higher quality scores than those of true particles. This trend is not observed in the forward region.

For the duplication rate, the whole barrel region is influenced by pile-up while the forward region is not.

Regarding the fake rate, the impact of the maxSeedsPerSpM cut is minimal in the forward region, suggesting that most seeds in this region corresponds to true particles. However, in the barrel region, filtering out low-quality seeds reduces the number of fake tracks reconstructed.

The barrel region then benefits from a small value of the maxSeedsPerSpM while the new region benefits from a high value. For the transition regions, a compromise as to be found between efficiency and fake rate.

Hashing

To maintain the timing performance, the explored approach keeps the maxSeedsPerSpM limit while attempting to mitigate its negative impacts. This is done by clustering similar space points into *buckets* and performing the seeding separately on each *bucket*. The Annoy[10] algorithm is used to perform the clustering.

Clustering algorithm: Annoy

Annoy is a Machine Learning algorithm of the k-Nearest Neighbors family. It approximates the neighborhood of a given point by expanding the search using distances between groups of points rather than direct distances between points. This process begins with the random selection of two points, then, a hyperplane is created between them, dividing the space into two sections. This division process is recursively applied to each section until each of them contains a maximal number of points. Internally, Annoy's splitting method is structured like a binary tree. The approximation of the neighborhood depends on the quantity of randomly generated trees.

When searching for the neighbors of a point, Annoy first considers the distances between the points in the same section across different trees, then expands the search to adjacent sections, starting from the ones with the smallest inter-section distance.

Searching for neighbors requires defining the distance between the space points, a metric is therefore necessary. The bucket size, which determines the number of neighbors, significantly impacts the clustering process. A larger bucket size increases the combinatorics, affecting timing performance, whereas a smaller size may fail to cluster sufficient space points from the same particle, compromising physics performance.

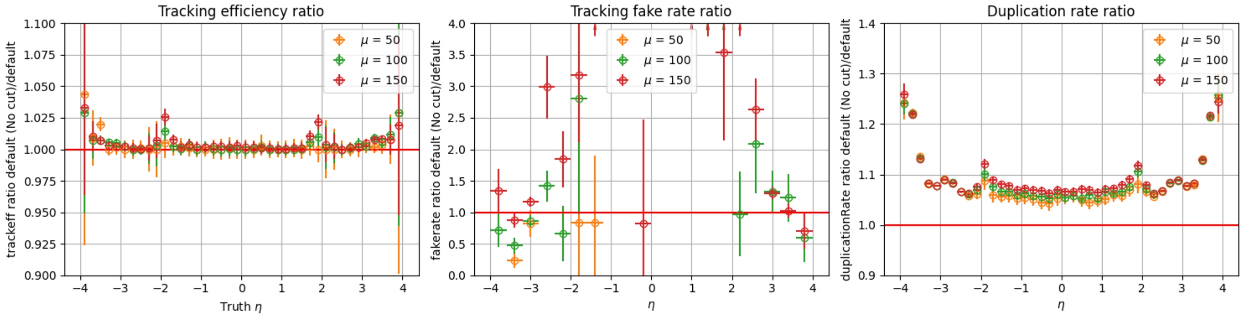

Figure 2: Physics performance ratios of the tracking chain in the default configuration without/with the maxSeedsPerSpM cut.

Metric and Bucket Size

The combination of the metric with the bucket size defines then the performance of the algorithm. At fixed *recall* performance (the fraction of space points of a track retrieved), the better the metric is, the lower the requirement on the bucket size.

The metric used is $\Delta\varphi$. It corresponds to the angle difference between the projections on the unit circle of the space points. It is well suited for radial tracks, the ones coming from the center of the detector and which are almost straight. As the influence of the magnetic field on high p_T tracks is minimal, it tends to keep $\Delta\varphi$ small, making the metric works well for those tracks.

To maintain good physics performance while reducing the combinatorics, the bucket size is chosen such that the total tracking efficiency is (almost) independent of the pile-up. Based on Figure 3, the bucket size is set to 100 space points. For this bucket size, the total tracking efficiency with Hashing reaches back the efficiency without Hashing for the values of μ up to 100.

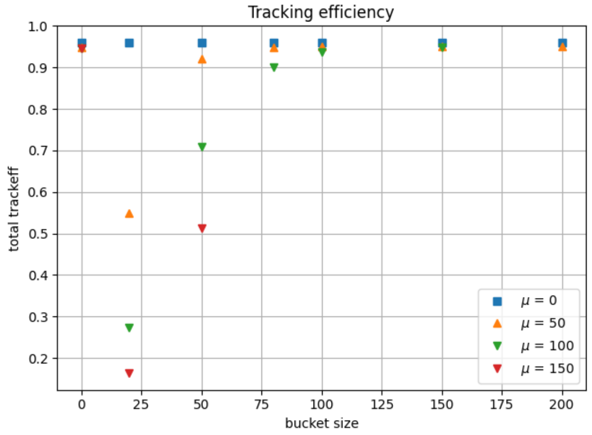

Figure 3: The total tracking efficiency as a function of the bucket size for different values of μ.

Super buckets

In the Hashing approach, space points that are close to each other are frequently in each other's bucket, thereby introducing overlaps between these buckets. A seed might then be reconstructed several times as it can be entirely found in several buckets. In practice, a seed is reconstructed 14 times on average, which ends up doubling the running time of the tracking chain with Hashing.

To reduce the overlaps between the buckets, a binning along the z axis is performed on the first layer of the detector, as shown in the Figure 4 (Left). The buckets corresponding to the space points found inside the same bins are merged together into a *Super bucket*, illustrated in the Figure 4 (Right). The number of Super buckets corresponds then to the number of z bins used.

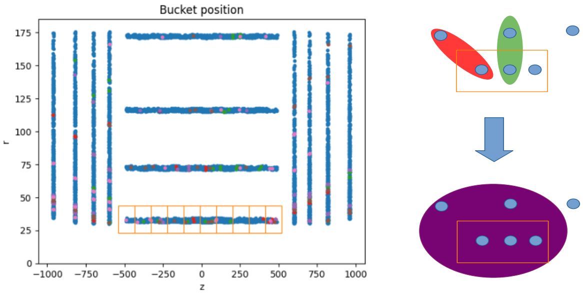

Figure 4: Visualization of the Super bucket construction with (**Left**) the position of the bins inside the detector and (**Right**) an illustration of the merging of the buckets inside a bin.

When this approach is applied using a single bin and a large enough bucket size, all space points are contained within the Super bucket, hence, corresponds to the configuration without Hashing.

Results & Discussion

The results of this study are shown on the Figure 5.

Binnings according to z (left column of the figure) and φ (right column of the figure) are compared.

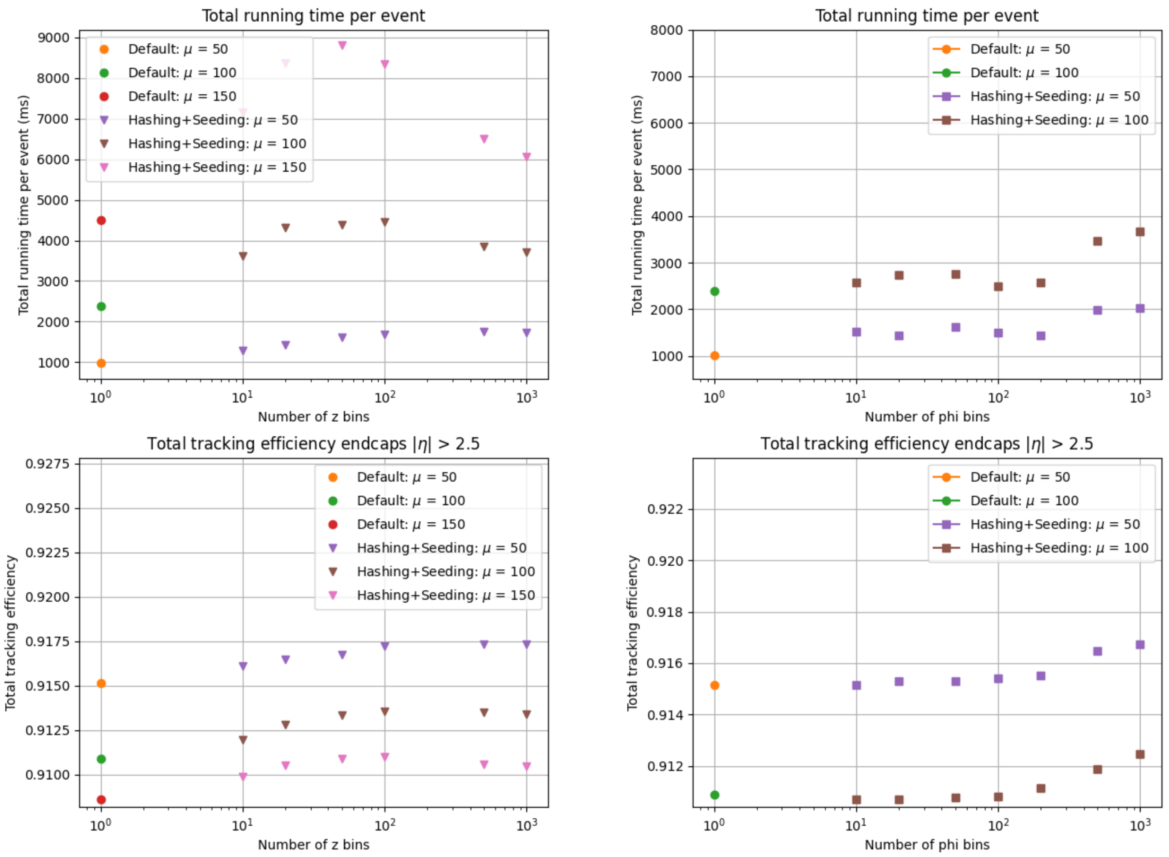

Figure 5: Timing (**Top Row**) and Physics (**Bottom Rows**) performance with binning along z (**Left Column**) and along φ (**Right Column**). The default configuration is shown with one bin. The $\Delta\varphi$ metric and a bucket size of 100 are used for all of those results.

While the binning according to z almost doubles the total running time (Figure 5 (Top Row) (Left)), the binning according to φ keeps similar timing with respect to the default configuration (Figure 5 (Top Row) (Right)).

The running time is related to the number of seeds found, as processing more seeds takes more time on average. The binning according to z then finds more seeds than the binning according to φ. This is due to the binning in z being unrelated to the metric used, regrouping then buckets with small overlaps between them, resulting in bigger Super buckets than the ones with a binning along φ, regrouping buckets with large overlaps between them as the metric depends on $\Delta\varphi$.

In the endcaps, both binnings improve the total tracking efficiency (Figures 5 (Bottom Row)), indicating that the seeds corresponding to truth particles have been recovered. This improvement confirms that this approach circumvent the maxSeedsPerSpM limit in the regions which benefit from it.

Conclusions & Outlook

This first study has shown that the Hashing approach leads to comparable performance with the default configuration with a slight improvement in the endcaps. It allows to have a trade off between timing and performance (z binning vs φ binning). However, the timing is not better than the standard approach with the current implementation.

The upcoming step is to switch to the more realistic geometry of the ITk detector. The geometry being more granular, considering metric learning approaches might be necessary in order to improve the performance. Varying the bucket size with respect to the detector region might also be considered as different behavior has been observed between the barrel and the endcaps.

A more realistic simulation including secondaries and more events is also needed to get closer to the HL-LHC conditions. The overall approach can also be extended by performing, not only the seeding, but also the track finding on the buckets, reducing further the combinatorics of the tracking chain. Finally, an hybrid software approach might be considered by selecting either the standard approach or the Hashing approach with respect to the detector region allowing to retain the best performance of both.

References

[1] The ATLAS Collaboration. ‘Technical Design Report for the ATLAS Inner Tracker Pixel Detector’. Geneva: CERN, 2017. https://doi.org/10.17181/CERN.FOZZ.ZP3Q

[2] The ATLAS Collaboration. ‘Technical Design Report for the ATLAS Inner Tracker Strip Detector’. Geneva: CERN, 2017. https://cds.cern.ch/record/2257755.

[3] The ATLAS Collaboration. ‘Expected Tracking and Related Performance with the Updated ATLAS Inner Tracker Layout at the High-Luminosity LHC’. Geneva: CERN, 2021. https://cds.cern.ch/record/2776651.

[4] The ATLAS Collaboration. ‘ATLAS Software and Computing HL-LHC Roadmap’. Geneva: CERN, 2022. https://cds.cern.ch/record/2802918.

[5] Salzburger, Andreas, Paul Gessinger, Fabian Klimpel, Moritz Kiehn, Bastian Schlag, Hadrien Grasland, Robert Langenberg, et al. ‘A Common Tracking Software Project’. C++, 2023. https://doi.org/10.5281/zenodo.5141419. https://github.com/acts-project/acts.

[6] Agostinelli, S., J. Allison, K. Amako, J. Apostolakis, H. Araujo, P. Arce, M. Asai, et al. ‘Geant4-a Simulation Toolkit’. Nuclear Instruments and Methods in Physics Research Section A: Accelerators, Spectrometers, Detectors and Associated Equipment 506, no. 3 (1 July 2003): 250-303. https://doi.org/10.1016/S0168-9002(03)01368-8.

[7] Edmonds, K, S Fleischmann, T Lenz, C Magass, J Mechnich, and A Salzburger. ‘The Fast ATLAS Track Simulation (FATRAS)’. Geneva: CERN, 2008. https://cds.cern.ch/record/1091969.

[8] Bierlich, Christian, Smita Chakraborty, Nishita Desai, Leif Gellersen, Ilkka Helenius, Philip Ilten, Leif Lönnblad, et al. ‘A Comprehensive Guide to the Physics and Usage of PYTHIA 8.3’. SciPost Physics Codebases, 10 November 2022, 8. https://doi.org/10.21468/SciPostPhysCodeb.8.

[9] Amrouche, Sabrina, Laurent Basara, Paolo Calafiura, Victor Estrade, Steven Farrell, Diogo R. Ferreira, Liam Finnie, et al. ‘The Tracking Machine Learning Challenge: Accuracy Phase’, 231-64, 2020. https://doi.org/10.1007/978-3-030-29135-8_9.

[10] Bernhardsson, Eric. ‘Approximate Nearest Neighbors Oh Yeah’. C++. 2013. Reprint, Spotify, 30 November 2023. https://github.com/spotify/annoy.

Vector boson scattering in the ATLAS detector

Mathieu Markovitch

Laboratoire de Physique des deux infinis Irène Joliot-Curie – Université Paris-Saclay

Abstract — Vector boson scattering processes probe the fundamental structure of electroweak interactions and provide a high sensitivity to new physics phenomena affecting gauge and Higgs couplings. These processes are among the rarest ones in the Standard Model[1] and were observed during last years in the Large Hadron Collider[2]. Vector boson scattering is sensitive to trilinear and quartic gauge couplings, which can be studied in the framework of the Effective Fields Theories to set model-independent constraints on Beyond Standard Model physics. The semileptonic final state, where one of the scattered gauge boson decays hadronically into a quark/antiquark pair and the other boson decays leptonically into electrons, muons or neutrinos, has good statistics and allows to study several different couplings since it is inclusive. This process is expected to be observed. The various and complementary Vector boson scattering analyses performed in the ATLAS experiment allow to start a combination of the different results in order to set limits on dimension-8 operators.

Introduction

The description of elementary particles and their fundamental interactions is given by the Standard Model (SM)[3]. Despite its great prediction power, the SM has several outstanding problems: it does not include gravitation, cannot explain naturally why the Higgs boson mass is so low, does not exhibit dark matter candidates, cannot explain the predominance of matter over antimatter... These issues could be solved by modifications or extensions of the SM, that may lead to observable effects. Experimental searches and measurements in the ATLAS experiment at the Large Hadron Collider (LHC) exploit many processes obtained from high-energy protons collisions in order to find signs of Beyond Standard Model (BSM) physics. Among these measurements, Vector boson scattering (VBS) allows to probe the most fundamental structure of the electroweak (EW) interaction.

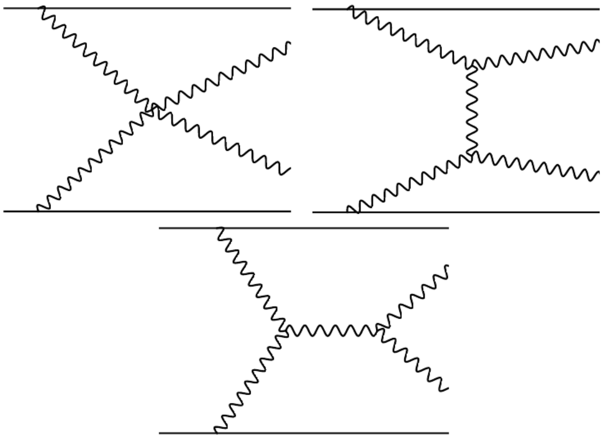

Figure 1: VBS graphs involving only gauge bosons (wiggly lines). The quarks are represented by straight lines.

VBS phenomenology

VBS are among the rarest processes of the SM, with typical cross-sections at the femtobarn level. It consists on the electroweak production of vector bosons associated with jets:

$$qq' \to V_3 V_4 jj$$

where the V_i are Z, W or γ. This is like a vector boson collision: high energy is needed. Figures 1 and 2 show different VBS Feynman graphs. A lot of different couplings can be involved: triple gauge couplings (TGCs), quartic gauge couplings (QGCs) and couplings with the Higgs boson. Without the Higgs boson, the cross-section of VBS processes would violate unitarity when this one increases, but adding diagrams with the Higgs boson cancels the divergence and gives a finite

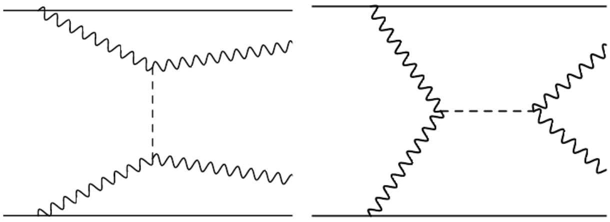

Figure 2: VBS graphs involving Higgs boson (dashed lines).

cross-section that makes the process visible. VBS observation is thus one of the proofs of an electroweak symmetry breaking and then an important corroboration of the SM[4]. However, since Higgs diagrams reduce the cross-section at high energy, they also make the process difficult to observe. TGC and QGC vertices are shown in Figure 3 Not all couplings are allowed in the SM: EW neutral couplings, such as $ZZ\gamma$ or $ZZZZ$, are forbidden. We can then search for deviations from SM in gauge couplings. VBS (and triboson) processes are the only ones that are sensitive to QGCs at tree-level. Thus they provide a unique way of probing BSM physics affecting these couplings. Alteration of QGC existing in the SM and addition of new QGC are called anomalous quartic gauge couplings (aQGC) and they can be studied in the Effective Field Theories (EFT) framework[5].

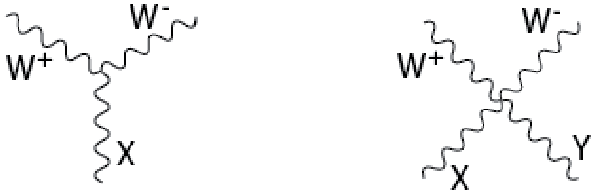

Figure 3: TGC (left) and QGC (right). X and Y are EW bosons such that charge is conserved.

EFT study of gauge couplings

If BSM physics exists, the fact that we have not seen it yet can be due to the fact that it is too weakly coupled or hidden in SM backgrounds (hence we need to increase statistics and improve theory predictions) or to the fact that it is at too high energy for the current accelerators (hence we need to increase the probed energy). EFT provide a model-independent way of looking at effects coming from BSM physics at an energy scale (Λ) that is not directly accessible. The idea is to expand the SM Lagrangian (mass dimension 4) to higher dimensions to get an effective Lagrangian:

$$\mathcal{L}_{EFT} = \mathcal{L}_{SM} + \frac{1}{\Lambda}\mathcal{L}_5 + \frac{1}{\Lambda^2}\mathcal{L}_6 + \frac{1}{\Lambda^3}\mathcal{L}_7 + \frac{1}{\Lambda^4}\mathcal{L}_8 + ... \quad (1)$$

written as sum of dimension-n terms:

$$\mathcal{L}_n = \sum_i C_i^n Q_i^n \quad (2)$$

where C_i^n are the Wilson coefficients and Q_i^n are the dimension-n operators that form a complete basis and are uniquely associated to the Wilson coefficients. In the SM there is no high dimension term hence Wilson coefficients are zero. Odd-dimension operators violate lepton or baryon number conservation and are usually ignored. Wilson coefficients associated to dimension-6 operators are constrained since dimension-6 can be probed with many analyses (*i.e.* different final states). Dimension-8 operators are not well known and can induce aQGCs, hence they constitute a VBS opportunity and we focus on them. In order to confront theory and measurement, we need to compute observables from EFT. They can be constrained using VBS processes. For instance we can predict cross-section from dimension-8 (squared) amplitude:

$$\mathcal{A}^2 = |\mathcal{A}_{SM}|^2 + 2\sum_i \frac{C_i}{\Lambda^4} Re(\mathcal{A}_i^* \mathcal{A}_{SM}) + 2\sum_i \frac{C_i^2}{\Lambda^8}|\mathcal{A}_i|^2 \quad (3)$$

$$+2\sum_{i \neq j} \frac{C_i C_j}{\Lambda^8} Re(\mathcal{A}_i^* \mathcal{A}_j) \quad (4)$$

where we can identify:

- A pure SM term $|\mathcal{A}_{SM}|^2$.
- An EFT-SM interference term linear in the Wilson coefficients $\sum_i \frac{C_i}{\Lambda^4} Re(\mathcal{A}_i^* \mathcal{A}_{SM})$.
- A quadratic EFT term $\sum_i \frac{C_i^2}{\Lambda^8}|\mathcal{A}_i|^2$.
- An EFT interference term between operators $\sum_{i \neq j} \frac{C_i C_j}{\Lambda^8} Re(\mathcal{A}_i^* \mathcal{A}_j)$.

The Eboli Model [6] provides a complete classification of dimension-8 operators with gauge bosons in initial and final states and respecting given symmetries. A valid dimension-8 operator can be built by combining different elements: four covariant derivatives of the Higgs field (*e.g.* $(D_\mu\Phi)^\dagger D_\nu\Phi(D^\mu\Phi)^\dagger D^\nu\Phi$) making a *scalar* operator, four field strength tensors (*e.g.* $B_{\mu\nu}B^{\mu\nu}B_{\alpha\beta}B^{\alpha\beta}$) making a *tensor* operator, or two covariant derivatives of the Higgs field and two field strength tensors (*e.g.* $B_{\mu\nu}B^{\mu\nu}(D_\beta\Phi)^\dagger D^\beta\Phi$) making a *mixed* (while dimension-6 operators can be obtained for instance by combining two covariant derivatives of the Higgs field and one field strength tensor or three field strength tensors). There are two useful scalar operators, to which we refer as f_{S0} and f_{S1}, seven useful mixed operators, to which we refer as f_{M0}, f_{M1}, f_{M2}, f_{M3}, f_{M4}, f_{M5} and f_{M7} and eight useful tensor operators, to which we refer as f_{T0}, f_{T1}, f_{T2}, f_{T5}, f_{T6}, f_{T7}, f_{T8} and f_{T9}. We often use the operator notation for the associated Wilson coefficient. The structure of each operator tells on which vertices this operator can have an impact (Table 1). The main problem for dimension-8 VBS studies is the unitarity violation: at high energy, aQGCs lead to interaction amplitudes that give probabilities higher than one. To prevent this, we usually introduce a cut-off (*clipping*) scale beyond which the

	SM				Not SM				
Operators	WWWW	WWZZ	WW$\gamma\gamma$	WWγZ	ZZZZ	ZZZγ	ZZ$\gamma\gamma$	Z$\gamma\gamma\gamma$	$\gamma\gamma\gamma\gamma$
f_{S0}, f_{S1}	X	X			X				
f_{M0}, f_{M1}, f_{M7}	X	X	X	X	X	X	X		
f_{M2}, f_{M3}, f_{M4}, f_{M5}		X	X	X	X	X	X		
f_{T0}, f_{T1}, f_{T2}	X	X	X	X	X	X	X	X	X
f_{T5}, f_{T6}, f_{T7}		X	X	X	X	X	X	X	X
f_{T8}, f_{T9}					X	X	X	X	X

Table 1: QGCs and operators impacting them.

Wilson coefficient is set to zero. Analyses can chose different clipping points but measured limits should beat unitarity limits. We can see in Figure 4 that the limit given by unitarity for the $ZZjj$ ATLAS analysis[7] is better than observed limits at energies higher than one TeV.

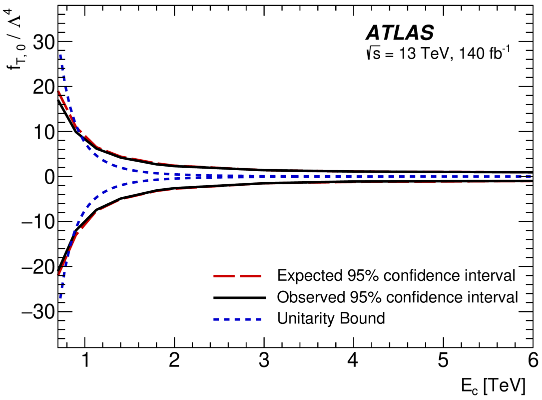

Figure 4: Expected, observed and unitarity limits for f_{T0} operator in $ZZjj$ analysis as function of clipping energy.

Search for VBS in semileptonic final state

Various analyses from LHC experiments study VBS. They focus on a dedicated final state *e.g.* $WWjj$ or $ZZ(\rightarrow llll)jj$. The semileptonic final state focus on the inclusive case where one gauge boson (W or Z) decays hadronically to a quark pair and the other one decays leptonically to a lepton pair:

- $V \rightarrow q\bar{q}'$, $Z \rightarrow \nu\bar{\nu}$ (*0-lepton* channel)
- $V \rightarrow q\bar{q}'$, $W \rightarrow l\nu$ (*1-lepton* channel)
- $V \rightarrow q\bar{q}'$, $Z \rightarrow l^+l^-$ (*2-leptons* channel)

where *lepton* is understood as *charged lepton*. These decays are interesting because the $V \rightarrow q\bar{q}'$ branching ratios are larger than the leptonic ones, allowing to observe more events. Moreover, the jets coming from the $q\bar{q}'$ pair can be well reconstructed in the high energy regime, which is more sensitive to aQGC. The main difficulty of the analysis is that these decays also have an important background of diboson QCD production as shown in Figure 5, Z production accompanied with jets (mainly in 0 and 2 leptons channels), W production accompanied with jets (mainly in 0 and 1 lepton channels) and top quark events (mainly in 1-lepton channel). The VBS signal (Figure 6) cannot be separated from other EW (non-VBS) diboson productions (Figure 7). We want to observe these signals in regions where VBS is enhanced. Multivariate techniques (RNN) are used to separate signal from the different backgrounds. Different objects need to be selected for this analysis: a pair of VBS *tagging* jets (hadronization of the quarks accompanying the scattering) that should be in opposite hemispheres and have transverse momentum $p_{\mathrm{T}} > 30$ GeV, invariant mass $m_{jj} > 400$ GeV and decay products of the gauge bosons. For the leptonically decaying boson:

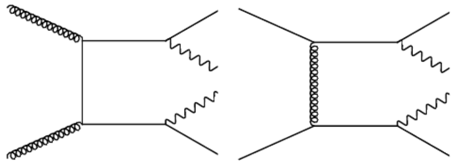

Figure 5: Two graphs for diboson QCD production.

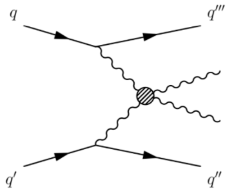

Figure 6: VBS signal. The central ball represents the different possible gauge couplings and propagators.

- 0-lepton channel: missing transverse energy $E_{\mathrm{T}}^{\mathrm{miss}} > 200$ GeV (only neutrinos).
- 1-lepton channel: one electron or muon with $p_{\mathrm{T}} > 30$ GeV, $E_{\mathrm{T}}^{\mathrm{miss}} > 80$ GeV (for the neutrino) and an additional b-quark veto.
- 2-leptons channel: two electrons or muons with $p_{\mathrm{T}} > 27$ GeV and invariant mass windows around Z mass.

For the hadronically decaying boson:

- Resolved regime: the two quarks lead to two small (radius parameter $R = 0.4$) jets.
- Merged regime: in case of high boost, the two quarks lead to one large (radius parameter $R = 1$) jet. In that case we use boosted jet tagging techniques based on jet substructures to identify the original boson.

The signal regions (SRs) of the analysis are defined based on the hadronically decaying boson: resolved, merged with purity (tight boson tagger working point) and merged with low purity (loose boson

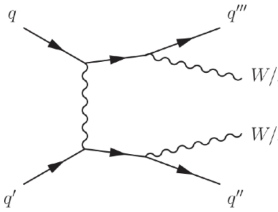

Figure 7: Non-VBS EW signal.

tagger working point), for each channel, which makes nine SRs. The control regions (CRs) are: V+jets resolved and V+jets merged (for each channel *i.e.* V=W for 1-lepton and V=Z for 2-leptons) and three top regions with a b-jet requirement instead of a b-veto (1-lepton channel only), which makes nine CRs. We then fit the signal strength parameter μ ($\mu = \sigma_{\mathrm{VBS}}^{\mathrm{observed}}/\sigma_{\mathrm{VBS}}^{\mathrm{SMpredicted}}$) as parameter of interest (POI). The standard fit is one POI for all channels and regions. Different systematics enter as nuisance parameters (NPs):

- Experimental systematics: reconstruction efficiencies of electrons and muons, jet energy scale and resolution, $E_{\mathrm{T}}^{\mathrm{miss}}$, tracks, b-tagging, luminosity, pile-up reweighting, boson tagging.
- Background systematics: modelling uncertainties, QCD and PDF on V+jets, diboson and top, initial and final state radiation on top, m_{jj}^{tag} reweighting and normalization
- SM signal systematics: QCD scale, PDF uncertainty, EW/QCD interference and parton shower

Other uncertainties are statistical and Monte-Carlo uncertainties. For aQGC searches, we have dedicated EFT samples in addition to the data and Monte-Carlo SM samples. EFT is then treated as signal and the SM EW signal is treated as background. QCD and PDF signal systematics apply on EFT signal. A unitarization procedure, as described in Section 9 of [8], is performed with clipping points 1.5, 2, 3, 5 TeV + no-clipping. As we have an inclusive analysis, all the operators from the Eboli model can be constrained. We fit one operator and one clipping point at a time.

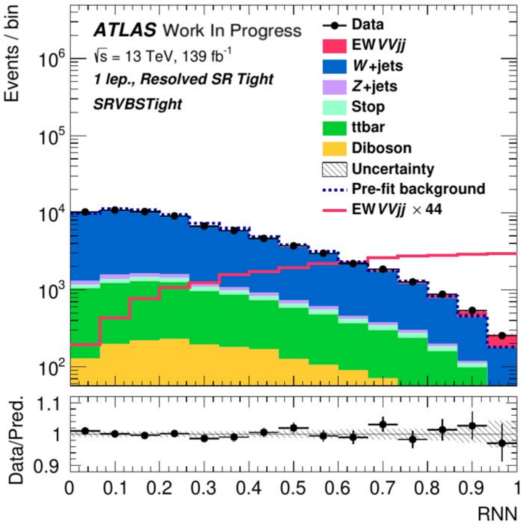

Figure 8: RNN distribution in the 1-lepton resolved (*tight*) signal region (log scale).

Coefficient/Λ^4	Expected limits [TeV^{-4}]	Observed limits [TeV^{-4}]
f_{S1}/Λ^4	[-6.8, 6.8]	[-8.1, 8.1]
f_{M0}/Λ^4	[-1.1, 1.1]	[-1.1, 1.2]
f_{T0}/Λ^4	[-0.17, 0.15]	[-0.12, 0.18]
f_{T1}/Λ^4	[-0.16, 0.17]	[-0.15, 0.14]

Table 2: Expected and observed limits on four Wilson coefficients without clipping.

Results

The analysis is currently unblinded and the statistical analysis is done. We expect EW production of vector bosons in semileptonic final states associated with jets to be observed with a significance higher than 5σ and a signal strength parameter compatible with 1 (SM value). The RNN distribution in one of the SRs (1-lepton resolved) is shown in Figure 8. We can see that the sum of Monte-Carlo SM backgrounds (mostly W+jets, $t\bar{t}$ and diboson+jets but also some Z+jets and single t) and signal (EW $VVjj$) fits the data very well. The dominant systematics are the theory systematics on signal. The next step of the analysis is the fiducial cross-section measurement and the finalization of aQGC interpretation. For now we have some un-unitarized contraints on the operators, as shown in Table 2.

Conclusion and outlook

VBS processes probe the fundamental structure of EW interactions. They are very rare and provide high sensitivity to BSM physics affecting gauge and Higgs couplings, which can be studied in a model-independent way in the EFT framework through anomalous gauge couplings. The semileptonic final state analysis allows to study a lot of couplings and to set good limits on operators affecting quartic gauge couplings. It will be part of a future ATLAS Run-2 aQGC combination, with WW, $ZZ(\to llll)$, $ZZ(\to ll\nu\nu)$, WZ, $W\gamma$ and $Z\gamma$ VBS analyses and WWW and $W\gamma\gamma$ triboson analyses. These final states have the opportunity to access QGC and allow to constrain dimension-8 operators (most studies previously focused on dimension-6 before). This combination is very promising but challenges are expected: we need to understand all the subtleties of the different analyses and to harmonize them since each analysis has its own regions, models and strategies. We plan to finish this effort next year.

References

[1] ATLAS Collaboration, *Standard Model Summary Plots* (2022) `http://cds.cern.ch/record/2804061/files/ATL-PHYS-PUB-2022-009.pdf`

[2] ATLAS Collaboration, *Observation of electroweak $W^{\pm}Z$ boson pair production in association with two jets in pp collisions at $\sqrt{s}$ = 13 TeV with the ATLAS detector*, arXiv:1812.09740 [hep-ex] (2019)

[3] S.F. Novaes, *Standard Model: An Introduction*, arXiv:0001.1283 [hep-ph] (2000)

[4] U. Schnoor, *Vector boson scattering at the LHC* (2011) `https://www.physik.hu-berlin.de/de/gk1504/block-courses/autumn-2011/program_and_talks/23_2011-10_schnoorulrike.pdf`

[5] C. Degrande *et al.*, *Effective Field Theory: A Modern Approach to Anomalous Couplings*, arXiv:1205.4231 [hep-ph] (2012)

[6] O. J. P. Eboli, M. C. Gonzalez-Garcia, *Mapping the genuine bosonic quartic couplings*, Physical Review D **93** 093013 (2016)

[7] ATLAS Collaboration, *Differential cross-section measurements of the production of four charged leptons in association with two jets using the ATLAS detector*, arXiv:2308.12324 [hep-ex] (2023)

[8] ATLAS Collaboration, *Measurement of electroweak $Z(\nu\bar{\nu})\gamma jj$ production and limits on anomalous quartic gauge couplings in pp collisions at $\sqrt{s}$ = 13 TeV with the ATLAS detector*, arXiv:2208.12741 [hep-ex] (2023)

Part II

Cosmology

session chaired by Michel AGUENA

Supernovae standardisation for cosmology with the ZTF Cosmo-DR2 volume-limited sample

Madeleine Ginolin

Institut de Physique des Deux Infinis

Abstract — Type Ia supernovae (SNe Ia) are both the tool that made the first measurement of the Hubble constant possible and the key to a new era of cosmology, dominated by systematics instead of statistics. SNe Ia absolute magnitudes naturally exhibit a 0.4 mag scatter, that can be reduced using what is called "standardisation", a process in which correlations between SN Ia magnitudes and lightcurve properties (colour and stretch) are exploited to minimise that scatter. Using the standardistation process reduces the scatter to a level down to around 0.15 mag. We analyse these standardisation relations in light of the new ZTF DR2 volume-limited sample. Thanks to its unprecedented statistics, we find that the stretch-residuals relation, previously thought to be linear, exhibits a strong (10.3σ) non-linearity. However, the colour-residuals relation appears linear. We also look at the stretch and colour distributions. The stretch distribution exhibits the expected bimodal behaviour seen in the literature. The colour distribution has a very red ($c \sim 0.5$) tail, not seen in previous surveys. By making appropriate environmental cuts, we are able to extract a "dust free" SNe Ia sample, where SNe are less affected by dust than in the full sample. This might be a promising avenue to mitigate dust-related issues in Type Ia cosmology.

Introduction

The current standard cosmological model is the so-called ΛCDM model, where CDM stands for Cold Dark Matter, representing ~ 25 % of the energy content of the Universe, while Λ is a cosmological constant, responsible for the main (~ 70 %) energy content of the Universe, Dark Energy. While this model reproduces very well most observations of the Universe with only six free parameters, it still has some issues, two of them being the unknown nature of both Dark Matter and Dark Energy.

One of the most debated issue in relation to ΛCDM is the tension over the speed at which the Universe is expanding, called the Hubble constant. Indeed, the value measured by Type Ia Supernovae (SNe Ia) anchored on Cepheids stand at $H_0 = 73.04 \pm 1.04$ km/s/Mpc [1, 2], whereas Planck Collaboration [3] measured 67.4 ± 0.5 km/s/Mpc using the CMB. This is often described as a late Universe vs primordial Universe issue, and could hint either at the need for a new model or at biases in one or both of the measures.

SNe Ia are a crucial tool in this debate. SNe Ia enabled the discovery of the expansion of the Universe [4], and later the acceleration of this expansion [5, 6]. They are "standardisable" candles. Indeed, when uncorrected, they exhibit a natural scatter of ~ 0.40 mag. In the early 1990s, Phillips et al [7] discovered a correlation between SN Ia magnitude and their lightcurve stretch x_1 (a measure of how fast or slow a SN Ia is declining). A few years later, Tripp et al [8] found a similar relation between SNe Ia magnitudes and their color c. Correcting for those relations, the scatter reduces to ~ 0.15 mag, dubbed as intrinsic scatter.

SNe standardisation

SN standardisation is the process of reducing SN Ia magnitude scatter. This is done by making use of the relation between SN magnitude and their properties. We first correct the observed peak magnitude in B-band m_B for SN colour (c) and stretch (x_1). We also add an extra standardisation term, accounting for the dependence of SNe Ia magnitudes on their host environment after colour and stretch standardisation [9, 10, 11, 12]. This term is usually called a mass step, as it is just adding or removing a constant γ depending on if the SN host mass is above or below a given value. It is not discussed here, but a full investigation of its value and dependency on environment proxy used is presented in Ginolin et al (2024a). The observed distance modulus is thus defined as:

$$\mu_{\text{obs}} = m_B - M_0 - \beta c + \alpha x_1 + p\gamma \tag{1}$$

Here $p\gamma$ is the mass step term discussed above (γ is the amplitude of the mass step and $p = \pm\frac{1}{2}$ depending on which side of the mass cut a SN is), and M_0 is the absolute SN Ia magnitude, which is degenerate with H_0. In this proceeding, we only focus on residuals, so the value of M and H_0 do not matter. Finally, we compute the residuals of the cosmology fit, defined as:

$$\Delta\mu = \mu_{\text{obs}} - \mu_{\text{cosmo}} \tag{2}$$

To compute μ_{cosmo}, we use the flat ΛCDM cosmology from `astropy` [13, 14], with Ω_m from Planck [3]. The redshifts used are part of the ZTF Cosmo DR2 release, described in the next section. We do not need to add any bias correction, as we are using a volume-limited sample.

Data

Zwicky Transient Facility

Zwicky Transient Facility the survey operated with the camera mounted on the Samuel Oschin Telescope located in Palomar Observatory (Southern California) [15, 16, 17]. This survey is optimised for transients, and in particular SNe Ia, combining a large field of view (47.7 deg^2) with short (30s) exposures, allowing for a full scan of the sky each night. It operates in three bands: g and r for the public survey and i for a private partnership. The median depth of the survey is 20.4 mag in r-band, corresponding to a $z \sim 0.1$ SN Ia. There is a spectrograph associated with the survey, called SEDmachine [18], mounted in the P48 in Palomar. This spectrograph is also optimised for SNe Ia, with a low resolution ($\frac{\lambda}{\Delta\lambda} \sim 100$), sufficient for SN classification, but allowing for 1h exposures. All SNe below the magnitude limit of the spectrograph (~ 19.5 mag) thus have a spectra.

Volume-limited sample DR2

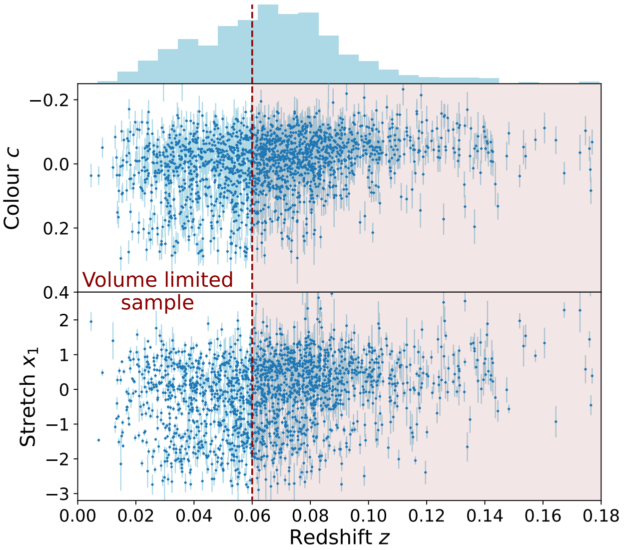

Figure 1: *Top:* Redshift histogram of all SNe Ia. The decrease at $z \sim 0.07$ is the signature of Malmquist bias, ie objects missing because they are too faint. *Middle:* SN colour vs redshift. There are fewer objects in bottom right part of the plot because red (high c) objects are fainter than blue objects. *Bottom:* Same as the middle plot but for stretch vs redshift. Here the fast decliners (low x_1) are fainter than slow decliners. The red line going through all the plots is the redshift cut used to get a volume-limited sample, at $z = 0.06$.

We use data from the Cosmo-DR2 sample, which spans all of ZTF I (March 2018 to the end of 2020). It is described in detail in Rigault & Smith et al. (2024). The lightcurves are fitted with `SALT2.4` [19]. The spectra taken by SEDm are reduced with a dedicated pipeline [20], and then fitted by `SNID` [21]. Redshifts are either coming from `SNID` or from a spectroscopic redshift when a host galaxy is found. Host association is performed using the DLR (Directional Light Ratio, a normalised measure of distance between the centre of a host and a SN) technique [22, 23]. All objects (lightcurve and spectra) have been visually checked by at least two people, in a collaboration effort to obtain the subtypes of each SN. Indeed, some Ia subtypes are usually not included in Hubble diagrams, as they are not standardisable in the same way as normal Ias (e.g. Ia-91t, SuperChandras...). The whole data set is comprised of 1178 spectroscopically typed SNe Ia.

In this analysis, we use the volume limited version of the DR2 data set. The effect of the slower-brighter and bluer-brighter relations is illustrated Figure 1. Indeed, we see that red SNe and fast-declining SNe start missing after a given redshift. This is due to their lower magnitude, combined with the magnitude limit of the survey. This in turn biases the sample, with the so-called Malmquist bias. One thus has to be very careful when looking at samples affected by selection effects. By doing an appropriate redshift cut, we get a volume-limited sample, ie a sample where no SNe in the corresponding volume are missed (or are missed due to random effects unrelated to the objects, e.g. bad weather, technical issue on the telescope...). We use the redshift cut prescribed by Amenouche et al. (2024), at $z_{\mathrm{max}} = 0.06$. A simple check of the robustness of that cut is to look at the redshift histogram in the top plot of Figure 1. Indeed, the histogram is increasing for all of the redshift range we use, and only starts to decreased due to missed objects at $z \sim 0.07$. After doing a few more quality cuts (described in details in Ginolin et al, 2024a,b), we get to our final sample of 725 SNe.

Results

Stretch distribution

We plot in Figure 2 the stretch distribution of the volume-limited sample. It exhibits a clear bimodal shape, as expected from Nicolas et al. [24]. We fit the whole distribution with a double Gaussian. The parameters of the two Gaussians are all compatible at the 1σ level with the ones presented in Nicolas et al [24] obtained from 114 SNe Ia from SNFactory [25]. We then split the sample into two using local (2 kpc around the SN) $(g-z)$ colour from PanSTARRS [26], used as a proxy for SN Ia progenitor age. Old population SNe (locally red environment, $(g-z)_{\mathrm{local}} > 1$) populate both stretch modes, while young population only exist in the high stretch mode. For the old population, the ratio between the high-stretch and low-stretch mode is $\sim 50\%$. For the low-stretch mode, we see a small fraction ($\sim 8\%$) of SNe in the low-stretch mode. This is consistent with Briday et al [27], who predicts

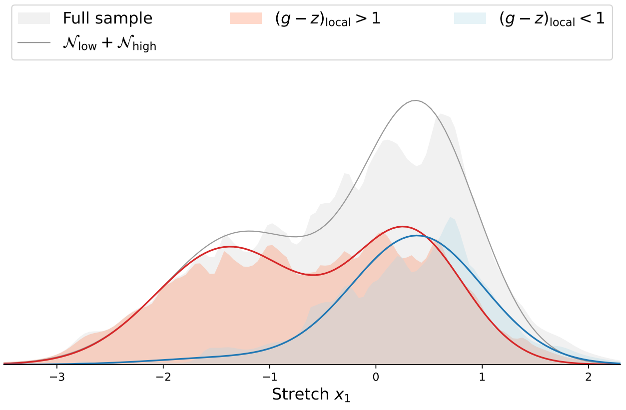

Figure 2: Adapted from Figure 1 of Ginolin et al (2024a). In grey is the stretch distribution for the whole sample, fitted with a double Gaussian (grey line). In red/blue are stretch distribution for SNe in locally red/blue environments (local colour $(g-z) \lessgtr 1$)), with the respective double Gaussian fits (red/blue lines).

a small contamination due to tracer inaccuracy.

Linearity of the stretch-residuals relation

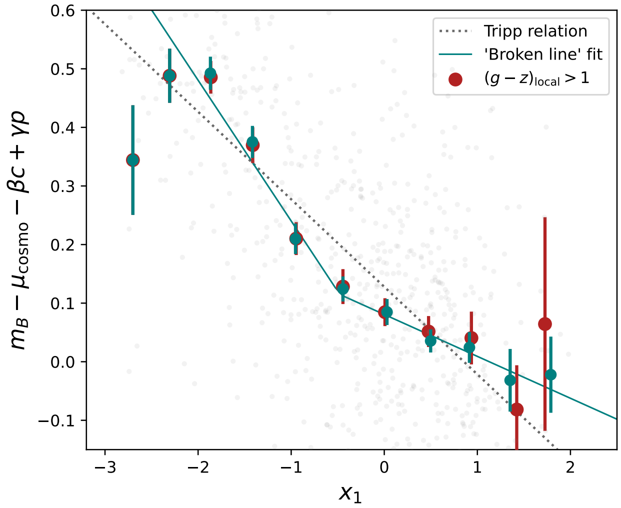

Figure 3: Adapted from Figure 6 of Ginolin et al (2024a). Residuals against stretch, binned by equal-sized stretch bins. The dotted line is the usual linear relation fitted, and the full line is the broken-α model we study. The red points are binned residuals for SNe Ia in locally red environments.

The first assumption we are able to challenge with the unprecedented statistics of the ZTF Cosmo DR2 is the linearity of the stretch-residuals relation. When plotting Hubble residuals binned by stretch, they do not fall on the linear Phillips relation, but rather appear to have a broken shape. We thus construct a new model, replacing the single α term in Eq. 1 by a term $\mathcal{A}(x_1)$, defined as follow:

$$\mathcal{A}(x_1) = \begin{cases} \alpha_{\mathrm{low}} & \text{if } x_1 < x_1^0 \\ \alpha_{\mathrm{high}} & \text{if } x_1 \geqslant x_1^0 \end{cases} \tag{3}$$

This adds two extra parameters to our model, the second α and the breaking point x_1^0.

Fitting this model to our data, we find $\alpha_{\mathrm{high}} = 0.071 \pm 0.011$, $\alpha_{\mathrm{low}} = 0.240 \pm 0.012$, a difference in α of $\Delta\alpha = 0.169 \pm 0.016$, a 10.3σ significance.

As stretch and environment are tightly correlated, as explained in the previous paragraph, this could be an effect of environment. To investigate this hypothesis, we also plot in Figure 3 the Hubble residuals binned by stretch only of SNe Ia residing in a locally red environment. We use red environment SNe Ia because they span the whole stretch range, contrary to blue environment ones. When only using the red environment SNe Ia, we still see the broken line, and fitting the broken-α model gives $\Delta\alpha = 0.149 \pm 0.024$, a 6.3σ significance. This indicates that the broken-α effect is not due to environment. Looking at the fitted breaking point, we have $x_1^0 = -0.48 \pm 0.10$, which corresponds to the gap between the high and the low-stretch modes in Figure 2. This may hint at a physically motivated difference between the two stretch modes, for example in the formation process.

Colour distribution

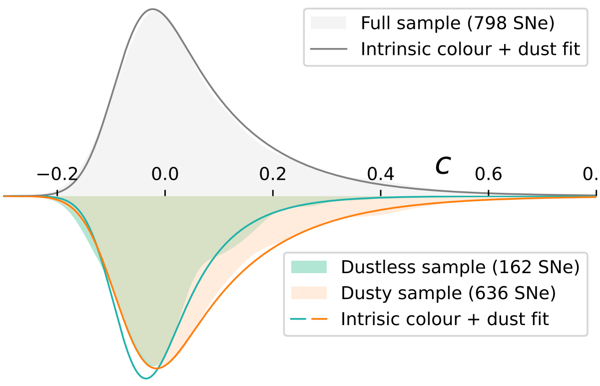

Figure 4: Adapted from Figure 1 of Ginolin et al (2024b). *Top:* Colour distribution for the full sample, fitted with the model from Brout & Scolnic [28] described in the corresponding section. *Bottom:* Colour distributions for the "dust free" sample (SNe in low stellar mass regions and away from their host galaxy centre) and the dusty sample (objects not in the dust free sample).

In the top plot of Figure 4, we plot the colour distribution for the full sample. The shape is clearly asymmetric, with a red tail extending to colours as red a $c \sim 0.6$. This was already noticed in Brout & Scolnic [28] when looking at the Pantheon+ data set [29]. Following the literature [30, 31, 32], we fit the colour distribution with a convolution of a Gaussian (thought to be the intrinsic colour distribution) with an exponential decay (thought to represent dust reddening), parameterised as:

$$P(c) = \mathcal{N}(c\,|\,c_{\text{int}}, \sigma_c) * \begin{cases} 0 & \text{if } c \leq 0 \\ \frac{1}{\tau} e^{-c/\tau} & \text{if } c > 0 \end{cases} \qquad (4)$$

Looking at the whole sample, we find $c_{\text{int}} = -0.085 \pm 0.005$, $\sigma_c = 0.0501 \pm 0.0035$ and $\tau = 0.156 \pm 0.007$.

Disentangling dust and intrinsic colour is crucial for cosmology, as dust not only reddens SN Ia, but also dims them. This thus has an impact on the estimation of distances with SN Ia magnitudes, ultimately biasing fitted cosmological parameters. An avenue to contain dust-related issues is to observe SNe Ia in the IR, where dust reddening is lessened [33, 34]. Using a "dust free" sample of objects might be another way of dealing with such issues.

Here, using the environmental proxies in the DR2, we apply to our sample a combination of cuts designed to isolate a "dust free", or at least less dusty sample. Note that these environmental cuts introduce a selection bias, which needs to be kept in mind were this sample used to do cosmology. We chose to combine a DLR cut with a local (2 kpc around the SN) stellar mass cut. We chose to use DLR= 0.8 as the cutting value, to isolate objects in the outskirts of galaxies, while still keeping a reasonable number of objects. The cutting value for the local stellar mass is $\log(M_\star/M_\odot)_{\text{local}} = 8.9$, which is the median value for the full sample. Those combined cuts isolate 162 objects. Their colour distribution is plotted in the bottom of Figure 4, along with the colour distribution of the other part of the sample. The "dust free" colour distribution has a reduced red tail, confirming that our cuts were well tailored to target dusty environments. However, it is still slightly asymmetric, showing that it is not fully dust free. This is also visible when fitting for the dust model. Indeed, the dust parameter τ, while significantly smaller than for the whole sample ($\tau_{\text{dustfree}} = 0.084 \pm 0.010$, 5.9σ away from the full sample value), is still not compatible with 0. Interestingly, we find $c_{\text{int,dustfree}} = -0.081 \pm 0.009$, $\sigma_{c,\text{dustfree}} = 0.046 \pm 0.006$, both compatible with the parameters for the full sample, with a respective difference of 0.09σ, 0.059σ. This strengthen the claim that the Gaussian distribution fitted indeed represents the intrinsic SN Ia colour distribution.

Linearity of the colour-residuals relation

In this section, we perform the same test of linearity of the colour-residuals relations as we did for stretch. The residuals vs colour relation is plotted in Figure 5. Unlike for stretch, this relation appears to follow the linear Tripp relation. We further confirm that by fitting a broken-line model. We find $\Delta\beta = 1.21 \pm 0.88$, (with $\beta_{\text{high}} = 3.66 \pm 0.06$ and $\beta_{\text{low}} = 4.87 \pm 0.87$), a 1.4σ difference. The error on β_{low} is high because the fitted breaking point is ~ 0, with most of the SNe being on the right side of the cut.

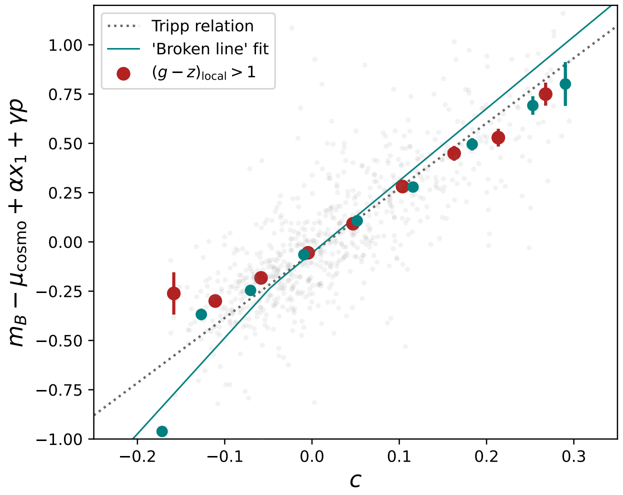

Figure 5: Adapted from Figure 3 of Ginolin et al (2024b). Same as Figure 3 but for the colour-residuals relation. The difference between the two slopes is not significant.

Conclusion

Concerning the stretch distribution, we confirm the bimodality seen in Nicolas et al [24]. Local colour is used to separate young and old progenitor populations. The stretch distribution for the young progenitor population is almost exclusively in the high-stretch mode, with an 8% contamination, compatible with predictions from Briday et al [27]. The stretch distribution of SNe from old progenitors has an half/half fraction of high/low stretch modes. Looking at the stretch-residuals relation, we find it to be non-linear, with $\alpha_{\text{high}} = 0.071 \pm 0.011$, $\alpha_{\text{low}} = 0.240 \pm 0.012$, a 10.3σ difference. This non-linearity is not caused by environment, as it is also present when looking at SNe Ia in locally red environments only. The colour distribution exhibits a very red tail, going out to $c \sim 0.6$. It is well described by a model including an (intrinsic) Gaussian and a exponential decay (due to dust). We define a "dust free" sample of 162 objects. The red tail is indeed reduced, with τ_{dustfree} being 5.9σ away from the full sample value, but there is still a slight asymmetry remaining that could be a signature of remnant dust. Nonetheless, the parameters of the Gaussian conceptually representing the intrinsic SN colour distribution are compatible with those of the full sample. Looking at the colour-residuals relation, we see no deviation from linearity ($\Delta\beta = 1.21 \pm 0.88$). All results as well as more thorough investigations of stretch and colour distributions and standardisation processes are presented in Ginolin et al (2024a,b).

References

[1] Freedman, W. L. 2021, ApJ, 919, 16

[2] Riess, A. G., Yuan, W., Macri, L. M., et al. 2022, ApJ, 934, L7

[3] Planck Collaboration. 2020, A&A, 641, A6

[4] Hubble, E. 1929, Proceedings of the National Academy of Science, 15, 168

[5] Riess, A. G., Filippenko, A. V., Challis, P., et al. 1998, AJ, 116, 1009

[6] Perlmutter, S., Aldering, G., Goldhaber, G., et al. 1999, ApJ, 517, 565

[7] Phillips, M. M. 1993, ApJ, 413, L105

[8] Tripp, R. 1998, A&A, 331, 815

[9] Kelly, P. L., Hicken, M., Burke, D. L., et al. R. P. 2010, ApJ, 715, 743

[10] Lampeitl, H., Smith, M., Nichol, R. C., et al. 2010, ApJ, 722, 566

[11] Sullivan, M., Conley, A., Howell, D. A., et al. 2010, MNRAS, 406, 782

[12] Childress, M., Aldering, G., Antilogus, P., et al. 2013, ApJ, 770, 108

[13] Astropy Collaboration, Robitaille, T. P., Tollerud, E. J., et al. 2013, A&A, 558, A33

[14] Astropy Collaboration, Price-Whelan, A. M., Sipőcz, B. M., et al. 2018, AJ, 156, 123

[15] Graham, M. J., Kulkarni, S. R., Bellm, E. C., et al. 2019, PASP, 131, 078001

[16] Bellm, E. C., Kulkarni, S. R., Graham, M. J., et al. 2019, PASP, 131, 018002

[17] Dekany, R., Smith, R. M., Riddle, R., et al. 2020, PASP, 132, 038001

[18] Blagorodnova, N., Neill, J. D., Walters, R., et al. 2018, PASP, 130, 035003

[19] Guy, J., Astier, P., Baumont, S., et al. 2007, A&A, 466, 11

[20] Rigault, M., Neill, J. D., Blagorodnova, N., et al. 2019, A&A, 627, A115

[21] Blondin, S. & Tonry, J. L. 2007, ApJ, 666, 1024

[22] Sullivan, M., Le Borgne, D., Pritchet, C. J., et al. 2006, ApJ, 648, 868

[23] Gupta, R. R., Kuhlmann, S., Kovacs, E., et al. 2016, AJ, 152, 154

[24] Nicolas, N., Rigault, M., Copin, Y., et al. 2021, A&A, 649, A74

[25] Aldering, G., Adam, G., Antilogus, P., et al. 2002, in Society of Photo-Optical Instrumentation Engineers (SPIE) Conference Series, Vol. 4836, Survey and Other Telescope Technologies and Discoveries, ed. J. A. Tyson & S. Wolff, 61-72

[26] Chambers, K. C., Magnier, E. A., Metcalfe, N., et al. 2016, arXiv e-prints, arXiv:1612.05560

[27] Briday, M., Rigault, M., Graziani, R., et al. 2021, A&A, 657, A22

[28] Brout, D. & Scolnic, D. 2021, ApJ, 909, 26

[29] Brout, D., Taylor, G., Scolnic, D., et al. 2022, ApJ, 938, 111

[30] Jha, S., Riess, A. G., & Kirshner, R. P. 2007, ApJ, 659, 122

[31] Mandel, K. S., Narayan, G., & Kirshner, R. P. 2011, ApJ, 731, 120

[32] Mandel, K. S., Scolnic, D. M., Shariff, H., Foley, R. J., & Kirshner, R. P. 2017, ApJ, 842, 93

[33] Galbany, L., de Jaeger, T., Riess, A. G., et al. 2022, arXiv e-prints, arXiv:2209.02546

[34] Jones, D. O., Mandel, K. S., Kirshner, R. P., et al. 2022, ApJ, 933, 172

Development of an ultra fast, likelihood-based, distance inference framework for the next generation of supernova surveys

Dylan Kuhn

Laboratoire de Physique Nucléaire et de Hautes Énergies

Abstract — *Context:* Type Ia supernovae are an extremely powerful tool to probe the expansion of the universe. However, supernovae surveys are magnitude limited which induces a selection effect called “Malmquist bias”. This bias needs to be corrected to measure the Dark Energy equation of state with precision at the percent level.
Method: We build a distance estimator based on the minimization of a single likelihood function. This likelihood encapsulates all the physical quantities describing the truncation of surveys at high redshifts, the standardization of type Ia supernovae as well as their uncertainties.
Results: We show that our method allows to reconstruct unbiased distances and standardization coefficients when the selection function is perfectly known, which is the case of photometric surveys. Work is in progress to include the estimation of the selection function in the estimator.

Introduction

Type Ia supernovae are defined as the product of carbon-oxygen white dwarf explosions. They are characterized by a high intrinsic luminosity which make them appear as bright as their host galaxy itself. Plotting their intrinsic luminosity in B-band with respect to time reveals (see figure 1) that they also are autosimilar events. Indeed, Tripp showed in 1998 that correcting the light-curves by two linear relations known as “brighter-bluer” and “brighter-slower” allows to decrease the dispersion at peak luminosity from 45% to 15% [7]. The residual dispersion is referred to as “intrinsic dispersion”.

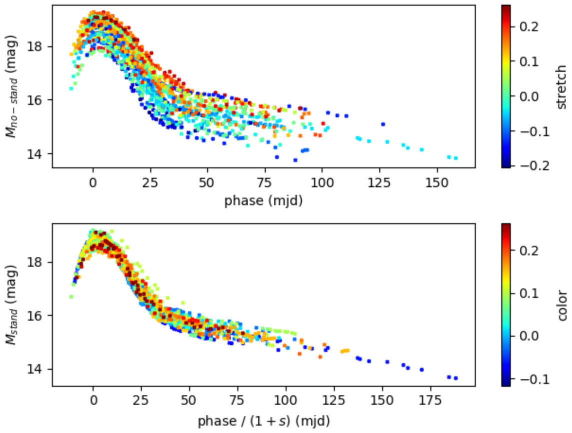

Figure 1: Non standardized (top panel) and standardized (bottom panel) light-curves from the Carnegie Supernovae Project dataset.

Both characteristics make type Ia supernovae ideal candidates to estimate distances at large scales. Moreover, building their Hubble Diagram (see figure 2), which maps the luminosity distance-redshift relation, showed that the Universe is actually not only expanding but also that its expansion is accelerated [4].
This led to the introduction of a new type of energy to counter the effect of gravity. We call this energy “Dark Energy” as we do not know its nature yet. However, we are able to measure its equation of state parameter w which links its density to its pressure by fitting the Hubble diagram with a cosmological model. For example, in the flat-wCDM model, the luminosity distance is written as:

$$d_L = \frac{c}{H_0}(1+z) \times \int_0^z \frac{dz'}{\sqrt{\Omega_m(1+z')^3 + (1-\Omega_m)(1+z')^{3(1+w)}}} \quad (1)$$

where H_0 is the current expansion rate of the Universe and Ω_m is the matter energy density. The famous ΛCDM model is a particular case where $w = -1$, making Dark Energy compatible with a cosmological constant. Currently, the uncertainty on w when we constrain it with type Ia supernovae only is about 10 to 20%. We reach a precision of approximately 5% when we combine supernovae data with other probes like CMB (see figure 3).
As we enter a precision era in cosmology, our aim is to reach eventually the percent level. For this we need to work on both statistic and systematic sources of errors. The errors related to statistics are about to be well handled by the introduction of two upcoming sur-

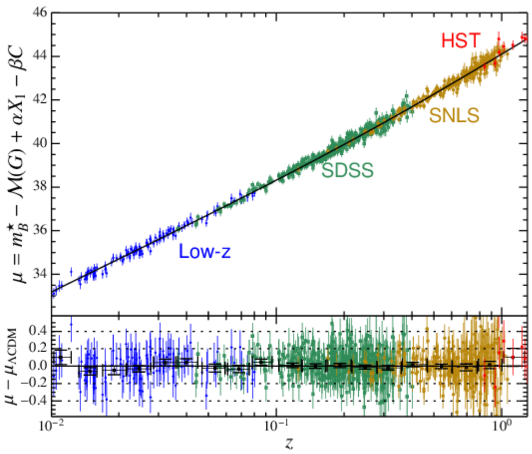

Figure 2: Hubble Diagram built from the Joint Light-curve Analysis dataset [1].

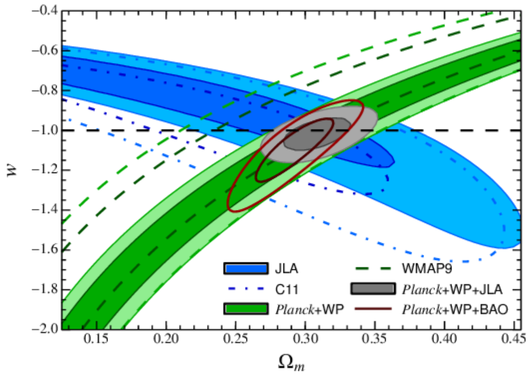

Figure 3: Confidence contours on w and Ω_m at 1 and 2σ from [1]. The blue contours represent the measure of both parameters using type Ia supernovae only.

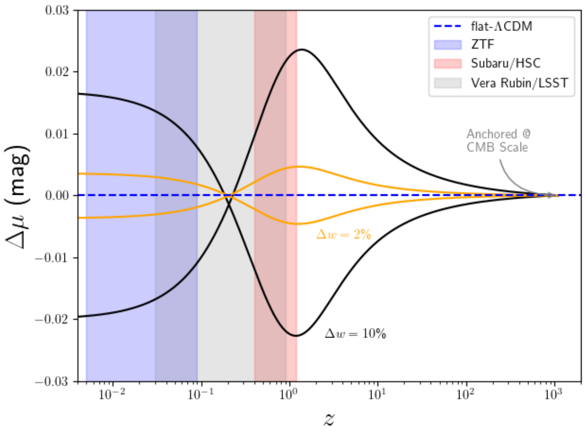

Figure 4: Deviation from the flat-ΛCDM model anchored to Cosmic Microwave Background when we vary w by 2% and 10%.

veys in the Hubble Diagram. First, the Zwicky Transient Facility (ZTF) survey is expected to add approximately 3000 type Ia supernovae at very low redshift ($0.005 \leqslant z \leqslant 0.09$). The Subaru/Hyper Suprime-Cam (HSC) goes deeper as it will add approximately 400 more supernovae at high redshift ($0.4 \leqslant z \leqslant 1.2$). The figure 4 shows that a precision of 3 mmag on the distances is required to probe variation of w of 2%. Considering an intrinsic dispersion of 15%, we obtain this precision for O(5,000) type Ia supernovae, which is perfectly reasonable when comparing to the merge between current worldwide statistics [5] and ZTF/HSC.

The estimation of distances is also affected by systematics, with one of the most important after calibration being a selection effect called “Malmquist bias”. Being able to see only the most luminous supernovae at high distances decreases the apparent mean magnitude of the population and, therefore, negatively biases the estimation of distances at high redshifts.

In current analyses, the value of this bias is determined by time-consuming simulations based on either a Bayesian framework or a multiple-time fitting approach [6, 3]. As a faster alternative, we propose a maximum likelihood-based method relying on a fast computation of the truncated likelihood function and its first-order derivatives. This new method allows us, for a given survey, to simultaneously estimate the luminosity distances of supernovae and the selection function of the survey. This prevents the distances from being biased and eases the propagation of uncertainties as all the parameters of the model are fitted at the same time. Eventually, the inference of luminosity distances is faster by a few orders of magnitude when compared to a classic Bayesian framework. This is essential to be able to deal with the 30-fold increase of statistics expected within the next decade.

Modeling of the Malmquist bias

The effect of the Malmquist bias can be illustrated on a toy model without standardization. First, we approximate the Hubble Diagram by an order-1 spline and compress the individual distances into binned distance moduli ξ which become the parameters of interest. Then, denoting M^* the absolute magnitude of type Ia supernovae (i.e. their apparent magnitude is they were at 10 pc from observer), $\mu = \Xi\xi$ the distances moduli and σ the intrinsic dispersion, one can write for a specific supernova:

$$m_i^* = M^* + \mu_i + \epsilon_i \text{ with } \epsilon_i \sim \mathcal{N}(0, \sigma^2) \qquad (2)$$

Thus, for each supernovae i, denoting m_{lim} the limit magnitude of the survey and σ_d the parameter which model the fluctuations of the observation conditions:

$$m_i = m_i^* \text{ if } m_i^* \leqslant m_{lim} + \kappa_i \text{ with } \kappa_i \sim \mathcal{N}(0, \sigma_d^2) \quad (3)$$

and m_i is unobserved otherwise. The negative log-likelihood function associated to this model is the following:

$$\begin{aligned}\Gamma = \sum_i \ln(2\pi) + 2\ln(\sigma) + \frac{1}{\sigma^2} r_i^2 + \\ 2\ln\left(\Phi\left(\frac{m_{lim} - M^* - \mu_i}{\sqrt{\sigma^2+\sigma_d^2}}\right)\right) - \\ 2\ln\left(\Phi\left(\frac{m_{lim} - m_i}{\sigma_d}\right)\right)\end{aligned} \tag{4}$$

where:

$$\Phi(z) = \frac{1}{2}\left(1 + \operatorname{erf}\left(\frac{z}{\sqrt{2}}\right)\right) \tag{5}$$

The novelty here is the addition of the two last terms, which take into account the truncation of the survey. In practice, type Ia supernovae are stardardized, meaning equation (2) becomes:

$$m_i^* = M^* + \mu_i + \sum_i \alpha_i Y_i + \epsilon_i \tag{6}$$

where for example the parameters Y_i can be the shape and the color. Therefore, type Ia supernovae are also affected by a measurement noise $\eta \sim \mathcal{N}(0, \mathrm{Cov}(m, Y_1, ..., Y_n)) = C$. Our model then becomes:

$$\begin{aligned}\begin{pmatrix} {m^*}_i \\ {Y_1^*}_i \\ {Y_2^*}_i \\ \vdots \\ {Y_n^*}_i \end{pmatrix} = \begin{pmatrix} \mu_i(z,\theta) \\ 0 \\ \vdots \\ 0 \end{pmatrix} \\ + \begin{pmatrix} \alpha_1 & \alpha_2 & \alpha_3 & \cdots & \alpha_n \\ 1 & 0 & 0 & \cdots & 0 \\ 0 & 1 & 0 & \cdots & 0 \\ 0 & 0 & 1 & 0 & 0 \\ \vdots & \vdots & 0 & \ddots & 0 \\ 0 & 0 & 0 & 0 & 1 \end{pmatrix} \begin{pmatrix} {X_1^*}_i \\ {X_2^*}_i \\ {X_3^*}_i \\ \vdots \\ X_{ni}^* \end{pmatrix} + \begin{pmatrix} \epsilon_i \\ 0 \\ \vdots \\ 0 \end{pmatrix}\end{aligned} \tag{7}$$

where the X_i are latent parameters we choose to fit to unbias the estimation of the α_i. The truncation effect is modeled in a similar way as in equation (3):

$$\begin{aligned}Y_i = Y_i^* + \eta_i \text{ with } \eta \sim \mathcal{N}(0, C) \text{ if } m_i \leqslant m_{lim} + \kappa_i \\ \text{with } \kappa_i \sim \mathcal{N}(0, \sigma_d^2)\end{aligned} \tag{8}$$

and Y_i is unobserved otherwise. The negative log-likelihood function also changes slightly and can be written as:

$$\begin{aligned}\Gamma = -\ln(|W|) + r^\dagger W r \\ + \sum_i 2\ln\left(\Phi\left(\frac{m_{lim} - \mu_i - \alpha_1 {X_1^*}_i - \cdots - \alpha_n X_{ni}^*}{\sqrt{\sigma_d^2 + \sigma^2}}\right)\right) \\ - 2\ln\left(\Phi\left(\frac{m_{lim} - m_i}{\sqrt{\sigma_d^2 + f(C_i)}}\right)\right)\end{aligned} \tag{9}$$

f is a function which depends on the covariance matrix of the observables. It makes the last term non computable in a general case when the observations are correlated. We are currently searching for approximations to compute the cumulative distribution function Φ in this specific case. Moreover, Whereas the described likelihood allows to unbias the standardization coefficients, its main drawback is that the dependancy of W in σ forces us to invert a $(3N, 3N)$ matrix at each iteration of the minimization denoting N the number of supernovae in the survey. Fortunately, this dependancy is simple enough to decompose W with the Schur complement technique. Writing:

$$W = \begin{pmatrix} C^{mm} + \sigma^2 I_N & C_1 \\ C_1^\dagger & C_2 \end{pmatrix}^{-1} \tag{10}$$

and $S^{-1} = Q(\Lambda + \sigma^2 I_N)^{-1} Q^\dagger$ and writing $r = (r_1, r_2)$ to match the structure of W, the χ^2 term can be written as:

$$\begin{aligned}r^\dagger W r = r_1^\dagger S^{-1} r_1 - 2 r_1 S^{-1} C_1 C_2^{-1} r_2 \\ + r_2^\dagger C_2^{-1} + r_2^\dagger C_2^{-1} C_1^\dagger S^{-1} C_1 C_2^{-1} r_2\end{aligned} \tag{11}$$

and the determinant of W can be written as:

$$-\ln(|W|) = \ln(|C_2|) + \sum_i \ln(\Lambda_i + \sigma^2) \tag{12}$$

The computation of the likelihood function is then in $O(N^2)$. To go even faster, we decided to fully write the minimization procedure in *JAX*. *JAX* is a *Python* librairy which allows auto-differentiation as well as GPU/TPU computation. At the end of the day, deriving unbiased distances from O(1000) supernovae only last for approximately 5s.

Characterization of the estimator

We compare the bias of two estimators: firstly, the classic maximum likelihood estimator (MLE) associated to:

$$\Gamma = -\ln(|W|) + r^\dagger W r \tag{13}$$

which does not take into account the truncation and secondly, the truncated maximum likelihood estimator (TMLE) we described in the previous section with a Monte-Carlo simulation. In both cases, we fit the binned distances ξ, the standardization coefficients α_i, the latent parameters X^* and the intrinsic dispersion

σ. However, for the TMLE, we suppose the parameters of the selection function m_{lim} and σ_d are known and fix them to avoid degeneracies. The results of the Monte-Carlo simulation are compiled in figure 5.
When the magnitudes of the supernovae are not well measured (i.e. $\alpha_i \sigma_{X_i^*} \sim \sigma$) and the number of degrees of freedom is high, the estimation of the variance is strongly biased (see figure 6). This is a well known statistics result. Denoting n the number of data and k the number of degrees of freedom:

$$\mathbb{E}(\hat{\sigma}) = \frac{n-k}{n}\sigma \tag{14}$$

To deal with this issue, we implemented a version of a restricted maximum likelihood estimator (ReMLE) inspired by [2].

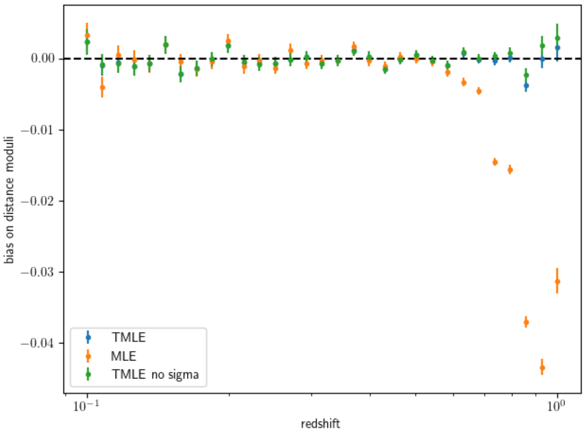

Figure 5: Bias on the distances when using the MLE (orange), the TMLE (blue) and the TMLE with fixed intrinsic dispersion (green). The bias of the MLE is expected when we add a truncation on the simulated data. However, we also observe a small bias on the TMLE when fitting the intrinsic dispersion. This bias is due to the bias of the variance estimator itself.

Conclusion

In this work, we successfully managed to build an unbiased estimator for distances. We decided to call it *EDRIS*, french for “Distance Estimator for Truncated Supernova Surveys”.
However, our model still presents some weaknesses which lead to two major open questions. To begin with, we highlighted the fact we supposed that the selection function was known in our simulations. Indeed, there a degeneracy between the limit magnitude of the survey and the distances. To prevent this degeneracy, we chose to put apart binned distances to fit the Hubble Diagram with a continuous cosmology. This said, we still have to check that every parameter in this approach is reconstructed without bias.

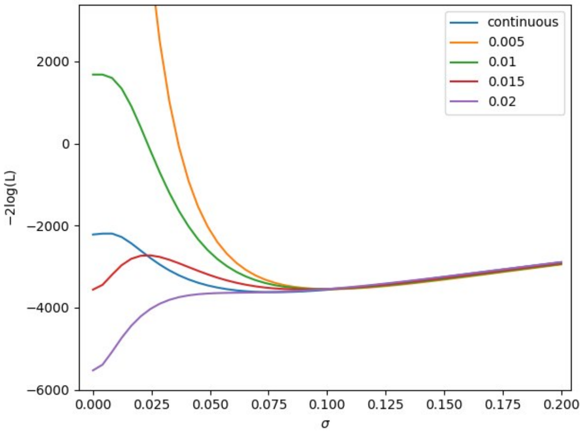

Figure 6: Profile of the negative log-likelihood function depending on the error on the color. The continuous case corresponds to a scenario where the error on the color is not constant but varies according to a continuous distribution.

Also, we are currently on the process of building a full simulation pipeline from light-curves to cosmology to support a future analysis featuring the upcoming data from ZTF/HSC. This pipeline, which aims to be as realistic as possible, will be a given opportunity to study the behaviour of the TMLE when we deviate from initial hypothesis. For example, we could see what happens when the selection function depends on the filters used for observations or when we train a light-curve fitter with a truncated survey.
The answer to these questions we be treated in detail in a future paper.

References

[1] Betoule, M., et al. Improved cosmological constraints from a joint analysis of the SDSS-II and SNLS supernova samples. Astronomy & Astrophysics, vol. 568, août 2014, p. A22.

[2] Harville, David A. Maximum Likelihood Approaches to Variance Component Estimation and to Related Problems. Journal of the American Statistical Association, vol. 72, n° 358, juin 1977, p. 320-38.

[3] Kessler, Richard, et Dan Scolnic. Correcting Type Ia Supernova Distances for Selection Biases and Contamination in Photometrically Identified Samples. The Astrophysical Journal, vol. 836, n° 1, février 2017, p. 56.

[4] Riess, Adam G., et al. Observational Evidence from Supernovae for an Accelerating Universe and a Cosmological Constant. The Astronomical Journal, vol. 116, n° 3, septembre 1998, p. 1009-38.

[5] Rubin, David, et al. Union Through UNITY: Cosmology with 2,000 SNe Using a Unified Bayesian Framework. arXiv:2311.12098, arXiv, 20 novembre 2023.

[6] Rubin, David, et al. UNITY: Confronting Supernova Cosmology's Statistical and Systematic Uncertainties in a Unified Bayesian Framework. The Astrophysical Journal, vol. 813, n^{o} 2, novembre 2015, p. 137.

[7] Tripp, Robert. A two-parameter luminosity correction for Type IA supernovae. Astronomy and Astrophysics, vol. 331, mars 1998, p. 815-20.

21-cm line signal from molecular cooling collapsing clouds in the Dark Ages

Hugo Plombat

Laboratoire Univers et Particules de Montpellier, UMR5299 CNRS/IN2P3 et Université de Montpellier F-34090

Abstract — We present the `CHEMFAST` code, that we developed to compute the cosmological 21-cm neutral hydrogen line inside collapsing matter overdensity. We precisely track evolution in the abundances of ions, atoms and molecules through a network of chemical reactions. Computing the molecular thermal function, due to the excitation of the rotational levels of the H_2 molecule, we find it strongly affects the gas temperature inside collapsing clouds from 10^6 to 10^8 $\mathrm{M}_\odot$. The gas temperature falls at end of the collapse, when the molecular cooling takes over the heating due to gravitation. We find that the 21-cm brightness temperature inside the collapsing cloud presents an emission feature, different from the one predicted in expansion scenario. It moreover follows the same behavior as the gas temperature, as it is also strongly affected by the molecular cooling.

Introduction

Probing the Universe history between the Cosmic Microwave Background (CMB) up to the light of the first stars in Cosmic Dawn, during the so-called Dark Ages, is very challenging because almost no signals are emitted from these times. During this epoch, baryonic matter predominantly existed in a neutral state, as the Compton coupling with radiation waned with cosmic expansion.

The 21-cm hydrogen line, arising from hyperfine spin-flip transitions in neutral hydrogen atoms, offers a promising avenue to probe the Dark Ages [1, 2]. Theoretical predictions indicate an absorption feature, which only depends of the cosmological model and the thermal history. This property makes it a very powerful tool to constrain the evolution and nature of our universe. Observations can yield the global signal, averaged across the sky, and the 21-cm power spectrum, which probes fluctuations on various scales. Unfortunately, observing the 21-cm line during the Dark Ages is exceptionally challenging due to foreground contamination orders of magnitude more intense. A lot of efforts are put into space or moon-based experiments (e.g. [3, 4]), which are all in very preliminary stages.

The formation of large scale structure is today an outstanding problem in cosmology. Structure formation initiates from the growth of small positive density fluctuations. The linear theory of perturbation, applied to the uniform isotropic cosmological situation, is now well understood. But as these fluctuations grow, their density contrast $\delta = \frac{\delta\rho}{\bar{\rho}}$ (where ρ is the matter energy density) approaches unity, and their behavior differs from the linear perturbations theory. These overdense regions evolve non-linearly, and are expected to drop out of the expansion of the universe (see e.g. [5, 6]). They collapse from their own gravity, forming the first bound structures of the universe, and setting the conditions for the appearance of the first stars [7, 8, 9, 10]. One of the most important consequence of the existence of a significant abundance of molecules is the crucial role the play on the dynamical evolution of the first collapsing structures at temperatures below a few hundred Kelvins. They contribute to the cooling of the baryonic gas and encourage fragmentation in the primordial clouds.

The understanding of the formation of these early structures is a fundamental question, and the observation of the 21-cm hydrogen line is a promising probe for mapping the distribution of matter over a large redshift interval. To do this, it is necessary to develop a detailed study of the dynamics in the first collapsing structures, as well as the signature we can expect to observe from them.

We have developed the code `CHEMFAST` initiated by Denis Puy, Daniel Pfenniger and Patrick Vonlanthen [11, 12, 13]. The initial intention of this code is to compute the abundances of atomic and molecular species in the context of cosmological expansion of the universe. We incorporated the computation of the global 21-cm line signal arising from atom collisions during the Dark Ages.
Then, by changing the equations of dynamics in the code, we follow a collapse scenario of overdense regions of 10^6 to $10^9 M_\odot$ using a simple homogeneous spherical model, including the gas pressure [14, 15]. We focus on the cooling effects on the baryonic gas arising from molecules during the collapse. We additionally compute the 21-cm signal from the forming primordial cloud, highlighting its distinct features compared to the global signal of the expanding universe.

21-cm hydrogen line in homogeneous expanding universe

The main goal of the `CHEMFAST` code we developed is to compute the abundances of atomic and molecular species in the context of cosmological expansion of a homogeneous universe, without considering any perturbations of its components. To do so, we need to solve a set of stiff differential equations. We used a chemical network containing 48 reactions between the species. Computing the rates of these reactions along the redshift evolution, we are able to follow the revolution of the numerical densities of each species. However these rates depend of CMB radiation temperature T_r, baryon kinetic temperature T_k, and their average numerical density n_b. It is necessary to simultaneously solve the differential equations ruling these quantities variation in order to track the abundance of atomic and molecular species throughout the Universe's evolution. In the following subsections, we describe the three outputs of `CHEMFAST` : the species abundances, the thermal evolution, and the 21-cm line computation in a homogeneous expanding universe.

Recombination and abundances Recombination processes become dominant when the reactions of photoionization are negligible. We define the redshift of recombination $z_{\rm rec}$, as the time at which the abundance of a neutral specy is equal to the one of its corresponding ion. On the top panel of Figure 1, we find the successive redshifts of recombination of $\rm H_e^{2+}$ ($z_{\rm rec, H_e{}^{2+}} \sim 5977$), $\rm H_e^+$ ($z_{\rm rec, H_e^+} \sim 2556$), $\rm D^+$ and $\rm H^+$ ($z_{\rm rec, D^+} = z_{\rm rec, H^+} \sim 1387$). The flatness of the abundances at $z < 100$ is caused by the inefficiency of collisional reactions due the expansion of the Universe which causes a decrease of species densities. On the bottom panel of Figure 1 we follow the formation of the most abundant molecules $\rm H_2$,HD and $\rm H_eH^+$. Their maximum abundance is reached far after the successive recombinations, around $z \sim 200-300$, in the Dark Ages period.They can contribute to a molecular thermal process affecting the gas temperature, that we describe in the second section.

Thermal evolution The thermal evolution depends on the tight coupling between radiation and matter, resulting on Compton scattering of CMB photons on free electrons. The expansion of the Universe induces a dilution of the matter which causes a loss of efficiency in matter-radiation coupling. This allows the cosmological recombination, the decreasing of free electrons abundance and accelerates the decoupling. We have plotted the evolution of mean temperature of radiation T_r and of kinetic gas temperature T_k, where thermal decoupling is clearly visible (see Fig. 2). We introduce a decoupling redshift $z_{\rm dec,1\%}$ for which the kinetic temperature is equal to 99% of the radiation temperature $T_k(z_{dec,1\%}) = 0.99\, T_r(z_{dec,1\%})$. The value of this redshift, $z_{\rm dec,1\%} \sim 596$. This redshift tells us that the thermal decoupling is progressive and not *instantaneous* at cosmological recombination, as both temperatures are still strongly coupled by this time. Far from the recombination, $z < 100$, the radiation temperature evolves in $(1+z)$ while the kinetic temperature evolves in $(1+z)^2$.

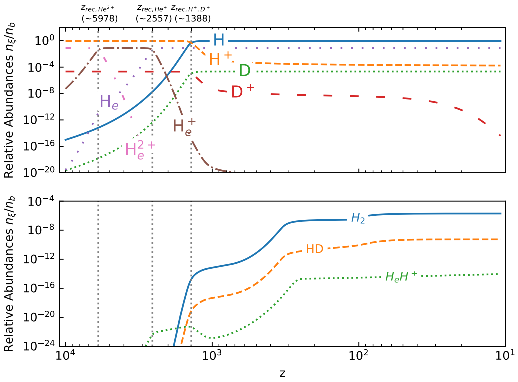

Figure 1: *Top :* Atomic species relative abundances n_ξ/n_b as a function of redshift, with n_ξ the numerical density of the specy, and n_b the total baryon numerical density. The four successive recombination ($\rm He^{2+}$, $\rm He^+$then $\rm D^+$ and $\rm H^+$) are indicated with vertical dotted line.
Bottom : Evolution of the molecular relative abundances as a function of redshift.

21-cm line A neutral hydrogen atom can undergo a hyperfine splitting of its 1S ground state in a state of alignment between the proton and electron spins, and a state of anti-alignment. The observed physical quantity of the 21-cm signal is a contrast between hydrogen clouds and the CMB at a given frequency (or redshift). This is known as the brightness temperature :

$$\begin{aligned} T_b(z) &= \frac{T_s(z)-T_r(z)}{1+z}\left(1-e^{-\tau_{21}(z)}\right) \\ &\sim \frac{3hc^3}{32\pi}\frac{A_{10}}{k_B\nu_0^2}\frac{n_H(z)}{H(z)\,(1+z)}\left(1-\frac{T_r(z)}{T_s(z)}\right). \end{aligned} \quad (1)$$

Where τ_{21} the 21-cm optical depth. h is the Planck constant, c the speed of light, k_B the Boltzmann constant, A_{10} define the spontaneous decay rate of the 21-cm spin-flip transition from excited to ground state, ν_0 is the rest frequency of the 21-cm line, n_H is the hydrogen numerical density, and $H(z)$ the Hubble parameter.

T_s is the excitation temperature of the line or spin temperature. Several mechanisms compete in the excitation of the hyperfine level. The two mechanisms of interest during the Dark Ages are the following :

- Absorption and stimulated emission of photons from the CMB radiation redshifted at the 21-cm wavelength. This makes the spin temperature tend towards T_r.

- Collisions with other hydrogen atoms, free electrons and protons. This makes the spin temperature tend towards T_k.

We have plotted, in Fig. 2 (top), the evolution of spin temperature along with the radiation and kinetic temperature. On the bottom, we show the 21-cm bright-

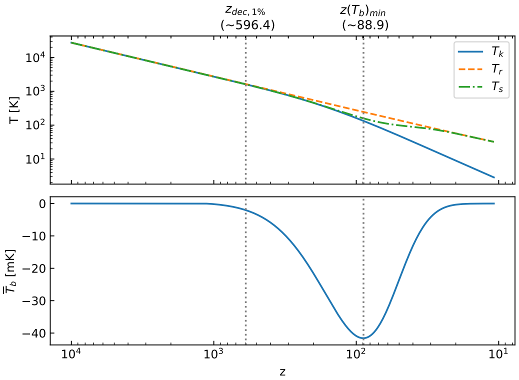

Figure 2: *Top:* Evolution of radiation temperature T_r (dashed line), baryons temperature T_k(full line) and 21-cm spin temperature T_s (dash-dotted line) as function of redshift. $z_{dec,1\%}$ corresponds to the redshift at which gas and radiation temperatures are decoupled at 1% : $T_k(z_{dec,1\%}) = 0.99\,T_r(z_{dec,1\%})$.
Bottom: Global brightness temperature as a function of redshift.

ness temperature. Their evolution can be separated in three distinct behaviors :

- Before matter-radiation decoupling, the spin temperature is also equal to the background one $T_s = T_r$. Differential brightness temperature T_b is at zero.

- Around $z \sim z_{dec,1\%}$ matter and radiation are slowly decoupling. Baryons are dense enough for the the collision mechanism to dominate in the 21-cm photons production. The spin temperature is thermalized to the baryon temperature $T_s \to T_k$, and the brightness temperature reaches a minimum of $T_b \sim -44$ mK at z closed to 89, see Fig. 2 (bottom). This value is in accordance with the state of the art literature (eg. [16], [17] [2]).

- Due the expansion of the universe, the baryons get more and more diluted, and the collision mechanism becomes ineffective. The spin temperatures relaxes to the background one $T_s \to T_r$ and the brightness temperatures turns back to zero.

Discussion With `CHEMFAST`, following differential equations for quantities in a homogeneous universe, we find back two important results.

Firstly, the complex chemistry that takes place during and after the successive recombinations allows the first molecules to be formed, in particular H_2. Their appearance is crucial in explaining the cooling of the gas during the formation of the first structures.

Moreover, by following the thermal history of the universe and the chemical reactions, it is possible to estimate the intensity of the global 21-cm signal due to the collision process during the Dark Ages. Estimating this signal is of great interest for cosmology. Its characteristics (shape, intensity, temporality) are totally independent of the astrophysical processes at work later, from Cosmic Dawn onwards. Its only dependence is, therefore, on cosmology [1] [2], and to the IGM thermal history, which is very sensitive to processes leading to an additional heating or cooling (e.g dark matter-baryon scattering [18] or millicharged dark matter [19]).

21-cm hydrogen line in collapsing clouds

In the context of the homogeneous expansion seen in the first part, the influence of molecules on the gas temperature is minimal, due to their very low abundance compared with other species. Their contribution is completely drowned out by the adiabatic cooling of the gas and the Compton heating associated with matter-radiation coupling. However, we know that the universe is not in fact homogeneous, but has small fluctuations in density, which explains the structures present today.

In this section, we focus on the evolution of a matter overdensity. When a density perturbation grows enough due to gravity in order to reach a density contrast $\delta = \frac{\delta\rho}{\bar{\rho}}$ comparable to unity, it can't be described anymore by the linear theory of perturbations. To follow the evolution of these non-linear perturbations, we consider a spherical collapse model with basic hypothesis. The model we use is based on the work of [14], extended by [15]. As in the homogeneous expansion case, we need to solve differential evolution equations for the baryonic density, radiation temperature, gas temperature, and every reaction from the reaction network. We additionally follow the evolution of the cloud's radius. In the following, we firstly describe the collapsing model implemented in `CHEMFAST`. We then introduce the thermal process induced by the presence of molecules, and highlight its importance in the description of the thermal evolution inside a collapsing overdensity. The final subsection is dedicated to the discussion of its impact on the 21-cm line signal.

Collapsing model We assume that the over-dense region we follow is isothermal, spherical, and without rotation. This matter sphere will first follow the expansion, before slowing due to the excess mass until the point when it starts to collapse back on itself.Following [14], we assume that the spectrum of mass is given by

$$\frac{\delta\rho}{\bar{\rho}} = \left(\frac{M}{M_0(z)}\right)^{\alpha} = \left(\frac{M}{M_0(0)}\right)^{\alpha}(1+z)^{-1} \qquad (2)$$

where M_0 is defined as a characteristic mass-scale with $M_0(z=0) = 10^{15} M_\odot$ which is the typical mass of a super-cluster today. Assuming a linear $t^{2/3}$ growth of the fluctuations with the expansion of the Universe, we take the power index $\alpha = -1/3$ (see [20]).

We consider a single collapsing mass M. We follow the collapse starting from the turnaround point, defined when gravity takes over the expansion, and the perturbation starts to increase in density, as it was only diluting slower than the background before this moment.

Molecular thermal functions The formation of primordial molecules such as H_2 generates thermal response due to the excitation of rotational levels of molecules. Rotational level populations depend on collisional reactions, and radiative processes (CMB radiation absorption or induced and spontaneous emission).

The expressions of the energy per volume unit that can by gained Γ_{mol} (heating) or lost Λ_{mol} (cooling) by the medium due to rotational level transitions help us to define the thermal molecular function :

$$\Psi_{mol} = \Gamma_{mol} - \Lambda_{mol} \tag{3}$$

Thermal evolution We focus on the analysis of an example collapse of mass $10^8 M_{\odot}$, which is a medium mass in the context of our model.

The gas kinetic temperature follows this differential equations [11] :

$$\frac{dT_k}{dt} = -\frac{2T_k}{r}\frac{dr}{dt} + \frac{2}{3n_b k_b}\left(\Psi_{mol} + \Lambda_{Compton}\right) \tag{4}$$

- The first term corresponds to heating due to gravitational contraction. It gets stronger as the radius r of the halo decreases and the collapsing velocity increases.
- $\Lambda_{Compton}$ correspond to the Compton coupling between matter and radiation.
- Ψ_{mol} represents the molecular thermal function. Here it contributes to cool the gas. Initially negligible, this contribution increases sharply as the density of the molecules increases and the gas temperature grows, until it becomes significant at the end of the collapse.

Compared to the expansion scenario, the molecular thermal function has a strong influence on the gas temperature.

Results In Figure 3 (top) we show again the gas, radiation and 21-cm spin temperatures, in the collapse context. In the first part of the collapse, the gas temperature (lined curve) remains stable. Compton coupling, which is still important, acts against gravitational heating due to the collapse of the cloud, and brings T_k back towards the radiation temperature (dotted curve). The gravitational heating term is $\propto \frac{\dot{r}}{r}$ and provides an acceleration of the heating that takes over the diminishing Compton coupling during the collapse. Finally, in a last phase of the collapse, T_k reaches a maximum around $1000K$. From this point, the molecular thermal function cools the medium more than it heats up by contraction. The gas temperature decreases despite the ongoing collapse. In this new context of collapse, we can again calculate the spin temperature T_s of the 21-cm hydrogen line. In Figure 3, T_s (dashed line) closely follows T_k throughout the collapse. Indeed, the species densities are actually increasing, therefore the collisional coupling is important and dominates the 21-cm line production. In the lower panel, we display the brightness temperature, computed by the equation (1). T_b is positive this time, which means that the signal is in emission, unlike the signal in the expansion scenario in Figure 2 which showed and absorption feature. This is because during the entire collapse, T_s is always greater than T_r. The term $\left(1 - \frac{T_r}{T_s}\right)$ in equation (1) therefore stays between 0 and 1. Moreover, we observe in T_b the same kind of peak than for T_k, caused by molecular cooling. Indeed, since the spin temperature completely follows T_k, it is sensitive to the same thermal processes, which is transmitted to T_b.

Conclusion

We have developed a calculation of the signal from the excitation of the hydrogen 21-cm line, taking into account only the collisional excitation that dominates during the Dark Ages. We first applied our code in the simple framework of an expanding homogeneous universe. Following the cosmological parameters ΛCDM from [21], we find the successive recombinations of $\mathrm{H_e^{2+}}$,H_e^+ and $\mathrm{H^+/D^+}$ at redshifts $z_{H_e^{2+}} \sim 5977$, $z_{H_e^+} \sim 2556$ and $z_{H^+/D^+} \sim 1387$. We computed as well the 21-cm line brightness temperature during the Dark Ages, taking into account the collisional excitation. It shows an absorption peak with an intensity of -40 mK at $z \sim 89$.

Finally, we computed the 21-cm line brightness temperature within collapsing halos. The signal has a very different signature from the homogeneous case. It is an emission feature, and is also affected by molecular cooling, in the same way as the gas temperature to which the brightness temperature is coupled. These particular signatures could present an observational interest at the smallest scales of the 21-cm power spectrum in the context of forthcoming HERA of SKA radio observations.

Acknowledgments

I thank Alice Faure, Chadi Meskini and Theo Simon for their support in the code writing, and Alice Faure again for her help in the code optimisation. These results have been made possible thanks to LUPM's cloud computing infrastructure founded by Ocevu labex, and France-Grilles.

References

[1] J. Burns et al., Dark Cosmology: Investigating Dark Matter & Exotic Physics in the Dark Ages using the Redshifted 21-cm Global Spectrum, 2019,BAAS, 51, 6

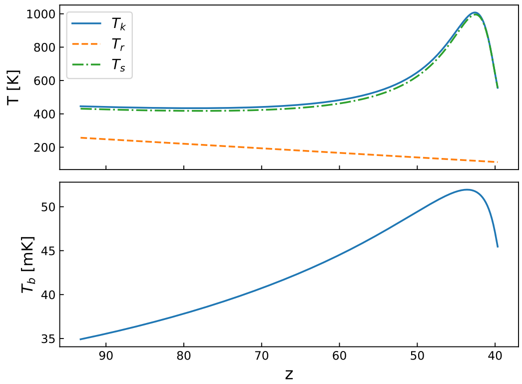

Figure 3: *Top:* Evolution of radiation temperature T_r (dashed line), baryons temperature T_k (full line) and 21-cm spin temperature T_s (dash-dotted line). The computation starts at the turnaround redshift of a 10^8 $M_\odot$ overdensity following the Lahav [14] collapse model. *Bottom:* Evolution of the 21-cm hydrogen brightness temperature T_b.

[2] R. Mondal and R. Barkana, Precision cosmology with the 21-cm signal from the dark ages, 2023, arXiv:2305.08593

[3] A. Goel et al., Probing the Cosmic Dark Ages with the Lunar Crater Radio Telescope, 2022, arXiv:2205.05745

[4] Y. Shi et al., Lunar Orbit Measurement of the Cosmic Dawn's 21 cm Global Spectrum, 2022, ApJ, 929, 32, arXiv : 2203.01124

[5] J.E. Peebles, The large-scale structure of the universe, 1980, Princeton University Press

[6] T. Padmanabhan, Theoretical Astrophysics, Volume III: Galaxies and Cosmology, 2002, Cambridge University Press

[7] N. Yoshida et al.,Formation of Primordial Stars in a ΛCDM Universe, 2006, ApJ, 652, 6-25

[8] M.Trenti and M. Stiavelli, Formation Rates of Population III Stars and Chemical Enrichment of Halos during the Reionization Era, 2009, ApJ, 694, 879-892

[9] S.Glover, The First Stars, 2013, arXiv:1209.2509

[10] V. Bromm, Formation of the first stars, 2013, arXiv:1305.5178

[11] D.Puy et al., Formation of primordial molecules and thermal balance in the early universe, 1993, A&A, 267, 337-346

[12] D. Pfenniger and D. Puy, Possible flakes of molecular hydrogen in the early Univers, 2003, A&A, 398, 447-454

[13] P. Vonlanthen et al., Chemistry of heavy elements in the Dark Ages, 2009, A&A, 503, 47-48

[14] O. Lahav, Cooling of population III objects in a pressure supported collapse, 1986, MNRAS, 220, 259-269

[15] D. Puy and M. Signore, Primordial molecules in the early cloud formation., A&A, 1996, 305, 371

[16] J. R. Pritchard and A. Loeb, 21 cm cosmology in the 21st century, 2012, arXiv:1109:6012

[17] S.R. Furlanetto et al., Cosmology at low frequencies: The 21 cm transition and the high-redshift Universe, 2006, Phys. Reports, 433, 181-301

[18] J. B. Muñoz et al., Heating of baryons due to scattering with dark matter during the dark ages, 2015, PRD, 92, 8

[19] J. B. Muñoz et al., A small amount of mini-charged dark matter could cool the baryons in the early Universe, 2018, Nature, 557, 684-686

[20] J. R. Gott and M. J. Rees, A theory of galaxy formation and clustering., 1975, A&A, 45, 365-376

[21] Planck Collaboration, Planck 2018 results. VI. Cosmological parameters, 2020, A&A, 641, A6

Part III

Beyond Standard Model

session chaired by Alexis VALLIER

Search for a heavy scalar X decaying to a scalar S and the Higgs boson in the $X \to SH \to b\bar{b}\gamma\gamma$ channel with ATLAS Run 2 data

Maxime Fernoux

Aix-Marseille Univ, CNRS/IN2P3, CPPM, Marseille, France

Abstract — A search for the resonant production of a heavy scalar X decaying into a Higgs boson and a new lighter scalar S, through the process $X \to S(b\bar{b})H(\gamma\gamma)$, where the two photons are consistent with the Higgs boson decay, is performed. The search is conducted using 140 fb^{-1} of the Large Hadron Collider (LHC) Run 2 data recorded by the ATLAS detector. The search is performed for $\leq m_X \leq 1000$ GeV and $15 \leq m_S \leq 500$ GeV. Parameterised Neural Networks (PNN) are used to enhance the signal purity and to achieve continuous sensitivity in a domain of the (m_X, m_S) mass plane. A log-likelihood fit is performed on the PNN score distribution to look for an excess with respect to the expected background compatible with a $X \to S(b\bar{b})H(\gamma\gamma)$ signal. If no excess is found, model independent upper limits will be set on the cross section times branching ratio.

Introduction

The discovery of the Higgs boson in 2012 by the CMS [1] and ATLAS experiments [2] was a remarkable success for the Standard Model of particle physics (SM). However, it does not mean the end of the story as many mysteries remain to be solved in the domain of elementary particles. A lot of phenomena such as the problem of dark matter, the neutrino oscillations or the description of gravity are not explained in a satisfactory manner by the Standard Model. That is why several theories (regrouped under the global Beyond Standard Model (BSM) label) predict the existence of additional scalar particles, especially in the Higgs sector (i.e involved in the Higgs mechanism explaining the existence of the mass of fermions and weak interaction bosons). Such particles could potentially be produced and observed at the Large Hadron Collider (LHC) at CERN. In these proceedings based on the work presented in [3], an overview of the search for two additional scalar particles X and S through the process $X \to S(b\bar{b})H(\gamma\gamma)$ with the ATLAS experiment [4] is presented. The search probes masses between 170 and 1000 GeV for X and 15 to 500 GeV for S using an integrated luminosity of 140 fb^{-1} ATLAS Run 2 data from proton-proton collisions at a centre of mass energy of $\sqrt{s} = 13$ TeV. The Feynman diagram of the main production mode of the process is drawn in Figure 1.

Those scalar particles X and S are predicted in models where the SM Higgs sector is extended such as the two-Higgs-doublet model (2HDM) [5] or the Next-to-Minimal Supersymmetric Standard Model (NMSSM) [6]. In order to be as general as possible, the search is model-independent and the only assumption made is that the $X \to SH$ resonance has a total width much smaller then the experimental resolution. Some research for those particles has already been done by other analyses at LHC, either in a similar [7] or different final state such as $b\bar{b}b\bar{b}$ [8] or $b\bar{b}\tau^+\tau^-$ [9]. However, the present work is the first to probe small values of m_X and m_S, below 200 GeV and 50 GeV respectively.

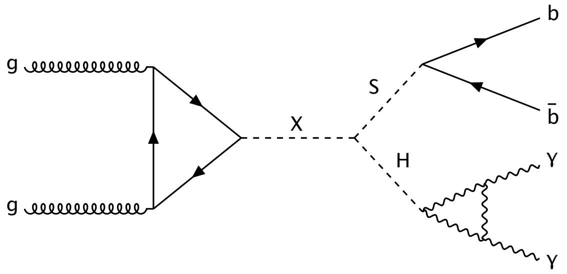

Figure 1: Feynman diagram of the gluon-gluon fusion (ggF) production of a heavy scalar X decaying into a scalar S and the SM Higgs boson in the $b\bar{b}\gamma\gamma$ final state.

Event selection

The initial event selection is identical to the one used in the SM $HH \to b\bar{b}\gamma\gamma$ analysis [10]. The requirements are :

- at least two isolated photons satisfying the ATLAS tight identification criteria. The leading photon must have a transverse impulsion $p_T > 0.35 m_{\gamma\gamma}$ and the subleading photon $p_T > 0.25 m_{\gamma\gamma}$
- The invariant mass of the two leading photons $m_{\gamma\gamma}$ must be between 105 and 160 GeV.

- No identified electrons or muons. This criteria is known as the lepton veto.
- The number of central jets (i.e with a pseudorapidity $|\eta| < 2.5$) is between 2 and 5 included.

A challenging situation arises for signals with $m_S << m_X$. In that case, the S boson is boosted and the b-jets originating from its decay will be really close to each other. This can lead the angular separation between the jets to get below the standard size of jets in ATLAS $\Delta R = 0.4$. They will then be reconstructed as only one jet as illustrated in Figure 2.

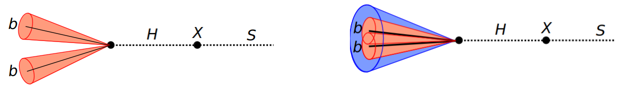

Figure 2: Sketch illustrating the collimated b-jets resulting in their reconstruction in a single jet when $m_S << m_X$ (right) as opposed to the separated b-jets (left).

.

To tackle this issue, two search regions are defined with either exactly one or two b-tagged jets and called merged and resolved region respectively. The regions are orthogonal to each other and no event with more than 2 b-tagged jets is selected in order to ensure orthogonality with other ATLAS searches with a large number of b-jets in the final state such as $X \rightarrow SH \rightarrow b\bar{b}b\bar{b}$. The selection efficiency on the different simulated signals is used to determine which region is used for which signal mass point. The fraction of signal events with two resolved b-tagged jets is found to get below 50% when the ratio m_S/m_X is < 0.09.

Analysis strategy

The invariant mass of the two leading selected photons $m_{\gamma\gamma}$ is used to make a first distinction between signal and background events. The signal $m_{\gamma\gamma}$ distribution peaks around $m_{\mathrm{H}} \approx 125$ GeV because of the characteristic $H \rightarrow \gamma\gamma$ decay. The background processes can be divided into two categories : resonant background, also called single-Higgs processes as they involve the same $H \rightarrow \gamma\gamma$ decay and, in opposition, non resonant background which is composed in majority of SM $\gamma\gamma$ + jets events.

A signal region (SR) is therefore defined to select events around the Higgs mass peak with $120 < m_{\gamma\gamma} < 130$ GeV. Events in the initial selection but outside the signal region form control region sidebands (SB) that are used to control and constrain the $\gamma\gamma$ + jets events normalization. The signal region criteria is the same for both the merged and resolved regions. The expected number of events in the signal regions of both selections is summed up in Table 1.

To distinguish signal from background inside the signal region, a multivariate analysis is used in the form of parameterized neural networks (PNN) [11].

	1 b-tagged	2 b-tagged
HH	$1.80\pm < 0.01$	$1.66\pm < 0.01$
ttH	11.38 ± 0.02	8.11 ± 0.01
ZH	7.36 ± 0.02	3.62 ± 0.01
ggH	47.4 ± 0.2	5.35 ± 0.07
Other single Higgs	20.05 ± 0.17	2.55 ± 0.07
$\gamma\gamma$+jets	3279.6 ± 7.2	284.1 ± 2.1
Other non resonant bkg	21.08 ± 0.42	9.73 ± 0.19
Total	3388.6 ± 7.2	315.1 ± 2.1
$m_X, m_S = (250, 110)$	-	9.47 ± 0.12
$m_X, m_S = (1000, 70)$	33.33 ± 0.22	-

Table 1: Expected number of events in the signal region with the 2 b-tagged and 1 b-tagged selections with statistical uncertainties. For signal, cross-section of 1 fb are used.

PNNs are deep sets neural networks that take as input a vector of event features $\bar{x}$ and a vector of parameters $\bar{\theta}$ and give as output a score which is function of $\bar{\theta}$. One of the interest of the PNN is that it allows us to train only one network and have an output on all mass points instead of having to train a dedicated network for each of the points, therefore allowing us to search in a large mass space.

Two PNNs are trained, one for each of the search regions. In the resolved region the parameters are the masses of the signal particles $\bar{\theta} = (m_X, m_S)$ whereas in the merged region the parameter is only $\bar{\theta} = (m_X)$. This is because the invariant mass of the single b-tagged jet is not properly calibrated, meaning that no information on m_S can be obtained from it. The events input features used to train the network are directly reflecting the masses of the X and S bosons we look for. In the resolved region, the invariant mass of the two b-jets and the modified invariant mass of both the two b-jets and the two photons $\bar{x} = (m_{b\bar{b}}, m^*_{b\bar{b}\gamma\gamma})$ are taken. The modified invariant mass is defined by $m^*_{b\bar{b}\gamma\gamma} = m_{b\bar{b}\gamma\gamma} - (m_{\gamma\gamma} - 125 \text{ GeV})$ in order to remove correlations between the PNN score and $m_{\gamma\gamma}$. In the merged region, the p_T of the only b-tagged jet and the modified invariant mass of the photons and the jet are used instead : $\bar{x} = (p^b_T, m^*_{b\gamma\gamma})$ where similarly $m^*_{b\gamma\gamma} = m_{b\gamma\gamma} - (m_{\gamma\gamma} - 125 \text{ GeV})$. The transverse momentum of the single jet is used because the invariant mass calibration is not assured as discussed before.

The training samples consist in simulated events from all available signal mass points and main sources of background as detailed in Table 1. : $\gamma\gamma$ + jets, $t\bar{t}H$, ZH and ggF single Higgs processes. In the merged region, the VBF single H and the Higgs pair production (HH) are also included since they are more important with this selection.

Experimental systematic uncertainties

The uncertainties on the different physical quantities measurements in the ATLAS detector affect the analysis in a various number of ways.

The number of events of signal and background samples in the selection and signal region is affected by the uncertainties on the variables used to make the selection like the p_T and the invariant masses. This first way of impacting the analysis is labelled as the uncertainty on normalization. Later on in the analysis, the PNN score distribution will also be affected by the uncertainties on the p_T or the position and width of the peak in the $m_{\gamma\gamma}$, $m_{b\bar{b}}$ and $m^*_{b\bar{b}\gamma\gamma}$ distributions : this is called the uncertainty on the shape.

The impact of the experimental systematic uncertainties on the yields in the signal region for the 2 b-tagged jets category for the main background samples and two probed signals is assessed in Table 2. The uncertainties are grouped on categories based on the object they affect, either the jets, the flavour of the jet or the photons. The yield uncertainty on the $\gamma\gamma$ + jets sample is not taken into account as it is controlled by the sidebands normalization.

		Yield uncertainty (%)			
	Source	ttH	ZH	HH	ggH
Event-based	Photon Trigger	1.0	1.0	1.0	1.0
	Pile-up reweighting	0.9	0.8	0.6	0.4
Photon	Photon Energy Res.	0.4	0.4	0.3	0.4
	Photon Energy Scale	0.2	0.2	0.1	0.1
	Photon ID	1.6	1.6	1.4	1.6
	Photon Isolation	1.6	1.6	1.5	1.6
Jet	Jet Energy Scale	1.4	0.9	0.6	1.8
	Jet Energy Res.	7.3	4.6	2.9	7.5
Flavour-tagging	b-jet efficiency	2.1	3.0	2.5	3.1
	c-jet efficiency	0.4	0.7	0.1	1.7
	light-jet efficiency	0.8	0.4	0.4	2.7

	$(m_X, m_S) =$	(250, 110)	(600, 170)
Event-based	Photon Trigger	1.0	1.0
	Pile-up reweighting	1.1	0.5
Photon	Photon Energy Res.	0.6	0.3
	Photon Energy Scale	0.5	0.4
	Photon ID	2.0	1.8
	Photon Isolation	1.7	1.4
Jet	Jet Energy Scale	1.2	0.4
	Jet Energy Res.	5.8	2.5
Flavour-tagging	b-jet efficiency	3.7	2.2
	c-jet efficiency	0.1	0.0
	light-jet efficiency	0.4	0.5

Table 2: Uncertainty (in %) on the yield in the SR for major backgrounds (top) and two probed signals (bottom) in the 2 b-tagged category.

The leading uncertainties on the background are found to be the ones related to the jet energy resolution and flavour tagging. Their magnitude is moderate since the effect on the normalization of a single sample remains below 8%.

For the signal, the uncertainty depends on the mass point considered. Some of them, like photons uncertainties are largely independent from the probed signal masses (m_X,m_S) whereas others such as flavour tagging systematics are widely depending on them. This is due to the b-tagging efficiency uncertainty being smaller in the high m_X region or when $m_X >> m_S$.

The analysis is also affected by other types of uncertainties, labelled as theoretical ones. They regroup the uncertainties on the physical constants that will affect the cross sections of the different processes (such as the strong interaction coupling α_S), and uncertainties on the modelling of the physical objects in the simulations. The shape uncertainty of the $\gamma\gamma$ + jets events is the dominant uncertainty on this side.

Results

The results of the analysis are obtained with a binned maximum log-likelihood fit on the PNN distribution for every probed signal. The parameter of interest of the fit is the cross section of the signal $X \to SH \to b\bar{b}\gamma\gamma$ process. If no excess is observed, upper limits are set on the cross section using the CL$_s$ method under the asymptotic approximation. The fit is simultaneously made over the signal region and the sidebands. The likelihood function is comparing in each bin the observed number of event to the expected number which are obtained from background simulated samples using a Poisson distribution. The binning used in the fit is constrained to have at least one expected background event in every bin. This is particularly relevant in the most signal-like bins where the asymptotic approximation could not be valid anymore if the number of background events is too low. Experimental systematic uncertainties as well as other sources of uncertainties are included in the fit as nuisance parameters.

Figure 3 presents the blinded expected limits on all considered points.

The expected limits range from 27 fb at m_X = 170 GeV to 0.14 fb at m_X = 1000 GeV. At low m_X, the sensibility of the analysis is affected by a lower signal selection efficiency due to a larger proportion of b-jets falling below the jet p_T reconstruction threshold. On the other hand, the sensibility of the analysis is increasing with higher m_X values because of the lower background whereas the signal selection efficiency remains constant.

Impact of experimental systematic uncertainties

The impact of the experimental systematic uncertainties on the analysis final results can be evaluated by comparing the upper limits obtained when they are taken into account and when they are not i.e when no

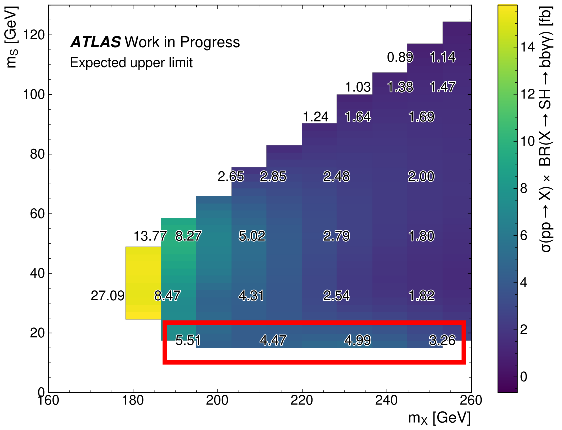

(a) Low m_X

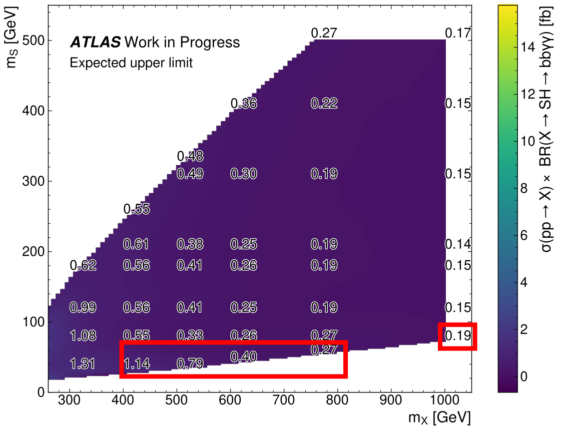

(b) High m_X

Figure 3: Blinded expected limits of the $X \to SH \to b\bar{b}\gamma\gamma$ process for (a) low and (b) high m_X. Points inside red rectangles are in the merged region.

nuisance parameters related to experimental uncertainties is included in the fit. Figure 4 show the ratio between those two limits for all points in the mass space.

The impact is largely depending on the region as expected because the normalization impact of the uncertainties on signal was already depending on the mass point. In the low m_X region, the impact on the limit can reach up to 18% due to both jet energy resolution and flavour tagging uncertainties being important. However for large values of m_X the impact is really small and remains below 1%.

Overall, the impact of the experimental systematic uncertainties is moderate and the leading uncertainties of the analysis are the theoretical ones, and especially the uncertainty on the modelling of the diphoton background whose impact on the limit is mostly between 5 to 10% and can reach up to 20%.

Conclusion

A search of a Beyond the Standard Model resonant particle X decaying into another BSM particle S and the Higgs boson in the $X \to S(b\bar{b})H(\gamma\gamma)$ final state is performed with the ATLAS detector Run 2 data. Two distinct research regions are defined depending on whether the $S \to b\bar{b}$ decay is boosted or not. In each region, a parameterized neural network depending on the probed masses of X and S is used to distinguish signal from background.

Expected upper limits on the signal cross section range between 27 fb at low m_X and 0.15 fb for large m_X values. Experimental systematic uncertainties are found to have a moderate impact on the results as their impact on the limit is mostly below 10% and even below 1% at high mass.

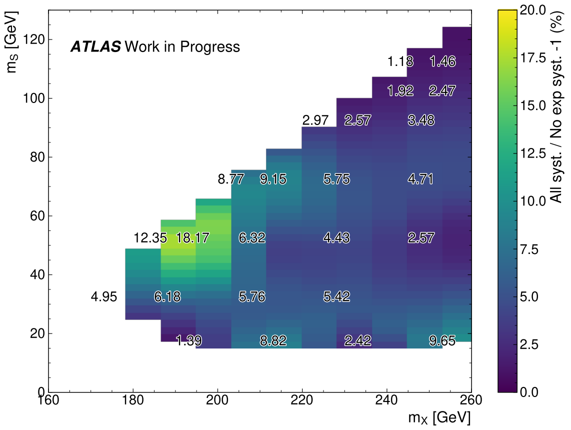

(a) Low m_X

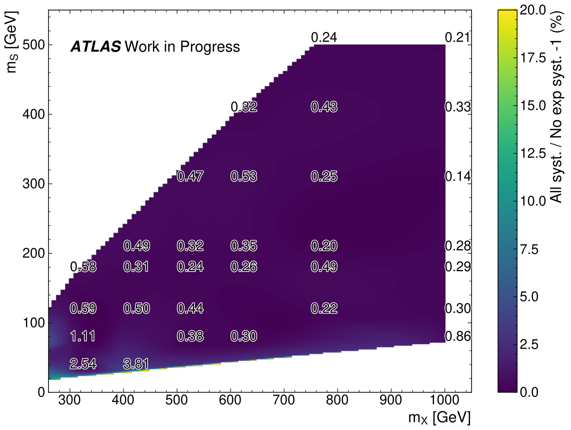

(b) High m_X

Figure 4: Ratio between blinded expected limits with and without taking into account experimental systematic uncertainties for (a) low and (b) high m_X.

References

[1] CMS Collaboration, *Observation of a new boson at a mass of 125 GeV with the CMS experiment at the LHC*, Phys. Lett. B 716 (2012) 30.

[2] ATLAS Collaboration, *Observation of a new particle in the search for the Standard Model Higgs boson with the ATLAS detector at the LHC*, Phys. Lett. B 716 (2012) 1.

[3] ATLAS Collaboration, *Search for a resonance decaying into a scalar particle and a Higgs boson in the final state with two bottom quarks and two photons in proton-proton collisions at a center of mass energy of 13 TeV with the ATLAS detector*, arXiv:2404.12915(2024)

[4] ATLAS Collaboration *The ATLAS Experiment at the CERN Large Hadron Collider*, JINST 3 (2008) S08003.

[5] I. F. Ginzburg, M. Krawczyk and P. Osland, *Two-Higgs-Doublet Models with CP violation*, arXiv:hep-ph/0211371 (2002).

[6] U. Ellwanger, C. Hugonie and A. M. Teixeira, *The Next-to-Minimal Supersymmetric Standard Model*, Physics Reports 496 (2010) 1.

[7] CMS Collaboration, *Search for a new resonance decaying into two spin-0 bosons in a final state with two photons and two bottom quarks in proton-proton collisions at* $\sqrt{s} = 13$ *TeV*, CMS-HIG-21-011 (2023).

[8] CMS Collaboration, *Search for a massive scalar resonance decaying to a light scalar and a Higgs boson in the four b quarks final state with boosted topology*, Physics Letters B (2022) 137392.

[9] CMS Collaboration, *Search for a heavy Higgs boson decaying into two lighter Higgs bosons in the* $\tau\tau bb$ *final state at 13 TeV*, JHEP 11 (2021) 057.

[10] ATLAS Collaboration, *Search for Higgs boson pair production in the two bottom quarks plus two photons final state in pp collisions at* $\sqrt{s} = 13$ *TeV with the ATLAS detector*, Phys. Rev. D 106 (5 2022) 052001.

[11] P. Baldi, K. Cranmer, T. Faucett, P. Sadowski and D. Whiteson, *Parameterized neural networks for high-energy physics*, Eur. Phys. J. C 76 (2016).

Search for new Z' boson in the dileptonic channel with missing transverse energy with the ATLAS detector at LHC.

Tom Cavaliere

Laboratoire d'Annecy de Physique des Particules

Abstract — A study is conducted to explore the existence of dark matter particles associated with a new neutral vector boson. The investigation uses proton-proton collisions at a center-of-mass energy of $\sqrt{s} = 13$ TeV, corresponding to a total integrated luminosity of 140 fb^{-1}, collected by the ATLAS detector at the Large Hadron Collider. The analysis focuses on the decay of a Z' boson into same-flavor light leptons ($e^+e^-/\mu^+\mu^-$) for Z' masses exceeding 200 GeV. No noteworthy deviation from the Standard Model prediction is observed. The findings of this exploration are interpreted within various scenarios, including dark-Higgs and light-vector benchmark models. Cross-section limits are established for each benchmark scenario, along with constraints on the coupling of the Z' boson to leptons.

Introduction

Since the second half of the 20th century, scientists have successfully validated the Standard Model (SM) by discovering all predicted particles, culminating in the identification of the Higgs boson at the Large Hadron Collider (LHC) in 2012 [1]. However, unresolved mysteries persist. Initially assumed to be massless within the SM, neutrinos were revealed to have a small yet measurable mass with the Super-Kamiokande experiment in 1998 [2]. Persistent puzzles include matter-antimatter asymmetry and the origin of the universe's mass, lacking satisfactory explanations. Notably, the discrepancy in galaxy rotation curves, first observed by astronomers Vera Rubin and Kent Ford in the 1970s, pointed to unseen mass, prompting the concept of dark matter. Consequently, an extension of the SM is necessary to address these unresolved questions.

Weakly Interacting Massive Particles (WIMPs) [3] stand out as promising candidates for dark matter. The possibility arises that these particles could be produced in proton proton (pp) collisions taking place at the LHC. Detecting their presence involves observing a momentum imbalance, known as missing transverse energy (E_T^{miss}), associated with SM particles recoiling from the interaction.

Signal model In this paper, two models defined in Ref [4] are used as benchmark for the search: the light vector and the dark higgs model. The associated Feynman diagrams at the leading order are shown at the top and bottom of Figure 1, respectively. These two models include a new Z' boson which appears in many BSM theories. It couples to fermions but not to other SM bosons. In addition, each model has a new dark sector. For the dark higgs model, a new dark higgs boson h_D is introduced. It has coupling to the Z' boson and to a pair of new dark matter particle candidates χ, in which it can decay and give the E_T^{miss} contribution. In the light vector model, the Z' boson has an off-diagonal coupling to the new dark sector, composed of two dark matter particle candidates, χ_1 and χ_2. In this model, the χ_2 decays into a χ_1, which gives the E_T^{miss} contribution, and into the Z' boson which decays subsequently into a pair of leptons. These two models introduce each six new free parameters and, following the recommendation in Ref [4], two benchmark scenarios are considered for each model: the heavy and the light dark-sector. Typical benchmark values of each of these parameters are shown in Table 1. Previously, a search of a Z' boson decaying into a pair of lepton ($e^+e^-/\mu^+\mu^-$) was done, but no deviation was found [5]. Including a final state featuring additional E_T^{miss} helps enhance the sensitivity to the discovery of a new Z' boson by effectively suppressing background contributions and provides a complementary signature. If the Z' boson decay results in undetected particles, the presence of E_T^{miss} can help capture those events, which might otherwise be missed.

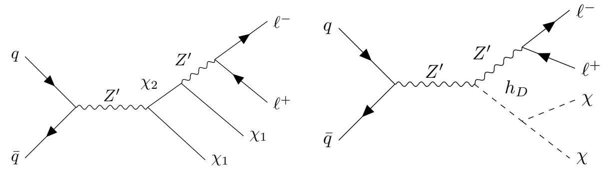

Figure 1: Feynman diagrams of the dark higgs (top), and the light vector (bottom) models.

Table 1: benchmark values of the parameters introduced by the dark higgs and the light vector, in the light and heavy dark sectors. g_D, g_q and g_l are the couplings between the Z' boson and the dark sector particles ($Z'Z'h_D$ or $Z'\chi_1\chi_2$), the quarks and the leptons respectively.

	Dark Higgs	Light Vector
Z'	$m'_Z > 180GeV$ $g_D = 1, g_q = 0.1, g_l = 0.01$	
Light dark sector	$m_\chi = 5GeV$ $m_{h_D} = 125GeV$	$m_{\chi 1} = 5GeV$ $m_{\chi 2} = m_{\chi 1} + m_{Z'}$ $+25GeV$
Heavy dark sector	$m_\chi = 5GeV$ $m_{h_D} = m_{Z'}$	$m_{\chi 1} = 5GeV$ $m_{\chi 2} = 2m_{Z'}$

The statistical analysis described in the last section, aims to search for dilepton ($e^+e^-/\mu^+\mu^-$) resonances in the invariant high mass spectrum.

ATLAS detector

ATLAS, as described in Ref [6], is a versatile detector characterized by a symmetrical cylindrical configuration relative to the LHC beam axis. The tracking detectors within the innermost layers operate within the pseudorapidity range of $|\eta| < 2.5$. Encircling this inner detector (ID) is a thin superconducting solenoid generating a 2 T axial magnetic field. The ID is further surrounded by electromagnetic and hadronic calorimeters, spanning $|\eta| < 4.9$. The outer layers of ATLAS incorporate an external muon spectrometer (MS) within $|\eta| < 2.7$, featuring three large toroidal magnetic assemblies, each with eight coils. The toroids' field integral ranges between 2.0 and 6.0 Tm across most of the acceptance range. The MS is equipped with precision tracking chambers and rapid triggering detectors. To manage data load, a two-level trigger system reduces the recorded event rate to an average of 1 kHz.

Analysis

Signal Region This analysis looks at possible scenarios where a new Z' boson decays into two oppositely-charged leptons along with undetected particles, making the observation only possible through a significant amount of missing transverse energy in the event. To ensure this, we set a requirement for the missing transverse energy to be greater than 55 GeV.
Two discriminating variables are used to define the signal regions (SRs) in this study: the mass of the lepton pair (m_{ll}), and the transverse missing energy significance ($E_T^{miss,sig}$). This last object is defined with this formulae :

$$E_T^{miss,sig} = \frac{|\mathbf{p}_T^{miss}|}{\sqrt{\sigma_L^2(1-\rho_{LT}^2)}} \tag{1}$$

where σ_L is the longitudinal component of the total transverse momentum resolution for all objects in the event while ρ_{LT} is the correlation factor between the parallel and perpendicular components of the transverse momentum resolution for each object. It is used to discern events where E_T^{miss} arises from undetected particles in the final state versus those where it originates from limited p_T resolution and identification inefficiencies. Since all signal models focus on Z' masses significantly larger than the Z mass, a cutoff is set at $m_{ll} > 180$ GeV to exclude events involving $Z \to ll$.
A veto on b-jets is also applied in the SR to reduce the background coming from top quark decays.
To improve the search's effectiveness, three different SRs are defined, covering various $E_T^{miss,sig}$ ranges. This helps because different signal models predict different distributions of missing transverse energy. We label these regions as SR 1, SR 2, and SR 3, with SR 1 ranging from 5 to 8 GeV, SR 2 from 8 to 12 GeV, and SR 3 for $E_T^{miss,sig}$ greater than 12 GeV.
The full set of selection is presented in Ref [8].

Background estimation A set of regions in the invariant mass spectrum is defined to have a good control on the contribution of each background. These regions are called Control Region (CR) and Validation Region (VR). They are orthogonal to each other, as well as to the SRs. This means that, considering the selection performed in each of them, an event cannot be assigned to more than one region. CRs are used to have a good estimation of the backgrounds in the SR. For each background, a CR is built and a normalization factor extracted with a background-only fit on the data. These normalization factors are then propagated into the corresponding background samples in the VR. In order to conserve a similar kinematics, the selection to make a CR orthogonal to a SR needs to be as close as possible as the selection made in the SR. CRs need also to be relatively pure in the background that it targets and to have a low signal contamination.
VRs are defined to validate the good modeling of the backgrounds. No fit is performed into them, only the propagation of the best-fit values of the normalization factors. If they show good agreement between the Monte-Carlo simulations and the Data, the normalization factors can then be propagated into the SRs. The requirements to define them are the same than the CRs : orthogonality, purety, and kinematically similar to the SRs.

The main irreducible backgrounds considered in this analysis are: top quark, Drell-Yan (DY) and diboson backgrounds. A CR and a VR for each background are constructed. Their definitions are present in Table 2. The estimation of the background coming from top quark decays is done in an $e\mu$ final state to achieve a very high purity. A sketch of these regions can be seen in Figure 2.

Table 2: Definition of the DY, diboson and top CRs and VRs.

	CR-DY	CR-Top	CR-Diboson
Channel	ee, $\mu\mu$	$e\mu$	ee, $\mu\mu$
m_{ll} [GeV]	> 180	> 180	[70,95]
Num. b-jets	0	-	0
$E_T^{miss,sig}$	1-3	5-8	> 12
	VR-DY	VR-Top	VR-Diboson
Channel	ee, $\mu\mu$	eμ	ee, $\mu\mu$
m_{ll} [GeV]	> 180	> 180	[95,120]
Num. b-jets	0	0	0
$E_T^{miss,sig}$	3-5	> 8	> 8

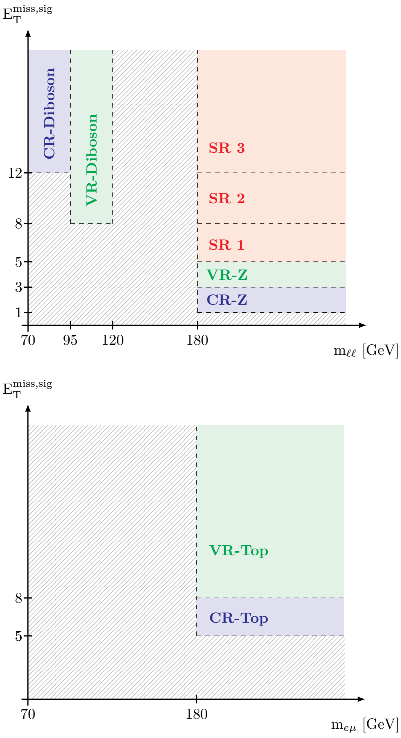

Figure 2: Sketch of the set of SRs, CRs and VRs in the m_{ll} and $m_{e\mu}$ versus $E_T^{miss,sig}$ planes.

Statistical Analysis

Data The analysis uses the data collected during the Run 2 of the LHC, spreading between 2015 and 2018.

Simulated sample Signal samples are generated with a Z' mass spacing of 100 GeV in the range between 200 GeV and 1 TeV with MadGraph v2.9.9 [9], and Pythia 8.230 [10] for the parton shower and the hadronization. For these samples, a simulation with a fast parametrization of the calorimeter response is applied in order to speed up the process. These generated signal samples are used to obtain signal distributions of the variable of interest m_{ll}, at the intermediate Z' pole mass values using a morphing approach based on a RooFit function [11]. For the backgrounds, Sherpa 2.2.11 [12] is used to do both the generation and the parton shower and the hadronization of the DY and diboson samples. For the top sample Powheg-Box [13] is used for the generation and Pythia 8.230 for the parton shower and the hadronization.

Binned statistical analysis model The Likelihood function L provides the probability of the observed data. It can be writen as follow :

$$L(\vec{n}|\vec{\theta},\vec{k}) = \prod_i P(n_i|S_i(\vec{\theta},\vec{k})+B_i(\vec{\theta},\vec{k}))\times\prod_j G(\theta_j) \quad (2)$$

where P stands for Poisson distribution, $\vec{n}$ are the data, $\vec{\theta}$ the nuisance parameters (NPs), $\vec{k}$ the parameters of interest (POI), n_i the number of events in bin i, $S_i(\vec{\theta},\vec{k}) + B_i(\vec{\theta},\vec{k})$ the prediction of signal plus background yield in bin i, and $G(\theta_j)$ is the modeling of the NP j with a gaussian pdf. Here, there is only one parameter of interest : the strength of the signal. The symbol μ will be used to refer to it. The Likelihood function can be rewritten in a simplified manner like this: $L(\mu,\hat{\boldsymbol{\theta}})$.

This likelihood function is fitted on the data in the SRs and CRs.

The fits are evaluated under the signal+background or background-only hypothesis in the m_{ll} SR spectrums, which are defined by 40 logarithmic bins. All of the limits presented in the next section are computed using the Asymptotic approximation [14].

To determine the local significance under the background-only hypothesis, a profile-likelihood-ratio-test statistic [15] is used.

Results

The full version of the results is provided in Ref [8]. This section presents a representative set of the results in the light vector model within the light-dark sector for both the ee and $\mu\mu$ channels.

The result of the fit of the likelihood function $L(\mu,\hat{\hat{\boldsymbol{\theta}}})$ on the data is shown in Figure 3, with the electron channel at the top and the muon channel at the bottom. The statistical and systematic uncertainties are shown together with dashed lines. The normalizations factors for each background extracted from the fits in the CRs are applied. The ratio in both channels show good agreement between the data and the Monte-Carlo simulation.

Local significance is independently computed for each channel and collectively. No excess over the SM processes is observed, as illustrated in Figure 4.

Upper limits on the signal cross section are computed in function of the Z' pole masses. The observed and expected limits, along with the 1σ and 2σ bands, are shown in Figure 5. The expected theoretical cross-sections for g_f equal 0.1, 0.05 and 0.01 are also shown. It can be noted than none of the signal samples are excluded when g_f is equal to 0.01. Finally, limits on the lepton couplings are extracted from the cross section limits. The observed and expected limits are shown in Figure 6.

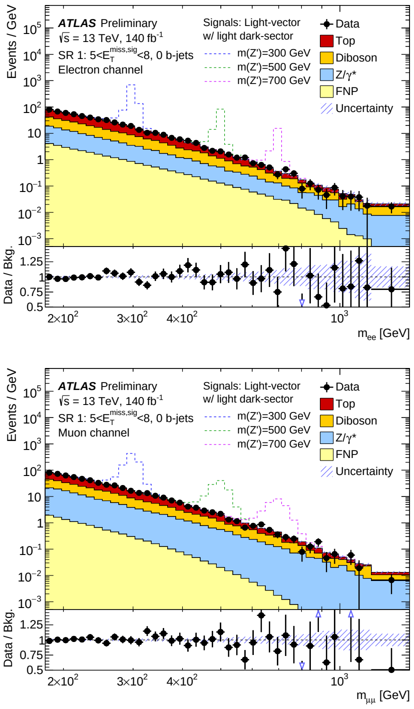

Figure 3: Results of the Signal+Background log likelihood fit on the data in the SR1 for both channel in the light vector model within the light dark-sector.

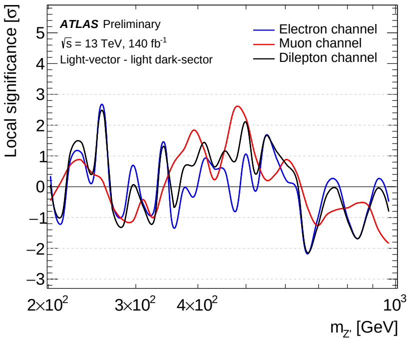

Figure 4: Result of the local significance in the electron channel and muons channel separately, as well as for the combination (dilepton channel), for the light vector model within the light dark-sector for each channel independently and collectively.

Conclusion

A search for a new Z' boson in the dilepton channel with large missing transverse energy probing a dark sector is presented. The results are based on the integrated luminosity collected during the Run 2 of the LHC with the ATLAS detector, representing 140 fb^{-1} of data. Two models, the dark higgs and the light vector model, are used as benchmarks for the search. No excess over the SM backgrounds is found and upper limits on the signal cross-section and on the lepton coupling are set.

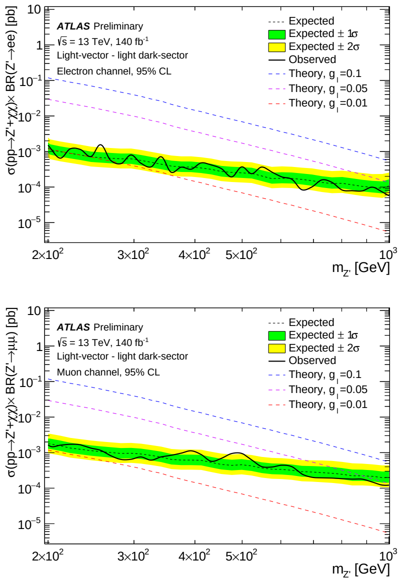

Figure 5: Cross-section upper limit results for the light vector model within the light dark-sector, for the electron channel (top) and the muon channel (bottom), together with the expected theoretical cross-sections for g_f equal 0.1, 0.05 and 0.01.

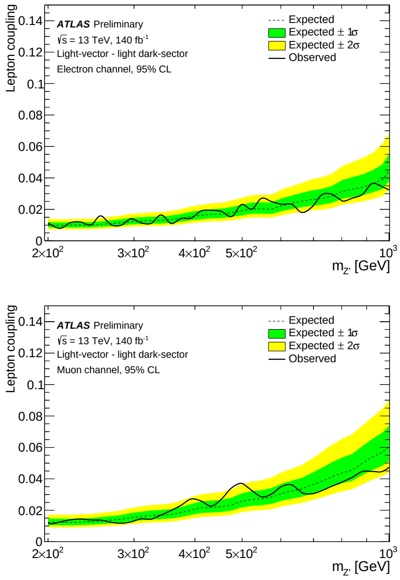

Figure 6: Lepton coupling upper limits for the light-vector model within the light dark-sector, for for the electron channel (top) and the muon channel (bottom). The limits are extracted from the cross section limit.

References

[1] ATLAS Collaboration, “Measurement of Higgs boson production and couplings in diboson final states with the ATLAS detector at the LHC,” *Physics Letters B*, November 2013. `https://doi.org/10.1016/j.physletb.2013.08.010`

[2] Evidence for oscillation of atmospheric neutrinos, 1998, Super-Kamiokande Collaboration

[3] L. Roszkowski, E. M. Sessolo and S. Trojanowski, Rept. Prog. Phys. **81** (2018) no.6, 066201 doi:10.1088/1361-6633/aab913 [arXiv:1707.06277 [hep-ph]].

[4] M. Autran, K. Bauer, T. Lin, and D. Whiteson, Searches for dark matter in events with a resonance and missing transverse energy, Physical Review D 92 (2015), issn: 1550-2368, url: http://dx.doi.org/10.1103/PhysRevD.92.035007.

[5] G. Aad et al., *Search for high-mass dilepton resonances using 139 fb^{-1} of pp collision data collected at LHC with the ATLAS detector*, Phys. Lett. B **796**, 68–87 (2019), DOI: 10.1016/j.physletb.2019.07.016.

[6] ATLAS Collaboration, The ATLAS Experiment at the CERN Large Hadron Collider, JINST 3 (2008) S08003.

[7] ATLAS Collaboration, Object-based missing transverse momentum significance in the ATLAS Detector, ATLAS-CONF-2018-038, 2018, url: https://cds.cern.ch/record/2630948.

[8] ATLAS Collaboration, Search for a new leptonically decaying neutral vector boson in association with missing transverse energy in proton proton collisions at $\sqrt{s} = 13$ TeV with the ATLAS detector ATLAS-COM-CONF-2023-046, 2023, url: https://cds.cern.ch/record/2863458

[9] J. Alwall et al., The automated computation of tree-level and next-to-leading order differential cross sections, and their matching to parton shower simulations, JHEP 07 (2014) 079, arXiv: 1405.0301 [hep-ph].

[10] T. Sjöstrand et al., An introduction to PYTHIA 8.2, Comput. Phys. Commun. 191 (2015) 159, arXiv: 1410.3012 [hep-ph].

[11] M. Baak, S. Gadatsch, R. Harrington, and W. Verkerke, Interpolation between multi-dimensional histograms using a new non-linear moment morphing method, Nuclear Instruments and Methods in Physics Research Section A: Accelerators, Spectrometers, Detectors and Associated Equipment 771 (2015) 39, issn: 0168-9002, url: https://www.sciencedirect.com/science/article/pii/S0168900214011814.

[12] E. Bothmann et al., Event generation with Sherpa 2.2, SciPost Phys. 7 (2019) 034, arXiv: 1905.09127 [hep-ph].

[13] S. Frixione, P. Nason, and C. Oleari, Matching NLO QCD computations with parton shower simulations: the POWHEG method, JHEP 11 (2007) 070, arXiv: 0709.2092 [hep-ph].

[14] A. L. Read, Presentation of search results: the CLS technique, J. Phys. G 28 (2002) 2693.

[15] G. Cowan, K. Cranmer, E. Gross, and O. Vitells, Asymptotic formulae for likelihood-based tests of new physics, Eur. Phys. J. C 71 (2011) 1554, arXiv: 1007.1727 [physics.data-an], Erratum: Eur. Phys. J. C 73 (2013) 2501.

Search for displaced top quark in the tracker of CMS

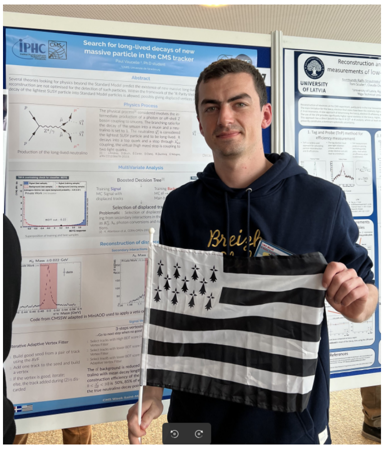

Paul Vaucelle

Université de Strasbourg, CNRS, IPHC UMR7178, F-67000 Strasbourg, France

Abstract — A search for massive long-lived particle decaying to a top quark in proton-proton collisions at $\sqrt{s} = 13$ TeV is presented in this paper. New long-lived particles are predicted in several extensions of the Standard Model. In the R-parity violated Minimal SuperSymmetric Model considered, the lightest SuperSymmetric particle is long-lived and decays into a top and a virtual stop quark which couples to a down and strange quark pair. Machine learning is used to distinguish signal displaced tracks from Standard Model prompt tracks for the reconstruction of displaced vertices.

Introduction

Many extensions of the Standard Model (SM) predict the existence of long-lived particles through weak couplings and/or high masses states making the production for these new particles to be highly suppressed. However, long-lived particles (LLP) are highly motivated by the R-Parity Violated Minimal SuperSymmetry Model (RPV-MSSM) [1, 2, 3, 4], Split-SuperSymmetry [5, 6, 7, 8, 9, 10], Stealth SuperSymmetry [11, 12], weakly interacting massive particles (WIMPs) [13, 14, 15], Gauge Mediated SuperSymmetry Breaking (GMSB) [16, 17, 18] and the hidden sector [19, 20, 21].

In this analysis, we search for long-lived neutral SuperSymmetric (SUSY) particles decaying in the tracker of CMS into SM particles, as allowed by the RPV-MSSM. These long lived SUSY particles are pair-produced from slepton decays in proton-proton collisions at a center-of-mass energy of 13 TeV. The CMS experiment collected an integrated luminosity of 137 fb^{-1} in 2016-2018. This analysis looks for displaced vertices coming from the decay of the pair-produced long-lived particles where the latter decay into SM particles producing jets and tracks in the tracker volume. The event topology, as well as the tracks and the secondary displaced vertices can be used to discriminate the displaced signature from SM backgrounds.

Signal Process

The signal process is shown in Fig.1 and characterized by the production of a Z/γ^* boson from proton-proton collisions at the LHC. Then, the boson produced couples to a pair of sleptons, being the Next-to-Lightest SuperSymmetric-Particle (NLSP), where the considered sleptons are the smuons. Since the slepton is the NLSP, it decays into a muon and the LSP that is the neutralino. The branching fraction for this decay is set to 100% in order to reduce the complexity of the model. The neutralino can only be a bino-like neutralino to allow the decay through the $\lambda^{''}$ RPV-coupling to lead to violation of the baryonic number and the production of a top quark in the final state. The sleptons are short-lived particles leaving prompt leptons as final state particles that can be used to trigger the signal events. Since the muons can be easily triggered on and easier to identify, the muon channel is chosen. The selectron channel can be added in the analysis in the future and the stau channel could also be considered in theory but is not studied in this analysis due to the complexity of the tau decay and the consequences on the event reconstruction.

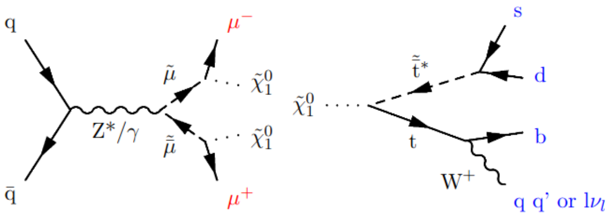

Figure 1: Neutralino production and decay from proton-proton collision at the LHC

The long-lived neutralino is assumed to decay into the tracker volume into a virtual stop and a top quark. The latter follows its SM decay channel where both hadronic and leptonic decays are considered for the W boson. The stop couples to SM quarks with the $\lambda^{''}$ RPV-coupling where the specific decay is given by $\lambda^{''}_{312}$

with 3, 1 and 2 being the generations of quarks considered. The stop couples to a down and a strange quark giving a heavy hadronic activity in the final state of the signal process. No mixing between particles of different generations is considered in the mixing matrices of sleptons and squarks, and mass states are in an equal proportion of left-handed and right-handed states also to reduce the complexity of the model. Full details about the model are given in [22].

For our signal, we consider a wide range of combination of values between the following parameters : the mass of the smuon $M_{\tilde{\mu}}$, the mass of the neutralino $M_{\tilde{\chi}_0^1}$, the proper lifetime of the neutralino $c\tau$, the RPV coupling λ''_{312} and the mass of the virtual stop $M_{\tilde{t}}$. The envisaged combinations are described in Table.1. The upper limit on $M_{\tilde{\mu}}$ is due to a low cross section ($\sim 0.1 fb$) but could be extended with more data-taking and the lower limit is due to the request of production of a top quark in the decay channel of the neutralino and also from previous experimental limits [23, 24, 25, 26, 27, 28, 29]. The cross-section of the pair-production of $\tilde{\mu}$ is entirely determined by $M_{\tilde{\mu}}$ as shown in Fig.2. For simplicity, all other RPV-couplings are null.

Parameter	Range Value
$\beta\gamma c\tau$(cm)	0.1 to 100
$M_{\tilde{\mu}}$ (GeV)	200 to 500
$M_{\tilde{\chi}_0^1}$ (GeV)	180 to 480
$M_{\tilde{t}}$(GeV)	>1000
λ''_{312}	10^{-3} to 10^{-1}

Table 1: Masses of the SUSY particles and the associated couplings considered in this analysis

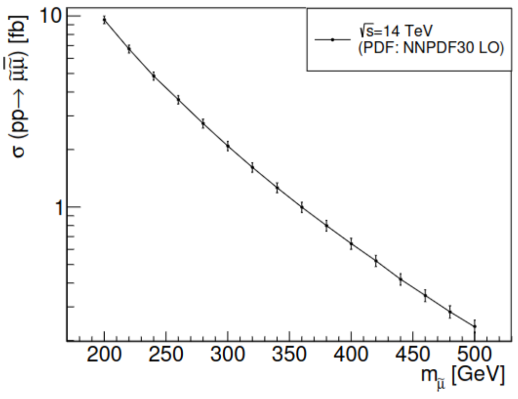

Figure 2: Cross-section of the smuons pair production as a function of the smuon mass. [22]

Reconstruction of background displaced vertices

This analysis aims at reconstructing displaced vertices from the decay of a neutral long-lived particle in the tracker of CMS. An important part of this analysis is devoted to the selection of displaced tracks coming from the decay of the neutralino. However, there are other sources of displaced tracks coming from Standard Model backgrounds such as V^0 candidates (K_S^0 and Λ^0), photon conversions and nuclear interactions within the material of the tracker of CMS. A veto is applied on the tracks associated to the reconstructed background vertices.

V^0 candidates

V^0 candidates stands for two hadrons : the K_S^0 meson and the Λ^0 baryon that are produced from the hadronisation of the strange quark. They have a long lifetime (about 10^{-10} s) and produce a displaced vertex that can be easily identified thanks to its low track-multiplicity (2-track vertices) and the invariant mass of the pair of tracks. The reconstructed invariant mass of the V^0 candidates is shown in Fig.3 for the K_S^0 meson and Λ^0 baryon. The tracks associated to these vertices in the red mass windows are removed from the analysis.

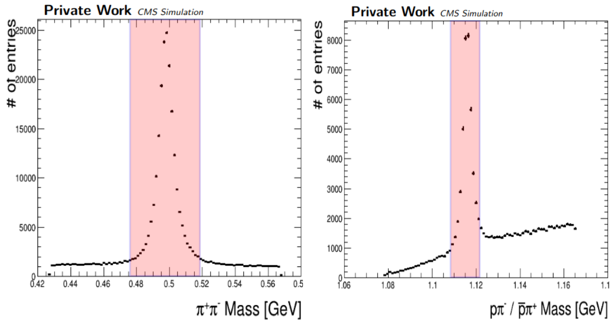

Figure 3: Invariant mass of the reconstructed K_S^0 (left) and reconstructed Λ^0 (right)

Secondary Interactions

In order to remove the maximum of background tracks, the procedure of removing tracks associated to V^0 candidates vertices is extended to other secondary interactions happening in the tracker volume, photon conversions and nuclear interactions. Selections are optimised to select these kinds of interactions but these vertices also have a low-track multiplicity and have to be reconstructed in the active (pixel and strip layers) and passive (beam pipe, barrel supports) layers of the tracker of CMS. The reconstructed secondary interactions vertices are shown in Fig.4 on the left. Regions with higher densities of vertices are easily seen, especially the first layers of pixels of the CMS tracker. The tracks associated to the vertices in Fig.4- right are removed from the analysis.

Selection of displaced tracks

After the removal of the main Standard Model sources of displaced tracks, the selection of displaced tracks

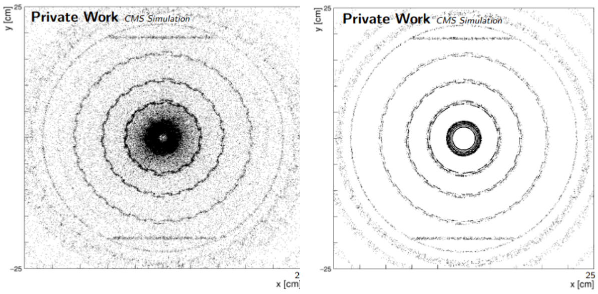

Figure 4: Transverse view of the reconstructed secondary interaction vertices (left) with the track-veto applied (right)

coming from the two neutralinos can be performed. First, the event can be reconstructed using the hadronic activity of the final state and then, the signal tracks can be selected using a machine learning technique.

Reconstruction of the event

The trigger system of CMS is used to select event with two prompt muons of opposite charge coming from the proton-proton collision point. Then, the final state of the neutralino signal being heavily hadronic, the event reconstruction is based on the jets from the decay of the neutralino. These jets can come from the coupling between the stop and the down and strange quarks as well as from the SM decay of the top quark. No particular restrictions are applied on the decay of the W boson from the top, both leptonic and hadronic decays are considered. Leptons originating from the W or from heavy-hadron flavour decays are also considered in the event reconstruction. The event topology and kinematics depends on the phase space of the signal studied: the smuon and neutralino masses, as well as the lifetime of the neutralino.

In the signal, neutrinos are pair-produced from the decay of the smuons, and decay further away in the tracker. Both neutralinos tend to be back-to-back in azimuth (ϕ) but close in η, meaning that there are two clusters of tracks, mainly coming from jets, back-to-back in ϕ. The 3D-space is then divided into two hemispheres, one for each neutralino. A precaution is applied as the prompt muons can overlap with the displaced jets, so the momentum of the prompt leptons are discarded in this building procedure to avoid any bias, then jets are re-ordered by decreasing value of p_T. The hemispheres are defined as follows :

- From the collections of jets ordered by decreasing value of p_T, the first jet is taken as the first axis of a first hemisphere
- Then, by looking at the other jets, if the geometric distance between the jet and the first axis is below a certain value, we add the momentum-vector of the two jets to redefine the first axis, else we build a second axis.
- Finally, we iterate over all the jets and assign them to one among both hemispheres and recompute the hemisphere momentum vector for each new jet

The goal of the analysis is to reconstruct one vertex per hemisphere.

Boosted Decision tree

Standard Model prompt tracks and signal displaced tracks can be hard to distinguish. A first selection (p_T > 1 GeV, $\frac{\chi^2}{DoF} < 5$ and the transverse impact parameter divided by its error above 5) is applied to reduce 90% of background tracks while keeping 95% of tracks from the neutralinos. To improve the selection, a Boosted Decision Tree (BDT) from the TMVA[30] toolkit of ROOT is implemented since no single cut on a kinematic variable allows to significantly increase the signal over noise ratio. This BDT uses various track parameter variables. The BDT is trained using all Standard Model backgrounds (mainly Drell-Yan and $t\bar{t}$) as background and a single signal sample with the following parameters : $M_{\tilde{\mu}} = 275$ GeV , $M_{\tilde{\chi}^1_0} = 225$ GeV, $\beta\gamma c\tau$= 50 cm. The output of the BDT is shown in Fig.5. A working point is defined and used to select signal tracks at a BDT value of 0.85 with a signal efficiency of 73% and background rejection of 99.5%.

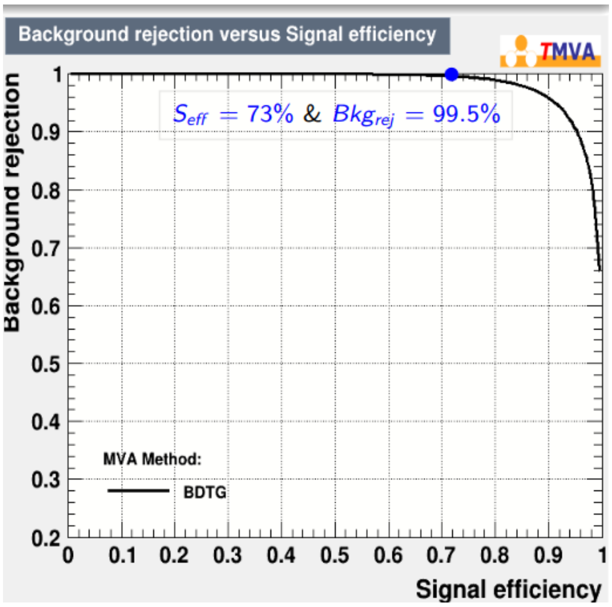

Figure 5: Boosted Decision Tree output where the blue dot is the working point used with the associated signal and background efficiencies

Since the event is geometrically divided into two hemispheres, the tracks selected are assigned to an hemisphere according to the geometric distance between a track and the closest hemisphere. A collection of displaced tracks is therefore built for each hemisphere and can be used to reconstruct displaced vertices.

Reconstruction of signal displaced vertices

In this analysis, one vertex is reconstructed per hemisphere using the Adaptive Vertex Fitter (AVF) [31]. Further improvement could be potentially obtained by looking for tertiary vertices coming from the b-jets but these jets can be hard to identify since b-tagging does not apply to largely displaced jets (dozens of centimeters) and also due to the decrease in resolution of the vertices.
For each hemisphere, we use the collection of the BDT selected tracks to build the vertices where we expect to have a collection enriched in signal displaced tracks. Then, we apply two different steps to try to build a vertex in an hemisphere:

1. The first iteration is the direct reconstruction of a vertex using all the BDT selected tracks. Its $\frac{\chi^2}{dof}$ has to be between 0 and 10.

2. if the previous step fails, an iterative implementation of the AVF is applied by considering first the two tracks with highest BDT values and adding an other one at each iteration, requesting a $\frac{\chi^2}{dof}$ between 0 and 10 at each iteration. The last vertex reconstructed with a good $\frac{\chi^2}{dof}$ is retained.

Results

Results are shown in terms of vertex reconstruction efficiency where it is defined as the ratio of the number of reconstructed vertices (with $0 < \frac{\chi^2}{Dof} < 10$) to the number of signal vertices that should be reconstructed. The purity is defined as ratio of matched vertices (the relative distance between a generated signal vertices and the reconstructed vertices must be lower than 10% of the generated decay length) with the number of vertices having a good χ^2 ($0 < \frac{\chi^2}{Dof} < 10$). The reconstruction efficiency and purity are shown In Fig.6. The resolution of these vertices is between 0.1 mm and 2 mm depending on the decay length of the neutralino.

The lower vertex reconstruction efficiency observed in Fig.6 for very low decay length (below 10 cm) is due to the high track density that prevents the AVF to properly reconstruct the vertices. The decreasing behavior at high decay length is due to the tracking efficiency decreasing rapidly with the distance.

Conclusion

In this paper, a search for displaced top quark through the decay of a massive long-lived particle in the tracker of CMS for the Run 2 of the LHC is introduced. This search is mainly based on machine learning to select displaced tracks in order to reconstruct signal displaced vertices reaching a signal vertex reconstruction efficiency of about 50% at a decay length of 50 cm for the neutralino.

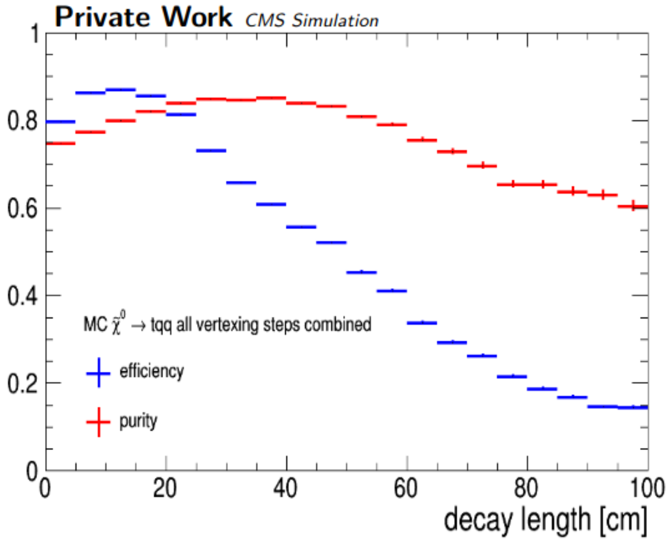

Figure 6: Signal vertex reconstruction efficiency (blue) and purity (red) as a function of the decay length of the neutralino

References

[1] P. Fayet, Supergauge invariant extension of the Higgs mechanism and a model for the electron and its neutrino, Nucl. Phys. B 90 (1975) 104,975, `https://doi.org/10.1016/0550-3213(75)90636-7`

[2] G. R. Farrar and P. Fayet, Phenomenology of the production, decay, and detection of new hadronic states associated with supersymmetry, Phys. Lett. B 76 (1978) 575,978, `https://doi.org/10.1016/0370-2693(78)90858-4`

[3] S. Weinberg, Supersymmetry at ordinary energies. 1. masses and conservation laws, 980 Phys. Rev. D 26 (1982) 287, `https://doi.org/10.1103/PhysRevD.26.287`

[4] R. Barbier et al., R-parity violating supersymmetry, Phys. Rept. 420 (2005) 1,982, `https://doi.org/10.48550/arXiv.hep-ph/0406039`

[5] G. F. Giudice and A. Romanino, Split supersymmetry ,Nucl. Phys. B 699 (2004) 65,958 , `http://dx.doi.org/10.1016/j.nuclphysb.2004.11.048`

[6] J. L. Hewett, B. Lillie, M. Masip, and T. G. Rizzo, Signatures of long-lived gluinos in split supersymmetry , JHEP 09 (2004) 070 , `http://dx.doi.org/10.1088/1126-6708/2004/09/070`

[7] N. Arkani-Hamed, S. Dimopoulos, G. F. Giudice, and A. Romanino, Aspects of split supersymmetry , Nucl. Phys. B 709 (2005) 3,965, `http://dx.doi.org/10.1016/j.nuclphysb.2004.12.026`

[8] P. Gambino, G. F. Giudice, and P. Slavich, Gluino decays in split supersymmetry , Nucl.967 Phys. B

726 (2005) 35, `http://dx.doi.org/10.1016/j.nuclphysb.2005.08.011`

[9] Arvanitaki, A., Craig, N., Dimopoulos, S. et al. Mini-Split. J. High Energ. Phys. 2013, 126 (2013). `https://doi.org/10.1007/JHEP02(2013)126`

[10] N. Arkani-Hamed et al., Simply unnatural supersymmetry, (2012).972 `https://doi.org/10.48550/arXiv.1212.6971`

[11] J. Fan, M. Reece, and J. T. Ruderman, Stealth supersymmetry. J. High Energ. Phys. 2011, 12 (2011). `https://doi.org/10.1007/JHEP11(2011)012`

[12] J. Fan, M. Reece, and J. T. Ruderman, A stealth supersymmetry sampler, HEP 07993 (2012) 196, `https://doi.org/10.48550/arXiv.1201.4875`

[13] Y. Cui, L. Randall, and B. Shuve, A WIMPy baryogenesis miracle, JHEP 04 (2012) 075,1004 , `http://dx.doi.org/10.1007/JHEP04(2012)075`

[14] Y. Cui and R. Sundrum, Baryogenesis for weakly interacting massive particles, Phys.1006 Rev. D 87 (2013) 116013, `http://dx.doi.org/10.1103/PhysRevD.87.116013`

[15] Y. Cui and B. Shuve, Probing baryogenesis with displaced vertices at the LHC, HEP1008 02 (2015) 049, `http://dx.doi.org/10.1007/JHEP02(2015)049`

[16] G. F. Giudice and R. Rattazzi, Theories with gauge mediated supersymmetry breaking, 984 Phys. Rept. 322 (1999) 419, `http://dx.doi.org/10.1016/S0370-1573(99)00042-3`

[17] P. Meade, N. Seiberg, and D. Shih, General gauge mediation, Prog. Theor. Phys. Suppl.987 177 (2009) 143, `http://dx.doi.org/10.1143/PTPS.177.143`

[18] M. Buican, P. Meade, N. Seiberg, and D. Shih, Exploring general gauge mediation, 989 JHEP 03 (2009) 016, `https://dx.doi.org/10.1088/1126-6708/2009/03/016`

[19] M. J. Strassler and K. M. Zurek, Echoes of a hidden valley at hadron colliders, Phys.995 Lett. B 651 (2007) 374, `http://dx.doi.org/10.1016/j.physletb.2007.06.055`

[20] M. J. Strassler and K. M. Zurek, Discovering the Higgs through highly-displaced vertices, Phys. Lett. B 661 (2008) 263, `http://dx.doi.org/10.1016/j.physletb.2008.02.008`

[21] T. Han, Z. Si, K. M. Zurek and M. J. Strassler , Phenomenology of hidden valleys at hadron colliders, JHEP 07 (2008) 008, `https://dx.doi.org/10.1088/1126-6708/2008/07/008`

[22] Andrea, J., Bloch, D., Conte, É. et al. Probing displaced top quark signature at the LHC Run 3. Eur. Phys. J. C 83, 299 (2023). `https://doi.org/10.1140/epjc/s10052-023-11470-6`

[23] The ATLAS Collaboration., Aad, G., Abbott, B. et al. Search for electroweak production of charginos and sleptons decaying into final states with two leptons and missing transverse momentum in pp collisions using the ATLAS detector. Eur. Phys. J. C 80, 123 (2020). `https://doi.org/10.1140/epjc/s10052-019-7594-6`

[24] The ATLAS collaboration, Search for direct production of charginos, neutralinos and sleptons in final states with two leptons and missing transverse momentum in pp collisions at $\sqrt{s} = 8$ TeV with the ATLAS detector. J. High Energ. Phys. 2014, 71 (2014). `https://doi.org/10.1007/JHEP05(2014)071`

[25] The ATLAS collaboration, Search for electroweak production of supersymmetric particles in final states with two or three leptons at $\sqrt{s} = 13$ TeV with the ATLAS detector. Eur. Phys. J. C 78, 995 (2018). `https://doi.org/10.1140/epjc/s10052-018-6423-7`

[26] The CMS Collaboration, Searches for electroweak production of charginos, neutralinos, and sleptons decaying to leptons and W, Z, and Higgs bosons in pp collisions at 8 TeV. Eur. Phys. J. C 74, 3036 (2014). `https://doi.org/10.1140/epjc/s10052-014-3036-7`

[27] The ATLAS collaboration, Search for direct slepton and gaugino production in final states with two leptons and missing transverse momentum with the ATLAS detector in pp collisions at $\sqrt{s} = 7$ TeV. Physics Letters B. 718. (2013), `https://doi.org/10.48550/arXiv.1208.2884`

[28] The CMS Collaboration, Search for supersymmetric partners of electrons and muons in proton-proton collisions at $\sqrt{s} = 13$ TeV. Physics Letters B. 790. (2019), `https://doi.org/10.48550/arXiv.1806.05264`

[29] The ATLAS Collaboration, Search for electroweak production of supersymmetric states in scenarios with compressed mass spectra at $\sqrt{s} = 13$ TeV with the ATLAS detector. Phys. Rev. D 97, 052010 (2018) `https://doi.org/10.48550/arXiv.1712.08119`

[30] P Speckmayer et al, TMVA - Toolkit for Multivariate Data Analysis, J. Phys.: Conf. Ser. 219 032057, 2020, `https://doi.org/10.48550/arXiv.physics/0703039`

[31] W. Waltenberger and R. FrÃ¼hwirth and P. Vanlaer, Adaptive Vertex Fitting. Journal of Physics G: Nuclear and Particle Physics. 34. (2007), `https://dx.doi.org/10.1088/0954-3899/34/12/N01`

Part IV

Instrumentation & Interdisciplinarity

session chaired by Sabrina SACERDOTI

The ATLAS High-Granularity Timing Detector: test beam campaigns and results

Oleksii Kurdysh

Laboratoire de Physique des 2 Infinis Irène Joliot-Curie (IJCLab)

Abstract — At high luminosity LHC, pile-up is expected to increase on average to 200 interactions per bunch crossing. Detector adjustments are needed; one of them in ATLAS is The High Granularity Timing Detector (HGTD), a new timing sub-detector. Its front-end is a fast and radiation-tolerant-enough sensor, Low Gain Avalanche Detectors (LGAD), being read out with ALTIROC, a dedicated ASIC designed for the HGTD detector. Contribution mainly describes the performance of LGAD+ALTIROC hybrids in 2021,2022 testbeam campaigns.

Introduction

The expected increase of the particle flux at the high luminosity phase of the LHC (HL-LHC) with instantaneous luminosities up to $L \approx 7.5 \times 10^{34} cm^{-2} s^{-1}$ will have a severe impact on the ATLAS detector performance. Run-4 (HL-LHC) $< \mu >$ will be $\approx$ 4 times larger compared to Run-3. The reconstruction and trigger performance for electrons, photons, as well as jets and transverse missing energy will be severely degraded in the end-cap and forward region, where the liquid Argon-based electromagnetic calorimeter has coarser granularity and the inner tracker has poorer momentum resolution compared to the central region.

In order to cope with the new environment, one of the things that will be done in ATLAS is the installation of a new timing sub-detector in the forward region (will cover the pseudo-rapidity range from 2.4 to about 4.0): HGTD (The High Granularity Timing Detector) will be installed in front of the liquid Argon end-cap calorimeters. HGTD will be there for pile-up mitigation and bunch-per-bunch luminosity measurements.

The Silicon sensor chosen for HGTD is Low Gain Avalanche Detectors (LGAD), as it provides an internal gain good enough to reach a large signal-over-noise ratio needed for excellent time resolution and is able to survive the necessary amount of irradiation. LGADs are n-on-p silicon detectors with an additional p-type doped layer containing charge multiplication to achieve an internal gain. Two silicon double-sided layers should provide precision timing information for minimum ionizing particles with a time resolution better than 50-70 ps per hit (i.e., 30-50 ps per track) to assign the particle to the correct vertex. Each LGAD readout cell has a transverse size of $1.3 \times 1.3 mm^2$, leading to a highly granular detector with about three million readout electronics channels. A dedicated ASIC for the HGTD detector, ALTIROC, is being developed in several phases, producing prototype versions of 2×2(ALTIROC0), 5×5(ALTIROC1), and 15×15(ALTIROC2,3) channels. HGTD modules are the LGAD and ALTIROC hybrids connected through a flip-chip bump bonding process. ALTIROC will measure TOA(Time of Arrival) and TOT(Time over Threshold), as illustrated in Fig.1.

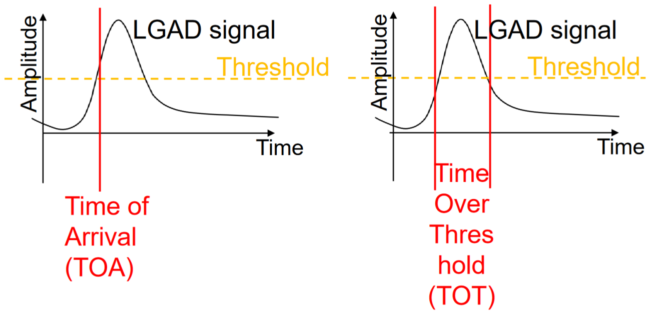

Figure 1: Illustration of TOA(left) and TOT(right)

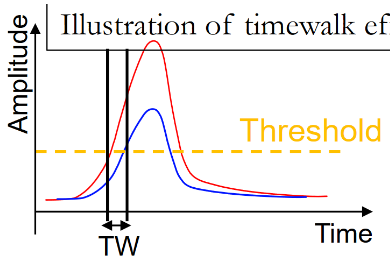

Figure 2: Illustration of timewalk

Contributions to hybrid time resolution are shown in Eq.1, Eq.2. $\sigma_{Landau}, \sigma_{TDC}, \sigma_{LHCclock}$ are fixed by LGAD design, ASIC TDC design, and clock distribution system, respectively. $\sigma_{TimeWalk}$ arises because TOA depends on signal amplitude(illustrated in Fig.2), leading to degraded resolution. However, if the amplitude is known, it can be corrected - this is why ALTIROC is measuring TOT - TOT is a proxy for the amplitude. The remaining term, jitter, which is uncorrectable, is illustrated in Fig.3.

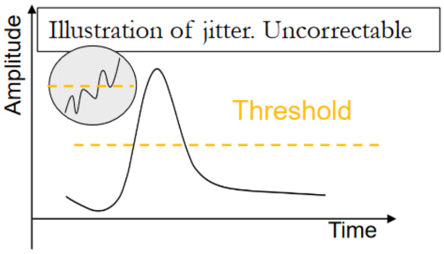

Figure 3: Illustration of jitter

$$\sigma^2_{\text{module}} = \underbrace{\sigma^2_{\text{Landau LGAD}}}_{\sim 25\text{ps}} + \sigma^2_{\text{ASIC}} \tag{1}$$

$$\sigma^2_{\text{ASIC}} = \underbrace{\sigma^2_{\text{TimeWalk}}}_{\text{corrected } <10\text{ps}} + \sigma^2_{\text{Jitter}} + \underbrace{\sigma^2_{\text{TDC}}}_{<10\text{ps}} + \underbrace{\sigma^2_{\text{LHCclock}}}_{<15\text{ps}} \tag{2}$$

Several test beam campaigns have been conducted at DESY and CERN SPS H6 beamline in 2021,2022. The performance of irradiated Carbon-enriched LGAD sensors has been studied. First full-size module prototypes of 15 × 15 arrays for the HGTD project have been tested from different manufacturers. The current version of LGAD is carbon enriched since it allows lower operating voltage, and this is needed to avoid Single Event Burnout: sensor break with a star-shaped pattern formed - as described in [1]. This sensor version performs as required after irradiation - see [2], in particular, Fig.4 shows the time resolution obtained. Below, the performance of ALTIROC1+LGAD and ALTIROC2+LGAD hybrids will be presented.

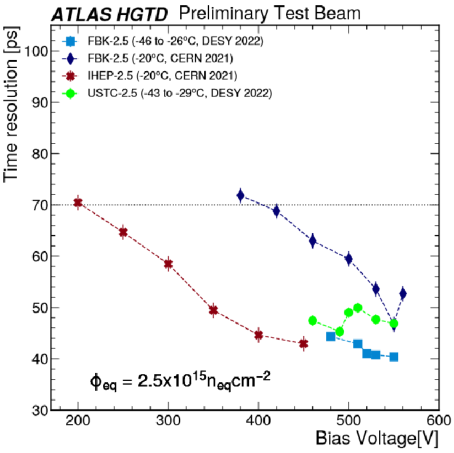

Figure 4: Time resolution of carbon-enriched(current prototype) sensors after irradiation

ALTIROC and testbeam setup, methodology

The significant change between ALTIROC1 and ALTIROC2 is that the latter is the first full-scale ASIC(Application-Specific Integrated Circuit) prototype with all 225 channels - chip organization is shown in Fig.5. The figure also shows debug-exclusive (will not be available in HGTD) possibility to probe signal (which is then digitized with scope) right after preamplifier - this is our best estimation of the signal that ASIC operates on.

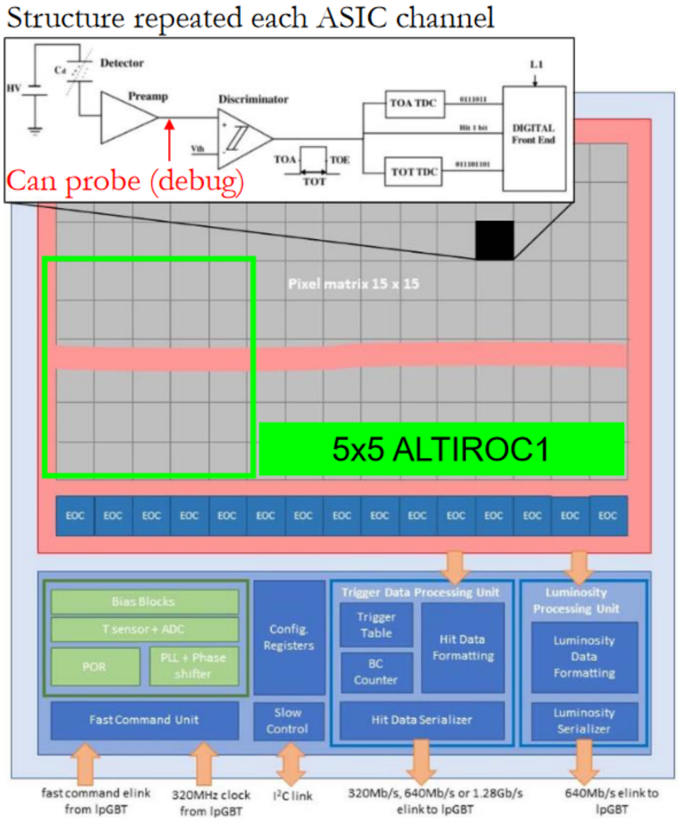

Figure 5: ALTIROC organization, in particular per channel

ALTIROC was put into the CERN SPS H6 testbeam to evaluate its performance in close-to-real-life conditions. Testbeam setup is shown in Fig.6. ALTIROC1 and ALTIROC2 setups are slightly different regarding reference devices used, leading to different methodologies of time resolution extraction.

During the ALTIROC1 test beam, two SiPMs were used for reference, each with comparable time resolution to hybrid, then to obtain a resolution of each one needs to solve the system showed in Eq.3, where each σ's on the left are obtained from the gaussian fit of corresponding ΔT.

$$\begin{cases} \sigma_{\Delta T(\text{SiPM1,SiPM2})} = \sigma_{\text{SiPM1}} \oplus \sigma_{\text{SiPM2}} \\ \sigma_{\Delta T(\text{hybrid,SiPM1})} = \sigma_{\text{hybrid}} \oplus \sigma_{\text{SiPM1}} \\ \sigma_{\Delta T(\text{hybrid,SiPM2})} = \sigma_{\text{hybrid}} \oplus \sigma_{\text{SiPM2}} \end{cases} \tag{3}$$

During ALTIROC2 testbeam (single) MCP, that has negligible(compared to hybrid) time resolution; therefore, to obtain hybrid resolution, it is enough to do Gaussian fit on difference shown in Eq.4, where LSB is a conversion factor from binary to ps, measured in testbench, and t_{clock} is an ASIC clock digitized by oscilloscope. The equation works because TOA provided by ASIC is measured with respect to the clock falling edge, and this same clock we digitize to obtain t_{MCP} relative to it.

$$\Delta T = -TOA \times LSB - (t_{MCP} - t_{clock}) \qquad (4)$$

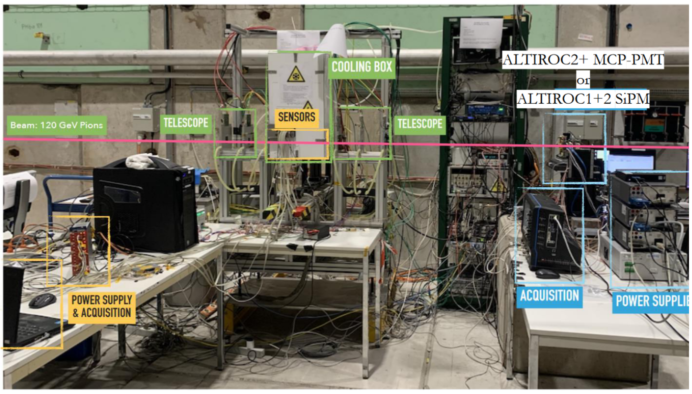

Figure 6: Testbeam setup used for hybrid test

ALTIROC1 performance

This section is a very short and incomplete summary of paper published not so long ago - see [3]

One caveat about this version is that TOA-TOT is not flat as expected - observed in testbeam dependence is shown on 7. This is attributed to a digital coupling synchronized with the 40 MHz clock. The effect can be corrected in data, where it is seen that its contribution is not more than 5ps. Relevant modifications to ASIC are implemented to reduce the effect in further versions.

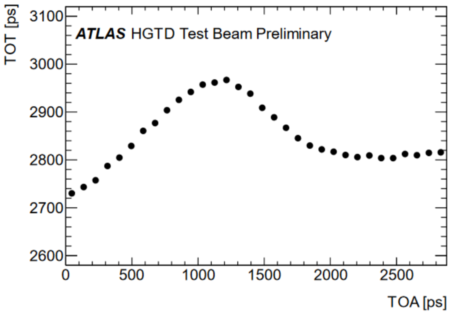

Figure 7: TOA-TOT dependence

Timewalk correction is done in data. Preamplifier probe amplitude (maximum of digitized probe signal) and ASIC TOT time walks together with fit used to correct it are shown in Fig.8. The time difference between ASIC and one of the SiPMs before and after time walk correction together with final hybrid resolutions are shown in Fig.9 (when time walk is corrected with probe) and in Fig.10. It can be seen that probe time walk correction is more effective than expected and gives the best-case time resolution. Resolution with ASIC TOT, the only thing we will have in HGTD, is worse by 6ps, but the result is still close to HGTD requirements.

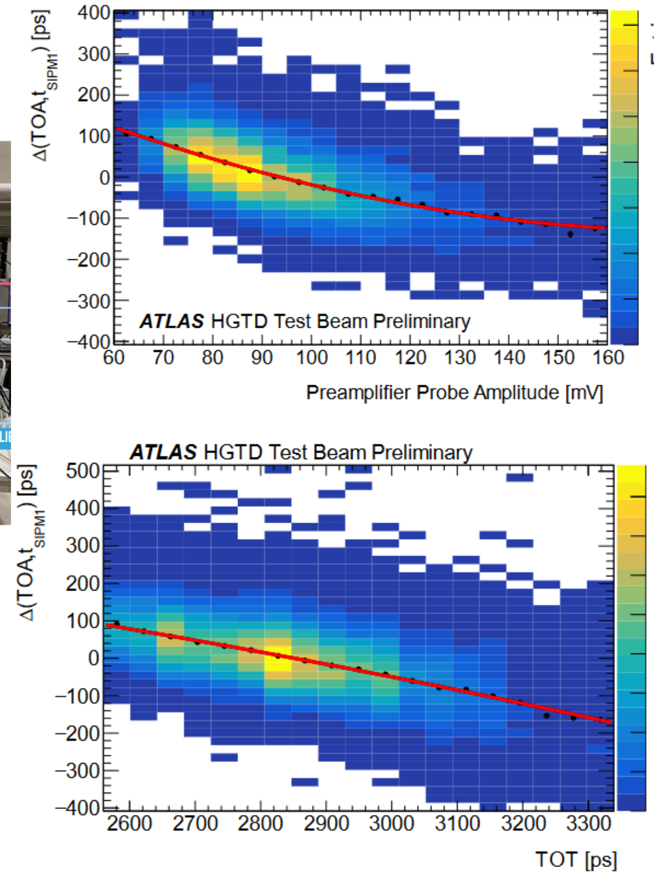

Figure 8: (top) preamplifier probe timewalk (bottom) ASIC TOT timewalk

ALTIROC2 performance

ALTIROC2 time performance is similar to ALTIROC1. Therefore, this section will be concerned with hybrid hit efficiency, measured as the ratio of the reconstructed tracks with a hit seen in ALTIROC to all the reconstructed tracks penetrating the hybrid area. Tracks are obtained with PaTrack software based on EUDET-type telescope measurements (consisting of 6 planes, and a hybrid is located between planes 3,4). The ASIC threshold used is 4.8 fC, and the charge obtained from the sensor is above 20 fC. The efficiency map obtained is shown in Fig.11, where not all 225 pixels are shown but only the one visible in the beam. It can be seen that pixels of expected dimensions have 100% efficiency, satisfying the requirement.

"Zooming" into each inter-pixel region, as shown in Fig.12, allows us to obtain the amount of inactive area.

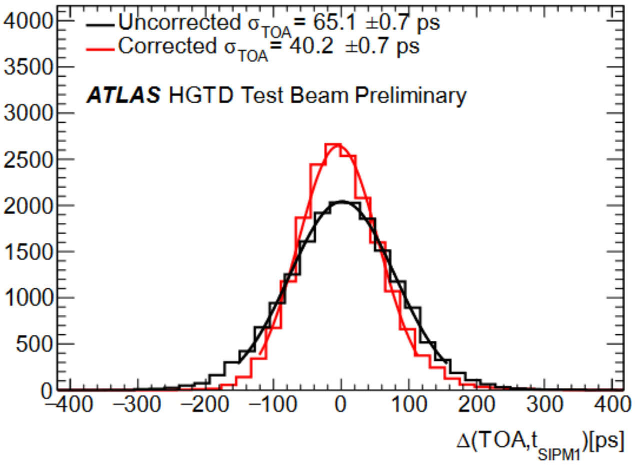

Figure 9: $\Delta T(hybrid, SiPM)$ before and after time-walk correction with probe

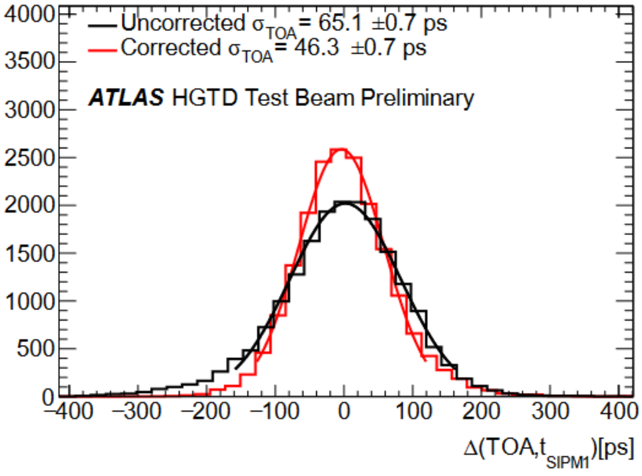

Figure 10: $\Delta T(hybrid, SiPM)$ before and after time-walk correction with ASIC TOT

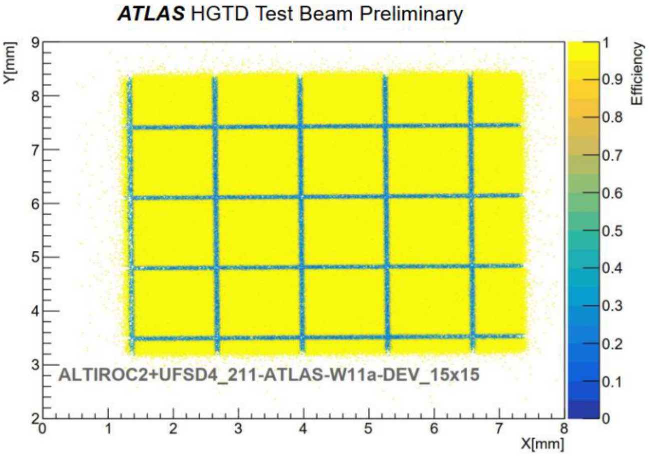

Figure 11: ALTIROC2 hit efficiency map

Taking 50% width of distribution(obtained from linear interpolation) as interpad size, the typical gap size is around 65 microns, as seen from Fig.13. Interpad size is uniform, and there is no difference between horizontal and vertical interpads.

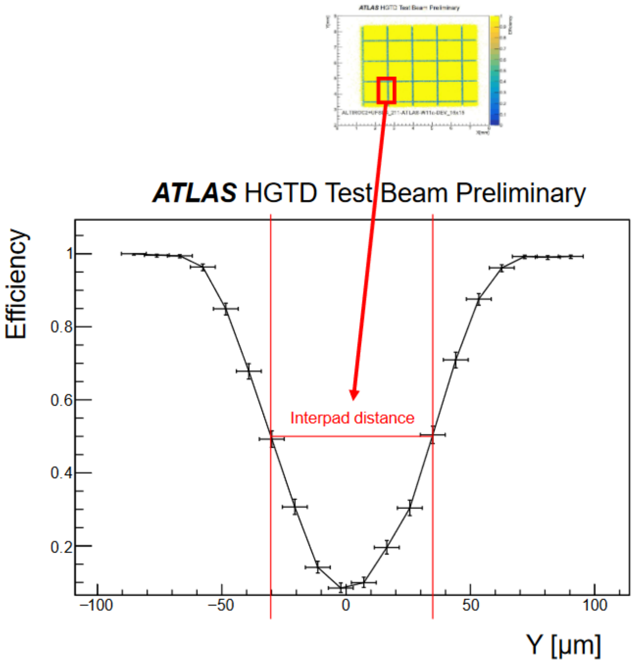

Figure 12: One example of interpad distribution and distance

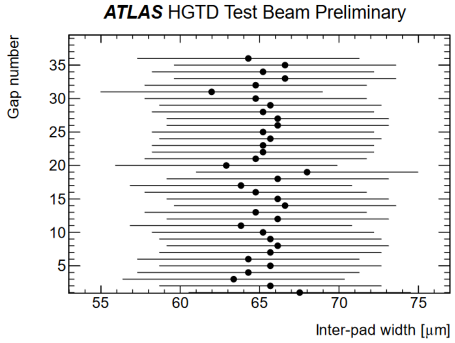

Figure 13: Sizes of all interpads visible in beam

Conclusion

ALTIROC1 and ALTIROC2 hybrids testbeam results are presented. Time resolution obtained with ALTIROC1 after ASIC TOT timewalk correction is 46.3± 0.7 ps. ALTIROC2 has similar timing performance, hit efficiency 100% and interpad size ≈ 65 micron. ALTIROC3 is available and has already been tested in testbeam; analysis is ongoing.

References

[1] L. A. Beresford, D. E. Boumediene, L. Castillo García et al. Destructive breakdown studies of irradiated LGADs at beam tests for the ATLAS HGTD, 2023

[2] S. Ali, H. Arnold, S. L. Auwens et al. Performance in beam tests of Carbon-enriched irradiated Low Gain Avalanche Detectors for the ATLAS High Granularity Timing Detector, 2023

[3] C. Agapopoulou, L.A. Beresford, D.E. Boumediene et al. Performance of a front-end prototype ASIC for the ATLAS High Granularity timing detector, 2023

High-energy ion beam analysis: the study of raw materials and manufacturing techniques for cultural heritage objects

Alexandre Gillon

Subatech - Nantes University

Abstract —
The non-destructive analysis of art and archaeological objects is central to heritage studies, enabling us to trace societies´ cultural evolution and technical history. This proceeding will focus on a current application of High-Energy Particle Induced X-rays Emission (HE-PIXE) analysis looking at raw material supply in silver coins minted in Nantes in the late 16^{th} century. A coupled analytical strategy has been experimented with a handheld X-ray spectrometer (p-XRF) to look for specific trace elements in the coins such as gold and indium.

Introduction

The South American mine at Potosi, in present-day Bolivia, has been in production since 1548. Nantes' trade with Spain favoured the use of Potosian silver to mint French coins from 1575 onward. Previous studies using the thermal neutron activation techniques [1, 2, 3] have highlighted indium as a trace element specific to Potosian silver. Gold is also a good tracer for silver as the two elements are very close chemically, so silver and gold are not separated during the silver ore refining process. However, studies reveal a significant difference between the concentrations of gold in Mexican silver and in Potosian silver (Figure 1). Analysis of the concentrations of those trace elements must help to distinguish Potosian silver from other sources.

Figure 1: Gold against indium content on previously analysed coins (data from [2])

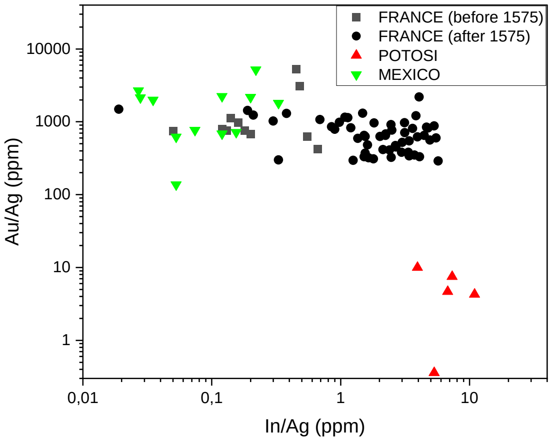

The concentration of gold in the Mexican/European group could easily reach hundreds of ppm whereas the Potosian group is lower than a hundred ppm. In light of previously published data, the arrival of Potosian silver in France (in 1575) is accompanied by the systematic recasting of old stocks of European and even Mexican silver. A mixture of several sources of supply has an impact not only on gold concentrations in coins but also on other trace elements such as indium in the case of Potosian silver.

French coins plotted in Figure 1 led to distinguish two groups with low and high indium concentrations. However, mixing silver sources should automatically reduce gold concentrations in French coins in the same way as it increases indium concentrations. A new look into the activity of the Nantes mint is provided by this study. We seek to investigate a large set of coins to conclude that there may be a decreasing trend in gold content and to classify Potosian silver coins from the others.

The joint analysis of the same coins using HE-PIXE and p-XRF methods aims to exploit the characteristic X-ray spectra with three detectors sensitive to low and high energy to identify and quantify trace elements.

Materials and Methods

Corpus

We have at our disposal a corpus of 42 silver coins minted in Nantes between 1561 and 1600 (Table 1). These coins come from private and museum collections. The aim of studying a large group of Nantes coins over a wide historical period is to provide quantitative data to support numismatic knowledge of this corpus.

We can expect to observe different behaviour depending on the period analysed. Through trade with Spain, the Nantes mint was a stronghold of "Atlantic" pro-

Table 1: Coins under study

Type	Head	Minting date	Number
Teston	Henri II	1561	1
Teston	Charles IX	1562 to 1573	14
Teston	Henri III	1575	1
Ecu	Charles X	1597 to 1598	10
Ecu	Henri IV	1598 to 1600	16

duction. According to [2], Potosian silver did not reach French coasts until 1575, so the coins minted under Henri II and Charles IX probably contained a high concentration of gold typical of European and Mexican sources. The city was also the headquarters of the "Ligueur", who opposed King Henri IV of France until the Edict of Nantes was signed on 30 April 1598. Some of the coins minted in 1598 (Figure 2) were probably made from an old stock of silver, as Nantes was under siege and the supply of silver was interrupted.

Figure 2: 1/4 d ecu - Charles X

Set up

HE-PIXE is carried out using a 68MeV α particle beam [4, 5, 6]. We use an SDD-type detector (X-PIPS SXD30M-150-500) for low-energy X-rays and an HPGE-type detector for high-energy X-rays (CAMBERRA 50 mm^2). Detectors are facing the target at a distance of 10 cm. The angle between the incident beam and detector axes is about 50°. Very low intensity (<1nA) is used to limit matrix activation and detector dead time (below 10%). The setup is illustrated in figure 3.

The handheld spectrometer TRACER-III-SD is used in addition to HE-PIXE analyses to characterize silver coins composition. Our XRF instrument is equipped with a Rh tube with a maximum power of 2W and a 10 mm^2 XFlash SDD-type detector. We used the same experimental conditions for all coins: a tube's supply voltage/current of 40 kV and 13 μA during 300 s. Light elements (Cu, Ag) are detected by their K X-ray lines and heavy elements by their L X-ray lines (Au). The incident beam is filtered to limit background noise in the energy region below 20 keV and improve the detection of gold L_α at 9.7 keV. The main excitation energy is given by Rh K_α line at 20.2 keV which is lower than In K edge energy so detection of indium by XRF is compromised. In addition, XRF device contains Palladium which produces X-rays that overlap the indium region.

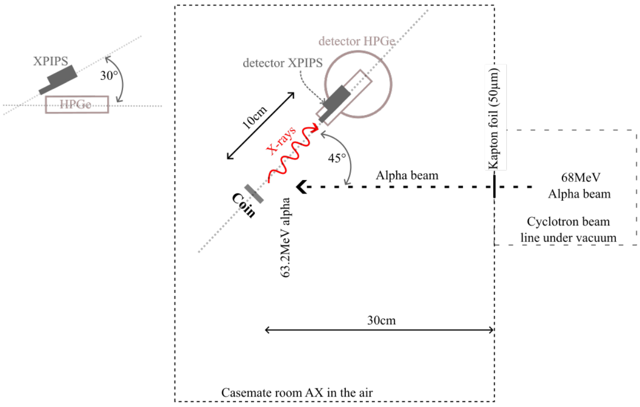

Figure 3: HE-PIXE set up

Analytical strategy

Indium detection by HE-PIXE is very challenging because of the low concentration of this trace element in Potosian silver. In addition, In K_α is close to Ag K_β line and the background in this region is impacted by nuclear reaction during irradiation. At the first stage to simplify the study, we look only at Au X-ray lines which must be easier to detect with our set-up. Comparing our investigations with historical knowledge and previous data published, we seek to isolate some coin groups with high and low gold content.

Silver coins under study are made with two different silver-copper proportions. We used standard materials as references for quantitative analysis, thick and homogeneous targets of certified composition. Table 2 gives the main element composition in each target.

Table 2: Composition of standards and coins

Element	AGA1	AGA2	Teston	1/4 ecu
Ag	77.6 %	88 %	89.9 %	91.7 %
Cu	20 %	10 %	10.1 %	8.3 %
Au	1480 ppm	507 ppm		
In	37 ppm	65 ppm		

P-XRF is more available than HE-PIXE which depends on the beam schedule of an accelerator. In addition, p-XRF spectra contain less background compared to HE-PIXE (high energy beam produces high energy γ that interacts with the detector and generates Compton background). On the other hand, in XRF analysis, the coins are placed right on the exciting window, very close to the detector compared to the HE-PIXE set-up. It implies that the solid angle is much lower in the case of HE-PIXE. The coin's surface is not flat and some black patina could appear as well as deformation over time. Those surface alterations could impact the X-ray detection by attenuation or shadow effect.

The probing depth of each element composing the coins is calculated at 90% attenuation. Au L_α at 9.7 keV comes from the first 16 μm. Considering K_α line of Rh at 20.2 keV as the main incident excitation energy for XRF analysis, we can evaluate X-ray attenuation at a given depth of 16 μm.

Table 3: Transmission coefficient of Rh K_α line in 16 μm

AGA1	AGA2	Teston	1/4 ecu
70 %	72 %	72.7 %	73 %

Table 3 shows that incident beam attenuation depends on the matrix composition, there is a gap of 5 % between AGA1 and the coins and a gap of 1 % between AGA2 and the coins. As AGA1 has a higher content of gold (1480 ppm) than AGA2 (507 ppm) it should be easier to detect with higher statistics in XRF and HE-PIXE spectra so we chose AGA1 as a reference for gold quantitative analysis.

With HE-PIXE the path of the α depends mainly on the density of the target. In the case of copper-silver matrix, the α range is about 600 μm. X-ray production cross section (CS) depends on α beam energy. It slightly decreases in depth of 16 μm compared to Rh tube X-ray attenuation.

Even if HE-PIXE incident beam is less surface dependent than XRF, X-rays emitted by the material are still attenuated on their way back to the detector. Detection of low energy X-rays like Cu K_α and Au L_α give near-surface information compared to higher energy lines like Ag K_α (up to 150 μm). HE-PIXE could be used to probe even deeper with Au K_α (up to 620 μm).

The previous points show an interest in coupling techniques and detectors. With HE-PIXE (two detectors) and p-XRF (one detector), we determine for each coin three independent measurements. This enhances the precision of our results and prevents errors in the data.

Results

The first observations were made on all the coins with the three detectors. X-ray spectra of a "1/4 d écu - Charles X" minted in 1599 is given in Figure 4. SDD-type detectors are limited to energy regions below 30 eV which include major elements as Cu and Ag as well as minor and trace elements like Zn, Pb and Au. Escape and pile-up peaks are detector artefacts. HPGe is sensitive to higher energy ranges and can detect the K X-ray lines of heavy elements (Figure 5).

Figure 4: HE-PIXE and XRF spectra of 1/4 d ecu - Charles X

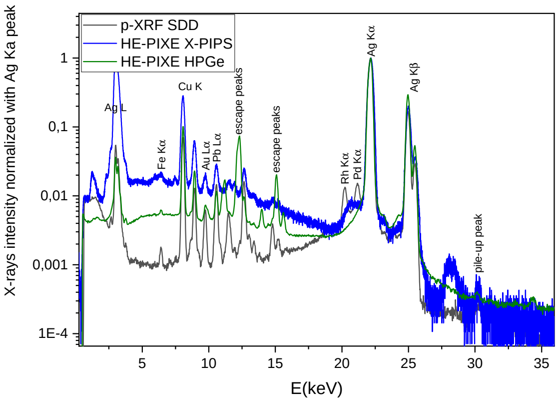

Figure 5: High energy spectrum - 1/4 d ecu - Charles X

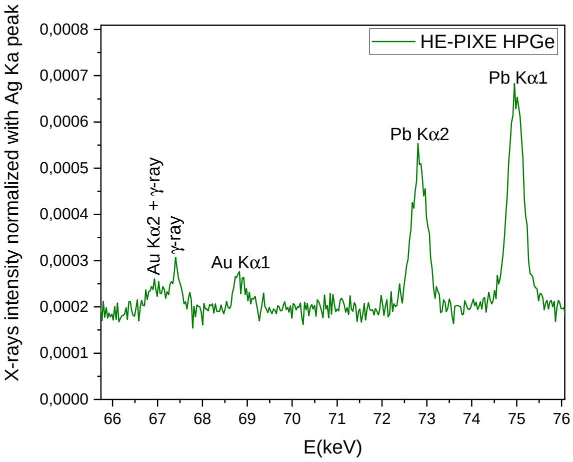

Figure 6, 7 and 8, shows respectively spectra of p-XRF, HE-PIXE with X-PIPS detector and HPGe detector for the coin and standard reference AGA1. Gaussian fit of the spectra is carried out using OriginPro software on the raw data.

Au L_α energy region is well defined with SDD detectors. Other peaks are detected in the same energy region. We see Zn K_β as there is 2% Zn in AGA1 (Figure 6). Ge K_α from HPGe detector crystal is always seen in the HE-PIXE spectrum (Figure 7).

Figure 6: p-XRF

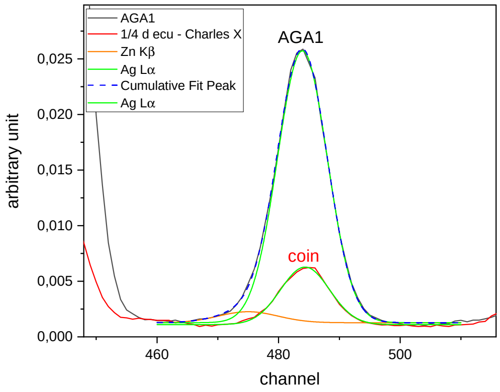

Figure 7: HE-PIXE with XPIPS

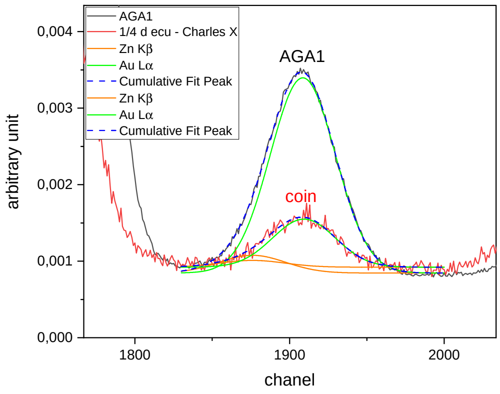

Figure 8: HE-PIXE with HPGe

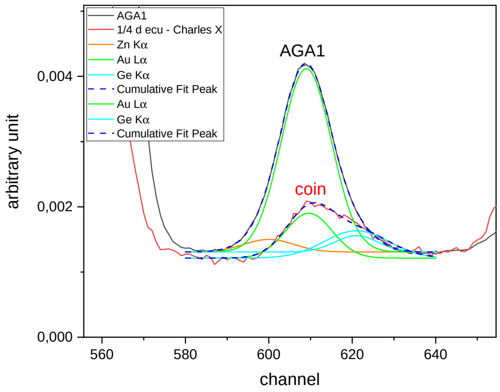

Conclusion

This work presents our analytical strategy to analyse gold in silver coin minted at Nantes by using HE-PIXE and p-XRF. Current analysis of our silver coin corpus is still in progress and final exhaustive results will be published soon. The search for tracers other than gold, such as indium and mercury, will also be investigated. The results of these analyses should provide new insights into the production and circulation of money, shedding light on the associated history and economy.

Other applications of ion beam analysis were performed at ARRONAX cyclotron. We have a lead pipe discovered during the excavation of the water supply system of a medieval castle (13^{th} - 14^{th} centuries). Proton Activation Analysis (PAA) is performed to characterize the composition of the metals used. Regarding the pipe solder joints, we look if the tin-lead concentration profile is homogeneous in all the solder joints to characterize the quality of the soldering technique. The analysis is based on the differential gamma ray attenuation of the Sn and Pb radioisotopes probed for several beam energies (17, 34, 45 and 68 MeV).

References

[1] E. Le Roy Ladurie, D. Richet, A. Gordus, J. Gordus, et E. Le Roy Ladurie,"Le Potosi et la Physique nucleaire", Ann. Hist. Sci. Soc., vol. 27, no 6, p. 1235 to 1256, 1972.

[2] E. L. R. Ladurie, J.-N. Barrandon, B. Collin, M. Guerra, et C. Morrisson, "Sur les traces de l'argent du Potosi", Ann. Hist. Sci. Soc., vol. 45, no 2, p. 483-505, avr. 1990, doi: 10.3406/ahess.1990.278849.

[3] M. F. Guerra, "The circulation of South American precious metals in Brazil at the end of the 17th century", J. Archaeol. Sci., vol. 31, no 9, p. 1225 to 1236, 2004, doi: https://doi.org/10.1016/j.jas.2004.03.018.

[4] C. Koumeir, F. Haddad, V. Metivier, N. Servagent, et N. Michel, "A new facility for High energy PIXE at the ARRONAX Facility", p. 9, 2010.

[5] D. Ragheb et al., "Development of a PIXE method at high energy with the ARRONAX cyclotron", J. Radioanal. Nucl. Chem., vol. 302, no 2, p. 895 to 901, nov. 2014, doi: 10.1007/s10967-014-3314-8.

[6] A. Gillon et al., "Elemental analysis by XRF and HE-PIXE on silver coins from the 16th-17th centuries and on a gilded crucifix from the 12th century", Eur. Phys. J. Plus, vol. 138, no 10, p. 945, oct. 2023, doi: 10.1140/epjp/s13360-023-04570-5.

Performance evaluation of the Siemens Somatom Go.Open Pro scanner with GATE

Gaëtan Raymond

LPC / Siemens Healthineers / Unicancer

Abstract — Reducing the dose delivered by CT scanners is a major public health issue [1]. The aim is to obtain scanner images that can be interpreted medically with the lowest possible dose [2]. The Monte Carlo simulation platform GATE [3,4,5] (www.opengatecollaboration.org) is being used to model Siemens Healthineers's Go.Open Pro scanner. GATE versions 9.3 and 10 beta are used to model the scanner's acquisition chain using Python scripts: primary photon generation, photon and electron interactions in the material, and detection electronics. Simulation results enable dose mapping in different test objects and reconstruction of 3D scanner images. This study enables GATE modeling to be compared with multi-center physical measurements at Unicancer: the dose for different acquisition protocols and subjects and the quality of the images produced are studied, compared and optimized. A multi-center measurement protocol is being built to test various dose reduction functionalities put forward by Siemens Healthineers (automatic intensity modulation, for example).

Introduction

The aim of this CIFRE doctoral thesis is to study and optimize the latest-generation scanners from the manufacturer Siemens Healthineers, in particular the Somatom Go.Open Pro model. This is a latest-generation radiotherapy treatment simulation CT scanner. It features dose reduction tools and iterative image reconstruction algorithms (SAFIRE). This device thus shares features of dedicated diagnostic scanners, and improved performance compared with older-generation simulation scanners:

- a Stellar technology detector made of ceramic (improved image quality through reduced electronic noise);
- a full rotation time of 0.35 s;
- a tin filter and a usable voltage range from 70 to 140 kVp in 10 steps, to adapt the dose delivered to each patient;
- CARE Dose 4D: Adaptation of mAs to patient size;
- CARE kV: Optimization of kilovolts (kV) to limit patient dose;
- TwinSpiral's use of dual-energy with a second photon spectrum for improved material characterization;
- automatic contouring by artificial intelligence according to location: DirectORGANS.

The dose is directly linked to image quality. Scanner acquisition parameters have a direct influence on dose: if the operator increases kVp or mAs, the dose will be higher. For pitch (ratio between the distance covered by the table during a rotation by primary beam collimation) and acquisition slice thickness it is the opposite. These parameters will also modify the image produced. They must therefore be adapted according to the clinical indication. The image must enable medical interpretation at the lowest possible dose.

This work can be divided into two parts:

- The first part concerns the *in silico* study of the Go Open Pro scanner using Monte Carlo GATE simulation. This study addresses both the delivered dose during examinations (on phantom and on the patient) and the image quality.
- A second part will be considered the implementation of optimized acquisition protocols between several French Cancer Centers (CLCC) members of Unicancer. This work has a purpose of dose measurements and image quality assessment.

Design and validation of Monte Carlo GATE simulations of the CT scanner Go.Open Pro

X-ray photon spectra

On the basis of the information available and using SpekCalc v1.1 software [6,7,8] the spectra of X-ray photons emitted by the scanner at different accelerator voltages (70, 120 and 140 kVp). The main parameters used in SpekCalc are

- the theta angle of the anode inclination to the axis of the incident electron beam;

- target material (tungsten, Z = 74); the tin filter will be taken into account as soon as the Siemens Healthineers data are available;
- the value of the first half-attenuation layer (CDA1) for filtration.

These spectra will be adapted according to the manufacturer's data. For the moment, inside water cube of 30 cm side, the depth of maximum dose for 120 kVp has been calculated at 7 mm without bowtie (Figure 1). This value is in good agreement with measurements carried out on the X-ray irradiator available at the LPC (X-Rad 320).

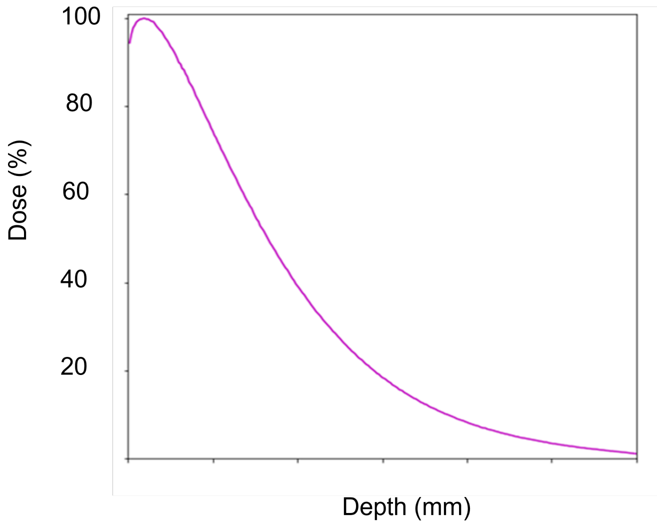

Figure 1: Dose depth profile inside water cube of 30 cm side for 120 kVp with GATE

Dosimetric study on Computed Tomography Dose Index (CTDI) phantom

Figure 2 shows a GATE v9.1 simulation of the scanner with a description of a phantom dedicated to computed tomography dose index (CTDI) measurement which corresponds to the dose per patient per slice in mGy.

This index is used to estimate the dose delivered by a scanner acquisition, as well as for quality control purposes. The results obtained with GATE are currently 30 % away from the values provided by Siemens Healthineers. These differences is explained by geometries assumptions and approximation of the spectra above.

Projection acquisition

Photons passing through the CTDI phantom, or any other object, then interact with a UFC (ceramic) detector comprising 58,880 pixels divided into 46 modules having 20 * 64 pixels. CT scans work basic principle is a tube-detector pair rotates around an object to obtain a 3D reconstruction of it. Without object translation, a 360° rotation of the RX tube can, for example, be broken down into 36 different positions every 10°. For each angular position, a mapping of the singles (signal after modeling of the detection chain) on the detector is called a projection. These projections are reconstructed using Python codes from GATE outputs. Two different projections (with and without the object to be imaged) are required to characterize the elements crossed by the photons in relation to the differences in attenuation for each pixel (line integrals). The first of 36 projections for a rotating tube of a water cylinder containing an aluminum cube is shown in Figure 3 below:

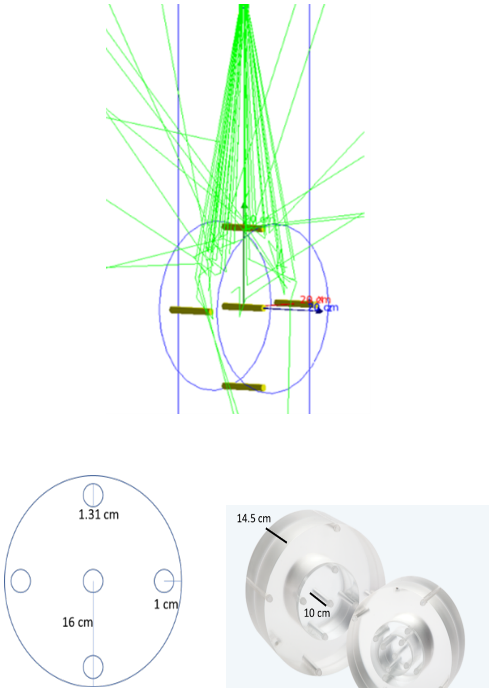

Figure 2: CTDI phantom schema, picture and GATE simulation

Figure 3: Projection of a water cylinder of 10 cm diameter with a central copper cube

Image reconstruction

With python scripts initially developed by M.Mouchet and the Reconstruction Tool Kit (RTK) [9], the projections are reconstructed into a 3D image according several parameters (Figure 4).

To conclude the simulation part, the work to be completed is as follow:

- Precise scanner geometry with manufacturer's information: spectra, tin filter, bowtie, collimation, detector;
- Dosimetric calculations: CTDI with and without tin filter, dose to organs in a phantom and voxelized patient images;

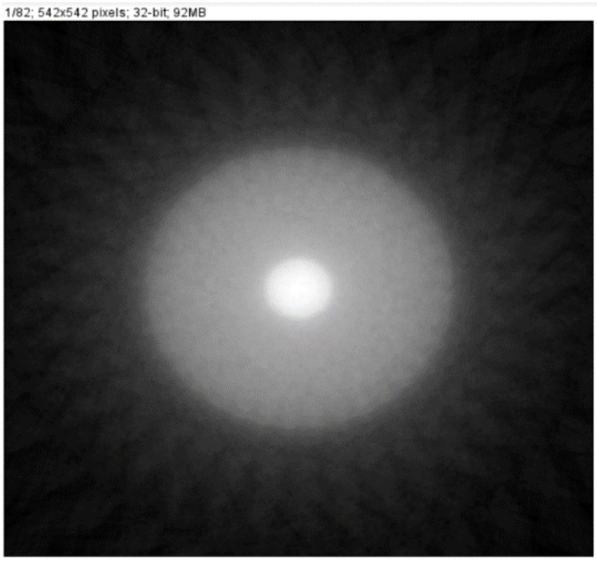

Figure 4: Image reconstruction with GATE and RTK

- Image reconstruction for phantoms and patients for several clinical protocols;
- GATEv10 beta full implementation.

For the time being, my Monte Carlo simulations are based on information provided by Siemens Healthineers.

In particular, the following parameters are approximated: X-ray energy spectra; bowtie; distances and detector composition. This project doesn't have a full access to the software and methods used for image reconstruction by Siemens Healthineers.

Implementation and evaluation of standardized scanner acquisition protocols

For dose studies

In addition to the CTDI measurements and dose profiles required by French regulations, automatic exposure controls are testing because they enable to adapt exposure individually to each patient. This is a major element of dose reduction put forward by manufacturers. The AAPM Task Group report 233 [10] proposes measurement protocols using readily available phantoms to test intensity modulation. A complete protocol is on going work.

For the study of image quality

According to SFPM report no. 41 published in March 2023, advanced and objective image quality metrics for computed tomography can take into account the non-linear and non-stationary properties of new iterative image reconstruction algorithms. Depending on various parameters, the Noise Power Spectrum (NPS) and the Task Transfer Function (TTF) are used to calculate a detectability index (d'). This index is used to estimate a medical doctor's ability to carry out a given task, such as detecting a lesion, taking into account the image's noise, signal and contrast conditions. A comparison of protocols and images obtained clinically on several go CT scanner between several French Cancer Center is on going.

References

[1] IRSN report "Analysis of data relating to the updating of DRLs in radiology and nuclear medicine for the years 2019 to 2021".

[2] J. Greffier et al (2015) Dose reduction with iterative reconstruction: Optimization of CT protocols in clinical practice. Diagn Interv Imaging 96:477-486

[3] D. Sarrut et al (2014) An analysis of the potential of GATE for radiation therapy and dosimetry applications Med. Phys. 41 (6) 064301/14

[4] S. Jan et al (2011) GATE V6: a major enhancement of the GATE simulation platform enabling modelling of CT and radiotherapy Phys. Med. Biol. 56 881- 901.

[5] S. Jan et al (2004) GATE: a simulation toolkit for PET and SPECT Phys. Med. Biol. 49 4543- 4561.

[6] G. Gavin et al (2007) Calculation of x-ray spectra emerging from an x-ray tube. Part I. Electron penetration characteristics in x-ray targets Med Phys. 2007 34(6):2164-74

[7] G. Gavin (2007) Calculation of x-ray spectra emerging from an x-ray tube. Part II. X-ray production and filtration in x-ray targets Med Phys. 2007 34(6):2175-86

[8] G. Gavin (2009) SpekCalc: a program to calculate photon spectra from tungsten anode x-ray tubes Phys Med Biol. 2009 54(19):433-38

[9] S. Rit et al (2014). The Reconstruction Toolkit (RTK), an open-source cone-beam CT reconstruction toolkit based on the Insight Toolkit (ITK). Journal of Physics: Conference Series, 489, 012079.

[10] Ehsan Samei et al (2019) Task Group No. 233 - Performance Evaluation of Computed Tomography Systems (TG233)

Part V

Astroparticle

session chaired by Sami CARROFF

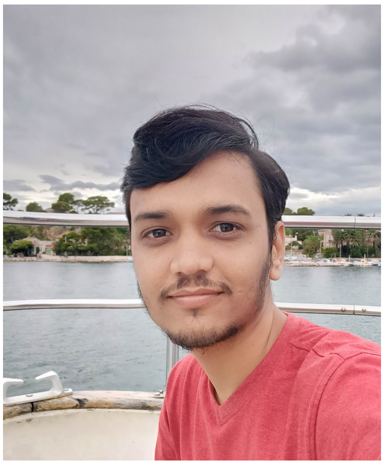

Direct detection of Axion dark matter with MADMAX

Vijay Dabhi

Centre de Physique des Particules de Marseille, Aix Marseille Univ, CNRS/IN2P3, CPPM, Marseille, France

Abstract — Dark matter is one of the major puzzles in fundamental physics. Axions are among the best-motivated dark matter candidates. MADMAX experiment will search for axions in the mass range around 100 μeV, which is currently favored by theory. Traditional axion cavity experiments are unable to access this mass range. Therefore, a novel detector concept called dielectric haloscope will be utilised. The MADMAX experiment based on this new concept, is in an R&D phase to validate the experimental approaches to be used for the final detector. There are several prototypes to validate different aspects like mechanics, piezo motors, RF behaviour, and physics studies. I'll present the current status of my work in the simulation, data analysis, and tests of various prototypes.

Introduction

CP violation is required for explaining the matter-antimatter asymmetry observed in the universe. CP violation is allowed in the standard model, but contrary to the weak sector, it has not been observed yet in the strong sector. This is puzzling because QCD Lagrangian contains a CP-violating term (θ)

$$L_{\text{CP}} = \theta \frac{\alpha_s}{8\pi} G^a_{\mu\nu} \tilde{G}^{\mu\nu}_a \tag{1}$$

, where α_s is the strong coupling constant and $G^a_{\mu\nu}$ is the gluon field tensor.

This term leads to a neutron electric dipole moment that is controlled by the θ parameter ($-\pi < \theta < \pi$) given [1] as

$$d_n = (2.4 \pm 1.0)\, \theta \times 10^{-3}\, e\, \text{fm} \tag{2}$$

Experimentally this electric dipole moment has not been detected yet, leading to an upper bound on theta

$$|\theta| < 0.8 \times 10^{-10} \tag{3}$$

Why does θ assume such a small value compared to the allowed values of $-\pi < \theta < \pi$ is known as the strong CP problem in particle physics.

Several solutions to this problem are proposed, and one of the most accepted solution is the Peccei-Quinn (PQ) mechanism [2]. Proposed by Roberto Peccei and Helen Quinn, it introduces a new U(1) symmetry in the QCD Lagrangian. The spontaneous symmetry breaking of this symmetry gives rise to a new light pseudo scalar boson that is called 'axion'.

Axion Properties

All the properties of axions are determined by one model parameter: the scale of the symmetry breaking. f_a. The original PQ mechanism set $f_a \approx f_{EW}$, which was quickly ruled out based on the experimental observations. The more recent models KSVZ and DFSZ set the scale $f_a \gg f_{EW}$. Since the mass and the interaction cross section of the axion with standard model particles are inversely proportional to f_a, both of them are very small. The small interaction cross section also means that axion is a very long lived particle. All these properties make axion a very good dark matter candidate that has been motivated by particle physics theory since 40 years. If the relation between axion mass m_a and the parameter f_a is relaxed, we have another class of dark matter particles called axion-like particles (ALPS).

The primary way to detect axions is through inverse Primakoff effect where an axion is converted to photon in the presence of external magnetic field. The strength of this interaction is described by the coupling $g_{a\gamma}$. As shown in the figure 1, very few experiments are currently probing the phase space of axion mass and $g_{a\gamma}$.

The axion mass range around 40-180 μeV is favoured by the post inflationary scenarios, where PQ symmetry is broken after inflation in the early universe [3]. The signal produced by the axions is very feeble because of their tiny mass and interaction cross section. Current axion experiments operate on the principles of using a microwave cavity to detect axions, which is not feasible for probing the mass range 40-180 μeV. There are new technologies needed to access this mass range.

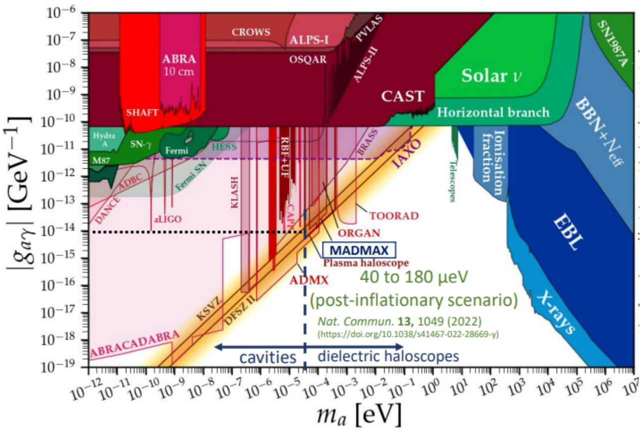

Figure 1: $g_{a\gamma}$ as a function of the axion mass. Since both of these quantities are determined from f_a, the value of $g_{a\gamma}$ is fixed for a given axion mass. The yellow bands are predicted by the theoretical models. (Plot taken from https://cajohare.github.io/AxionLimits/)

MADMAX

MADMAX collaboration [4] (formed in 2017) will probe the axion mass range of 40-180 μeV using the new technology of dielectric haloscope to boost the axion signal. In the presence of external magnetic field, the axion field a(t) gives rise to an oscillating electric field E(t). Since the amplitude of E(t) depends on the dielectric constant of the medium, it creates a discontinuity at the interface between two mediums. This leads to the emission of electromagnetic waves perpendicular to the interface. As shown in figure 2, photon emissions at several interfaces between dielectric disks and vacuum can be constructively interfered (or in resonance) to enhance the very feeble signal of E(t). By putting a reflecting mirror on one side, a leaky resonant cavity can be designed where an enhanced or boosted signal is received on one side.

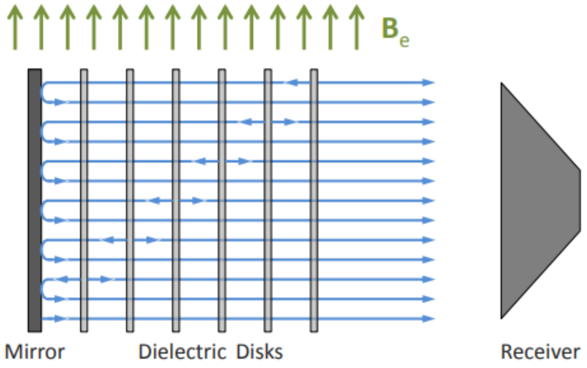

Figure 2: Dielectric haloscope with several dielectric disks and a reflecting mirror in the presence of external magnetic field

There are several experimental challenges in constructing a dielectric haloscope for axion detection. The signal power P_{sig} can be expressed as:

$$P_{sig} = 10^{-22}\text{W} \times \left(\frac{\beta^2}{50000}\right) \times \left(\frac{B_e}{10\text{T}}\right)^2 \times \left(\frac{A}{1\text{m}^2}\right) \times C^2_{a\gamma} \tag{4}$$

with dielectric disks of 1 m^2 area, 10 T dipole magnet and a power boost factor of 50000, the signal power is 10^{-22}W, which is what cutting edge electronics can detect. A power boost factor β^2 is defined as relative power of a booster as compared to the power coming from just a mirror

$$\beta^2 = \frac{P_{booster}}{P_{mirror}} \tag{5}$$

Moreover, the detected signal P^{det}_{sig} can be expressed

$$P^{det}_{sig} = 10^{-22}\text{W} \times \left(\frac{SNR}{5}\right) \times \left(\frac{T_{sys}}{4\text{K}}\right) \times \left(\frac{4\text{ days}}{t}\right)^{\frac{1}{2}} \tag{6}$$

Therefore, a system temperature of 4K and several days of data taking is needed for a signal to noise ratio (SNR) of 5. Finally, the dielectric disks need to be positioned at μm precision in the presence of very high magnetic field and cryogenic temperatures. All of these technologies are needed to construct the final detector of MADMAX shown in figure 3.

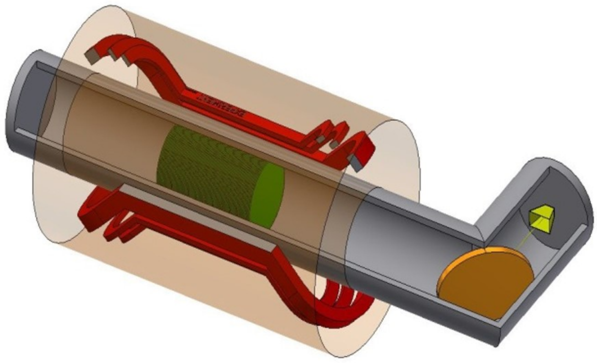

Figure 3: Final MADMAX experiment design (expected to be completed after 2028) with 9T dipole magnet, cryostat to cool the system to 4K temperature, and the booster that consists of 80 sapphire dielectric disks of 1.25 m diameter

Prototypes

The final detector has many challenging technologies which needs to be developed. For this purpose several prototypes have been constructed to validate certain key technologies. The prototypes, their description, availability and their goals are given in the table 1.

All the prototypes are built using sapphire dielectric disks to scan the ALPs mass range around 100 μeV that corresponds to the frequency range around 20

Name	Setup	Goal	Availability
CB100	3 fixed disks, $\phi = 100$ mm	RF studies, first physics	2021
P200	1 movable disk, $\phi = 200$ mm	piezo motors, mechanics	2021
CB200	3 fixed disks, $\phi = 200$ mm	RF studies, Scan ALPS	2023
OB300	3 movable disk, $\phi = 300$ mm	Scan ALPS	2024

Table 1: MADMAX prototypes built/being built to progress and validate many technologies needed for the final experiment

GHz. I participated to different aspects of the work for the prototypes CB100, P200 and OB300.

Figure 4: CB100 experimental run March 2023 inside Morpurgo magnet with 1.6 T magnetic field over 21 days at CERN

The CB100 prototype was used to make two experimental runs in March 2022 and 2023 inside the Morpurgo magnet at CERN. The goal of the tests were to understand the RF behaviour of the system and make the first physics analysis of ALPs search using a prototype. The experimental setup of these tests can be seen in figure 4 where CB100 is placed inside the dipole Morpurgo magnet and connected to low noise amplifier (LNA) and further receiver chain for collecting the data. I participated in the data monitoring during the tests. The magnetic field of 1.6 T, physical temperature of the LNA, booster and the electronic system temperature was very stable for 21 days of data taking in 2023 and 10 hours of data taking in 2022. The variance of noise residuals (relative difference between the data and the Savitzky-Golay filter applied to the data) showed a time dependence given by Dicke equation as

$$\tau = \frac{1}{B\sigma^2} \tag{7}$$

, where B is the bandwidth of the spectrum analyser (the distance between each measurement in frequency) and σ is the variance in the residuals.

The data taken during these runs are being analysed by the collaboration. The calibration of the electronics chain is used to calculate the LNA parameters. The noise generated by the LNA propagates inside the booster and interferes with itself to produce the dominant noise for the setup. The observed noise temperature of the system is well reproduced by ADS simulations of LNA and Booster in the region of interest. This allows for the calculation of the boost factor of CB100 and to calculate the sensitivity of the experiment in the search for ALPs.

CB100 prototype has three fixed disks. Since, moving the disks is necessary to scan the axion mass, several tests were made using the prototype P200 to confirm the workings of the disk positioning system. The tests were made in different conditions of room temperature (DESY), cryogenic temperature (CERN), and magnetic field of 1.6 T (CERN). In P200 prototype, three motors are used to move a single 200mm sapphire disk. The motors were tested with and without the disks in different settings. The motors are moved using a controller and the position of the disk distance is measured using a laser interferometer by placing a mirror on the surface of the disk. The accuracy of the interferometer was better than 100 nm. Many parameters of the piezo motors like the motor target position, disk measured position, minimum step size, time, motor drift positions, etc were measured. One of the key metric of the motor positioning system is the position error, which is defined as the difference between the target position of the motor and the measured position of the disk using the interferometer. One of the summary plots in figure 5 shows the mean position error for many tests in difference conditions. From this plot, it is seen that the mean position error in all test conditions is less than 10 μm. With the analysis I have performed of all the tests confirms that the piezo motor positioning system works at cold (up to 5K) temperatures and under magnetic field (1.6 T).

The upcoming prototype OB300 will utilize technologies developed from the construction and the operation of CB100 and P200 prototypes. It is under construction at DESY, Hamburg and planned to be ready early 2024. I participated in the disk surface measurements and simulation of realistic disk shapes inside the booster geometry. The simulations were used to quantify the impact of the realistic disk shapes on the boost factor and to optimize the disk configurations for maximum boost factor in OB300. The disk surface measurements were made at CPPM for 4 sapphire disks of 300 mm diameter with O(1) μm precision. It was found that

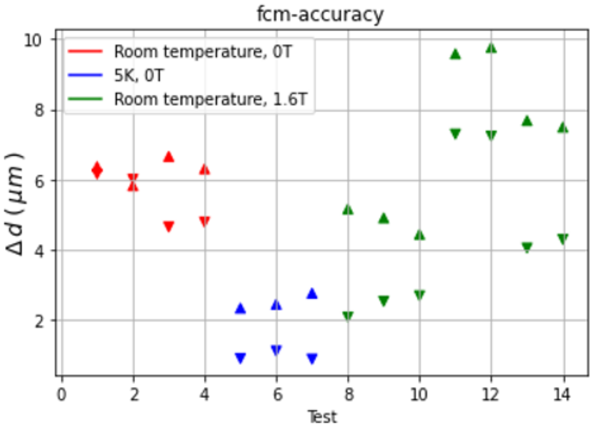

Figure 5: A summary plot of the position error for 14 tests of disk positioning system at room temperature (red) , cold up to 5K (blue), inside magnetic field of 1.6 T (green). The up triangles show the position error for the forward part of the motor movement and the down triangles show the position error for the backward part of the motor movement.

all 8 disk faces had a similar shape that comes from the manufacturing process. The min-max deviation in the surface height for the disks was around 0.2 mm with around 50 μm RMS deviation. I used the realistic shapes of the disks to make the simulations of the OB300 booster. For this study I used the algorithm developed by the MADMAX collaboration that uses recursive Fourier propagation of EM field with a given geometry of the booster to calculate the boost factor [5] [6]. The boost factor also heavily depends upon the distances between the disks and the distance between the mirror and the first disk (to make constructive interference as showed in figure 2). In minimally resonant disk configurations, the impact of realistic shapes was up to 20 % reduction in the boost factor. The ordering of the disks and their orientation toward the mirror seems to play a part as well. The algorithm can also optimize these distances to maximize the boost factor given various computational parameters. Starting from a theoretical resonant set of distances, I used the optimizer to calculate the maximum boost factor in a given disk configuration with a particular ordering and disk orientation towards the mirror. For ideal flat disks, the maximum boost factor obtained was around 2200. With four possible choices of disks (selecting three at a time for OB300) and two possible orientations of each disk, there were 192 total realistic disk configurations to optimize. In the best disk configurations, the boost factor was reduced by 50 % as seen in figure 6. The disk ordering and disk orientations play a big role, with most ordering and orientations producing a reduction of 70 % in the boost factor compared to the ideal perfectly flat disk shapes.

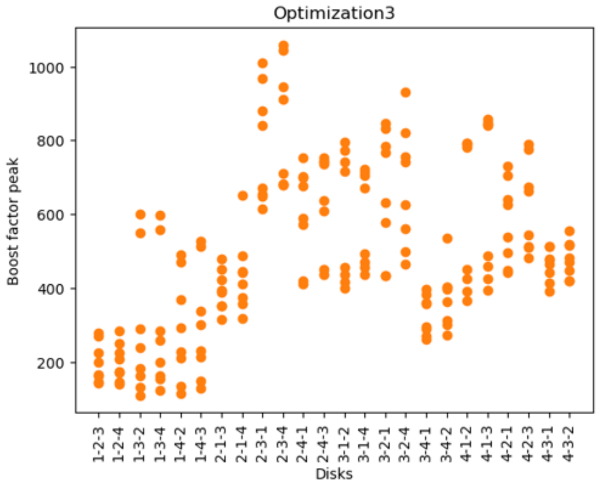

Figure 6: The maximum boost factor for different ordering of the disks. It is seen that some orderings perform much better than other.

Conclusion

In the strong interaction, CP violation is yet unobserved despite being allowed in the standard model. Introduced 40 years ago by Peccei-Quinn, axions can solve the strong CP problem and also be a good dark matter candidate. In the post-inflationary scenario, the axion mass lies in the range 40-180 μeV. This is the mass range that will be probed by the MADMAX collaboration. With current technologies, it is difficult to probe this mass range. Therefore, the MADMAX collaboration is developing a novel technology of dielectric haloscope.

Since there are many technological challenges in constructing a dielectric haloscope, several prototypes are used to develop and validate the key technologies. The experimental runs at CERN using the prototype CB100 shows the working of the prototype inside a dipole magnet and the RF understanding of the system. The P200 prototype shows the workings of the booster mechanics and the piezo motor positioning system at 5K temperature and 1.6 T magnetic field.

There are many plans for the continuation of the prototyping work. In March 2024, the prototype CB100 will be used to scan for ALPS inside a cryostat at the Morpurgo magnet at CERN. The final prototype of the MADMAX experiment, OB300 will be assembled early 2024. OB300 booster will be used for an ALPs scan inside a cryostat and Morpurgo magnet in 2025/2026.

References

[1] I. G. Irastorza. An introduction to axions and their detection. arXiv:2109.07376, SciPost Physics Lecture Notes 45 (2022) 1

[2] R. D. Peccei and H. R. Quinn. CP Conservation in the Presence of Pseudoparticles. Phys. Rev. Lett. 38 (1977) 1440

[3] M. Buschmann et al. Dark matter from axion strings with adaptive mesh refinement. arXiv:2108.05368, Nat Commun 13 (2022) 1049

[4] MADMAX Collaboration. A new experimental approach to probe QCD axion dark matter in the mass range above 40 μeV. arXiv:1901.07401, Eur. Phys. J. C 79 (2019) 186

[5] A. J. Millar, G. G. Raffelt, J. Redondo, and F. D. Steffen. Dielectric Haloscopes to Search for Axion Dark Matter: Theoretical Foundations. arXiv:1612.07057, JCAP 01 (2017) 061

[6] S. Knirck et al. A First Look on 3D Effects in Open Axion Haloscopes. arXiv:1906.02677, JCAP 08 (2019) 026

Investigating AGN Variability with the Cherenkov Telescope Array

Guillaume Grolleron ***for the Cherenkov Telescope Array Consortium***

Sorbonne Université, CNRS/IN2P3, Laboratoire de Physique Nucléaire et de Hautes Energies, LPNHE, 4 place Jussieu, 75005 Paris, France

Abstract — Active Galactic Nuclei (AGN) stand as enigmatic cosmic powerhouses, harboring supermassive black holes at their centers. Blazars are AGN with a jet oriented toward the observer. Their emission spans from radio to very high-energy gamma rays. Understanding their spectral variability provides crucial insights into the underlying physics governing these astrophysical phenomena. The Cherenkov Telescope Array (CTA) is poised to revolutionize high-energy gamma-ray astronomy, offering unprecedented sensitivity and energy resolution. In this contribution, we will discuss the CTA's prospects for studying blazar variability.

Introduction

The forthcoming Cherenkov Telescope Array (CTA) represents a leap forward in the field of ground-based imaging atmospheric Cherenkov telescopes (IACT). It is set to enhance the sensitivity to gamma rays above 20 GeV by a factor of five to ten, depending on the energy range, surpassing existing IACT capabilities. Consequently, the CTA will offer unprecedented perspectives on the Universe, particularly in terms of its non-thermal emissions. CTA will be composed of two sites, one by hemisphere. The northern site will be located at La Palma in Spain and will be focused on extra-galactic sources. The southern site will be in the Atacama desert in Chile.

Active Galactic Nuclei (AGN) are known for their emission across the full electromagnetic spectrum, resulting from a combination of thermal and non-thermal processes. A significant portion of the non-thermal emission emanates from relativistic jets near the central black hole, which have the capability to accelerate particles to high speeds. In the case of blazars, a type of AGN with jets directed towards Earth, notable changes in both flux and spectral characteristics are observed. The variability of AGNs occurs across different timescales, from the brief AGN flares lasting minutes to hours, to longer-term changes spanning years [13]. The rapid variability of AGNs is especially intriguing, as it sheds light on the nature of the emitting region, the underlying emission processes, as well as the acceleration processes that are energizing the particles in the jet (leptons or hadrons) [2, 5].

Studying the long-term behavior of AGNs allows for the construction of their power spectral density (PSD), which often reveals a transition from pink noise at lower frequencies to red noise at higher frequencies [18]. This PSD break frequency, previously identified in X-ray studies [8], is known to scale with the black hole mass and the accretion rate [19, 15]. While characterizing this PSD break at very high energies is challenging with current IACTs, the CTA might enable the reconstruction of this feature for several sources.

These proceedings focus on the AGN flare studies and long-term monitoring program within the CTA, a crucial part of the AGN CTA Key Science Project [21]. The long-term project involves observing 15 selected AGNs over a minimum of ten years, at least once a week during their visible periods. The objective is to reconstruct the AGN flux distribution and the proportion of time they remain above a certain flux level, known as the duty cycle of jetted AGNs, in an unbiased manner. Additionally, we aim at assessing the CTA's capacity to investigate rapid jet variability in AGNs and differentiate between hadronic and leptonic processes. These proceedings are a follow-up of [11, 4, 3]. Concerning the long-term study, we are using simulated observations of selected AGN over 20 years. From these simulations we evaluate our ability to reconstruct the flux distribution and PSDs using CTA observations. Here we start investigating which sources are the best candidates for high-accuracy PSD reconstruction. About the AGN flares, we performed simulations based on specific models, to study the capacities to observe spectral variability.

In the following sections, we first present the AGN modelling that we used to carry this study out. Then in a second part, we explain how CTA observations are simulated, as well as the spectral and flux reconstruction. Finally we show some interesting results before concluding about prospects with CTA.

AGN modelling

Modelling of the long term AGN behavior

The complete description of the AGN long-term modelling can be found in [11]. To summarize, we are generating a time series of flux normalization and spectral index based on [9]. We are using some hypotheses. First, the distribution of the observed flux is considered as log-normal. Then we adjusted the fractional variability $F_{\rm var}$ which is defined in [20], to scale with existing observations performed with current IACT on Mrk 421 and Mrk 501, two famous and bright blazars [10]. To generate the spectral index time series, we are considering the well known harder-when-brighter behavior [12, 14]. This behavior means that the very-high-energy spectrum of the AGN becomes harder when the flux is increasing. Finally, we model the time-dependent evolution of the AGN gamma-ray spectra $\Phi(E,t)$ by assuming as spectral shape a log-parabola with exponential cut-offs, yielding:

$$\Phi_z(E,t) = \Phi(t)\left(\frac{E}{E_0}\right)^{-\Gamma(t)-\beta ln\frac{E}{E_0}} e^{-\frac{E}{E_{\rm cut}}} e^{-\tau_{\gamma\gamma}(E,z)} \tag{1}$$

where E_0 is the reference energy, $\Phi(t)$ is the differential flux at the reference energy, $\Gamma(t)$ the spectral index, β the log-parabola curvature and $E_{\rm cut}$ the cutoff energy. The last factor in Equation 1 describes the absorption of VHE photons in the extragalactic background light (EBL) with the optical depth $\tau(E,z)$ depending on the source's redshift, z, taken from the work of [7] and the gamma-ray energy. The generated spectra are presented in Figure 1 for the case of PKS 1510−089.

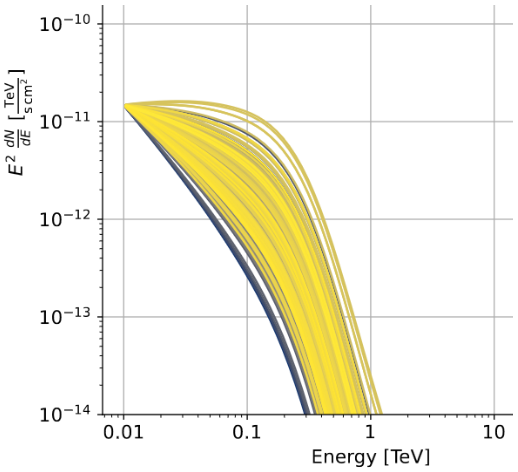

Figure 1: The generated spectra for PKS 1510-089, colors display the time evolution.

Modelling of the fast variability of AGN

Concerning AGN flares, we are using phenomenological models based on observations of famous flares that occurred in the past and have been observed with current instruments. Here we will focus on a model built to fit the 2016 TeV flare of BL Lacertae [1]. This model has been presented in [16] and is assuming synchrotron self-compton (SSC) emission, where accelerated particles are electrons. It is a single-zone leptonic model in which electrons are assumed to be injected with a power-law shape and then cool down as they radiate. They produce synchrotron emission, and inverse Compton scatter off with their own synchrotron emission. The resulting time-dependant spectrum is presented in Fig. 2

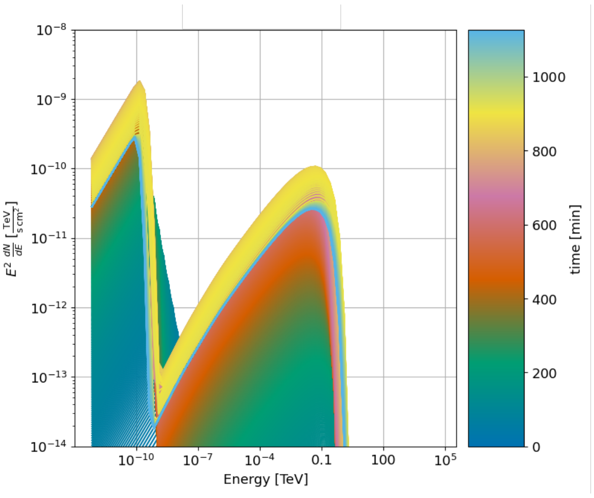

Figure 2: The time evolution of BL Lac spectrum during the flare. Colors are going from dark blue to light blue.

Simulations and reconstruction of AGN observations with CTA

For the simulation of CTA observations, we utilize the CtaAgnVar[1] tool. This pipeline is specifically developed for simulating and analyzing AGN observations with CTA. It is built upon GAMMAPY, the high-level analysis framework for CTA [6]. The CtaAgnVar pipeline generates an observation sequence using an input AGN time-dependent spectral model. It considers CTA's observational constraints and the night-time visibility of the source. This process includes monitoring the zenith angle of sources and dynamically selecting the appropriate instrument response functions (IRF) [17]. By doing so, it enables the realistic simulation of gamma-like events, followed by fitting these simulations with an analytical spectral model. The light curve reconstruction is achieved by applying a range of spectral models to the simulation data.

---

[1] `https://gitlab.cta-observatory.org/guillaume.grolleron/ctaagnvar`

Results

Long-term light curve and PSD reconstruction

Here we simulated a 20 years data set for PKS 1510−089, observed from the southern site of CTA based on a weekly cadence. Each observation lasts 30 min. As we are considering visibility of the source, the resulting number of observations per year is about 20. The reconstruction of the light curve is performed by fitting a set of spectral models to the simulation. The simplest hypothesis is a power law described by setting $\beta = 0$ and $E_{cut} \to \infty$ in Equation 1. A more complex version is a log-parabola (with $\beta \neq 0$) or a power law with exponential cutoff (a finite E_{cut}), and the most complex is the combination of both (log-parabola with exponential cutoff). For each time bin, a more complex model is preferred if the simplest one can be rejected at a 3σ level, at least, based on a likelihood ratio test. As the log-parabola and the power law with exponential cutoff have the same complexity, the model providing the highest likelihood value is preferred. The reconstructed light curve is presented in Fig. 3.

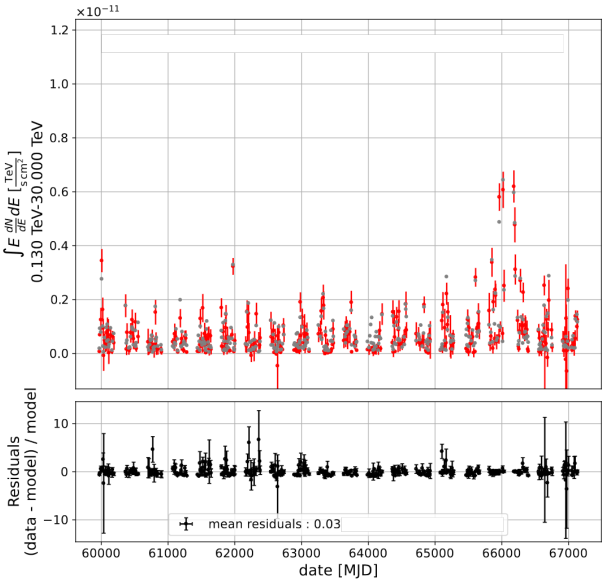

Figure 3: Reconstructed light curve and residuals computed between the simulated and reconstructed data for PKS 1510−089 for the full simulation lasting 20 years. Gray points are the injected values and red points are the reconstructed ones.

Having obtained the light curve, we can proceed to estimate, through a periodogram analysis, the PSDs for each source following [9]. The PSD reconstruction uses the same method as presented in [11]. The resulting PSD for PKS 1510−089 is presented in Fig. 4. We can see that the PSD slope of 1 that has been injected is well reconstructed, as well as the Poisson plateau at high frequencies. We will investigate the capabilities of CTA to reconstruct PSDs with a break between two different slopes in an upcoming work.

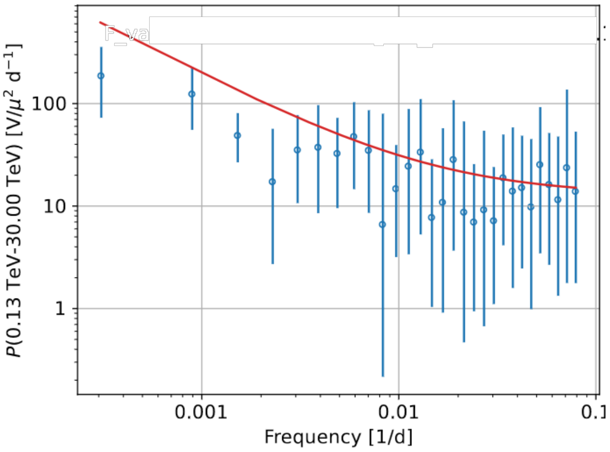

Figure 4: PSD estimate (blue points) of the simulated data for PKS 1510−089. The red line shows the injected PSD (modulo the floor level at high frequencies) used to simulate the input data.

Reconstruction of AGN flares

Light curve

The light curve for the flare of BL Lac has also been reconstructed and is shown in Fig. 5. We are here in an optimistic case where the whole flare (both the rising and the falling edges) has been observed. We performed simulations in less optimistic cases to assess to what extent the entire flare needs to be caught in order to conclude on the spectral variability.

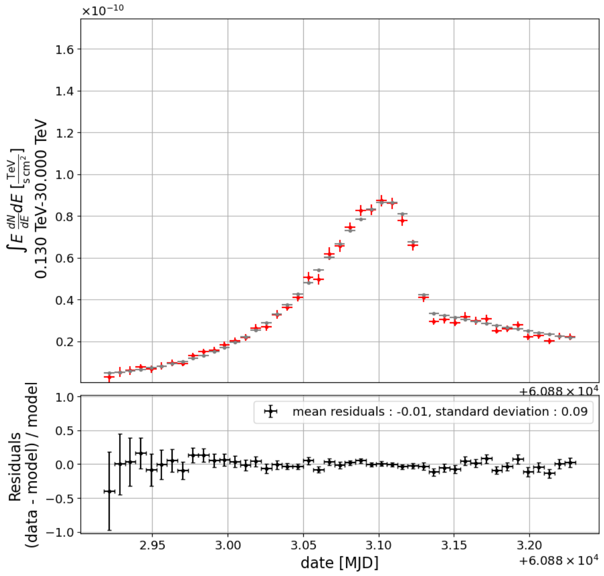

Figure 5: Reconstructed light curve and residuals computed between the simulated and reconstructed data for the simulated flare of BL Lac. Gray points are the injected values and red points are the reconstructed ones.

Hardness ratio (HR) hysteresis

An interesting probe of the spectral variability is the hardness ratio. This quantity is computed using the energy flux Φ in two separated sub-bands of an energy range, as the ratio between the flux in a sub-band over the flux in the total energy band, as follows:

$$\mathrm{HR} = \frac{\Phi(E_2, E_3)}{\Phi(E_1, E_3)} \tag{2}$$

with $E_1 \leq E_2 \leq E_3$. In Fig. 6 the evolution of the flux versus HR is presented in a specific energy band. We can see that an hysteresis pattern is predicted by the input phenomenological model. It means that the spectral evolution is energy dependent, which is not predicted by all types of models for AGN flares. Therefore, the capacity to characterize an hysteresis in such a parameter space is very interesting to discriminate between models, and ultimately to discriminate hadronic and leptonic processes. For now, the quantification of such hysteresis pattern has not really been investigated in the literature and we are currently working to develop such an estimator. Thus we only present here an hysteresis that is predicted by a phenomenological model that is clearly visible from the reconstruction of CTA simulated observations, the significance of its existence will be provided in an upcoming publication.

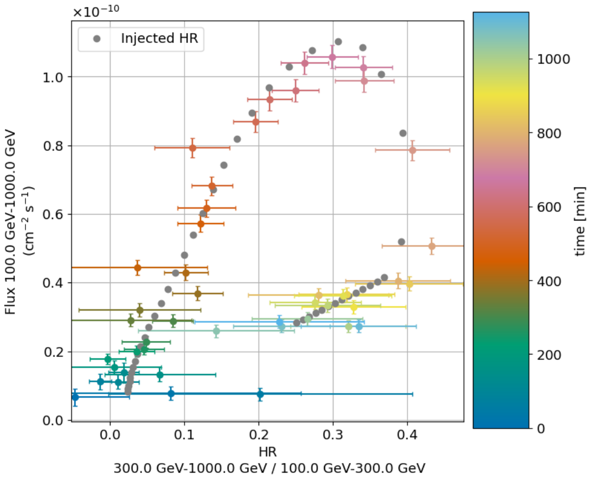

Figure 6: Reconstructed HR computed between 100 GeV, 300 GeV and 1 TeV. Reconstructed points are colored, colors show the time evolution from purple to red. Gray points are the value predicted by the injected model.

Conclusion

In summary, this paper highlights a segment of the studies on AGN variability conducted by the CTA Extragalactic Science Working Group. Specifically, it addresses the long-term monitoring of AGNs with CTA, illustrated with simulations of PKS 1510−-089. These simulations demonstrate the feasibility of reconstructing the input Power Spectral Density (PSD). More comprehensive results are detailed in [11], where a broader range of sources from the CTA AGN Key Science Project were examined. These findings suggest that CTA could effectively determine the duty cycle of jetted AGNs.

Regarding AGN flares, initial findings imply that CTA may, for the first time, detect hysteresis cycles in the Very High Energy (VHE) band. Such cycles would be indicative of the acceleration and radiative processes occurring within the jet. The potential observation of these cycles would provide a new metric to refine theoretical models.

References

[1] Abeysekara, A. U., Benbow, W., Bird, R., et al. 2018, ApJ, 856, 95. doi:10.3847/1538-4357/aab35c

[2] Blandford, R., Meier, D., & Readhead, A. 2019, ARA&A, 57, 467. doi:10.1146/annurev-astro-081817-051948

[3] Cangemi, F., Hovatta, T., Lindfors, E., et al. 2023, arXiv:2304.14208. doi:10.48550/arXiv.2304.14208

[4] Cerruti, M., Finke, J., Grolleron, G., et al. 2023, arXiv:2309.09615. doi:10.48550/arXiv.2309.09615

[5] Cerruti, M. 2020, Galaxies, 8, 72. doi:10.3390/galaxies8040072

[6] Donath, A., Terrier, R., Remy, Q., et al. 2023, A&A, 678, A157. doi:10.1051/0004-6361/202346488

[7] Domínguez, A., Primack, J. R., Rosario, D. J., et al. 2011, MNRAS, 410, 2556. doi:10.1111/j.1365-2966.2010.17631.x

[8] Edelson, R. & Nandra, K. 1999, ApJ, 514, 682. doi:10.1086/306980

[9] Emmanoulopoulos, D., McHardy, I. M., & Papadakis, I. E. 2013, MNRAS, 433, 907. doi:10.1093/mnras/stt764

[10] Gréaux, L., Biteau, J., Hassan, T., et al. 2023, arXiv:2304.00835. doi:10.48550/arXiv.2304.00835

[11] Grolleron, G., Becerra González, J., Biteau, J., et al. 2023, arXiv:2309.12157. doi:10.48550/arXiv.2309.12157

[12] H.E.S.S. Collaboration 2010, A&A, 520, A83. doi:10.1051/0004-6361/201014484

[13] Hovatta, T. & Lindfors, E. 2019, New A Rev., 87, 101541. doi:10.1016/j.newar.2020.101541

[14] Kapanadze, B., Romano, P., Vercellone, S., et al. 2014, MNRAS, 444, 1077. doi:10.1093/mnras/stu1504

[15] McHardy, I. M., Koerding, E., Knigge, C., et al. 2006, Nature, 444, 730. doi:10.1038/nature05389

[16] Morris, P. J., Potter, W. J., & Cotter, G. 2019, MNRAS, 486, 1548. doi:10.1093/mnras/stz920

[17] Cherenkov Telescope Array Observatory and Cherenkov Telescope Array Consortium 2021, CTAO Instrument Response Functions - prod5 version v0.1. doi:10.5281/zenodo.5499840

[18] Rieger, F. M. 2019, Galaxies, 7, 28. doi:10.3390/galaxies7010028

[19] Uttley, P., McHardy, I. M., & Papadakis, I. E. 2002, MNRAS, 332, 231. doi:10.1046/j.1365-8711.2002.05298.x

[20] Vaughan, S., Edelson, R., Warwick, R. S., et al. 2003, MNRAS, 345, 1271. doi:10.1046/j.1365-2966.2003.07042.x

[21] Zech, A., Mazin, D., Biteau, J., et al. 2019, Science with the Cherenkov Telescope Array, 231. doi:10.1142/9789813270091_0012

Search for Lorentz Invariance Violation with the first data of the Large-Sized Telescope-1 of the Cherenkov Telescope Array.

Cyann Plard ***on behalf of the CTA-LST Project***

Laboratoire d'Annecy de physique des particules

Abstract — Lorentz invariance violations (LIV) are allowed by some quantum gravity models that aim to unify general relativity and quantum field theory, that encounter difficulties describing physics around the Planck scale ($E_P \sim 10^{19}$ GeV). LIV can lead to an energy-dependency of the photons velocity, allowing them to become subluminal or supraluminal. This effect would appear around a characteristic energy called quantum gravity energy E_{QG} and could be observed from Earth with a delay on the arrival time of gamma-rays produced by active and highly variable sources. In this analysis, we go over all data of active galactic nuclei of LST-1, the first telescope of the Cherenkov telescope array, searching for variable observation nights. We have found three variable nights and combined two of them to extract a limit on the quantum gravity energy.

Introduction

General relativity and quantum mechanics are two fundamental pillars of modern physics and merging them is one of its biggest challenges. For this purpose, many proposals have been put forward, generally called quantum gravity (QG) models. As part of the few observable predictions coming out, Lorentz invariance violations (LIV) are allowed by numerous QG models and can be investigated using various cosmic messengers[1]. Amongst them, gamma-rays are a good candidate. First, they propagate on straight lines so that it is easier to link their detection to sources with known distances. Second, they are produced by abundant and very bright sources hence allowing them to be detected at extragalactic distances. This also makes effects of fast variability in their emission easier to see. These two elements are fundamental ingredients to facilitate the detection of a potential LIV effect. Gamma-rays can be detected from Earth using imaging atmosphere Chrenkov telescopes (IACTs) that exploit their reaction with the atmosphere components and, in particular, the Cherenkov light emitted by secondary particles. The Cherenkov telescope array (CTA)[2] will be the next generation of such telescopes and will be constituted by a hundred of telescopes, separated in two sites. So far, one telescope has been constructed, the LST-1[3], which is located at La Palma and is currently in commissioning phase. The following analysis is performed using its first data.

Lorentz invariance violation search with high energetic gamma-rays

The quantization of spacetime performed by QG models can lead to a modification of the dispersion relation of massless particles, which in its simplest form can be writen as [4]:

$$E^2 = p^2c^2 \left[1 \pm \sum_{n=1}^{\infty} \alpha_n E^n \right], \tag{1}$$

where p is the photon momentum, c the standard speed of light in vacuum and $\alpha_n \in \mathbb{R}$. Taking this expression at the first order, the next ones can be considered as negligible so that we can set $\alpha_1 = \frac{1}{E_{QG}}$, where E_{QG} is the characteristic QG scale, called quantum gravity energy, at which the LIV phenomena would become significant. This characteristic energy is a free parameter, but it is expected to approach the Planck energy scale ($E_P \sim 10^{19}$ GeV).

The massless particle speed derived from this relation gets an energy-dependency and then photons may become superluminal or subluminal. Assuming that two photons i and j are emitted at the same time but at different energies E_i and E_j from an astronomical source, one can study a delay on their arrival time on Earth, expressed as [5]:

$$\Delta t \simeq \pm \frac{E_i - E_j}{H_0 E_{QG}} \, \kappa_1(z), \tag{2}$$

where H_0 is the Hubble constant and $\kappa_1(z)$ is a propagation term accounting for the universe expansion and that increases with the redshift z. Then, the criteria risen by this equation are that the sources that can efficiently constrain E_{QG} should be at cosmological distance and with a large range of energy, making TeV gamma-rays an interesting probe. In addition, as a telescope would detect an incoming flux of gamma-rays, the sources should be very active to have enough statistics and be highly variable. Indeed, if the flux as a function of time shows a variability pattern, a time-shift between low and high energies photons could be constrained. Then, three types of sources can be used: pulsars, gamma-ray bursts (GRBs) and flaring active galactic nuclei (AGNs).

However, there is no guarantee that photons of different energies are emitted at the same time by the sources: an intrinsic time delay may exist. Then, the lag we would observe from Earth would be the sum of these two delays, and it would be impossible to separate them. Nevertheless, under the hypothesis that such an intrinsic lag does not depend on the travelled distance or would not be strictly identical for all sources, these two delays could be discriminated by combining different sources[6], even different flares of one AGN. Then, one can measure the lag per energy, corrected by the travelled distance, expressed as:

$$\lambda = \frac{\Delta t}{\kappa_1(z)(E_i - E_j)} = \pm \frac{1}{H_0 E_{QG}}, \tag{3}$$

with the units of time per energy : s.TeV^{-1}.

The goal of our analysis is to put a limit on the characteristic energy E_{QG}, that is a value for which we would already have seen such a LIV effect if the quantum gravity energy was allowed for such an energy range at this given order $n = 1$. This work is part of the consortium between different IACTs experiments, H.E.S.S., MAGIC and VERITAS, for the LIV study and has been joined recently by LST. In the future, we are looking forward to combine all the data available of these experiments to extract a limit on the quantum gravity energy.

Search and characterisation of variability in LST-1 data

As explained before, a LIV study requires a time-variability of the flux, and to have sufficient continued data, we are looking for variability during a whole observation night. To do so, we analysed all data of AGNs of LST-1 from January 2021 to June 2023, with a standard quality selection[7], using `Gammapy`[8][9], the official high-level data analysis framework of CTA. We calculated the significance (in the Li&Ma sense [10]) for each observation night of a given source and considered that it was detected if the significance was over 5σ. Then, for each significant night, we computed its lightcurve, that is the flux as a function of the time, and fitted it with a constant function such that the night is considered as variable if the p-value is excluded at 5σ (equivalently). We found 3 variable observation nights for BL Lacertae (BL Lac) at a redshift of 0.069: the 8th and 9th of August 2021 and the 20th of October 2022. For now, only the two first nights are included in the study.

However, before applying the proper LIV analysis on the variable nights, it is necessary to first optimize the background rejection, using a selection on the reconstructed data that we call the *gammaness* cut[7]. The gammaness is a score from 0 to 1 attributed to each event after its reconstruction, indicating how likely the primary particle would be a gamma-ray (score of 1) instead of a background event (cosmic-ray particles, in particular protons) (score of 0). Applying a cut on this score, we select a dataset of events with a corresponding value of gammaness over this cut. The research of variable nights has been done using a dataset selected with a standard cut of 0.6. Since this datasets is separated into two decorrelated samples, variable and non-variable nights, we can use the non-variable sample to optimize the cut for the LIV analysis that is performed on the variable one. For this, we applied different gammaness selection on the reconstructed data to get different corresponding datasets. For each one, we calculated the combined significance S_{cut} of all nights of the non-variable sample:

$$S_{\text{cut}} = \sqrt{\sum_{\text{non-variable nights}} S_n^2}. \tag{4}$$

We selected then the gammaness cut value for which the combined significance of the non-variable sample is maximized. For BL Lac, we obtained a value of 0.9. Then, for the rest of the analysis, we used the variable-sample of the dataset corresponding to this specific gammaness cut.

To be able to distinguish a time-shift between photons of different energies, a variability pattern needs to be extracted from the lightcurve of each night. Such a model is considered as describing enough the variability if it fits the lightcurve with a p-value over 0.05. As a LIV effect is supposed to be negligible at low energies, one can compare this LIV-free sample to a high energies one, defined with the median of counts. For this, we use the Band comparison (BC) method, introduced by the Whipple collaboration[11], in which the lightcurves are subdivided into time bins. The high energies lightcurve is fitted with the variability model extracted from the low energies one. Then, the two samples are considered compatible if the p-value is over 0.05. This method is a simple first approach to verify that there is no LIV detection. The selected parametric models chosen for the low-energies lightcurves of the 8th and 9th of August 2021 are shown on fig. 1 with their respective p-value.

Furthermore, the LIV-analysis is performed under the hypothesis that the spectra (flux versus energy) does not vary with time. To verify this, we first test if a log parabola model is preferred over the null hypothesis that the spectra is described by a power law (p-value validated at 5σ). Then, for different time bins, we extracted the parameters of the selected model fitted on the spectra and we verified that there is no significant disagreement. Fig. 2 shows, for each night, the chosen time bins of their lightcurves and the corresponding in-

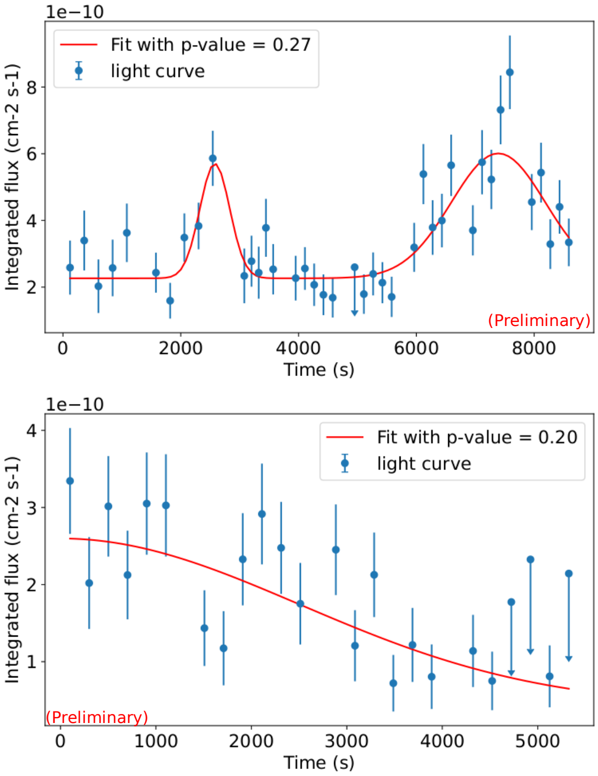

Figure 1: Variability template of the low-energies lightcurve of the two observation nights. Top: the 8th of August 2021 with a double Gaussian and a constant (5 time bins per ∼20 minutes of observation). Bottom: the 9th of August 2021 with a Gaussian and a constant (3 time bins per ∼20 minutes of observation).

dexes of the power law fitted on their spectra.

Now that we have verified the time-independency of the spectra and extracted a template of the variability of each observation night, we can use it to get a limit on E_{QG} at the first order.

Extraction of a constraint on LIV

To perform the analysis, a software called `LIVelihood` has been developped[6], based on the `Root C++` framework[1], to combine data of different experiments in the context of the Gamma-LIV consortium. It uses the method of the maximum likelihood (ML)[12], an unbinned version of the BC method, allowing the analysis to not rely on the choice of the time bin. The likelihood is maximized for the λ_n parameter (eq. 3) that best recovers the low energy LIV-free sample when a transformation is applied from it to the high energy dataset. The likelihood for a given source is built with a probability density function (PDF) that describes the probability P to detect a gamma-ray i with a given reconstructed energy $E_{R,i}$ at a given time t_i such that:

$$L_S(\lambda_n) = -\sum_i \log\left(\frac{dP(E_{R,i}, t_i; \lambda_n)}{dE_R dt}\right). \quad (5)$$

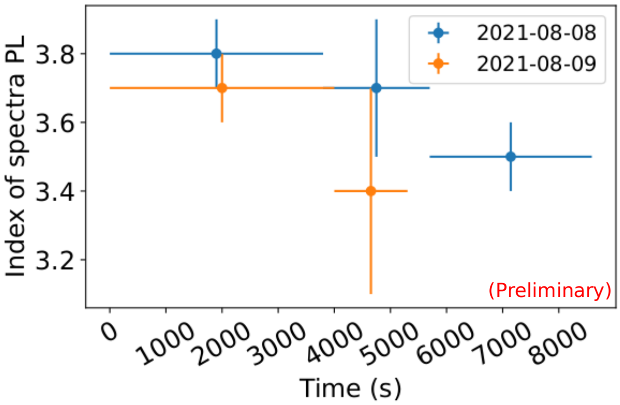

Figure 2: For the two nights of the analysis, indexes of the power law model fitted on their spectra for different time bins of their lightcurves.

The PDF is expressed as follows:

$$\frac{dP}{dE_R dt} = W_s \frac{\int \mathrm{IRF}(E_T, E_R, t) \times F_s\left(E_T, t; \lambda_n\right) dE_T}{N'_s} + \sum_k W_{b,k} \frac{\int \mathrm{IRF}(E_T, E_R, t) \times F_{b,k}\left(E_T\right) dE_T}{N'_{b,k}}. \quad (6)$$

It is the sum of the respective PDF of the signal and two different backgrounds k, weighted by W_s and $W_{b,k}$ such that $W_s + \sum_k W_{b,k} = 1$, and normalised by N'_s and $N'_{b,k}$. The background is divided into two part: the hadronic one, which is the main pollution in the observed data as hadrons can also produce Cherenkov light in the atmosphere, and the baseline, which is the constant part of each lightcurve. The likelihood takes into account the instrumental response functions (IRFs) with the factor IRF $= \mathrm{E_{ff}A}\left(E_T, t\right) \mathrm{MM}\left(E_T, E_R, t\right)$. They are obtained with Monte-Carlo simulations of "real" gamma-rays with a true energy E_T and are time-dependent. The migration matrix (MM) is a comparison between the true energy E_T and the reconstructed one E_R by the telescope for each event. The effective area (E$_{\mathrm{ff}}$A) is the area of a perfect instrument that would detect all incoming gamma-rays of energy E_T. It depends of the observation conditions and in particular on the zenith angle of the source, so that it changes over time. F_s and $F_{b,k}$ factors account for the convolution between the lightcurve and the spectra (which is supposed being time-independent) for the signal and the two backgrounds respectively. Then, the combination of different sources or flares can be done by summing their respective likelihood:

$$L_{\mathrm{comb}}(\lambda_n) = \sum_{\text{all sources}} L_s(\lambda_n). \quad (7)$$

Performing 1000 simulations of the combined dataset by using the variability template we extracted before, we produce first a calibration plot, that is a comparison of the reconstructed lag λ_n^{rec} by the software and an injected one λ_n^{inj}. It is expected to correspond to a

---

[1] https://root.cern.ch

linear function $\lambda_n^{rec} = a \times \lambda_n^{inj} + b$ with $a = 1$ and $b = 0$. Such a plot is shown in fig. 3 for our dataset at the first order. The blue envelope shows the 1σ error accounting for the statistical uncertainty while the orange one is the Monte-Carlo error. We obtain that a is compatible with 1, meaning that the method is not biased, but b is not compatible with 0, which indicates that there is an offset. However, this offset is negligible compared to the statistical uncertainty, it is therefore not expected to create a fake lag.

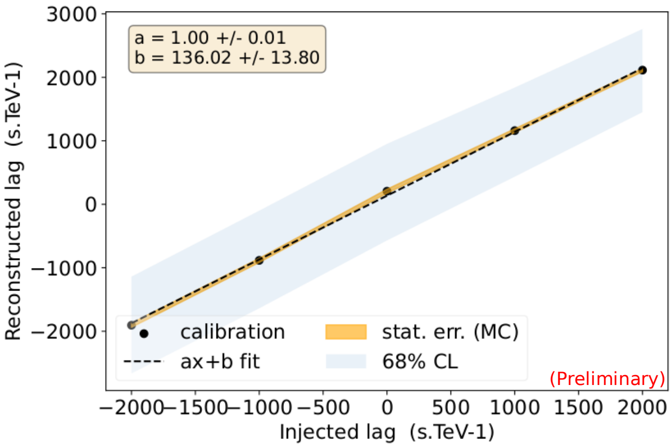

Figure 3: Calibration plot for simulations of the combined dataset of the 8th and 9th of August 2021.

After verifying that the reconstruction is not biased, we can reconstruct the lag from real data, using this time a likelihood nearly the same as before but with a different hadronic background PDF:

$$\frac{dP_h}{dE_R dt} = W_h \frac{dN_{\text{off}}}{dE_R} \times \frac{1}{T} \times \frac{1}{N_h'}, \tag{8}$$

with T the total time of a given observation night and N_{off} the total number of events in sky regions of the field of view in which only background events are expected, following the reflected-region background method[13]. We obtain then a reconstructed lag of $\lambda_1 = (2060^{+2811+2479}_{-2899-2143})$s.TeV^{-1}, where the first error encounters for the statistical uncertainty of the simulations while the second encounters for the statistical uncertainty of the lightcurve template, obtained by letting all parameters free in each of the 1000 simulations.

As we obtained a lag compatible with 0, we can extract the corresponding limit on E_{QG} by using eq.3 with the error at 2σ of λ_1. In this analysis, the $\kappa_1(z)$ term has been designed with the Jacob & Piran model[5]. Then, we get the following limit on the quantum gravity energy at 2σ: $E^1_{\text{QG,lim}} = 4.2 \times 10^{16}$GeV, in the subluminal case. Fig. 4 shows a comparison of this limit with other obtained from different IACTs experiments in function of the redshift of the source. This analysis is the first one to perform a combination of AGN flares.

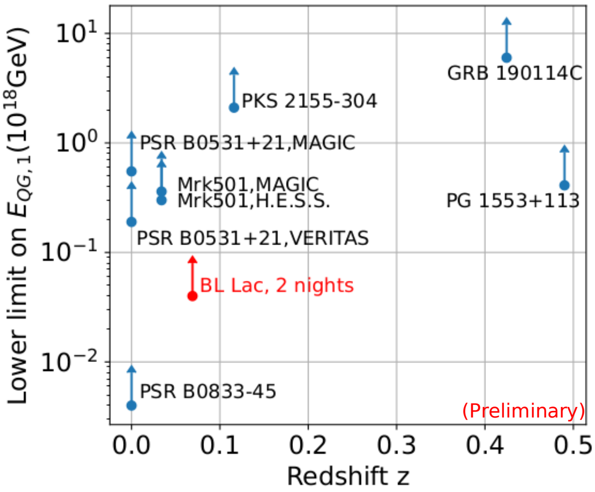

Figure 4: Comparison between limits obtained from various IACT experiments[6].

Conclusion

We studied all the data of AGNs of the first telescope of the CTA experiment, LST-1, in order to find variable nights. We found three suitable observation nights of the BL Lac source and combined two of them to extract a limit on the quantum gravity energy at the first order with real data. This limit is the first one obtained from a combination of AGN flares and from a systematic and non-biased analysis based on the time lag. We are currently working on the combination with the third variable night of BL Lac. Then, all data of LST-1 will be ready to be combined with dataset of other IACTs experiment through the consortium.

Acknowledgments We gratefully acknowledge the funding from the French Programme d'investissements d'avenir through the Enigmass Labex.

References

[1] Addazi et al., Quantum gravity phenomenology at the dawn of the multi-messenger era A review, Progress in Particle and Nuclear Physics, 2022

[2] Guetta, The Cherenkov Telescope Array: layout, design and performance, Proceedings of 37th International Cosmic Ray Conference, 2021

[3] Mazin et al., Status and results of the prototype LST of CTA, Proceedings of 37th International Cosmic Ray Conference, 2021

[4] Amelino-Camelia et al., Tests of quantum gravity from observations of gamma-ray bursts, Nature, 1998

[5] Jacob & Piran, Lorentz-violation-induced arrival delays of cosmological particles, Journal of Cosmology and Astroparticle Physics, 2008

[6] Bolmont et al. , First Combined Study on Lorentz Invariance Violation from Observations of Energydependent Time Delays from Multiple-type Gamma-Ray Sources. I. Motivation, Method Description, and Validation through Simulations of H.E.S.S., MAGIC, and VERITAS Data Sets, The Astrophysical Journal, 2022

[7] Abe et al., Observations of the Crab Nebula and Pulsar with the Large-sized Telescope Prototype of the Cherenkov Telescope Array, The astrophysical journal, 2023

[8] Acero et al., Gammapy: Python Toolbox for Gamma-ray Astronomy, 2022, v1.0, Zenodo, doi:10.5281/zenodo.7311399

[9] Donath et al., Gammapy: A Python package for gamma-ray astronomy, Astronomy & Astrophysics, 2023

[10] Li & Ma , Analysis methods for results in gamma-ray astronomy, Astrophysical Journal, 1983

[11] Biller et al., Limits to Quantum Gravity Effects on Energy Dependence of the Speed of Light from Observations of TeV Flares in Active Galaxies, Phys.Rev.Lett, Astropart.Phys., 1999

[12] Martinez & Errando, A new method to study energy-dependent arrival delays on photons from astrophysical sources, 2009

[13] Berge et al., Background modelling in very-high-energy gamma-ray astronomy, Astronomy and Astrophysics, 2007

Virgo calibration and data reconstruction uncertainty computation

Cervane Grimaud

Laboratoire d'Annecy de Physique des Particules - CNRS

Abstract — After the first gravitational wave detection in 2015, ground interferometers like Virgo received significant instrumental upgrades in order to reach better sensitivity. With each upgrade came new challenges, in this proceeding we focus on describing calibration and data reconstruction. First we explain why we need to calibrate the interferometer in order to reconstruct the gravitational wave signal and we describe the different calibration steps. Then we detail the reconstruction algorithm and its uncertainty computation method before presenting preliminary results of this new method.

Introduction

Gravitational waves (GW) are deformations of the space time metric propagating at the speed of light and predicted in 1916 by Albert Einstein as a consequence of the General Relativity theory [1]. Gravitational waves are emitted by accelerated massive objects. The sources that are able to produce gravitational waves with an amplitude detectable by the current generation of ground interferometers, with a 10 Hz to a few kHz bandwidth, are astrophysical sources like compact binary coalescences. The GW detection is currently performed with a network of 4 interferometers placed all over the world within the LVK collaboration: LIGO with 2 detectors in the United-States, Virgo with one detector in Italy near Pisa, and KAGRA with one detector in Japan. The interferometer final output data, used to study GW, is the detector strain h(t) with its associated uncertainty. The first gravitational wave was detected in 2015 by the two LIGO interferometers and was emitted by a Binary Black Hole coalescence [2]. This detection was made during the first observing run O1 of the LIGO and Virgo collaboration. We are currently in the middle of the fourth observing run O4 with the LVK collaboration.

In the first part of this proceeding we explain how the Virgo interferometer is able to detect gravitational waves. In a second part, we describe the Virgo calibration process and the data reconstruction principle before focusing on the uncertainty computation method and its first results.

Virgo interferometer

Virgo is a 3 km long arms Fabry-Perot interferometer (ITF). Figure (1) shows a schematic representation of the detector optical layout for the current O4 run. A laser beam is sent towards a beam splitter (BS) which splits the beam into two beams of equal power that propagate in each of the interferometer arms (North and West). At the end of both arms, the beams are reflected by the two end mirrors (NE and WE mirrors) towards BS where they interfere. We can observe the interference dark fringe signal at the detection photodiode. Two additional mirrors are placed at the beginning of each arms (NI and WI) allowing to create Fabry-Perot cavities inside both arms, in order to increase the effective length traveled by the beams. Each mirror is suspended by a chain of pendulums inside a vacuum tower, in order to consider each mirror as free test masses above the suspension's resonant frequency ($\sim$ Hz) [3].

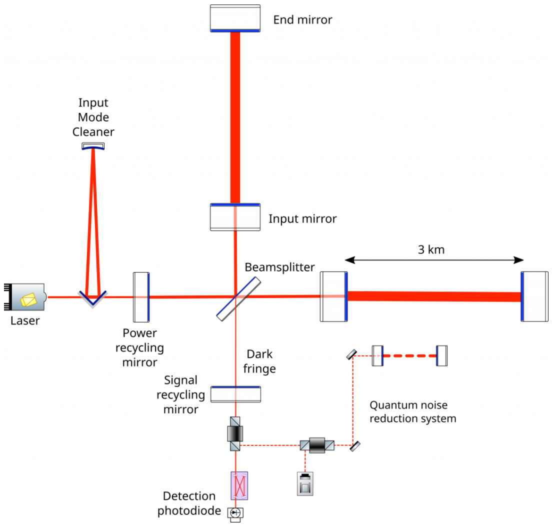

Figure 1: *Schematic representation of the optical layout of the Advanced Virgo interferometer [4]*

When a gravitational wave passes on the interferometer, it changes the differential arm length $\Delta L = L_N - L_W$, where L_N and L_W are respectively the length of the north arm and the west arm. This modifies the effective lengths traveled by the laser beams inside each arm, thus changes the interference power seen by the detection photodiode. The gravitational strain is linked to ΔL by $h = \frac{\Delta L}{L_0}$, where L_0 is the arm length at rest (3 km). A typical ΔL value for a gravitational waves of compact binary mergers is of the order of 10^{-19} m. Trying to measure such small length variation is really difficult as a lot of phenomena can move the mirrors at this scale and effectively simulate a gravitational wave signal. To counteract this, the interferometer needs to be controlled.

Controlling the interferometer

In order to control the interferometer, to keep every mirror aligned and to keep the cavities in resonance, we need to use control loops. They are used to control different parameters, like cavity length, and to control precisely mirror relative positions. To be able to induce motion of the mirrors position electromagnetic actuators (EM) are used, they are composed of four magnets glued at the back of each mirrors and four coils located right in front of them inside the towers. Using those coils, we can create a magnetic field which will make the mirror moves. Such motion can be seen in the dark fringe signal. The control signals are used to attenuate noises inside the ITF but it also attenuates possible gravitational wave signals. It is thus not possible to simply take the output signal of the detector as the gravitational wave strain h. We need to reconstruct it by subtracting the control signals contribution to the dark fringe signal. This means that we need to precisely know those contributions, and for that we need to calibrate the responses of each mirror actuators, to calibrate the detection photodiodes readout electronics and to know the interferometer's optical response.

Virgo calibration

The Virgo calibration process is composed of several steps necessary to calibrate every elements needed for the signal reconstruction. In the next sections we describe the signal injection process and two of the main calibration steps.

Signal injection

In the previous section we described the EM actuators, but two other types of actuators are used in the calibration. First, the Photon Calibrator (PCal) is able to induce mirrors motion by using the radiation pressure of an auxiliary laser beam that is sent towards the center of the mirror [5]. Secondly, the Newtonian Calibrator (NCal) is able to modulate the end mirror positions via variations of the local Newtonian gravitational field induced by a rotor placed outside the vacuum towers [6].

Using the PCals and NCals, it is possible to move mirrors at given frequencies to inject signals inside the interferometer that can be seen as power variations at the detection photodiode. There are two different types of signal injections, the lines injections, where we induce sinusoidal displacement of the mirrors at specific frequencies, and the noise injections, where the displacement is made over a full frequency band. During the calibration procedure both of those injection types are used. The PCal system is used as reference for all the calibration steps. So, it is mandatory to calibrate the PCals first, in order to know the induced mirror displacement from the laser power.

PCal power calibration

The mirror displacement induced by the Pcal laser beam is given by the formula

$$\Delta x(f) = -\frac{1}{M}\frac{2cos(\theta)}{c}\frac{\Delta P_{ref}(f)}{(2\pi f)^2}$$

with θ the angle of incidence of the auxiliary laser beam on the end mirror [7]. So in order to know Δx, a very precise measurement of the reflected laser beam power, ΔP_{ref}, is needed. This is done using an integrating sphere as power detector. The first step of the Virgo calibration is to precisely calibrate the PCal system in order to use it as a reference for all the other calibration steps. The power calibration requires to use power detector references (other integrating spheres) that are themselves calibrated by metrology institutes (NIST and PTB) within a broader intercalibration scheme of the LVK collaboration, where the power detectors are periodically shipped to the different detectors over the world [5].

Actuator response calibration

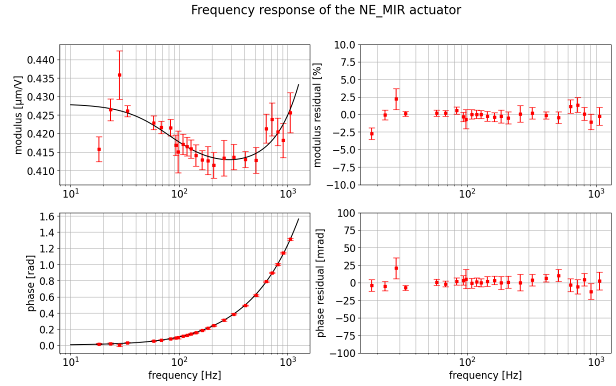
Frequency response of the NE_MIR actuator

Figure 2: *Example of calibration result for the actuator response of the NE mirror electromagnetic actuator. The top plots are the modulus and the bottom ones the phase of the actuator response. The left side represent the measurement result with the red points the data and the black line the fitted model. The right side is the residuals of the model.*

The next step of the calibration is to compute the different mirror EM actuator responses. This is made as a series of calibration transfers between different systems, comparing a system of reference to another one that needs to be calibrated. It is based on the comparison of the detector's response R to two different injection paths. First an injection I_{ref} applied with a calibrated actuator of reference with a response model A_{ref} and second and injection I_{new} applied with the actuator to calibrate A_{new}. The output signal of the interferometer S can be written as a combination of the injection signal, the actuator model and the interferometer response, $S = I_i \times A_i \times R$. From the two data sets we can compute two transfer functions that can be combined to extract the actuator response of the system we want to calibrate. We get :

$$A_{new} = (\frac{S}{I_{new}}).(\frac{S}{I_{ref}})^{-1} \times A_{ref}$$

This is the general method for actuator calibration that we apply to all mirror actuators [8]. An example of calibration result for the NE mirror electromagnetic actuator is shown in the figure (2).

Data reconstruction uncertainty

Thanks to this calibration step, it is possible to reconstruct the gravitational wave signal. Then, the reconstruction uncertainty coming from the models and from the reconstruction algorithm is monitored using the method described below.

Principle of the reconstruction

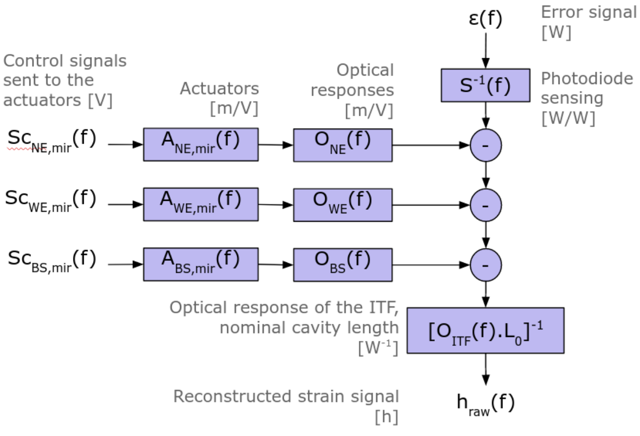

Figure 3: *Schematic representation of the reconstruction algorithm Hrec, which subtracts the contribution of the mirrors longitudinal controls to the dark fringe signal* $\epsilon(f)$.

Hrec is able to compute the reconstructed gravitational wave strain $h(t)$ from the dark fringe power variation $\epsilon(t)$ (with the calibration model S) by subtracting the contribution of each longitudinal control signal, using the actuator models A_i that are measured during calibration and optical responses models O_i that are permanently adjusted in Hrec. This allows to get the h_{raw} visible at the bottom of fig. (3). After this step we get the final strain by subtracting linearly permanent calibration lines and various noises [8].

Monitoring the reconstruction

However this process is affected by uncertainty coming from the actuators models and from the optical response model adjustment. So, we need to monitor it to assess if the reconstruction is working properly and to provide the reconstruction uncertainty. To do this we use a measurement called h_{raw}/h_{inj}, where we do the transfer function between the Hrec output h_{raw} and h_{inj}. h_{inj} is a quantity computed by injecting a signal on NE or WE mirror inside the ITF with a PCal or EM actuator and reconstructing it using this actuator response model directly without using Hrec. This allows to compare what is reconstructed in h_{raw} and what we know we are injecting with h_{inj}. If Hrec is working perfectly the result of the transfer function should be 1 for the modulus and 0 for the phase, deviations from those values give an information on the reconstruction bias and uncertainty.

There are two different types of measurements used to monitor the Hrec bias. The first type refers to the 20 permanent lines that are always injected on the end mirrors of the interferometer between 30 Hz and 1 kHz. The second type refers to weekly lines, which are only injected once a week during a few minutes. There are 46 weekly lines (26 plus the 20 permanent ones) injected between 18 Hz and 1258 Hz.

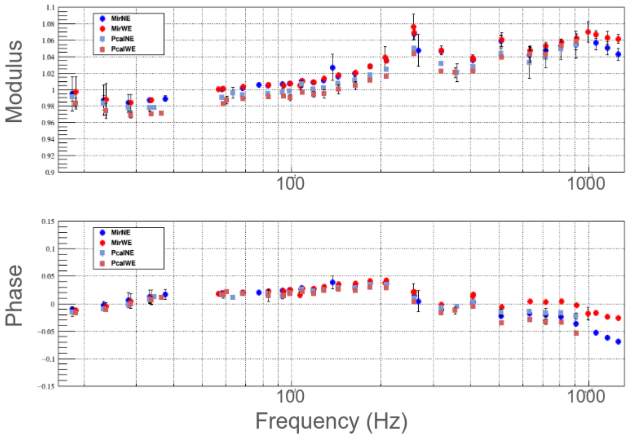

Figure 4: *Result of a* h_{rec}/h_{inj} *measurement from the 1st to the 8th of December 2023. We can see both weekly and permanent lines on this plot. The top plot is the modulus and the bottom one the phase. The different color points are for the different mirrors (NE and WE) and actuator combinations (PCal and EM).*

In Fig.(4) we can see the result of a h_{rec}/h_{inj} measurement for the 1st and the 8th of december 2023. We can observe a bias of a few percent on the modulus and of less than 50 mrad on the phase over the full frequency range.

Uncertainty computation method

But monitoring the bias is not enough, we want to be able to characterize the uncertainty of the reconstruction process over the full frequency range.

The uncertainty computation method uses the weekly lines data points. It takes an average of the modulus and phase value over a given time period and with the mean values and error values, compute a Gaussian distribution of the data. Then, a random selection of N points is performed inside the modulus and phase distributions of all the 46 frequency lines. With the N randomly selected sets of data, we do a linear interpolation between the 46 points, computing a value of modulus and phase every 0.125 Hz frequency bin for the 10 Hz to 5 kHz frequency range. For the low frequencies, before the first weekly line frequency, we take the first interpolation coefficient computed with the closest two lines and use it to compute the interpolated value until the 10 Hz bin. At high frequency, the interferometer is not controlled so we set the last frequency bin to 1 for the modulus ans 0 for the phase. Finally, we get N sets of interpolated data points, which means that we get a N points distribution for every frequency bin. From those distributions we can compute a mean and a rms, which represent the Hrec bias and the Hrec uncertainty for both the modulus and the phase for each frequency bin.

Result

In the figure (5) we can see a preliminary result of the uncertainty computation method used with only the weekly lines injected from the 4th of August to the 2nd of September 2023. The black line represents the Hrec bias and the orange area the Hrec uncertainty. This result is preliminary as it does not take into account the PCal or actuators calibration systematic uncertainties on h_{inj}. Also, in the future, we may add the permanent lines into the uncertainty computation in order to better deal with uncertainty variations on a shorter time scale.

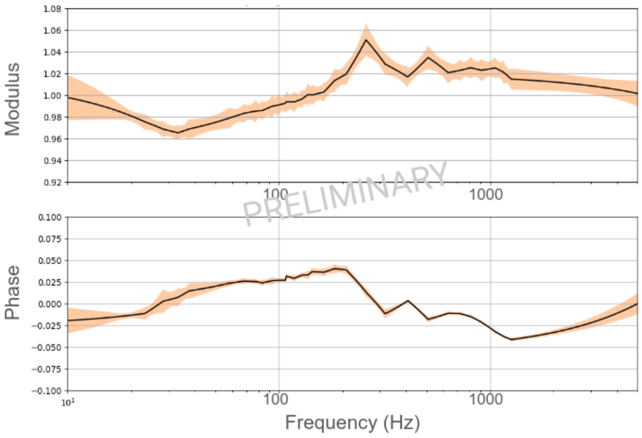

Figure 5: *Preliminary result of the uncertainty computation method for weekly lines injected from the 4th of August to the 2nd of September 2023.*

Conclusion

In this proceeding, we explained how the Virgo interferometer is able to detect gravitational waves. We focused on the calibration and reconstruction steps in order to explain why we need to calibrate the interferometer and how the calibration impacts the gravitational strain reconstruction. With GW detectors becoming more and more sensitive it is very important that the calibration precision does not become a limiting factor. To prevent this, new processes have been implemented especially regarding the PCals with the intercalibration scheme. This effort will be visible in the improvement of the reconstruction uncertainty for which we have presented the computation method. Once the calibration uncertainty will be added to the computation we will need to perform more measurements to increase the number of data available for the computation to get an accurate reconstruction uncertainty. The plan is to be able to do daily measurements with a limited number of injection to not disturb the science acquisition too much but still be able to get enough statistics to monitor the interferometer calibration and provide accurate numbers for h(t) uncertainty over at least a daily timescale.

References

[1] A. Einstein, Näherungsweise Integration der Feldgleichungen der Gravitation, 1916

[2] LIGO and Virgo scientific collaboration, Observation of Gravitational Waves from a Binary Black Hole Merger, Physical Review Letters, 2016

[3] Virgo Collaboration, Advanced Virgo Technical Design Report, VIR-0128A-12, 2012

[4] Virgo Collaboration website, https://www.virgo-gw.eu/science/detector/optical-layout/

[5] D. Estevez et al, The Advanced Virgo Photon Calibrator, Classical and Quantum Gravity, 2021

[6] D. Estevez et al, Newtonian calibrator tests during the Virgo O3 data taking, Classical and Quantum Gravity, 2021

[7] D. Estevez, Upgrade of Advanced Virgo photon calibrators and first intercalibration of Virgo and LIGO detectors for the observing run O3, PhD thesis, 2021

[8] Virgo Collaboration, Calibration of Advanced Virgo and Reconstruction of the detector strain h(t) during the Observing Run O3, Classical and Quantum Gravity, 2021

Ionization of a single nanoparticle by heavy Cosmic Ray with the *NanoCR* experiment

Thibault Nguyen Trung[1] ***with M. Chabot***[1]***, O. Sublemontier***[3]***, E. Dartois***[2]***, I. Ribaud***[1]***, J. Duprat***[4]***, T. Pino***[2]***, K. Béroff***[2]

[1] *Laboratoire de physique des deux infinis Irène Joliot-Curie (IJCLab), CNRS-IN2P3, Université Paris-Saclay*
[2] *Institut des Sciences Moléculaires d'Orsay (ISMO), CNRS, Université Paris-Saclay*
[3] *Institut Rayonnement Matières de Saclay (IRAMIS-NIMBE), CEA-CNRS*
[4] *Institut de Minéralogie de Physique des Matériaux et de Cosmochimie (IMPMC), CNRS, Muséum National d'Histoire Naturelle, Sorbonne Université*

Abstract — The NanoCR experiment focuses on studying how cosmic rays interact with nanoparticles and aims to understand the mechanism through which the nanoscale elements of interstellar dust undergo Coulomb explosion to return to the gas phase. To simulate this interaction, a beam of Argon ions generated by the *Andromede* accelerator was used to mimic cosmic rays, while employing spherical grains of polystyrene as analogs for hydrogenated carbonaceous interstellar dust. The experiment involves measuring the charge state distributions of these nanoparticles during a single collision with heavy ions sampling different stopping power. The NanoCR experimental setup will be detailed, accompanied by the presentation of results obtained from collisions between 100nm radius nanoparticles and a 1.5 to 9 MeV Argon ion beam. This collaborative endeavor involves four laboratories, ISMO, NIMBE, IMPMC, and IJCLab, where the *Andromede* accelerator is located.

Introduction

The Interstellar Medium (ISM) composed of gas and dust is traversed by cosmic radiation and exposed to stellar ultraviolet radiation, an external field attenuated in dense clouds. Hydrogen and Helium dominate the cosmic ray abundances, as reported by J. Z. Wang et al. 2002 [1]. Heavier elements constituting approximately 1% of cosmic particles play a significant role, given that the electronic stopping power; equivalent to the energy deposited; increases with the projectile atomic number to the power of 2 (M. Chabot 2016 [5]; Ziegler et al. 2010 [3]). The interaction between cosmic rays and the dust and gas within the ISM is pivotal for the chemical evolution of interstellar and circumstellar environments. Heavy and slow cosmic rays interact with very small dust particles (approximately 100 atoms), causing them to undergo coulombic explosion. This process enriches the gas phase with complex molecules (M. Chabot et al. 2019 [2]). The upper limit for dust size at which multifragmentation occurs remains unknown. The NanoCR experiment is designed to provide physics insights for determining this size limit in coulombic explosion. To replicate the interaction between cosmic rays and dust, accelerated particles are employed as cosmic ray analogs, with polystyrene nanoparticles serving as analogs for interstellar dust.

Experimental Set-up

The NanoCR experiment schematic is presented figure 1. The polystyrene nanoparticles, initially in an ethanol liquid mixture, are transformed into aerosol form using a nebulizer[11]. These monodisperse nanoparticles have a radius of 100nm, which aligns with the average radius for carbonaceous material in the interstellar medium as reported by J.C. Weitgartner & B.T. Draine 2001 [4]. The nanoparticle flow is directed into an Aerodynamic Lens System from CEA-NIMBE (e.g F.-A. Barreda et al.[6]). The operational principle of which is illustrated in figure 2. This component consists of multiple chambers separated by diaphragms of varying sizes. The pressure gradient from the entrance to the exit induces aerodynamic forces on the nanoparticle flow, concentrating them into a monokinetic nanoparticle beam.

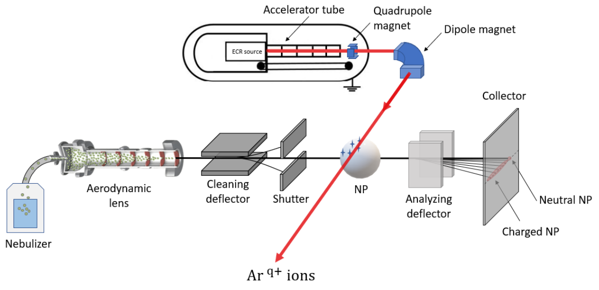

Figure 1: NanoCR experiment scheme

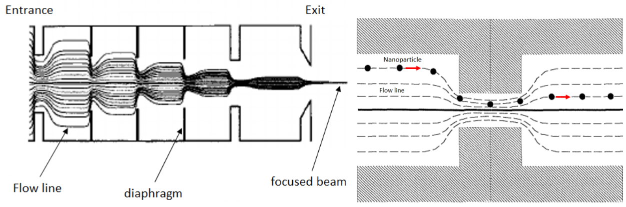

Figure 2: Left: Aerodynamic Lens Scheme from J.T. Jayne 2000 [7], modified. Right: Focusing effect from J. Schreiner & al. 1998 [8]

The nanoparticles subsequently traverse an initial electrostatic deflector, eliminating charged particles produced during the nebulization process and leaving a neutral beam at the entrance of the collision chamber, that we call "charge cleaning" hereafter. Within this chamber, the nanoparticles intersect with Argon ions generated by an Electron Cyclotron Resonance ion source Microgan from Pantechnik. These ions are accelerated using the 4 MV Pelletron accelerator *Andromede* [9] from the Mosaic Paltform [10]. To achieve a given kinetic energy, adjustments were made to both the the accelerating voltage and the ions charge state from Ar^{1+} to Ar^{3+}. Both neutral and ionized nanoparticles then pass through a second electrostatic deflector after the collision, deviating particles proportionally to their charge assuming constant velocity. Ultimately, all nanoparticles are collected on a microscope slide for further analysis.

Analysis Procedure

Using a confocal microscope from Vacuum and surfaces platform[12], a series of 250 pictures of $100\mu m$ each is taken along the analysing deflector deviation axis and all the observed element are sorted by position and shape with ImageJ software [13]. The figure 3 represents the calibration deposition of nanoparticles without ion beams or charge cleaning.

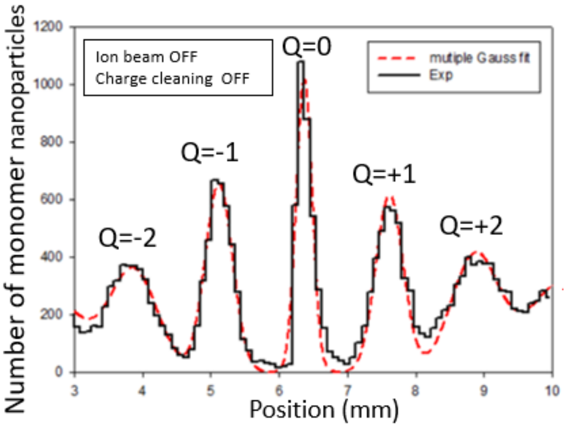

Figure 3: Position distribution of nanoparticles when ion beam & cleaning are off. The charge comb observed is the response of the system R to a given charge

Positive and negative charges produced in the nebulizer are observed on the microscope. Using each charge q peak position x_q and their standard deviation σ_q with equation 1, the fitted calibration parameters are obtained: x_0 the neutral nanoparticle peak position, σ_0 the standard deviation of the nanoparticle beam, σ_E the standard deviation of the nanoparticle kinetic energy and Δ_x the longitudinal deviation along the deposition axis. The system's response $R(q)$ to a given charge q is computed using these parameters in equation 2, which allows us to transform a position distribution of nanoparticles to a charge distribution.

$$x_q = x0 + q \times \Delta_x \qquad \sigma_q = \sqrt{\sigma_0^2 + (q \times \sigma_E)^2} \tag{1}$$

$$R(q) = \sum_q \frac{1}{\sqrt{2\pi}} e^{-0.5 \times \frac{(x_0 - x_q)^2}{\sigma_q^2}} \tag{2}$$

Two assumptions were made to obtain the charge distribution from the experiment. First, the collision process follows a Poisson's law; the probability of k collision is computed as in equation 3.

$$P_k = \frac{\lambda^k}{k!} \times e^{-\lambda} \tag{3}$$

The second hypothesis posits an independence between the collision process and the charge of the nanoparticle. The nanoparticle total charge distribution D_{tot} is the sum of convoluted single collision charge distribution $D_{k=1}$, as written in equation 4. The single collision charge distribution was obtained with a χ^2 minimization between the experimental data and the system's response of the total charge distribution.

$$D_{tot} = \sum_{k=1}^{n} P_k \times D_k \qquad D_{k+1} = \sum_k D_k \circledast D_{k=1} \tag{4}$$

When charge cleaning is active, only the nanoparticles that become charged through the collision process are collected on the slice. Figure 4 illustrates the experimental count of these nanoparticles after interacting with 1.5 MeV Argon ions, depicted by the blue curve as a function of the deposition axis.

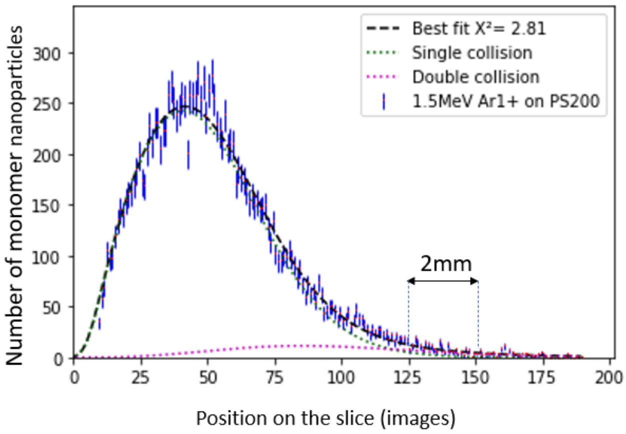

Figure 4: Polystyrene position distribution after collision with 1.5 MeV Ar^{1+} ions. Single and double collision contributions are shown with dotted lines.

For clarity, only nanoparticles with an area corresponding to a single ball of polystyrene are plotted and labeled as monomers. The position $x = 0$ denotes the deposit location of neutral nanoparticles, deliberately omitted from the plot.

Results

The single collision charge distribution of 1.5 MeV Argon ions on PS200 obtained as previously explained is shown in figure 5. The curve shape within errors bars has rough cut at low charge and a tail for high charges. Same charge distribution study has been conducted for different ion beam energy.

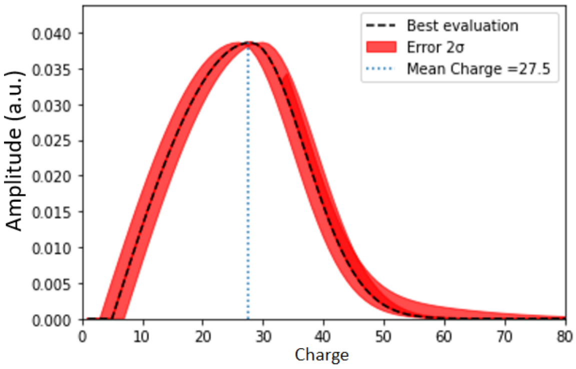

Figure 5: Charge distribution for single collision between PS200 nanoparticles and 1.5 MeV Ar^{1+} ions.

The acquired charge distributions were analyzed using statistical moments. Figure 6 illustrates the mean charge of PS200 after collisions with ion beam energies ranging from 1.5 to 9 MeV and the corresponding electronic stopping power taken from SRIM[3] table. The mean charge exhibits a linear growth pattern with the electronic stopping power. This observation is reasonable as the electronic stopping power leads the ionization process. It is imperative to replicate these results in the upcoming experiment. PS100 nanoparticles will also be employed to investigate the size effect.

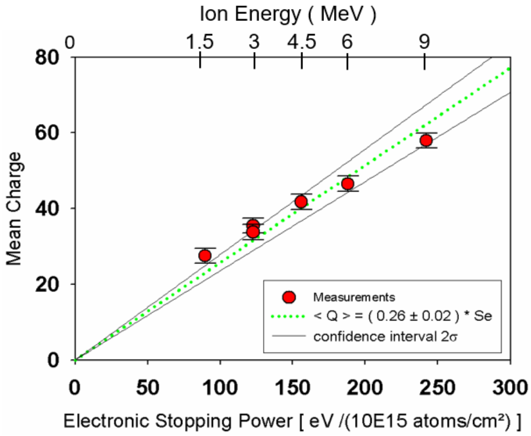

Figure 6: Mean charge of the experimental charge distributions for single collision between PS200 and several ion energies.

References

[1] J. Z. Wang et al. 2002, "Measurement of Cosmic-Ray Hydrogen and Helium and Their Isotopic Composition with the BESS Experiment" The Astrophysical Journal, Volume 564, 244-259. https://iopscience.iop.org/article/10.1086/324140.

[2] M. Chabot, K. Béroff, E. Dartois, T. Pino and M. Godard, 2020, "Coulomb explosion of Polycyclic Aromatic Hydrocarbons Induced by Heavy Cosmic Rays: Carbon Chains Production Rates", The Astrophysical Journal, Volume 888, 17-32. https://iopscience.iop.org/article/10.3847/1538-4357/ab584f.

[3] J.F. Ziegler, M.D. Ziegler, J.P. Biersack, 2010, "SRIM - The stopping and range of ions in matter", Nuclear Instruments and Methods in Physics Research Section B: Beam Interactions with Materials and Atoms, Volume 268, Issues 11-12, https://doi.org/10.1016/j.nimb.2010.02.091.

[4] J.C. Weingartner & B.T. Draine, 2001, "Dust Grain Size Distributions and Extinction in the Milky Way, LMC, and SMC, Astrophys. J. 548, 296-309. https://iopscience.iop.org/article/10.1086/318651.

[5] M. Chabot, 2016, "Cosmic-Ray slowing down in molecular clouds : Effets of heavy nuclei", Astronomy&Astrophysics, Volume 585, A1. https://doi.org/10.1051/0004-6361/20142544.

[6] F.-A. Barreda, C. Nicolas, J.-B. Sirven, F.-X. Ouf, J.-L. Lacour, E. Robert, J. Yon, C. Miron, O. Sublemontier, 2014, "Characterization of nanoparticle beams focused with an aerodynamic lens system", Sci Rep 5, 15696. https://doi.org/10.1038/srep15696.

[7] J.Jayne, John & D. Leard, X. Zhang, P. Davidovcits, K. Smith, C. Kolb, D. Worsnop, 2000, "Development of an Aerosol Mass Spectrometer for Size and Composition Analysis of Submicron Particles", Aerosol Science and Technology Volume 33, 49-70. https://doi.org/10.1080/027868200410840.

[8] J. Schreiner , C. Voigt , K. Mauersberger , P. McMurry & P. Ziemann (1998) "Aerodynamic Lens System for Producing Particle Beams at Stratospheric Pressures", Aerosol Science and Technology, 29:1, 50-56, https://doi.org/10.1080/02786829808965550.

[9] Andromede Project, IJCLab, Orsay. 10-EQPX-0023, CNRS IDF Sud, Orsay Physics, Université Paris-Saclay. https://anr.fr/ProjetIA-10-EQPX-0023.

[10] MOSAIC platform, IJCLab, Orsay. https://mosaic.ijclab.in2p3.fr/.

[11] PALAS AGK-2000 nebulizer, https://www.palas.de/product/agk2000.

[12] Vacuum and surfaces platform, IJCLab, Orsay. https://maverics.ijclab.in2p3.fr/plateforme-vide-et-surfaces/.

[13] ImageJ software, https://imagej.net/software/imagej/.

Review of background Study in S2-only Analysis in XENON1T Experiment

Yongyu Pan

LPNHE, Sorbonne Université, Université de Paris,
CNRS/IN2P3, Paris, France

Abstract — The XENON1T experiment is a direct dark matter detection experiment in the form of weakly interacting particles (WIMPs) scattering off nuclei. Without requiring a scintillation signal, we can set constraints on light dark matter (DM) models using only the ionization signals. This paper reviews the background study done in S2-only analysis in XENON1T experiment. We developed a strong data selection to identify three background components: low-energy β decays on the cathode wires, coherent nuclear scattering of ^8B solar neutrinos (CEvNS) and electron recoil (ER) from high Q-value β decays.

Introduction

A large number of astrophysical observations [1] have demonstrated the existence of a non-luminous component of massive dark matter (DM) beyond Standard Model, making up about 26% of the mass-energy of the universe. Weakly interacting massive particles (WIMPs) are among the most well-motivated dark matter candidates [2].

The XENON1T experiment [3] at the INFN Laboratori Nazionali del Gran Sasso (Italy) focuses on searching for weakly interacting massive particles (WIMPs) scattering elastically off xenon atoms. XENON1T is a dual-phase time projection chamber (TPC) operated with a total of $\sim$ 3.2 tonnes of ultra-pure liquid Xe (LXe) with 2 tonnes as the active target. The TPC is cylindrical in shape, 96 cm in diameter and 97 cm in height. The top and bottom surfaces are fitted with 248 Hamamatsu 3-inch photomultiplier tube (PMT) arrays [4, 5].

The observable signals are the scintillation (S1) and ionization (S2) signals from energy depositions. S2 signal is produced by electroluminescence in gaseous xenon from electrons drifted upwards under an electric field, and got extracted from the liquid into the gas. The longitudinal (z) position is reconstructed using the time difference between the prompt S1 signal and the S2 signal. The position in the (x,y) plane is reconstructed by the S2 signal pattern in the upper PMT array. In addition, the S2/S1 ratio can be used to distinguish between nuclear recoils (NRs) from WIMPs and neutrons, as well as electron recoils (ERs) from γ and β, which constitute the main background of the XENON1T experiment [3].

Data selection

Dual-phase LXe TPCs are most sensitive to DM with masses $m\chi \geq 6\,\mathrm{GeV\,c^{-2}}$, as lighter DM is unable to transfer enough energy ($\sim$ 3.5 keV) to xenon nuclei to produce detectable S1 at a sufficient rate. However, with the ionization signals S2s by secondary scintillation, particles transferring as low as 0.7 keV for nuclear recoils and 0.186 keV for electronic recoils can be detected [6]. Here, S2-only analysis refers to the reanalysis of XENON1T's data without S1s.

We use the main science run (SR1) of XENON1T [7] with a live time of 258.2 days. We use 30% of the SR1 events as training data, uniformly distributed in time, to determine event selection and to identify a region of interest (ROI) of integrated S2 charge for each dark matter model and mass. Only the remaining 70% (search data, 180.7 days) is used to calculate the limits of the DM parameters. We choose a selection set to remove identifiable background components for different DM models.

Figure 1 shows the efficiencies of the most impactful cuts with S2 size. Without S1, it is difficult to accurately estimate the event depth z. However, the width of S2 waveform in time is correlated with z due to the diffusion of electrons during the drift. The events with S2 widths larger than 835 ns are excluded to eliminate the β decays occurring on the cathode wires as they have unusually small S2 due to charge loss. Many have detectable S1 and can be easily removed by depth related cuts on with S1 [8]. Similarly, width cut can suppress the events from decay on the electrodes at the top of the TPC with atypically narrow S2 width. The width cut efficiency is calculated with simulated S2 waveforms, which show agreement with those observed in deuterium-deuterium plasma fusion neutron

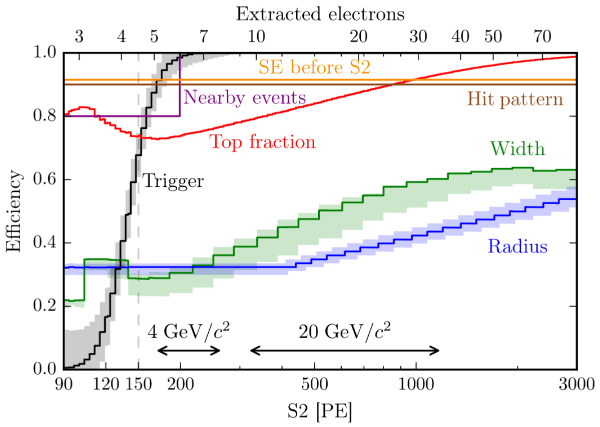

Figure 1: Efficiency of main event selection (fraction of events passed) versus S2 size. Solid lines bands to the ± 1σ variation of the model parameters. The arrows indicate the S2 ROI for the 4 and 20 GeV c^{-2} spin-independent NR DM analyses. The top horizontal axis shows the corresponding number of extracted electrons to S2[8].

generator calibration data [9]. We also remove events reconstructed at high radii R which are with unusually small S2 due to the charge loss on TPC walls. Its efficiency is estimated using ^{83m}Kr calibration data. The top fraction cut is to remove events constituted by more than 66% light from the top PMT array which is normally events in gaseous phase. The efficiency is calculated from binomial fluctuations in photon detection [8].

Pileup of randomly emitted single-electron (SE) signals contributes to the background in S2-only analysis, originating from elections trapped at the interface and elections captured by electronegative impurities (e.g. O_2) in the liquid xenon. This population can be removed by three cuts. Firstly, their S2 hit pattern is inconsistent with that of the single scattering. The related cut has a 90% efficiency measured with neutron generator data. Secondly, SE before S2 cut is to exclude single electron (SE) signals up to $\sim$ 1 ms before the largest S2 which can also suppress gas events with broader S1 and therefore often misidentified as S2. Thirdly, Nearby events cut can reduce the enhanced SE emission [10] close in time and position to high energy events [11].

Background characterization

The best-fit detector response model from Ref. [11] is used, setting the detection threshold as 0.7 keV for NRs and as 186 eV for ERs, as the LXe charge yield Qy has never been measured below these energies [8]. While we do not have access to a complete model for S2-only analysis, we can quantify the three components of the background and compare the observed events to our nominal signal and background models, as shown in Figure 2. The first one is the ER background from high Q-value β decays, mainly ^{241}Pb [11], is flat in our energy range of interest. The second one is coherent nuclear scattering of ^8B solar neutrinos (CEvNS). The third one is from low-energy β decays on the cathode wires. For S2 $\geq$ 300 PE ($\sim$ 0.3 keVee), we observe rates well below 1 /(tonne·day·keVee), while below 150 PE the rate rises rapidly, which may be due to the unknown background.

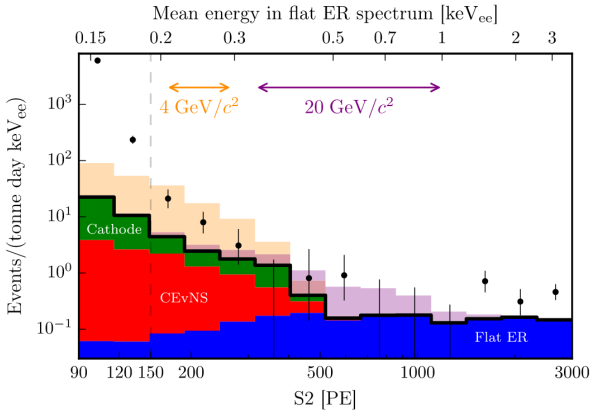

Figure 2: Distribution of events passing all cuts (black dots); error bars show statistical 1σ uncertainties. The thick black line shows the summed background model consisting of three components. The light orange (purple) histogram shows the signal model for the 4 GeV c^{-2} (20 GeV c^{-2}) DM model excluded at 90% confidence level. The arrows show the ROIs. The top x-axis indicates the average energy of the after-cuts events[8].

Conclusion

The background of few electrons S2 signals in XENON1T is investigated. We attributed this background to impurities within the LXe target volume. A strong data selection criteria optimizes the signal-to-noise ratio of the XENON1T ionization signal. Above 0.4 keVee, < 1 /(tonne·day·keVee) event is observed.

References

[1] Bertone, G. & Hooper, D. History of dark matter. *Reviews Of Modern Physics.* **90**, 045002 (2018)

[2] Roszkowski, L., Sessolo, E. & Trojanowski, S. WIMP dark matter candidates and searches - current status and future prospects. *Reports On Progress In Physics.* **81**, 066201 (2018)

[3] Aprile, E., Aalbers, J., Agostini, F., Alfonsi, M., Amaro, F., Anthony, M., Antunes, B., Arneodo, F., Balata, M., Barrow, P. & Others The XENON1T dark matter experiment. *The European Physical Journal C.* **77**, 1-23 (2017)

[4] Barrow, P., Baudis, L., Cichon, D., Danisch, M., Franco, D., Kaether, F., Kish, A., Lindner, M.,

Undagoitia, T., Mayani, D. & Others Qualification tests of the R11410-21 photomultiplier tubes for the XENON1T detector. *Journal Of Instrumentation.* **12**, P01024 (2017)

[5] It, X., Aprile, E., Agostini, F., Alfonsi, M., Arazi, L., Arisaka, K., Arneodo, F., Auger, M., Balan, C., Barrow, P. & Others Lowering the radioactivity of the photomultiplier tubes for the XENON1T dark matter experiment. *The European Physical Journal C.* **75** pp. 1-10 (2015)

[6] Akerib, D., Alsum, S., AraÃºjo, H., Bai, X., Bailey, A., Balajthy, J., Beltrame, P., Bernard, E., Bernstein, A., Biesiadzinski, T. & Others Low-energy (0.7-74 keV) nuclear recoil calibration of the LUX dark matter experiment using DD neutron scattering kinematics. *ArXiv Preprint ArXiv:1608.05381.* (2016)

[7] Collaboration, X., Aprile, E., Aalbers, J., Agostini, F., Alfonsi, M., Althueser, L., Amaro, F., Anthony, M., Arneodo, F., Baudis, L. & Others Dark matter search results from a one ton-year exposure of XENON1T. *Physical Review Letters.* **121**, 111302 (2018)

[8] Aprile, E., Aalbers, J., Agostini, F., Alfonsi, M., Althueser, L., Amaro, F., Antochi, V., Angelino, E., Arneodo, F., Barge, D. & Others Light dark matter search with ionization signals in XENON1T. *Physical Review Letters.* **123**, 251801 (2019)

[9] Lang, R., Pienaar, J., Hogenbirk, E., Masson, D., Nolte, R., Zimbal, A., RÃ¶ttger, S., Benabderrahmane, M. & Bruno, G. Characterization of a deuterium-deuterium plasma fusion neutron generator. *Nuclear Instruments And Methods In Physics Research Section A: Accelerators, Spectrometers, Detectors And Associated Equipment.* **879** pp. 31-38 (2018)

[10] Sorensen, P. & Kamdin, K. Two distinct components of the delayed single electron noise in liquid xenon emission detectors. *Journal Of Instrumentation.* **13**, P02032 (2018)

[11] Stouffer, S., Suchman, E., DeVinney, L., Star, S. & Williams Jr, R. The american soldier: Adjustment during army life.(studies in social psychology in world war ii), vol. 1. (Princeton Univ. Press,1949)

Study of the PeVatron candidate SNR G106.3+2.7 observed at Large Zenith Angle with LST-1 and MAGIC

Marie-Sophie Carrasco

Aix Marseille Univ, CNRS/IN2P3, CPPM, Marseille, France

Abstract — The quest for PeVatrons, sources of cosmic rays accelerated up to PeV energies, saw an exciting development in 2021 when LHAASO detected 12 ultra-high energy (UHE) gamma-ray Galactic sources. Among those sources, the supernova remnant G106.3+2.7 (also called the Boomerang SNR) is a promising hadronic PeVatron candidate. Gamma-ray astronomy performed with Imaging Atmospheric Cherenkov Telescopes (IACTs) is the tool of choice when it comes to looking at the most energetic sources of the Universe with the best angular resolution ($< 0.1°$). We are currently observing the Boomerang SNR with LST-1, the Large Sized Telescope prototype of the Cherenkov Telescope Array, together with the two IACTs of the MAGIC experiment. Observations at Large Zenith Angle allow us to explore the 1-50 TeV region of the energy spectrum with an angular resolution sufficient to resolve the source's morphology. Such observations raise challenges regarding the reconstruction and the analysis of the data, namely the rapid change of energy threshold and signal properties with the telescope pointing. To improve the uniformity of the response as function of the zenith angles we worked on optimizing the Random Forest based reconstruction pipeline.

Introduction

Supernovae Remnants (SNRs) are among the main candidates for PeVatron sources, cosmic accelerators able to accelerate cosmic rays (CRs) up to PeV energies. Accelerated CRs will produce gamma-rays carrying about a tenth of the primary CR's energy, making very high and ultra high energy gamma-ray astronomy the ideal tool to look for PeVatrons.

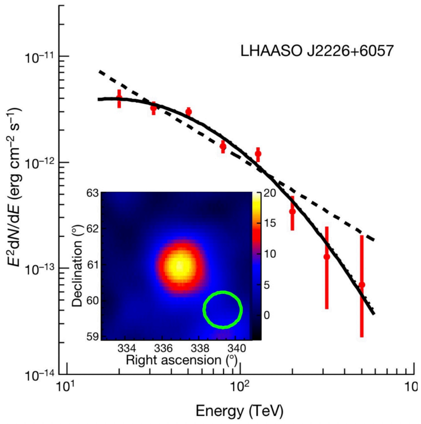

Figure 1: LHAASO J2226+6057 emission spectrum, associated to the SNR G106.3+2.7. The source is detected up to 0.57 PeV.[2]

SNR G106.3+2.7 is a Galactic hadronic PeVatron candidate. Discovered in the '90s, it was first detected at very high energies (VHE, E_γ >100 GeV) by gamma-ray observatories at the end of the '00s [1]. Then in 2021, the LHAASO Collaboration announced it was among the 12 detected Galactic sources of ultra high energy (UHE, E_γ >100 TeV) gamma-ray emissions (cf. fig. 1) [2].

We are observing SNR G106.3+2.7 with the two Imaging Air Cherenkov Telescopes (IACTs) from the MAGIC experiment and with the first prototype of Large-Sized Telescope (LST-1), an IACT of the Cherenkov Telescope Array Observatory (CTAO). In this contribution, we present our work on the analysis of the LST-1 mono data taken at Large Zenith Angle (LZA). We describe the challenges raised by LZA observations and how faced them by optimizing the reconstruction pipeline using a new method of Random Forest (RF) interpolation.

Scientific context

SNR G106.3+2.7 is a composite supernova remnant (SNR), shaped as a comet when seen in radio. The head region is composed of the SNR forward shock colliding with a HI gas region, and of a pulsar wind nebula (PWN) powered by the pulsar PSR J2229+6114[1]. The tail is formed by the SNR shock front expanding through the interstellar medium into a low-density cavity. Overlapping with the tail is a dense molecular cloud which appear to be correlated with VHE emmissions [3].

---

[1] The PWN is also called the Boomerang SNR due to its shape when seen in radio.

Since its first description by Joncas & Higgs in 1990, SNR G106.3+2.7 has been the subject of an extensive multiwavelength campaign [4]. The most recent observations confirm UHE emissions from SNR G106.3+2.7 but the origin of the emission is not resolved due to the poor angular resolution measurements.

Our goal is to resolve the source in the 1-50 TeV energy range with an angular resolution better than 0.1° to perform a morphological and spectral analysis of the Boomerang SNR. This would contribute to the determination of the source nature as a leptonic or hadronic accelerator, characterized by gamma-ray emissions from accelerated electrons or protons, respectively (cf. fig. 2).

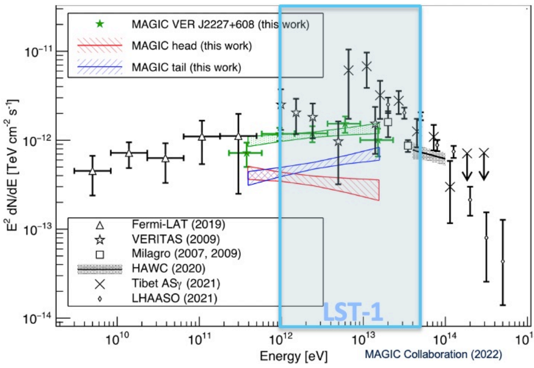

Figure 2: SNR G106.3+2.7 gamma-ray spectra from MAGIC, Fermi-LAT, VERITAS, Milagro, HAWC, Tibet AS$_\gamma$ and LHAASO [1]. The blue box shows the 1-50 TeV range we aim to explore.

Detection principle

Extensive air shower physics

When a VHE particle reaches the Earth, its interaction with the atmosphere will generate an extensive air shower (EAS) of secondary particles.

The nature of the primary particle dictates the EAS characteristics. Indeed, gamma-rays interact with the Coulomb field created by the atmospheric nuclei, initiating an electro-magnetic cascade: a succession of electron-positron pair production and Bremsstrahlung emissions. For hadronic primary cosmic rays, the incident particle will collide on the atmospheric nuclei and produce nuclear fragments among which π_0 meson decaying in gamma-rays leading to electro-magnetic cascades, as well as long-lived muons and neutrinos.

The shower development is constrained by the energy of the incident particle and the altitude of its first interaction point. Due to energy loss processes, each $e^\pm$ sees its energy rapidly decreasing. Below the critical energy (E$_C$ =83 MeV in air), the energy loss processes become dominant and the shower extinguishes. [5]

The secondary charged particles of the EAS propagate faster than light in the medium, leading to a cone of Cherenkov light emissions (cf. fig. 3) [6].

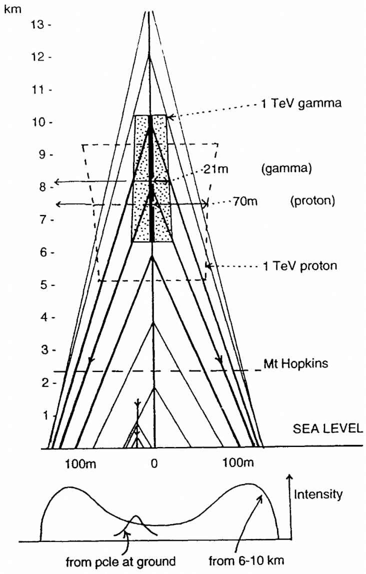

Figure 3: Geometry of Cherenkov rays in EAS. 50% of the light is emitted from the stippled box region for a gamma-ray induced shower, and from the dashed-line box region for a proton shower of the same energy. This results in a peak of light density on the ground just beyond 100 m from the center for a median EAS maximum altitude H_{max} of 8.1 km.[7]

Instrumentation

Imaging Air Cherenkov Telescopes (IACTs) are ideal to perform VHE gamma-ray astronomy. They allow to detect with a good resolution the Cherenkov light produced by the EAS generated by VHE gamma-rays when they reach the Earth's atmosphere. Within the lightpool, which typically reaches ∽100 m in diameter, the Cherenkov light is collected by the telescope mirrors and the shower images are formed on the camera located at the focal plane of the dish.

The IACT we are using to observe our source is LST-1, the first prototype of the Large-Sized Telescope (LST) of the Cherenkov Telescope Array Observatory (CTAO). CTAO is the next generation ground-based instrument for gamma-ray astronomy at very-high energies. The prototype was built for the CTAO's northern hemisphere array, located at the Observatorio del Roque de los Muchachos, on the La Palma island (Canary islands, Spain). The northern site design was optimized for the CTAO's low-to-medium energy range (20 GeV - 5 TeV), with an alpha configuration of 13 IACTs, neighbouring the two MAGIC cherenkov telescopes [8]. Currently in the commissioning phase, LST-1 is already taking data with its 23-meter diameter parabolic reflective surface and 1855 photomultiplier tubes (PMTs) camera.

Analysis

EAS image analysis

The camera images are calibrated and cleaned to keep only the pixels (1 pixel being equivalent to 1 PMT) illuminated by the Cherenkov light of the shower. The resulting image is parameterized with the Hillas parameters method to describe the shower in the camera referential (cf. fig. 4). The main parameters used for further analysis are described in the table 1. The intensity of the image, i.e. the number of Cherenkov p.e., is proportional to the energy of the incident primary particle [5], while the other parameters are mainly used together with the timing information of the illuminated pixels of the image .

Parameter	**Description**
Intensity	Total charge, i.e. total number of p.e. in the shower image
Centroid	Image position (x_c, y_c), obtained as a charge weighted average of the pixels coordinates along the two camera axes
Length	Dispersion of the shower image along its major axis
Width	Dispersion of the shower image along its minor axis
Ψ	Tilt angle of the image major axis with respect to the horizontal axis of the camera
Skewness	Deviation of the image shape from gaussianity in terms of asimmetry
Kurtosis	Deviation of the image shape from gaussianity in terms of outliers importance

Table 1: Description of the main Hillas parameters used to describe an EAS image [9]. The Hillas parameters are used to reconstruct the energy, the direction and the nature of the incident primary particle.

Random Forest-based event reconstruction

The EAS development is a stochastic process. Primary particles with different energy, direction and nature can result in EASs with same shower parameters, and vice versa. Random Forests (RF) are Machine Learning (ML) algorithms that proved to be superior in comparison with traditional reconstruction techniques. ML tools use large simulation datasets to train on, effectively taking into account the stochastic nature of the events.

Along with other parameters like the telescope pointing coordinates, the shower Hillas parameters are fed to 4 Random Forest (RF) algorithms trained on Monte-Carlo (MC) simulations to perform the event reconstruction:

1. a regressor to predict the primary particle energy,
2. a regressor and a classifier for the prediction of the primary particle direction
3. a classifier to identify the primary particle nature (gamma or hadron). [2]

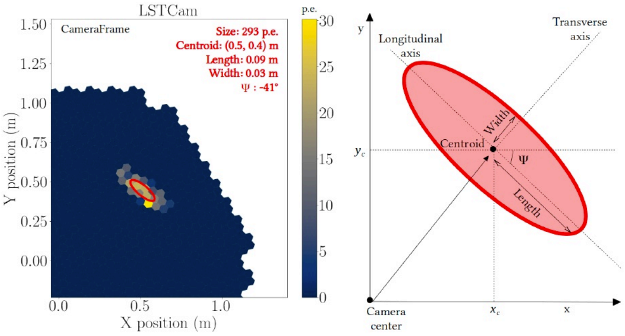

Figure 4: Image of an extensive air shower formed on the LST camera's PMTs (left) and a representation of its Hillas parameterization described in table 1 [9].

To train the RF, evaluate the performances and perform higher level analysis, the source is simulated observed at various pointings. We use the term MC "node" to refer to the MC simulations that are associated with a single telescope pointing.

Large Zenith Angle observation

Although the LST is designed for the lower energy range, it is possible to reach higher energies by observing the source at Large Zenith Angle (LZA), i.e. pointing at zenith angle $\geq 60°$.

At LZA the detected γ-ray induced showers have a larger inclination. The shower maximum height H_{max} is at a higher altitude, resulting in a larger geometrical distance between the telescope and the shower maximum L_{max}.[3].

The size of the effective collection area A_{eff} is constrained by the Cherenkov lightcone size. With larger L_{max} the light pool radius is increased at the detector level, increasing A_{eff}. The larger effective collection area allows IACTs to achieve a better sensitivity at higher energies [10]. However, this improvement raises new challenges regarding the reconstruction.

The larger distance from the observer results in a decreased angular size in both longitudinal and transverse directions. The image centroid, corresponding to the contribution of the shower maximum emission, is closer to the point which corresponds to the gamma-ray direction on the camera for showers with large inclination. The resulting image is shrinked to the camera center and have a more circular shape [11].

The larger distance from the shower maximum and the larger optical depth of atmosphere to cross results in a lower mean photon density, a higher Cherenkov light attenuation due to scattering and absorption. There is an increased risk of encountering local regions of bad weather conditions between the emission point

---

[2] In our case, the signal consists in high-energy primary gamma-ray initiated EAS ($E_\gamma \geq 1$ TeV), and most of the background comes from protons.

[3] On average, $H_{max}(z = 0°) = L_{max}(z = 0°) \approx 7.5$ km a.s.l. for a 3 TeV γ-ray induced EAS when observed at zenith. At LZA, we get $H_{max}(z = 60°) \approx 12$ km a.s.l., corresponding to $L_{max} = 24$ km, more than 3 times $L_{max}(z = 0°)$ [11]

and the detector. The resulting images contain less photons and are smaller in size.

As a result, the reconstruction energy threshold is increased, and the energy and angular resolutions are degraded.

In turn, zenith-dependent features introduce a bias in the RF reconstruction. This bias is due to the fact that the current pipeline uses RF trained on MC simulations performed at discrete values of pointings.

A real data event is reconstructed considering the closest MC node pointing used to train the RF. At LZA, features like the image size are varying fast as a function of the observation zenith angle. Consequently, the RF reconstructed energy presents artefacts in the form of distinct reconstruction regions dependent of the closest training zeniths (cf. fig. 5).

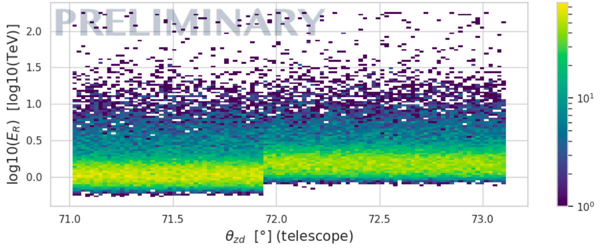

Figure 5: Real data event energy reconstructed by standard RF as a function of telescope pointing zenith. Two distinct reconstruction regions are visible, one via the training node at z_{tel}=71°, the other one via the training node at z_{tel}=73°.

Reconstruction optimization

We generated a denser MC production along the declination line to limit the bias (cf. fig. 6). The denser MC production reduced the bias and the step between the reconstruction regions, but it didn't solve completely the problem.

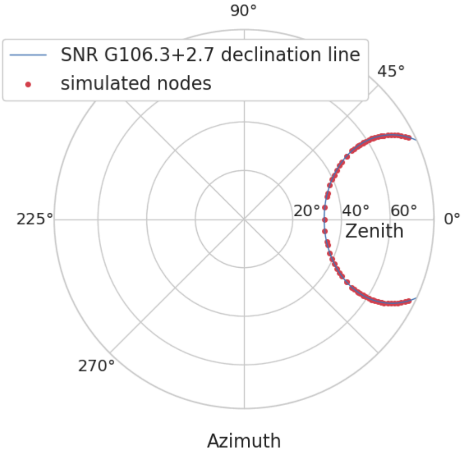

Figure 6: Sky map of the dense set of MC simulation nodes of SNR G106.3+2.7 (red dots) observed along its declination line (blue line). The nodes are used for the Random Forest training and the data/MC comparison.

We developed a new reconstruction pipeline, where each event is reconstructed by interpolating the predictions from the two RFs trained on the closest simulations above and under the zenith of the telescope pointing.

It is a linear interpolation in zenith, the interpolation parameter t being obtained with:

$$t = (z_{tel} - z_1)/(z_2 - z_1) \quad (1)$$

where z_{tel}, z_1, and z_2 are the pointing zeniths of the event and of the closest lower and upper MC simulations used to train the RF respectively. The reconstructed value y, e.g. the energy, is then obtained with:

$$y = y_1(1 - t) + y_2 \times t \quad (2)$$

where y_1, y_2 are the values predicted with RFs trained on the closest lower and upper MC simulations respectively.

The interpolation of the RF predictions proved to be a very effective way to improve the data reconstruction. Together with the denser MC production, this reduced significantly the bias and the different reconstruction regions disappeared (cf. fig. 7).

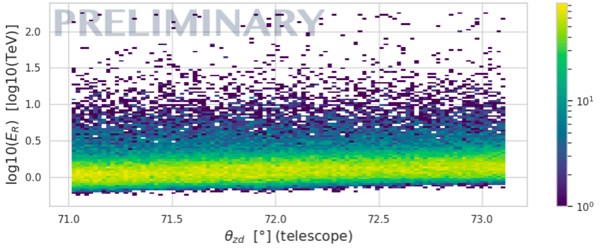

Figure 7: Event energy reconstructed by the interpolated RF method as a function of telescope pointing zenith. The RF were trained on the denser MC line.

Discussion

The work we have presented has been done in the context of the observations with LST-1 and MAGIC of the promising hadronic PeVatron candidate SNR G106.3+2.7.

This work was focused on LST-1 mono data analysis only. In the future, we will perform analysis of the joint LST-1+MAGIC stereo data.

The source is observed at Large Zenith Angle to resolve its energy-dependent morphology from 1 to 50 TeV with an angular resolution $\leq 0.1°$. We used a new method of interpolated Random Forest predictions to improve the uniformity of the response as function of the zenith angles. This method has significantly improved the data reconstruction for LZA observations.

We are now working on the optimization of the extended source analysis at E>1TeV, as well as the modeling of the possible gamma-ray emission scenarios.

References

[1] MAGIC Collaboration et al. (2022). MAGIC observations provide compelling evidence of the hadronic multi-TeV emission from the putative PeVatron SNR G106.3+2.7. Astronomy & Astrophysics. https://doi.org/10.1051/0004-6361/202244931

[2] Cao et al. (2021). Ultrahigh-energy photons up to 1.4 petaelectronvolts from 12 gamma-ray Galactic sources. Nature, 594(7861), 33-36.

[3] Ge et al. (2021). Revealing a peculiar supernova remnant G106. 3+ 2.7 as a petaelectronvolt proton accelerator with X-ray observations. The Innovation 2.2.

[4] Pope et al. (2023). A Multiwavelength Investigation of PSR J2229+ 6114 and its Pulsar Wind Nebula in the Radio, X-Ray, and Gamma-Ray Bands. The Astrophysical Journal 960.1: 75.

[5] Naurois (2012). Very High Energy Astronomy from H.E.S.S. to CTA. Opening of a New Astronomical Window on the Non-Thermal Universe.

[6] Grieder, P. K. (2010). Extensive air showers: high energy phenomena and astrophysical aspects-a tutorial, reference manual and data book.

[7] Hillas, A. M. (1996). Differences between Gamma-Ray and Hadronic Showers. Space Science Reviews 75 : 17-30. https://doi.org/10.1007/BF00195021.

[8] Hofmann, W., & Zanin, R. (2023). The Cherenkov Telescope Array. arXiv preprint arXiv:2305.12888.

[9] Verna, G. (2022). Study of the PeVatron candidate SNR G106. 3+ 2.7 and optimization of the CTA-North sensitivity at high energies (Doctoral dissertation, Aix-Marseille).

[10] Acciari et al. (2020). MAGIC Very Large Zenith Angle Observations of the Crab Nebula up to 100 TeV. Astronomy & Astrophysics. https://doi.org/10.1051/0004-6361/201936899

[11] Konopelko et al. (1999). Effectiveness of TeV-ray observations at large zenith angles with a stereoscopic system of imaging atmospheric Cerenkov telescopes. Journal of Physics G: Nuclear and Particle Physics, 25(9), 1989.

Part VI

Hadronic Physics

session chaired by Batoul DIAB

Introduction to Hadronic Physics

Batoul Diab

CERN

Abstract — This contribution serves as an introduction to the field of hadronic physics, exploring the specific topics discussed during the dedicated session at the JRJC.

What is a hadron?

Matter, all around us, is made of atoms which are composed of protons, neutrons, and electrons. Protons and neutrons are made up of elementary blocks of matter called quarks. The quarks are held together by photon-like particles called gluons. This interaction is one of the fundamental forces of nature known as the strong force. In particle physics, any particle that is composed of quarks and gluons and is subject to the strong nuclear force is categorized as a hadron, protons and neutrons being the most abundant. The theory that describes this is Quantum ChromoDynamics (QCD) that assigns a charge called color to quarks as well as gluons. The strong coupling constant α_S, shown in Fig. 1, describes the strength of the interaction [1]. At low energy, $\alpha_S \rightarrow 1$ which means quarks are confined within color-neutral hadrons, either with two valence quarks, making mesons, or three making baryons[1]. At high energy, $\alpha_S \rightarrow 0$. In that case the quarks are weakly bound and can be treated as individual particles with asymptotic freedom. There are different approaches used in theoretical physics to study the strong force such as Lattice QCD and perturbative QCD.

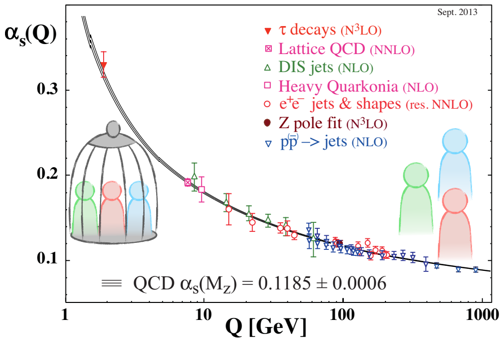

Figure 1: The strong coupling constant α_S as function of energy [1]

Unveiling quark and gluon properties

How did we even know of the existence of quarks and gluons? Inelastic scattering is one of the common tools used to study various phenomena in physics. To study the internal structure of a proton, one could fire electrons at high energy and observe how the electrons bounced off. A high energy scale allows the electrons to probe deep inside the proton, thus, the name Deep Inelastic Scattering (DIS). Such experiments conducted at SLAC showed that when firing electrons very close to the protons, some would bounce off while some other would pass through, indicating the existence of point-like objects inside the proton, later identified as quarks. On the other hand, gluons were discovered in electron-positron experiments at DESY [3, 4], where events containing three experimental signatures of elementary particles, known as jets, were observed. The e^+e^- annihilation can produce a virtual photon that then produces a pair quark-antiquark but cannot produce three quarks. The third jet was found to be the signature of a new particle with different characteristics than the quarks, a new particle called gluon. An event display of such a case is shown in Fig. 2.

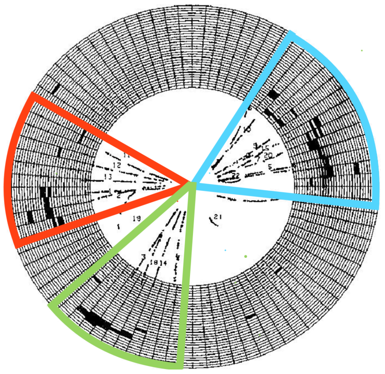

Figure 2: 3-jet event recorded at $\sqrt{s} = 33$ GeV with the JADE detector at PETRA, DESY [6].

---

[1] Exotic hadrons that have 4 or more valence quarks are also possible [2]

The quark-gluon plasma

In normal matter conditions, quarks and gluons are confined into hadrons. However, QCD calculations [7] indicate that above a critical temperature, T_c, or energy density, ε_c, strongly interacting matter undergoes a phase transition from hadronic matter to a soup of deconfined quarks and gluons, called the Quark-Gluon Plasma or QGP [9]. In 2000 CERN announced the discovery of a "new state of matter in heavy-ion collisions at the SPS" that "features many of the characteristics of the theoretically predicted quark-gluon plasma" based on many measurements from different experiments [10]. Basically, powerful accelerators collided heavy nuclei that formed many small fireballs in which the nucleons "melted" into a quark-gluon plasma. A representation of a heavy-ion collision is shown in Fig.3. When the two accelerated nuclei collide, the protons and neutrons begin to interact. The QGP, where the quarks and gluons are deconfined from hadrons, is then created for a very short time, as the system cools down and hadrons start forming again. These hadrons are what we detect in giant machines around the collision that act as cameras for such events. We can measure how much the emerging hadrons are affected by the presence of the QGP by comparing to proton-proton (pp) collisions. For example, a particle called J/ψ is suppressed by the QGP. Its components, a c quark and its antiquark, can lose the interaction that keeps them bound, due to the color states in the medium acting as a screening effect. Another effect occurs when gluons and quarks lose energy in the medium by scattering and emitting gluon radiation, which affects jets, their experimental signatures, in a phenomenon called "jet quenching", illustrated in Fig.4.

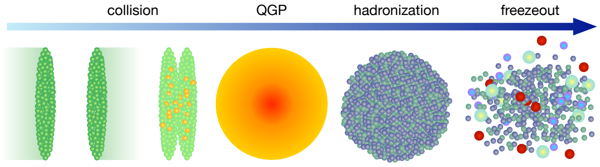

Figure 3: Schematic illustration of the evolution of a relativistic heavy-ion collision.

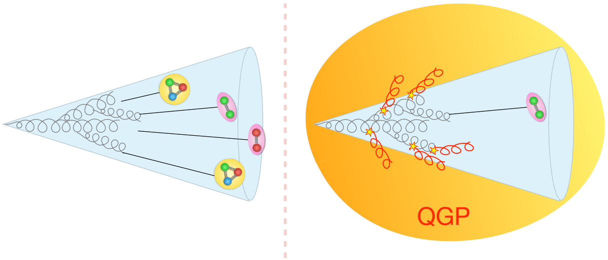

Figure 4: Schematic illustration of the evolution of a jet with and without the presence of the QGP, highlighting jet quenching.

When two heavy nuclei collide, it can occur head-on. In this case, the collision is called central and the nuclei overlap completely, unlike peripheral collisions, where the nuclei overlap only partially. In non-central heavy-ion collisions, the colliding matter takes on an oval shape as shown in Fig. 5. Since particles emerging from the collision tend to exhibit a collective behavior, one can imagine that this collectivity can be affected by the shape of the QGP produced in the overlap region. Particles would be more accelerated along the shorter x-axis than the longer y-axis, resulting in an asymmetry, or anisotropy, in the coordinate and momentum distributions. Experimentally, we measure the anisotropy in order to investigate the shape of the collision [12]. The elliptic flow, v_2, is the second coefficient of the Fourier expansion of the azimuthal distribution with respect to the reaction plane (the xz plane in Fig. 5). Higher order coefficients probe more complex shapes: the triangular flow measured with v_3, and the quadrangular flow measured with v_4 [13].

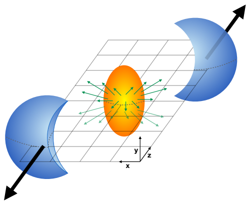

Figure 5: A schematic representation of the collision zone between two incoming nuclei [11].

Both contributions at the hadronic session of the JRJC focused on the quark-gluon plasma, one theoretically and the second experimentally.

References

[1] G. Dissertori, ASDHEP 26, 113 (2016)

[2] Belle collaboration, PRL 100, 142001 (2008)

[3] PLUTO collaboration, PLB 82, 449 (1979)

[4] DESY collaboration PLB 86, 399 (1979)

[5] K. Fabricius *et al.*, PRL 45, 867 (1980)

[6] S. Bethke and A. Wagner, EPJH 47, 16 (2022)

[7] F. Karsch, LNP 583, 209 (2002)

[8] J. C. Collins, PRL 34, 1353 (1975)

[9] E. V. Shuryak, WS, 211 (1995)

[10] U. W. Heinz and M. Jacob, arXiv:nucl-th/0002042 (2000)

[11] R. Nouicer, EPJP 131, 70 (2016)

[12] R. Snellings, NJP 13, 055008 (2010)

[13] B. Alver and G. Roland, PRC 81, 054905 (2010)

Quantum vs. semi-classical description of in-QGP quarkonia in the quantum Brownian regime

Aoumeur Daddi Hammou[1] ***with S. Delorme***[1,2]***, P.-B. Gossiaux***[1]***, T. Gousset***[1]

[1] *SUBATECH, IMT Atlantique, Nantes Université, IN2P3/CNRS*
Alfred Kastler 04, 44307 Nantes, France
[2] *Institute of Nuclear Physics, Polish Academy of Sciences*
ul.Radzikowskiego 152, 31-342, Kraków, Poland

Abstract — In these proceedings, we analyse the validity of semi-classical approximation in describing the in-QGP quarkonium dynamics. To this end, we solve the quantum master equation and its associated semi-classical equation in the quantum Brownian regime. We compare their predictions for a couple of observables which could highlight a possible breakdown of semi-classical approximation and call for a full quantum description of in-QGP quarkonia.

Introduction

Heavy quarkonia are considered among the most promising probes of Quark-Gluon Plasma (QGP) formed in Ultra-Relativistic Heavy-Ion collisions (URHIC). For a reliable use of such probe, we need a rigorous formalism, derived from first principles, which could describe the real time and out-of-equilibrium evolution of in-medium quarkonia while it keeps a full track of the quantum nature of our system. In addition, the formalism should consider the static as well as dynamical effects of QGP on heavy quarkonia on equal footing. Among the possible formalisms, the open quantum systems formalism outstands due to its simplicity. Within this framework, the evolution of our system is governed by a quantum master equation which, by implementing semi classical approximations (SCA), results into the standard and the more simple semi-classical transport equations as Boltzmann and Fokker-Planck / Langevin equations. The latter had already shown, prior to the use of open quantum system techniques, a good success in describing in-medium quarkonium transport, in spite of their model dependence in considering some QGP effects. Therefore, starting from the fact that the semi classical transport equations are approximates of, the more fundamental, quantum master equations, it is legitimate to wonder about their range of validity and a quantitative comparison between the full quantum and semi classical descriptions become mandatory to put our understanding of in-medium quarkonium transport on stronger ground. In these proceedings, we review briefly the derivation of the quantum master equation in the quantum Brownian regime and its associated semi classical Fokker-Planck / Langevin equation as was first derived in [1], and extended in [2, 3]. Then, for the sake of testing the validity of SCA, we discuss some comparative results issued from one dimensional resolution of the two equations and draw some conclusions on SCA validity.

Theoretical framework

Quarkonium interaction with QGP implies the exchange of quantum coherence as well of energy between the two systems. Therefore, quarkonia must be studied as an open quantum system. Indeed, by taking advantage of the hierarchy in dynamical time scales between the constituents of the global system, quarkonia-QGP, we can trace out the QGP degrees of freedom and derive a master equation that describes the dynamics of quarkonia under the influence of the QGP.

Starting from Non-Relativistic QCD (NRQCD) and working in the quantum Brownian regime of open quantum systems that corresponds to the high-temperature regime, with respect to quarkonium binding energy i.e $T \gg E$, we derive the following master equation [1, 2, 3]

$$\begin{aligned}\frac{\mathrm{d}\hat{\rho}_{Q\bar{Q}}}{\mathrm{dt}} &= -i\left[\hat{H}_{Q\bar{Q}} + \Delta\hat{H}_{Q\bar{Q}}, \hat{\rho}_{Q\bar{Q}}(t)\right] \\ &\quad + \int_{\boldsymbol{x},\boldsymbol{y}} W(\boldsymbol{x}-\boldsymbol{y})\left(\tilde{n}^a_{\boldsymbol{x}}\hat{\rho}_{Q\bar{Q}}\tilde{n}^a_{\boldsymbol{y}} - \tfrac{1}{2}\left\{\tilde{n}^a_{\boldsymbol{y}}\tilde{n}^a_{\boldsymbol{x}}, \hat{\rho}_{Q\bar{Q}}\right\}\right)\end{aligned} \tag{1}$$

with

$$\tilde{n}^a_{\boldsymbol{x}} = n^a_{\boldsymbol{x}} - \frac{i}{4T}\dot{n}^a_{\boldsymbol{x}} \tag{2}$$

where $n^a_{\boldsymbol{x}}$ refers to the local color charge density and

$$\Delta \hat{H}_{Q\bar{Q}} = -\frac{i}{2}\int_{\boldsymbol{x},\boldsymbol{y}} V\left(\boldsymbol{x}-\boldsymbol{y}\right)\left[n^a_{\boldsymbol{x}} n^a_{\boldsymbol{y}}, \hat{\rho}_{Q\bar{Q}}\right] \tag{3}$$

being the QGP induced modification to $\hat{H}_{Q\bar{Q}}$ called Lamb shift, and encodes Debye screening. Similarly, the correlator $W\left(\boldsymbol{x}-\boldsymbol{y}\right)$ represents the QGP induced imaginary potential.

In order to derive the semi-classical equation from the quantum master eq. (1), we implement a semi-classical expansion of in this last. It consists in assuming a small extension of the density matrix along the off diagonal direction. i.e non-vanishing density matrix elements are localized around the diagonal or, equivalently, the system has short quantum coherence length beyond which any superposition would be extremely suppressed.

Indeed, close to thermal equilibrium, the off diagonal elements of the density matrix are of the form $\left\langle \boldsymbol{r}\left|\hat{\rho}_{Q\bar{Q}}\right|\boldsymbol{r'}\right\rangle \sim \exp(-\frac{\left(\boldsymbol{r}-\boldsymbol{r'}\right)^2}{\lambda^2_{th}})$, where $y \equiv \boldsymbol{r}-\boldsymbol{r'}$ encodes the coherence length. Therefore, the density matrix would be quasi-diagonal and allow for a semi-classical description provided our system has a short thermal wavelength.

The implementation of semi-classical approximation when considering a discrete basis, eg. color basis, is not quite transparent, so we will restrict ourselves to QED limit of the Lindblad equation (1). Therefore, an expansion in QED limit of Lindblad equation (1) in terms of coherence length followed by Wigner transform leads into the semi classical Wigner equation [1]:

$$\begin{aligned}\frac{\partial W(\boldsymbol{r},\boldsymbol{p})}{\partial t} \quad = \quad & \Big[-\frac{2\boldsymbol{p}.\boldsymbol{\nabla_r}}{M} - \boldsymbol{\nabla_r} V\left(\boldsymbol{r}\right).\boldsymbol{\nabla_p} + \frac{\eta(\boldsymbol{r})}{2}\boldsymbol{\nabla}^2_{\boldsymbol{p}} \\ & + \frac{\gamma(\boldsymbol{r})}{M}\boldsymbol{\nabla_p}\boldsymbol{p}\Big] W\left(\boldsymbol{r},\boldsymbol{p}\right)\end{aligned} \tag{4}$$

Drift and drag coefficients are related by Einstein relation

$$\gamma_{ij}\left(\boldsymbol{r}\right) = \frac{1}{2T}\eta_{ij}\left(\boldsymbol{r}\right) = \frac{1}{4T}\left(\mathcal{H}_{ij}\left(\boldsymbol{r}\right)+\mathcal{H}_{ij}\left(0\right)\right) \tag{5}$$

with $\mathcal{H}\left(\boldsymbol{r}\right)$ being the Hessian matrix of imaginary potential.

It could be shown that the Gibbs-Boltzmann distribution

$$W_{st}\left(\boldsymbol{r},\boldsymbol{p}\right) = N\exp\left[-\frac{1}{T}\left(\frac{\boldsymbol{p}^2}{M}+V\left(\boldsymbol{r}\right)\right)\right] \tag{6}$$

is a steady state solution of eq. (4) with N being a normalisation constant. But the quantum dynamics relax to different steady state.

Our aim now is to carry out a comparative analysis of the two equations, namely, the Lindblad and Fokker-Planck equations, respectively.

The main idea behind such comparison is to identify the regime of validity of semi-classical approximation used, implicitly, in most of phenomenological models based on Fokker-Planck [1] or, equivalently, Langevin equation, and identify cases where the semi-classical description may break down and a full quantum description becomes mandatory. To this end, we consider that the benchmark in terms of accuracy is the results corresponding to Lindblad equation (1), since the semi-classical equation (4) was merely an approximate of it in the limit of a small coherence length. Therefore, once the results corresponding to semi-classical description differ noticeably from that of the full quantum case, we may conclude a breakdown of semi-classical approximation and its corresponding equation (4).

Numerical study

The comparative analysis presented in these proceedings is based on a one-dimensional resolution of Lindblad equation (1) and Langevin equation associated to Fokker-Planck equation (4), using the same expressions of the real and imaginary potentials, $V\left(r\right)$ and $W\left(r\right)$, respectively, derived and studied in detail in [4].

We adopt as initial state a 1S-like state given by

$$\psi\left(r\right) = \left(\frac{1}{\pi\sigma^2}\right)^{\frac{1}{4}} e^{-\frac{r^2}{2\sigma^2}} \tag{7}$$

with a variance $\sigma = 0.38$ (fm).

Since the medium temperature plays a major role in quantum decoherence as well as thermalization, and in order to have a deeper insights on its effect in the comparative study, quantum versus semi-classical, we solved the equations using four different temperatures[2] $T = [0.2, 0.3, 0.4, 0.6]$ (GeV). We evolve the system up to a final time $t_f = 20$ (fm/c) within a box of size 20 (fm), i.e $r \in [-10, 10]$ (fm).

The expectation value of a given observable is based on the density matrix or, equivalently, the Wigner function which keeps a full track of our system's state.

$$\left\langle \hat{O}\right\rangle = Tr\left(\hat{\rho}_{Q\bar{Q}}\hat{O}\right) = \int_{\boldsymbol{r},\boldsymbol{p}} W\left(\boldsymbol{r},\boldsymbol{p}\right) O\left(\boldsymbol{r},\boldsymbol{p}\right) \tag{8}$$

Therefore, as a first quantitative confrontation of the approximate semi-classical description to to the fundamental quantum one, we compute the trace distance between their respective Wigner functions

$$\mathrm{d}\left(t\right) = \sqrt{\int \mathrm{drdp}\left(W_{QM}-W_{SC}\right)^2} \tag{9}$$

where W_{QM} and W_{SC} refers to Wigner functions resulted from quantum and semi-classical dynamics, respectively. The smallest trace distance is, then, the closest the two descriptions are to each other with the semi-classical approximation remaining valid.

---

[1] This applies to the quantum Brownian regime, while, for the low temperature regime we use Boltzmann equation that is based on kinetic description.

[2] Notice that the lowest temperature we are considering , i.e $T = 0.2$ (GeV), is at the intersection between the quantum Brownian and optical regimes.

We present[3] in Fig. 1 the time evolution of trace distance for various QGP temperatures. The band widths in plots quantifies the effect of the inclusion or removal of the superoperator $\propto \dot{n}_{\boldsymbol{x}} \dot{n}'_{\boldsymbol{x}}$ in Lindblad equation which is subdominant but necessary to assure to the positivity of the master equation.

Independently of the QGP temperature considered, we notice, in Fig. 1, an increase of trace distance at a first stage of its time evolution before reaching a maximum that is followed by a decrease to a stationary value. This behavior could be traced back to the presence of quantum effects [4] at very early times, which are subsequently washed out by the QGP induced decoherence. Therefore, as long as such quantum effects are present and dominant in the dynamics of quarkonium state, then, the trace distance tends to increase due to the role of higher-order quantum corrections that are neglected in derivation of semi-classical equation. Such increase continues until quantum decoherence takes over and dominates the dynamics which, by turn, damps such quantum effects and leads to the decrease observed.

Evidently, at higher temperatures, the quantum decoherence becomes more efficient and the quantum effects could not survive enough to affect noticeably the dynamics of the quarkonium state. Therefore, the trace distance reaches lower values at higher temperatures and starts to decrease earlier.

Focusing on the early-time behavior of quarkonium state and based on Fig. 1, we see for T=[0.2, 0.3] (GeV) a distance of 16% and 10% between the quantum and semi-classical Wigner functions, respectively, so the accuracy of a semi-classical description is questionable in this case. Still, even at the relatively high temperatures, i.e T=[0.4, 0.6] (GeV), we have non negligible values of trace distance at very early times, around 8% and 6.5%, respectively. However, we expect that the Markovian approximation, adopted in our case, implies a negligible dependence of the late time observations on early time dynamics of our system and, by turn, on such early-time discrepancies between the two descriptions. This last observation implies the importance of describing in-QGP quarkonium transport with non Markovian quantum dynamics to get stronger conclusions about the validity of semi-classical approximation.

We may argue that the classicalisation of quarkonium state should rend its dynamics at late time blind to whether we consider quantum, semi-classical or classical description, therefore, the trace distance is expected to vanish at late times, while this is not the case in Fig. 1. Such non-zero values of late time trace distance are due to the different steady state, in the two descriptions, into which the quarkonium state relaxes.

Now, it would be interesting to see how the difference between the tow descriptions is reflected on various other observables that probe thermalization, and population of quarkonia.

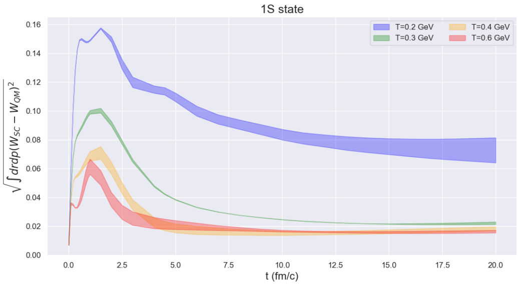

Figure 1: Time evolution of trace distance for various QGP temperatures with an initial 1S state.

Since the momentum kicks of QGP constituents on quarkonium are crucial in understanding its quantum state classicalisation and dissociation, in addition to thermalization, we should study the dynamics of quarkonium mean square momentum $\langle p^2\left(t\right)\rangle$. The early-time behavior of this last observable allows better understanding of decoherence, while late time behavior encodes insights on thermalization. We show in Fig. 2, the time evolution of root mean squared momentum.

In contrast to semi-classical dynamics, as expected, the quantum dynamics by Lindblad equation does not relax to Gibbs-Boltzmann distribution . Moreover, the quantum dynamics overheats the system over all its time evolution compared to semi-classical case. Therefore, we expect the overheating of quarkonium state in quantum description case to result into a larger depletion of 1S-like initial state population compared to semi-classical dynamics.

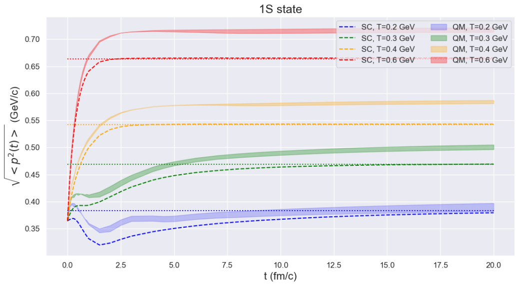

Figure 2: Time evolution of root mean squared momentum for various QGP temperatures with an initial 1S state. The dotted lines refer to the stationary values expected from Gibbs-Boltzmann distribution, i.e $\sqrt{\langle p^2\rangle}_\infty = \sqrt{MT/2}$.

To this end, we compute the survival probability of the initial 1S-like state and generating probability of the other higher states, namely, 2S-like state in our case. The probability P_i of finding a quarkonium in a state "i" is defined by

$$P_i\left(t\right) = Tr\left(\left|\psi_i\right\rangle\left\langle\psi_i\right|\hat{\rho}_{Q\bar{Q}}\left(t\right)\right) = \int \mathbf{drdp} W_i\left(\boldsymbol{r},\boldsymbol{p}\right) D\left(\boldsymbol{r},\boldsymbol{p},t\right) \tag{10}$$

where $W_i\left(\boldsymbol{r},\boldsymbol{p}\right)$ is the Wigner function, or transform,

---

[3] In the plots, "QM" stands for quantum results and "SC" stands for semi-classical results.

[4] Which are fully captured by the quantum description while only approximately by semi-classical deception.

of the state's wave function $\psi_i(\boldsymbol{r})$ on which we are projecting , while, $D(\boldsymbol{r}, \boldsymbol{p}, t)$ is the Wigner function of quarkonium state undergoing quantum or semi-classical dynamics.

We show in Fig. 3, the survival probability of the initial 1S-like state.

Since the equilibrium values of $\sqrt{\langle p^2(t)\rangle}$ are larger in the quantum description for all temperatures, then, as expected, this description overdamps the ground state population at late time compared to semi-classical description.

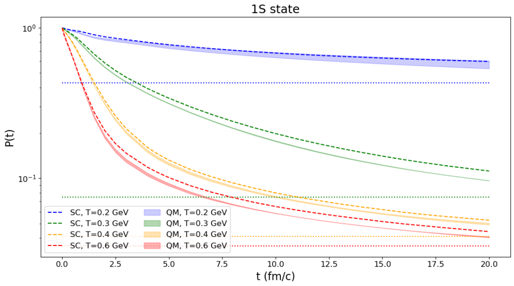

Figure 3: Survival probability of 1S state. Dotted lines are the equilibrium values expected from Gibbs-Boltzmann distribution.

We turn now to discuss the generation probability of the excited 2S-like state[5]. This brings some new features into our study, in particular, its associated Wigner function contains an interference term, hence, non-zero negative volume. Such interference term, that is pure quantum effect, will turn out to be crucial in our comparison of the two descriptions.

We see in Fig. 4 (top) that corresponds to $T = [0.3, 0.4, 0.6]$ (GeV), a very good early time agreement, while, at late time, the quantum description predicts lower probabilities compared to semi-classical description, which is again could be explained by the larger equilibrium values of $\sqrt{\langle p^2(t)\rangle}$ in the former compared to the last.

For the case of the lowest QGP temperature i.e $T = 0.2$ (GeV), the quantum effects survive longer and are expected to impact noticeably the quarkonium dynamics. Indeed, we notice in Fig. 4 (down) that the semi-classical description breaks down at early time, i.e $t \leq 1$ (fm/c), since it predicts a negative probability which is obviously a nonphysical result, while, the probability from quantum description is well behaving. However, we notice that the generation probability quickly takes off and becomes positive in semi-classical description, which is due mainly to decoherence.

The breakdown of SC description in case of 2S state at low T could be attributed to the "dangerous cross terms" in its Wigner function [5].

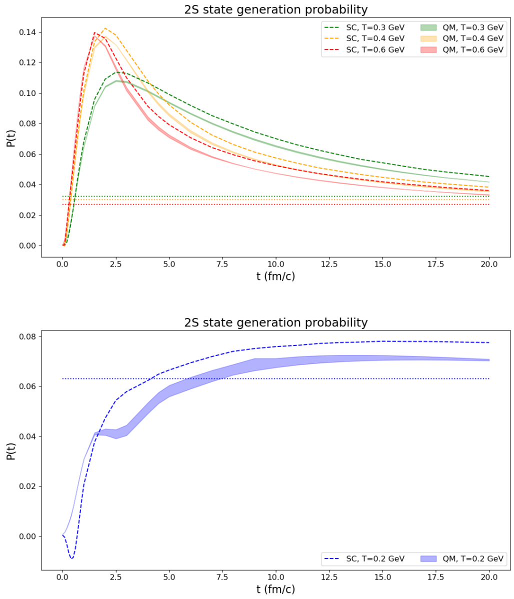

Figure 4: Generation probability of 2S state for $T = [0.3, 0.4, 0.6]$ (GeV) (Top) and $T = 0.2$ (GeV) (Down). Dotted lines are the equilibrium values expected from Gibbs-Boltzmann distribution.

$$\Psi_{2S}(r) = \frac{1}{\sqrt{2}}\left(\psi_1(r) \pm \psi_2(r)\right) \tag{12}$$

corresponding to a Wigner function

$$W_{2S}(r,p) = \frac{1}{2}W_1(r,p) + \frac{1}{2}W_2(r,p) \pm W_{int}(r,p) \tag{13}$$

The interference term W_{int} results from cross terms as $\psi_1^*\psi_2$ and contains very oscillating terms

$$W_{int}(r,p) \propto \cos\left(\frac{rp}{\hbar c}\right), \sin\left(\frac{rp}{\hbar c}\right) \tag{14}$$

which spoil the semi-classical expansion of unitary part in eq. (1), and necessitate a "selective resummation" w.r.p to coherence length or, equivalently, to $\hbar$ of higher order quantum corrections, see [5].

Conclusions

In these proceedings, we showed that the semi-classical description reproduces very well the results obtained with full quantum description, especially, at high QGP temperature. However, for low QGP temperatures a noticeable discrepancy is observed at early times due to the non negligible contribution of quantum corrections to the dynamics. Such discrepancy gets enhanced for quarkonium excited states that have quantum interference terms which require a careful implementation of semi-classical approximation.

---

[5] In our work, we use the following as an expression of its wave function:

$$\psi_{2S}(r) = Ae^{-\frac{r^2}{B^2}} + Cr^2e^{-\frac{r^2}{D^2}} \tag{11}$$

with A=-0.68 (fm$^{-\frac{1}{2}}$), B=0.22 (fm), C=3.4 (fm$^{-\frac{5}{2}}$), and D=0.79 (fm).

References

[1] J-P.Blaizot et al. JHEP 2018.6 (2018): 1-57.

[2] S.Delorme et al. EPJ Web Conf. 258 (2022) 05009.

[3] Y.Akamatsu. Prog. Part. Nucl. Phys. 123 (2022): 103932.

[4] R.Katz et al. Eur.Phys.J.A 58 (2022) 10, 198

[5] J.E. Heller, J. Chem. Phys. 65.4 (1976): 1289-1298.

J/Ψ flow measurements in Pb-Pb collisions with the ALICE detector at LHC

Victor Valencia

Subatech

Abstract — The ALICE experiment at the Large Hadron Collider (LHC) explores the Quark-Gluon Plasma (QGP) by colliding heavy ions. This exotic state of matter recreates the conditions of the first instants of the universe where quarks and gluons ran freely. The QGP is an extremely dense and hot medium that behaves almost as a perfect fluid with the lowest shear-viscosity to entropy density ratio ever estimated. The collective behavior exhibited during the hydrodynamic expansion can be explored through the analysis of anisotropic particle momentum distributions. In the initial moments of a semi-peripheral collision, an almond-shaped overlap region emerges, the anisotropies of this initial geometry transforms via pressure gradients to final momentum anisotropies of detected particles (anisotropic flow). Heavy quark bound pairs called quarkonia are unique probes to study the properties of the deconfined medium. The measurement of quarkonia's flow also provides an opportunity to investigate their partial thermalization, giving crucial information about quarkonium suppression and regeneration mechanisms. Moreover, anisotropic flow can also explore the energy loss experienced by heavy quarks in the QGP. In this paper, we will introduce some J/ψ flow measurements using particle correlations and we will discuss some theoretical interpretations.

Introduction

The typical energy density of our current Universe results in quarks being confined in bound states. Nevertheless, if heavy ions collide with large energies, deconfined states can be created. Heavy-Ion Collisions (HIC) study the behavior of nuclear matter in such high energy regimes [1]. During the initial instants of the HIC, hard scattering processes take place (jets, heavy quarks production...) as calculated by perturbative Quantum Chromodynamics (pQCD). Around $t \sim 1$ fm/c, the system reaches thermal equilibrium and the hydrodynamic expansion of the quark gluon plasma (QGP) takes place. Inside the hot medium, all color charges are free, meaning that partons (quarks and gluons) are deconfined. However, the QGP behaves almost as a perfect fluid, the medium is strongly coupled. At $t \sim 10$ fm/c when the temperature is lower than a certain T_C critical value (150 - 160 MeV), a phase transition occurs where all partons hadronize into pions, Kaons, protons, etc. These final hadrons, which may further decay into other states, are the particles observed in experimental measurements. In HIC, due to the early formation time of heavy states, quarkonia are excellent probes to determine the fundamental QGP properties.

Anisotropic flow

In heavy-ion collisions, the anisotropic flow is a response of the medium to the initial spatial coordinate anisotropy [2]. This initial anisotropy, quantified by the eccentricity, characterizes the overlap of colliding ions. As the system expands, the initial spatial anisotropy transforms into momentum space anisotropies (see figure 1) This transformation manifests as an azimuthal dependence in the distribution of particles relative to the reaction plane. Anisotropic flow is highly sensitive to the underlying properties of the system during its early stages of evolution. Due to the periodicity in the azimuthal angle ϕ, a Fourier expansion series [3] can be used to describe the final azimuthal particle distribution:

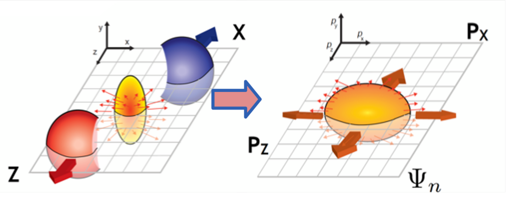

Figure 1: Schema of the expansion of the QGP

$$\frac{dN}{d\phi} = 1 + 2\sum_{n=1}^{\infty} v_n \cos[n(\phi - \psi_n)] \tag{1}$$

Anisotropic flow is described by coefficients v_n of the Fourier series, where n is the harmonic number. Experimentally, we obtain this quantity by doing the average for all tracks and events:

$$v_n = \langle \cos[n(\phi - \psi_n)] \rangle. \tag{2}$$

where ψ_n is the symmetry plane [4]. The v_1 coefficient is usually referred to as directed flow, while the v_2 coefficient is called elliptic flow. These v_n coefficients are dependent on p_{T} and y [5]. In experiment, the symmetry plane ψ_n is hardly known, one method involves estimating it in order to compute the corresponding v_n.

Another method to estimate the anisotropic flow is the multi-particle correlations technique, which involves azimuthal correlations among observed particles. For example, we can compute the average of two-particle correlations for all collisions and tracks: $\langle \cos n(\phi_1 - \phi_2) \rangle$. In reality, a shift δ_2 arises from correlations unrelated to the initial system's geometry, so-called non-flow contributions:

$$\langle \cos[n(\phi_1 - \phi_2)] \rangle = \langle v_n^2 + \delta_2 \rangle. \tag{3}$$

The main non-flow contributions are mostly produced by jets, di-jets or even resonance decay that can produce large correlations that bias the flow measurement results.

In two-particle correlations, $\delta_2 \propto \frac{1}{M}$, where M represents the multiplicity (number of tracks). To mitigate non-flow effects, we can employ multi-particle correlations. For example, if we consider 4-particle correlations, the following average needs to be evaluated: $\langle \cos[n(\phi_1 + \phi_2 - \phi_3 - \phi_4)] \rangle$. The commonly computed quantity is the cumulant [6], where internal correlations are subtracted from the main particle correlation according to:

$$\begin{aligned} c_n(4) = {} & \langle \cos[n(\phi_1 + \phi_2 - \phi_3 - \phi_4)] \rangle \\ & - \langle \cos n(\phi_1 - \phi_3) \rangle \langle \cos n(\phi_2 - \phi_4) \rangle \\ & - \langle \cos n(\phi_1 - \phi_4) \rangle \langle \cos n(\phi_2 - \phi_3) \rangle. \end{aligned} \tag{4}$$

Again, in experiment, this quantity is equivalent to $c_n(4) = \langle v_n^4 + \delta_4 \rangle$, where the non-flow component scales as $\delta_4 \propto \frac{1}{M^3}$ and is more suppressed than 2-particle correlations.

Charmonia and charm quark

Charmonium states (like J/ψ) are expected to melt at high T [7]. In such conditions, a significant density of color charges in a small volume generates a color screening effect. When the range of the interaction becomes smaller than the size of charmonia, the strong interaction cannot form heavy bound states anymore, then heavy quarks dissociate. This is the so-called suppression mechanism [8]. At LHC, a regeneration mechanism of charmonia has been also observed [9]. The abundance of charm and anti-charm pairs is non-negligible and statistically two charm pairs that were firstly dissociated can be recombined later into a charmonium state. As charm quarks interact with the expanding QGP, they might exhibit a different behavior than light quarks (u,d,s). By measuring the flow of J/ψ, we can gain information about the partial thermalization of charm quarks, that acquires flow from the surrounding medium [10]. Notably, D-meson flow measurements suggest the active participation of charm quarks in the collective anisotropic flow of the QGP fluid [11]. The problem is that the light-flavor quark of the D-meson contribute to the flow, making it challenging to conclude about the flow of charm quarks. This is why it is particularly interesting to study the flow of J/ψ particles.

Experimental set up

The ALICE detector is designed to study Pb-Pb nuclei collisions [12]. The detector is composed of two main parts, the central barrel and the muon spectrometer.

The central barrel is positioned at midrapidity, it constitutes a collection of detectors surrounding the nominal interaction point where the QGP state is formed [13]. The first tracking detector locate the primary and secondary vertices with a good resolution ($\sim$ 100 micrometers). Additionally, two scintillator detectors in coincidence counts particles, triggering Minimum Bias (MB) collisions and providing an estimation of the centrality.

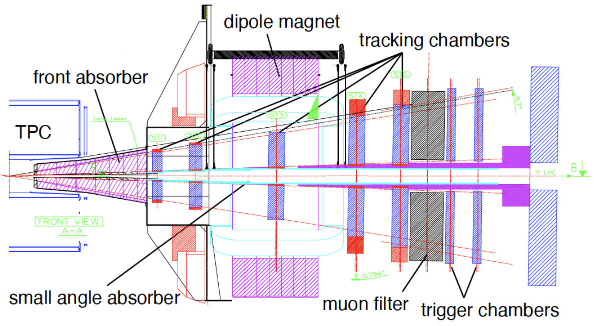

Figure 2: Muon Spectrometer of ALICE.

In the forward region $2.5 < y < 4$, the Muon Spectrometer [14] (shown on figure 2) studies heavy quark mesons via the muonic decay channel, going to very low p_{T}. The detector is composed by a very thick absorber that reduces the flux of initial hadrons by a factor of 100 and rejects most of the particles from secondary interactions with small p_{T} (mainly electrons). To reconstruct the particle's trajectory, the muon tracking chambers (MCH) are used. They consist of five stations with two detection planes consisting of 5 mm gas gap drift multi-wire proportional chambers (MWPC) with segmented cathode plane(CPC). The MWPC detect charged particles and give positional information by tracking the trails of gaseous ionization. A dipole magnet of 820 tons generates a strong magnetic field (0.7 T) that bends trajectories of charged particles. The measurement of the radius of curvature determines the muon momentum. A muon filter (iron wall) is also located after the tracking chambers to reduce the background, stopping muons with small momentum (most of them coming from the decay of kaons and pions). Finally, the Muon Trigger (MTR) selects high p_{T} muons with a 4 GeV/c threshold. During Run 2, the data acquisition system involved triggered data. However, in Run 3, significant changes have been implemented in the data-taking system. The upgraded electronics in ALICE now enable continuous readout mode. Moreover, the incorporation of new detectors such as the

Muon Forward Tracker (MFT) has improved the spatial resolution of the muon spectrometer, facilitating the discrimination between primary and secondary vertices. Notably, the MTR no longer serves as a trigger, it has transformed into the Muon Identifier (MID).

Run 2 J/Ψ flow analysis

In this section, we show how to measure the flow of J/ψ by doing correlations between charged particles at midrapidity and one J/ψ particle in the forward region. The main idea behind this analysis is to create a pseudo-rapidity gap, suppressing non-flow correlations. In the following, the J/ψ elliptic flow extracted with the scalar product (SP) method is presented from Run 2 data [15]. This is a two-particle correlation technique based on the scalar product of different flow vectors Q_n. These vectors are defined as the sum over all complex vectors of charged tracks of a given event, for the harmonic n:

$$Q_n = \sum_{i=1}^{N} e^{(in\phi_i)}. \tag{5}$$

where ϕ_i is the azimuthal angle of the particle i and N is the number of charged tracks in an event. To suppress non-flow correlations, we create a pseudo-rapidity gap by building two flow vectors, the dimuon flow vector $Q_n^{\mu\mu}$ and the complex conjugate of the event flow vector Q_n^{A*} for soft charged particles. The flow coefficients can be expressed in the following way:

$$v_n^{SP} = \langle Q_n^{\mu\mu} Q_n^{A*}/R_n \rangle. \tag{6}$$

Here, $\langle ... \rangle$ represents the average over all tracks from all events. The normalisation factor R_n that corrects the event flow component is equal to:

$$R_n = \sqrt{\frac{\langle Q_n^A Q_n^{B*} \rangle \langle Q_n^A Q_n^{C*} \rangle}{\langle Q_n^B Q_n^{C*} \rangle}}. \tag{7}$$

where Q_n^B and Q_n^C are the n-th harmonic event flow vectors in two additional regions in the central barrel.

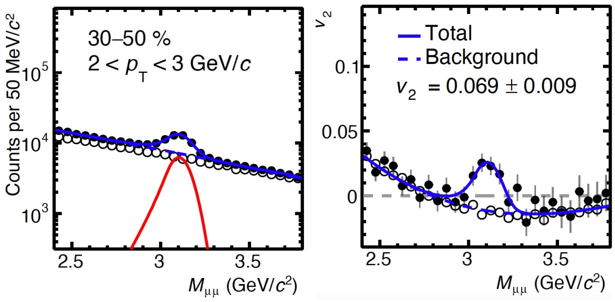

Figure 3: At left, signal extraction with the dimuon invariant mass spectrum. At right, the elliptic flow of dimuon as function of $m_{\mu\mu}$, each point corresponds to the average v_2 value of all dimuon pairs in one bin of $m_{\mu\mu}$. Only statistical uncertainties are shown.

In figure 3, the mean value of v_2 over all dimuon pairs in each bin of the invariant mass is calculated [16]. This is done with a global fit using the following formula:

$$v_n = v_n^{sig} \alpha + v_n^{bkg}(1-\alpha). \tag{8}$$

where v_n^{bkg} is parametrized by functional forms in order to reproduce the background dimuon contributions (estimated with an event-mixing procedure). v_n^{sig} is extracted by fitting the total dimuon v_n and $\alpha = \frac{S}{S+B}$ is the signal to background ratio extracted from the invariant mass distribution fit (see figure 3). Fitting systematically the v_2 for different p_T ranges, we can obtain a measurement of the elliptic flow of J/ψ as shown in figure 4.

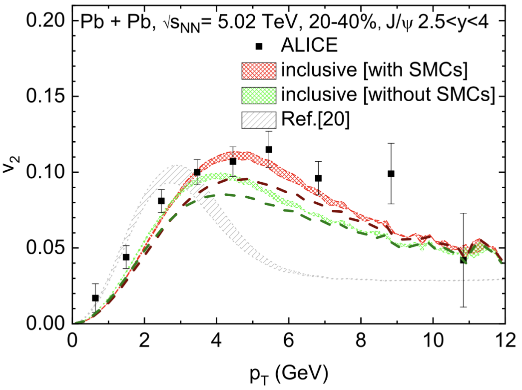

Figure 4: Elliptic flow as a function of p_T for inclusive J/ψ in 5.02 TeV Pb-Pb collisions [17]. The red and green bands correspond to c-quark spectra in RRM evaluated at τ = 5.2 fm/c. The dashed lines are for τ = 4.2 fm/c. The grey band corresponds to previous calculations.

Results and theorical interpretations

Heavy-ion collisions at the Relativistic Heavy-Ion Collider (RHIC) and the Large Hadron Collider (LHC) have done extensive charmonium measurements. At low energies, RHIC has shown a remarkable suppression of charmonia in semi-/central Pb-Pb collisions relative to the proton-proton reference [18]. At high energies, the LHC measured a smaller suppression compared to RHIC [19]. Those measurements can be understood with different models. One scenario for the production of charmonium is the Statistical Hadronization Model (SHM) [20]. This model assumes that there is a common freeze-out temperature for all hadrons. The number of charmonium states is fixed according to thermal weights:

$$N_{c\hat{c}} = \frac{1}{2} g_c V [\sum_i n_{D_i} + n_{\Lambda_i} + ...] + g_c^2 V [\sum_i n_{\Psi_i} + n_{\chi_i} + ...]. \tag{9}$$

where V is the volume of the thermal medium, g_c represents the charm fugacity and n represents the thermal densities of different states. Another scenario to explain the J/ψ production at the LHC is the Transport Model (TM). This model employs the integration of a Boltzmann kinetic equation to obtain the yield evolution of charmonia as function of time:

$$\frac{dN_{\psi}(t)}{dt} = -\Gamma_{\psi}(t)[N_{\psi}(t) - N_{\psi}^{eq}(t)]. \qquad (10)$$

where $N_{\psi}(t)$ and $N_{\psi}^{eq}(t)$ is the number of suppressed and regenerated J/ψ and Γ_{ψ} is the reaction rate. The transport model reproduces the experimental v_2 data of J/ψ at small p_{T}. The positive coefficient at low p_{T} supports the regeneration mechanism with the charm quark flow 4. The elliptic flow of J/ψ directly reflects the momentum field of individual charm quarks within the medium. At high p_{T}, it is not clear if the v_2 of J/ψ could be explained by charm energy loss. An analysis of a large data sample could offer valuable insights into this phenomenon.

However, the new transport model called Resonance Recombination Model (RRM) [17] implements new charm distributions transported through the QGP using Langevin simulations. The model also accounts for charm space-momentum correlations (SMCs) coming from the expanding medium (see the figure 4). It also uses a new path-dependence for J/ψ suppression, increasing the elliptical flow value with respect to previous predictions. As shown in figure 4, the new model RRM is able to amplify the recombination processes to higher momenta than previous predictions. There is a good description of ALICE data. This implies the significance of recombination processes for a large p_{T} range(0 to 8 GeV). A measurement of $v_2^{J/\psi}$ employing 4-particle correlations to mitigate non-flow could offer valuable insights to the v_2 J/ψ puzzle.

Run 3 measurement

In order to extract the J/ψ signal, we need to take into account the acceptance and efficiency of the muon spectrometer. To estimate it, realistic simulations are needed.

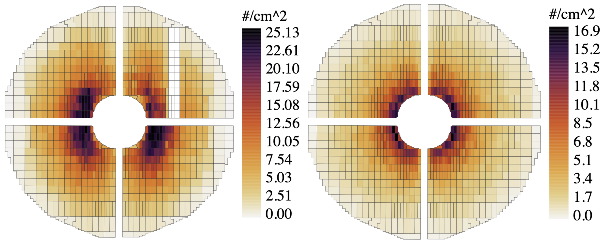

Figure 5: Comparison of MCH chambers between data (at left) and simulations (at right).

A comparison of data and Monte Carlo (MC) simulation is shown in figure 5. By distinguishing the dead regions in the data, we can reproduce a realistic status of the detector in MC simulations. Then a realistic acceptance x efficiency ($A \times \epsilon$) can be calculated in the following way:

$$A \times \epsilon = \frac{N^{rec}}{N^{gen}}. \qquad (11)$$

where N^{gen} and N^{rec} are the number of generated and reconstructed J/ψ. Many other simulations were made to take into account the track finding and detector response. The design of the MCH chambers and the track reconstruction algorithm were optimised to improve the mass resolution and the tracking efficiency. The final J/ψ candidates are obtained by combining all pairs of Opposed Sign (OS) muon tracks in the spectrometer's acceptance.

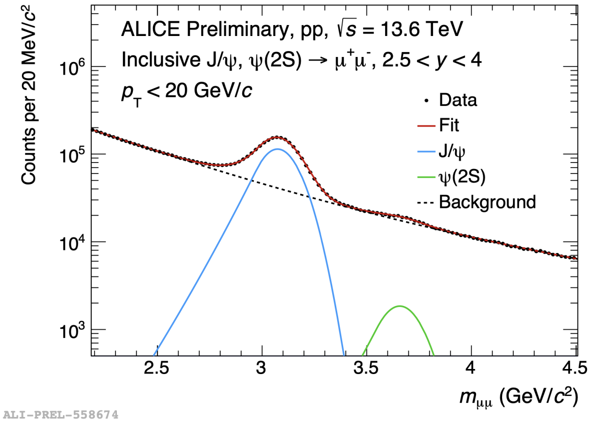

Figure 6: The inclusive J/ψ and $/\psi_{2S}$ signal extraction integrated over p_{T} ($0 < p_{\mathrm{T}} < 20$ GeV/c) and rapidity ($2.5 < \mathrm{y} < 4$).

The raw number of J/ψ is extracted by fitting the OS dimuons invariant-mass distribution as shown in figure 6. Furthermore, to measure the flow of J/ψ, correlations between charged barrel tracks and J/ψ particles is required. The application of the previously discussed multi-particle correlations technique (see formula 4) will need to be done.

Conclusion

In these proceedings, we introduce the theoretical and experimental framework of anisotropic flow studies, which is a manifestation of the collective behavior of the medium during the hydrodynamic expansion. We also mentioned the importance of charmonium states, being unique probes to study the properties of the QGP. In particular, we saw that J/ψ flow provides information into the partial thermalization of charm quarks within the medium. The J/ψ flow analysis shown involves correlations with charged particles, using a pseudorapidity gap technique. We introduced multi-particle correlations and cumulants as tools to mitigate non-flow effects. We also discussed the theoretical interpretations of the experimental results, considering models such as the Statistical Hadronization Model, Transport Model, and the Resonance Recombination Model. Finally, the extraction of J/ψ signal at forward rapidity with Run 3 data has been shown.

References

[1] Gines Martinez Garcia, *Introduction à l'étude expérimentale de la matière hadronique dans les collisions entre ions lourds. Le Plasma de Quarks et de Gluons.*, `https://tel.archives-ouvertes.fr/tel-00370481/file/TheseDeHabilitation.pdf`

[2] Jean-Yves Ollitrault, *Anisotropy as a signature of transverse collective flow*, *Phys. Rev. D*, 1992, 46, 229-245. `https://doi.org/10.1103/PhysRevD.46.229`

[3] S. Voloshin, Y. Zhang, *Flow study in relativistic nuclear collisions by Fourier expansion of azimuthal particle distributions*, `https://doi.org/10.1007/s002880050141`

[4] Ante Bilandzic, Raimond Snellings, Sergei Voloshin, *Flow analysis with cumulants: Direct calculations*, `https://doi.org/10.1103/physrevc.83.044913`

[5] ALICE collaboration, *J/ψ elliptic and triangular flow in Pb-Pb collisions at* $\sqrt{s_{\mathrm{NN}}} = 5.02\mathrm{TeV}$, *Journal of High Energy Physics*, 2020, 10. `https://doi.org/10.1007/jhep10(2020)141`

[6] Philippe Di Francesco, Maxime Guilbaud, Matthew Luzum, Jean-Yves Ollitrault, *Systematic procedure for analyzing cumulants at any order*, *Physical Review C*, 2017, 95, 4. `https://doi.org/10.1103/physrevc.95.044911`

[7] Matsui, T., Satz, H., *J/ψ Suppression by Quark-Gluon Plasma Formation*, *Phys. Lett. B*, 1986, 178, 416-422. `https://doi.org/10.1016/0370-2693(86)91404-8`

[8] Kai Zhou, Nu Xu, Zhe Xu, Pengfei Zhuang, *Medium effects on charmonium production at ultrarelativistic energies available at the CERN Large Hadron Collider*, *Physical Review C*, 2014, 89, 5. `https://doi.org/10.1103/physrevc.89.054911`

[9] Xiaojian Du, Ralf Rapp, *Sequential regeneration of charmonia in heavy-ion collisions*, *Nuclear Physics A*, 2015, 943, 147-158. `https://doi.org/10.1016/j.nuclphysa.2015.09.006`

[10] P. Braun-Munzinger, J. Stachel, *(Non)thermal aspects of charmonium production and a new look at J/ψ suppression*, *Physics Letters B*, 2000, 490, 3-4, 196-202. `https://doi.org/10.1016/s0370-2693(00)00991-6`

[11] ALICE Collaboration, *D-meson azimuthal anisotropy in midcentral Pb-Pb collisions at* $\sqrt{s_{\mathrm{NN}}} = 5.02\mathrm{TeV}$, *Physical Review Letters*, 2018, 120, 10. `https://doi.org/10.1103/physrevlett.120.102301`

[12] ALICE Collaboration, *The ALICE experiment at the CERN LHC*, *K. Aamodt et al. [ALICE]*, `https://inspirehep.net/literature/796251`

[13] ALICE Collaboration, *Performance of the ALICE experiment at the CERN LHC*, `http://dx.doi.org/10.1142/S0217751X14300440`

[14] P. Crochet for the ALICE collaboration, *The ALICE forward muon spectrometer*, `https://cds.cern.ch/record/530359/files/ali-2001-058.pdf`

[15] S. Acharya, D. AdamovÃ¡, A. Adler, J. Adolfsson, M. M. Aggarwal, G. Aglieri Rinella, M. Agnello, N. Agrawal, Z. Ahammed, S. Ahmad, S. U. Ahn, Z. Akbar, A. Akindinov, M. Al-Turany, S. N. Alam, D. S. D. Albuquerque, D. Aleksandrov, B. Alessandro, H. M. Alfanda, R. Alfaro Molina, B. Ali, Y. Ali, *J/ψ elliptic and triangular flow in Pb-Pb collisions at* $\sqrt{s_{\mathrm{NN}}} = 5.02$ *TeV*, *Journal of High Energy Physics*, 2020, 10, 141. `http://dx.doi.org/10.1007/JHEP10(2020)141`

[16] Robin Caron, *Quarkonium Azimuthal Anisotropy in Ultrarelativistic Heavy-Ion Collisions with ALICE at the LHC*, `https://tel.archives-ouvertes.fr/tel-03387833v2`

[17] He, Min and Wu, Biaogang and Rapp, Ralf, *Collectivity of J/ψ Mesons in Heavy-Ion Collisions*, `http://dx.doi.org/10.1103/PhysRevLett.128.162301`

[18] Grandchamp, L. and Rapp, R., *Charmonium suppression and regeneration from SPS to RHIC*, `http://dx.doi.org/10.1016/S0375-9474(02)01027-8`

[19] J. Adam et al., *J/ψ suppression at forward rapidity in Pb-Pb collisions at* $\sqrt{s_{\mathrm{NN}}} = 5.02$ *TeV*, `http://dx.doi.org/10.1016/j.physletb.2016.12.064`

[20] AA, P. Braun-Munzinger, K. Redlich, J. Stachel, *Statistical Hadronization Model*, `https://indico.cern.ch/event/91745/contributions/2113547/attachments/1096805/1564596/glasgow10.pdf`

Part VII

Neutrino Physics

session chaired by Chiara LASTORIA

Deeply Learning from Neutrino Interactions with the KM3NeT neutrino telescope

Santiago Peña Martínez

Université Paris Cité, CNRS, Astroparticule et Cosmologie, F-75013 Paris, France

Abstract — KM3NeT/ORCA is a large-volume water-Cherenkov neutrino detector, currently under construction at the bottom of the Mediterranean Sea at a depth of 2450 meters. The main goal of this experiment is to determine the neutrino mass ordering as well as measure atmospheric neutrino oscillation parameters. Beyond these goals, the detector also exhibits sensitivity to diverse beyond standard model neutrino physics such as non-standard neutrino interactions, sterile neutrinos, and neutrino decay. This contribution describes the use of a machine learning framework for building Deep Neural Networks (DNN) and Graph Neural Networks (GNN). The DNN is optimized for energy regression, while the GNN is intended for the regression of inelasticity in neutrino interactions. By combining data from six detection units, the optimization of these models attempts to improve the oscillation analysis by using a sizable data sample of 433 kton-years from KM3NeT/ORCA. The performance of the DNN is assessed by determining the sensitivity to oscillation parameters in comparison with the conventional energy reconstruction methods of maximizing a likelihood function. The results demonstrate the DNN's ability to provide an improved energy estimate, exhibiting less bias within the context of oscillation analyses. Furthermore, the GNN exhibits certain potential in estimating the inelasticity of a small number of events, providing valuable insights for future improvements and tunings. This research not only contributes to the refinement of neutrino detection methodologies but also serves as an example of how the use of machine learning techniques may improve the precision of data analyses in the realm of neutrino physics.

Introduction

The KM3NeT neutrino telescope, presently being constructed in the Mediterranean Sea [2], consists of two water-Cherenkov detectors built on different sites: ARCA and ORCA. The Cherenkov light created by charged particles resulting from neutrino interactions in water is the main detection principle. This emitted light is collected by arrays of photomultiplier tubes (PMTs) housed in glass spheres, forming digital optical modules (DOMs). A vertical string with 18 equally spaced DOMs is called a Detection Unit (DU). Each DOM holds 31 PMTs arranged to provide directional and timing information from the incoming photons.

The ORCA detector will comprise 115 DUs instrumented with a total of 2070 DOMs, with a volume of approximately about 7 Mton. The modularity of the detector allows it to take data even without the full number of DUs being deployed. The main goal of ORCA is to determine the neutrino mass ordering and measure atmospheric neutrino oscillation parameters. Monte Carlo (MC) simulations from an early detector configuration with 6 DUs are employed in this study. This configuration is called ORCA6 and has a livetime of 510 days, which corresponds to 433 kton-years in terms of exposure of instrumented mass.

The reconstruction of the neutrino energy is an essential component for the oscillation analysis of KM3NeT/ORCA. Present methods for the energy reconstruction rely on the maximization of a likelihood function, this function is modeled from a hypothesis for the distribution of light emanating from a neutrino interaction. This distribution is either a track-like pattern when it is induced by charged outgoing muons or a shower-like pattern when it is generated by an electromagnetic or hadronic cascade involving charged secondary particles. Nevertheless, this method has some limitations. For the case of the track-like topology, the reconstruction relies on the assumption that the muon propagates in a straight line without scattering. For the shower-like topology, the produced lepton is, for instance, an electron inducing an electromagnetic cascade that is assumed to produce light in a spherically symmetric way. Both hypotheses, however, fail to cover the full picture of the interaction. When a neutrino interacts with a nucleus, it not only yields an outgoing lepton but also a shower of hadrons producing additional light.

The study presented here is divided into two parts. The first one makes use of the current energy estimates and combines them with extra information from the reconstruction and triggering of the event, this aims to recover the representation of the full event [5]. By the use of auxiliary information and the conventional energy estimates from each hypothesis as an input, a Deep Neural Network (DNN) yielding an improved energy estimate is built. To build the DNN, the best set of hyperparameters (parameters that the network can not learn by itself) are defined based on the performance of the network on validation data with respect to a given metric. Standard regression problems in machine learning use the mean squared error (MSE) between the value given by the DNN and the target value as a metric and loss function. However, for the purposes of studying neutrino oscillations, this metric is not optimized to extract the physics information of the interactions. The interest relies on the sensitivity to the oscillation parameters θ_{23} and Δm^2_{31} which are responsible for the oscillations in the atmospheric neutrino sector. In the best-case scenario, during training time, the loss function should be a proxy for the sensitivity of the measurement to the oscillation parameters just mentioned. This partially incorporates this information in the loss function on an event-by-event basis. This is done by giving higher weights to events sensitive to oscillations. Finally, the results from the network optimized are compared with the standard methods.

The second part exposed here consists of the use of Graph Neural Networks (GNN) for the reconstruction of the inelasticity of a neutrino interaction. The inelasticity of the interaction is given by the Bjorken y variable as $y = 1 - E'/E$, where E' corresponds to the energy of the lepton emitted in the interaction and E the energy of the neutrino before the interaction. In other words, the Bjorken y is the fraction of energy that is not taken by the outgoing lepton. As ν and $\bar{\nu}$ have different distributions of Bjorken y, the reconstruction of it allows for discriminating both of the signals, at least statistically. An oscillation resonance from the atmospheric neutrinos going through the earth occurs only for ν or $\bar{\nu}$ depending on the Mass Ordering (MO). It has been shown that the measurement of the inelasticity for a Cherenkov telescope helps to boost the signal of the MO ν and $\bar{\nu}$ [9]. The GNN is trained for the regression task of simultaneously estimating the energy of the track and shower component of the neutrino event.

Deep Neural Network for combined energy estimate

Building the network

To do the regression task for energy estimation, a neural network is built using Keras [3]. The network architecture is composed of an input layer, succeded by multiple densely connected hidden layers with an activation function, the output layer is then a single node.

The network's inputs include the standard energy estimates associated with the track and the shower hypothesis, the track length serving as an energy proxy, information about the number of triggered hits (individual photons detected by a PMT), DOMs, and DUs, and scores from the particle identification (PID) training. The values for the energy estimates from the simulations span a range from 1 GeV to 1 TeV, presenting a wide spectrum for the network to correctly focus on. However, this may cause difficulties in regression from events with true energies within the energy range relevant to oscillation studies (5 - 40 GeV). The loss function will be dominated by the higher energies biasing the network to focus on energy scales not suitable for atmospheric neutrino oscillations. Therefore, the energy estimates were converted into a logarithmic scale for training, the motivation for this is that the energy uncertainty is expected to be relative, i.e. a percentage of the true energy of the event. This will translate to a constant uncertainty assumed in the loss function. Additionally, the maximum energy for the training sample is consequently set to be 100 GeV, allowing the network to learn from a wider range of values and to improve the performance for the energies in the region of interest. Charged Current (CC) and Neutral Current (NC) interacting events were simulated. The event types used for training are ν_μ CC, $\bar{\nu}_\mu$ CC, ν_e CC, $\bar{\nu}_e$ CC, ν_τ CC, $\bar{\nu}_\tau$ CC, ν NC, and $\bar{\nu}$ NC events. Furthermore, a batch normalization layer is applied at each layer. This allows to normalize the input data from layer to layer [10].

Network architecture

A skip connection architecture was implemented. This architecture allows the layer outputs to skip connections serving as input to different layers by concatenation at different stages. The main motivation for this is to ease the job of the network so it learns the complementary information between the input and the output instead of learning the whole function. For this particular situation, the input and output of the network are both energy estimates, the network will learn complementary information to what is present in the standard estimates. With this method, the information from the energy estimates will not be washed out during the message passing. However, at the level of oscillation analysis, the energy given by the network did not show any improvement over the standard energy estimates. This is related to the problem of misalignment [11], the network is optimized for the wrong feature. From the training data, it is only natural for the network to learn the distribution of the energy without focusing on oscillation effects. Therefore, events with high sensitivity to oscillation effects are not special, they could even be regressed worse than other non-oscillating events.

Weighting the events and training

To make the network aware of oscillation effects during training a novel method to set up the weights for training events was implemented. This method consists of weighting more heavily the events sensitive to oscillations. The standard weight for a MC event is $w = w(\Delta m^2_{31}, \theta_{23})$, where Δm^2_{31} and θ_{23} are the oscillation parameters, in particular the parameters the ORCA detector is sensitive to. The quantity $\Delta w = |w(\Delta m^2_{31}, \theta_{23}) - w(\Delta' m^2_{31}, \theta'_{23})|$ will correspond to the difference between the weight of the same event with different oscillation parameters. For charged current events, Δw will be non-zero and will have a strong dependence on the direction and energy of the event.

During training, each event is weighted as follows:

$$w_{osc} = K\Delta w + w. \tag{1}$$

Where K is a hyperparameter responsible for the importance given to the oscillation weights during the training. The larger the K the more important the events feeling oscillations will be.

To optimize the performance of the neural network, a hyperparameter optimization procedure to search for the optimal values of the hyperparameters was implemented. The set of features given as input to the network is an additionally hyperparameter taken into account. The Optuna package in Python [1], which implements a Bayesian optimization algorithm (TPE) to efficiently scan the hyperparameter space, was used for this purpose. The procedure presented here iterates different sets of hyperparameters and computes the sensitivity given by the $\Delta\chi^2$ between two oscillation hypotheses when training is done. The result is a $\Delta\chi^2$ value for each set of hyperparameters, the set of hyperparameters with the highest $\Delta\chi^2$ is selected. Once the selection of the network hyperparameters is done, a full fit of the MC to an Asimov dataset including systematic effects for the oscillation analysis is computed. This validates the output given from the network compared with the standard methods. The results of the neural network that performed the best are consequently evaluated.

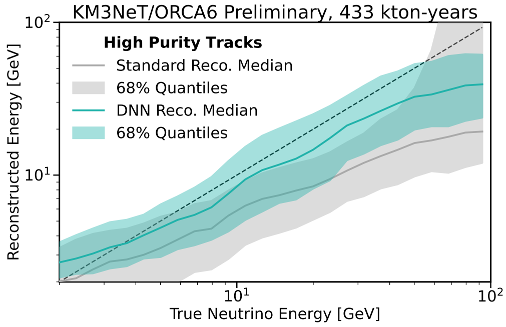

(a) High Purity Tracks class

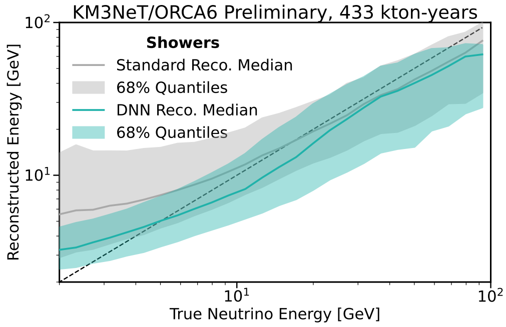

(b) Showers class

Figure 1: Energy response functions for different classes of neutrino events. Events are reconstructed using the standard method and the DNN to compare.

Results and discussion

Energy response function

The energy response function of the neural network is compared with the standard reconstruction method in Figure 1, for different event samples. The energy given by the DNN shows lower bias compared to the standard reconstruction method. The DNN also shows a better alignment in both tails of the energy range. This hints that the DNN is able to correct the necessary biases and combine the information from the different estimates for the distributions of the event energy.

Sensitivity to oscillation parameters

The most accurate way to quantify the performance of the network is by computing the sensitivity to oscillation parameters. The sensitivity is given as a $\Delta\chi^2$ for every combination of $(\Delta m^2_{31}, \theta_{23})$ using the energy from the DNN and by comparing this with the standard energy estimates. At every point in the $(\Delta m^2_{31}, \theta_{23})$ contour, the log-likelihood is minimized relative to all nuisance parameters defined for the main oscillation analysis of the experiment [6].

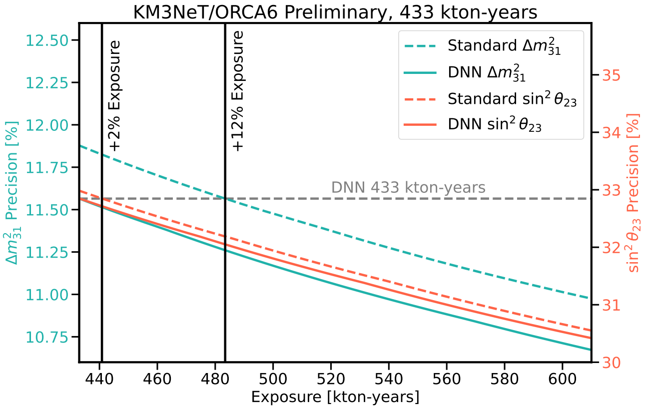

Figure 2: Precision to oscillation parameters $\sin^2\theta_{23}$ and Δm^2_{32} as a function of exposure in kton-years for the DNN and the standard energy estimates.

To assess the improvement coming from the use of the DNN for the analyses, we compute the exposure needed to achieve the same level of precision on the oscillation parameters. Results are shown in Figure 2. The figure shows that the better precision of the DNN for the Δm^2_{32} parameter is equivalent to having 12% more exposure, while for the $\sin^2(\theta_{23})$ parameter it is equivalent to having 2% more exposure.

Graph Neural Networks for Bjorken y reconstruction

Network setup

The architecture of the GNN is inspired in the ParticleNet architecture [7]. The overall architecture is made up of three Edge Convolutional blocks [8] followed by a global pooling layer and two fully connected layers. This last layer outputs two nodes that contain the desired variable and the error on regression.

The input of the network consists of a graph made up of a number of nodes containing information about the snapshot hits of the event that triggered the detector. The nodes of the graph created directly from the hits collected by the PMTs of the events will have the time, 3D position, and 3D direction as attributes. This 7D collection of nodes will aggregate to build the graph structure via edges with a central node.

Training of the GNN

The Bjorken y is defined as the fraction of energy from the initial neutrino interaction given to the hadronic shower; therefore it has a continuous value between 0 and 1. This behavior complicates the decision on which loss function to use because, for regression problems, standard loss functions are made such that they penalize the distance between the regressed value and the true value in an unbounded range. Limiting the loss function to work on a fixed range uniformly implies tailoring a well-behaved non-orthodox loss function. A simple way to avoid this complication by using a standard log normal loss which outputs a prediction and an uncertainty on this prediction. In addition to this, the network will have two sets of output nodes. One set will have as a target the energy carried by the track from the outgoing lepton, the other node will have as a target the energy of the shower produced by the hadrons. From these quantities of the energy components, it is possible to retrieve the original Bjorken y as

$$y = \frac{E_{Sh}}{E' + E_{Sh}} = \frac{E_{Sh}}{E}, \tag{2}$$

where E is the energy of the initial neutrino, E_{Sh} is the energy of the hadronic shower and E' is the energy of the outgoing lepton. This idea of the loss function can be thought of as an extension of the energy regression of the full event. The network learns not only the total energy of the neutrino, but also get individual information about the components of the events as well as the inelasticity of it.

The event selection for training consists of ν_μ CC and $\bar{\nu}_\mu$ CC events in the range of energies of $1 - 100$ GeV. The purpose of the selection is to train on events producing an outgoing lepton (μ^- or μ^+) which leaves a clear track in the detector in addition to producing a hadronic shower. The energy range is chosen to minimize the number of events that are partially contained inside the detector volume.

Results and discussion

Figure 3 shows the Bjorken y estimated by the GNN from the combination of the regressed energy of the track and the shower component of an event. The reconstructed value is not significantly correlated with the true value. The distribution of reconstructed events is centered around a value ~ 0.15 for most of the cases. This value agrees with the mean value of the inelasticity of the training sample. It is to be investigated further why the network fails to learn the correlation with the true value. By applying a cut on the quality of the regression for the shower component, the reconstructed Bjorken y shows an improved correlation with its true value, but the variance of the values is large. This means the network is having difficulties with the shower component in most of the cases. The performance of the GNN improves when the true value corresponds to high values of Bjorken y. This hints that the light coming from the shower component may be overshadowed by that from the track component.

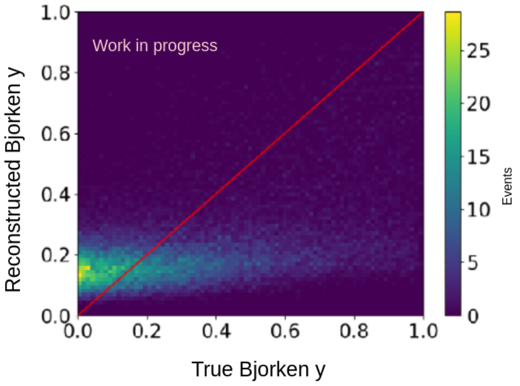

(a) No cut on regression quality

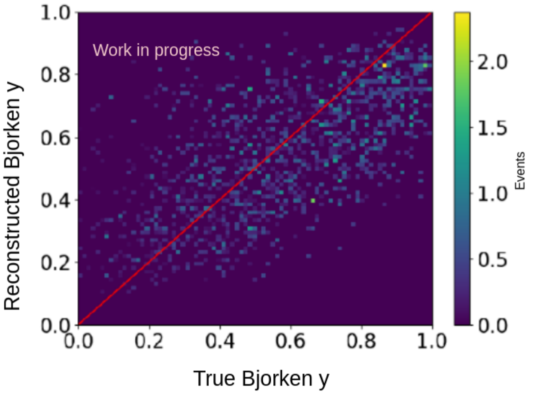

(b) Cut on regression quality

Figure 3: Estimation of the Bjorken y from the GNN vs the true value from MC for two sets of of cuts.

Although the reconstruction of the Bjorken y from the GNN shows a biased behavior, the tool of selecting events given by the uncertainty on the performance allows to identify events which have a better chance of being correctly reconstructed. This information could be used, these events can be investigated one by one to analyze its characteristics and topology. The added value of this is to get more information about the values of the features that the network correctly identifies to give an accurate value when doing the regression. The next steps would be to use these events to improve the training sample or modify the loss function use these Bjorken y characteristics in the events and focus the loss on these values.

References

[1] Akiba, T., Sano, S., Yanase, T., Ohta, T. & Koyama, M. Optuna: A Next-generation Hyperparameter Optimization Framework. *Proceedings Of The 25th ACM SIGKDD International Conference On Knowledge Discovery And Data Mining.* (2019)

[2] Adrian-Martinez, S., Ageron, M., Aharonian, F., Aiello, S., Albert, A., Ameli, F., Anassontzis, E., Andre, M., Androulakis, G., Anghinolfi, M. & Others Letter of intent for KM3NeT 2.0. *Journal Of Physics G: Nuclear And Particle Physics.* **43**, 084001 (2016)

[3] Chollet, F. "keras." (https://keras.io) (2015)

[4] Bourret, S. Neutrino oscillations and earth tomography with KM3NeT-ORCA. (Université Sorbonne Paris Cité,2018)

[5] Peña Martínez, S. PoS(ICRC2023)1035,(2023)

[6] Carretero, V. PoS(ICRC2023)996,(2023)

[7] Qu, H. & Gouskos, L. Jet tagging via particle clouds. *Physical Review D.* **101**, 056019 (2020)

[8] Wang, Y., Sun, Y., Liu, Z., Sarma, S., Bronstein, M. & Solomon, J. Dynamic graph cnn for learning on point clouds. *ACM Transactions On Graphics (tog).* **38**, 1-12 (2019)

[9] Ribordy, M. & Smirnov, A. Improving the neutrino mass hierarchy identification with inelasticity measurement in PINGU and ORCA. *Physical Review D.* **87**, 113007 (2013)

[10] Ioffe, S. & Szegedy, C. Batch normalization: Accelerating deep network training by reducing internal covariate shift. *International Conference On Machine Learning.* pp. 448-456 (2015)

[11] Gao, L., Schulman, J. & Hilton, J. Scaling laws for reward model overoptimization. *International Conference On Machine Learning.* pp. 10835-10866 (2023)

Multi-messenger observations with the KM3NeT telescope: search for high energy neutrinos coinciding with Fast Radio Bursts

Felix Bretaudeau

Subatech, IMT Atlantique, CNRS-IN2P3, Nantes Université

Abstract — The KM3NeT experiment is a next-generation neutrino telescope, consisting of two separate detection structures, organised as arrays of light sensors, and immersed in the depths of the Mediterranean Sea. The two detectors are the Oscillation Research with Cosmics in the Abyss (ORCA), located off the coast of France, and the Astrophysics Research with Cosmics in the Abyss (ARCA), off the coast of Sicily. Identical in design but differing by scale, these two detectors observe neutrino interactions in the sea water through Cherenkov light produced by the interaction products at different energy ranges. Specifically, ORCA aims at detecting atmospheric neutrinos to study their oscillation parameters, while ARCA will focus at higher energies on astrophysical neutrinos and the characterisation of their sources. Among the latter topic, Fast Radio Bursts (FRB) are good candidates for multi-messenger emissions due to the huge energy involved in their burst. I will present the method and criteria of a multi-messenger analysis intended to search for spatial and temporal coincidences of astrophysical neutrino signals from KM3NeT with a FRB catalog of around 800 sources among which 55 have been observed in this period, ranging from January 2020 to November 2021, and were visible from the KM3NeT site.

Introduction

Starting with the detection of the first galactic supernova SN 1987A, seen both in photons and neutrinos, and followed later by the first binary neutron star merger [1], seen in gamma rays and gravitational waves, astronomy has entered the multi-messenger era. Since then, several events of the Universe have been monitored in more than one channel of observation [2], so-called *Universe messengers*. Depending on the observation channel one can access different information on the production processes and the source itself. Along with electromagnetic radiations, gravitational waves, and cosmic rays, neutrinos are a newly observed type of cosmic messengers that are showing a growing interest in the field of astrophysics. Until recently, the most favored channel is the photon with various energies along the electromagnetic spectrum. In the 2000's, a very puzzling type of emission was detected in the radio band, the Fast Radio Burst (FRB) [3]. It has been detected as a huge amount of energy emitted coherently over a very short time (on the millisecond scale or less, see Fig. 1), although nowadays it has not been fully yet explained. A way to increase our knowledge of FRBs and their sources is to use multi-messenger observations implying a FRB and another type of messenger, like the multi-wavelength observation of FRB20200428A[1], shown in Fig. 1, and a Hard X-Ray burst coming from the magnetar SGR 1935+2154 [4]. Travelling extragalactic distances without being impeded, carrying direct information of their production mechanisms, neutrinos are a privileged channel to understand the sources that produced them, that could provide the key to understand FRB sources. A large-volume neutrino telescope, the KM3NeT experiment, is being built in the Mediterranean Sea and will be able to conduct surveys of the sky, real-time analyses, and high energy neutrino searches for multi-messenger purposes [5]. Although the detector is not fully built yet, the infrastructure already allows for data taking and analyses. This work is focused on the selection of neutrino events that originate from the same time and location in the sky as FRBs that have been observed already and could be correlated to them. After introducing the KM3NeT experiment, and stating the characteristics of a possible dual emission of neutrinos and FRBs, the strategy of this analysis will be presented.

The KM3NeT Experiment

KM3NeT is a large volume neutrino detector, plunged at the bottom of the Mediterranean Sea, continuously

---

[1] FRBs are name following the format *FRBYYYY-MM-DDX*, X being the letter assigned in order of appearance during the day

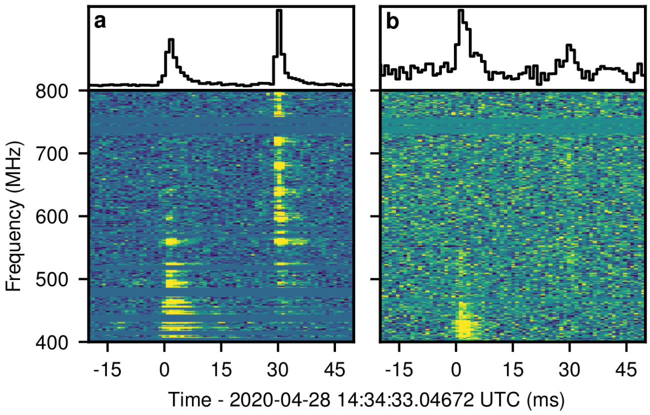

Figure 1: Double-structure Fast Radio Burst FRB20200428A, detected both by (a) the CHIME and (b) the ARO instruments. It was detected in temporal correlation with a Hard X-ray burst. Both figures show the total intensity normalized dynamic spectra below and the band-averaged time-series on top. [4]

monitoring both the atmospheric neutrino flux and the cosmic neutrino flux, coming from galactic and extragalactic sources. The signal from neutrinos is collected through the Cherenkov light emitted by ultrarelativistic neutrino interaction products in the seawater. The KM3NeT telescope is able to reconstruct both the energy and direction of the interacting neutrino [6]. The Cherenkov radiation is collected by PMTs, grouped in Digital Optical Modules (DOMs), which are in turn arranged in strings (the so-called Detection Units or DUs), held straight by an anchor and a buoy at its ends. KM3NeT is based on and improves the ANTARES experiment, which took data from 1999 to 2022; thanks to a larger infrastructure, ARCA and ORCA will allow to access an unprecedented wider energy range from the GeV to the PeV and cover an extended physics program [6]. First, studying oscillations from atmospheric neutrinos produced by cosmic rays in the atmosphere in the range from 1 GeV to 100 GeV and constraining with high precision oscillation parameters and determine the neutrino mass ordering [7], with the ORCA (Oscillation Research with Cosmic in the Abyss) detector. Then, at higher energies (above the TeV, where fluxes of atmospheric neutrinos are less dominant) allowing to study astrophysical neutrinos and constraining models of their sources with ARCA (Astrophysics Research with Cosmic in the Abyss). Recently, the first neutrino observations were made by IceCube, on neutrino-emitting galaxies NGC 1048 and TXS 0506+056 [8], or evidence of the Galactic Plane signal in the neutrino channel [9]. KM3NeT will have access to different astrophysical sources in the Southern Hemisphere, notably the Galactic Center. It will be therefore essential to work together with telescopes located in the South, like the future radio-telescope SKA (Square Kilometer Array), in order to combine surveys of the experiments, send and receive alerts. Additionally, KM3NeT can detect Supernovæ neutrinos thanks to its large flux in the MeV range, and is also sensitive to some exotic sources [11]. The pointing capabilities of KM3NeT at high energies can be used to search for multi-messenger observations, connecting a neutrino emission with another transient emission like a Fast Radio Burst.

Fast Radio Bursts in the Multi-Messenger Context

Since the first FRB in 2007 [12], several hundred more have been observed, from which some properties of the progenitors have been derived such as the duration, fluence, scattering and dispersion, and rotation measures. They encode the properties of the bright coherent bursts coming from extra-galactic distances, emerging from a mechanism that has an environment with an energetic, dense, perturbed, and magnetized plasma [3]. This plasma is therefore a possible source of hadronic accelerations and by conventional processes like the photopion process [13], source of high energy neutrinos. Some of the bursts turned out to be artificial terrestrial emissions [14], but eventually, FRBs have established themselves as extragalactic radio emissions of unknown sources; some have also been localized by interferometry in galaxies [15, 16, 17], but no sources were identified from these distances. Until then, many different production models were investigated. The detection of the first repeating source FRB20121102A in 2016 [18, 19] helped in invalidating cataclysmic models (implying the destruction of the source) for at least a category of FRBs. Furthermore, thanks to the first and only multi-wavelength detection of the FRB 20200428A associated with the galactic magnetar SGR1935+2154, models of neutrino production from magnetars have emerged [13, 20]. From these models, it is possible to extrapolate the expected neutrino fluxes and energies and to optimise the neutrino analysis for events similar to the ones associated with SGR1935+2154. The sketch in Fig. 3 shows the neutrino emission sites that have been studied in the surroundings of a magnetar. The three sites (magnetosphere, current sheets, and shocked regions) are all close-by, meaning the time delay between a FRB and a neutrino is almost simultaneous. Typically, the distance between the magnetar and the shocked regions of around $\sim 10^{12}$cm is covered in $\sim$ 30s for a particle with speed c. This hypothesis enables us to look for strong time correlations. However, the flux and energy of neutrinos produced by such processes are poorly constrained, because it strongly depends on the baryonic load (the density of baryons in the region) and the photon background (the X-rays or Gamma rays with which baryons interact and produce neutrinos). These two quantities are highly uncertain and complicate the implementation of a comprehensive strategy. Thus, the analysis conducted must be as model-independent as possible, since FRB sources are not constrained yet. The *Cut-and-Count* analysis method (described in the next section) is well suited

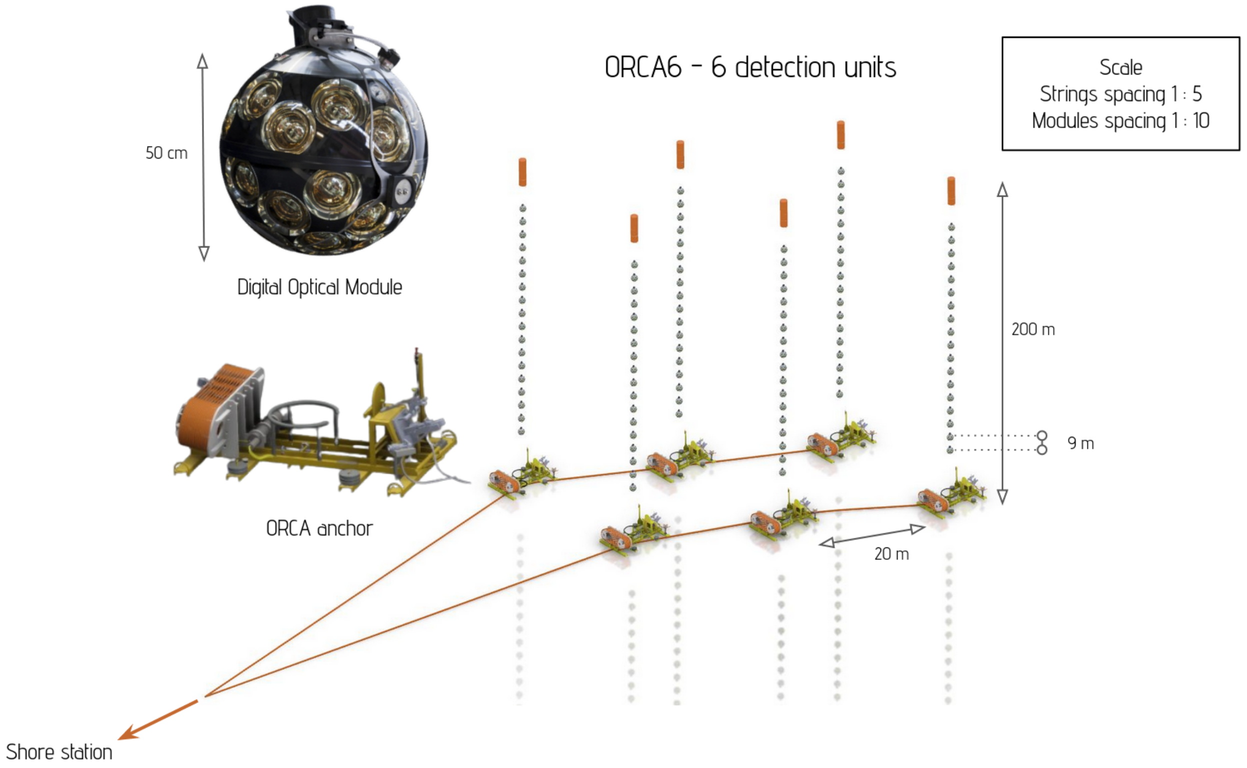

Figure 2: Layout of the ORCA detector, mounted with 6 detection units as it was in 2021. All dimensions except strings and modules spacing are to scale. The ORCA detector will consist of 115 lines in its final configuration.

for this purpose.

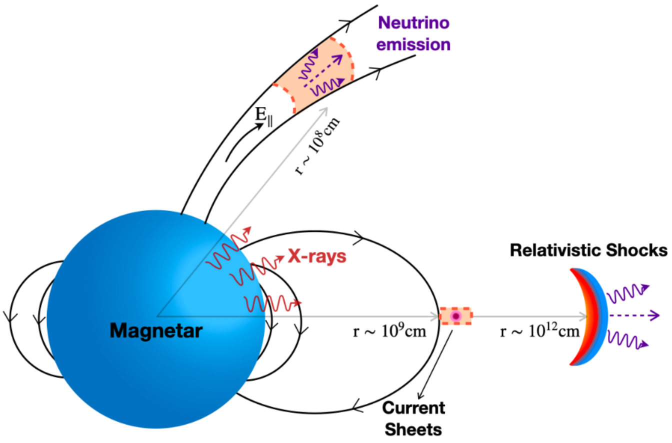

Figure 3: Possible neutrino production sites in the magnetar environment: the magnetosphere (top), current sheets (middle), and relativistic shocked regions (right). Neutrinos are represented by purple arrows. [13]

Analysis Strategy

The data used in this analysis consists of up-going muon neutrino event candidates recorded from January, 27th 2021 to March 31st, 2022 with the ORCA detector. The ORCA detector being under construction, only 6 detection units were running, which represents about 5% of the final size of ORCA (Fig. 2). During this period, 123 FRBs were detected from various radiotelescopes, 55 of which were in the up-going sky from the site of KM3NeT. A pre-selection is realized, consisting of removing bad quality candidate events. This is determined by the number of triggered hits (a collection of light in several PMTs), i.e. number of PMT pairs triggered within a DOM for this event. The selection threshold is set to a minimum of 20 triggered hits. Additionally, the data-taking runs are selected on the event rate criterion, the number of candidate events passing the low-level selection divided by the run duration. In order to correlate in time the FRB and possible neutrino signal, a time window of 1000 s was chosen, centered around the FRB. The last part of the selection is linked to the analysis method. To be properly model-independent and to have a significant correlation, the used method is the binned Cut-and-Count analysis (see references in [5]). An ON zone is defined (a search cone centered around the FRB direction), as well as an OFF zone (the elevation band centered around the FRB elevation). The OFF zone has a similar background as the ON zone. It is used to compute the background, from data of all selected runs, and then re-scaled to the size of the ON zone and duration of the time window. Cuts are performed on both the dataset and the corresponding simulation that is used to estimate the signal. Namely, the size of the ON region is one parameter, and the probability of the event to be an astrophysical neutrino, expressed in terms of

FRB Name	FRB 20210408H		FRB 20210327A		FRB 20210212G		FRB 20200508A	
Eq. coord. (RA-Dec [°])	204.3 ; -28.3		75.9 ; 26.2		93.2 ; 4.6		135.4 ; -65.6	
Loc. coord. (Alt-Az [°])	9.4 ; 144.0		-5.0 ; 313.3		-39.7 ; 24.2		-60.9 ; 152.8	
Repeater	None		FRB 20201124A		FRB 20180301A		None	
Metric	**MDP**	**3σ**	**MDP**	**3σ**	**MDP**	**3σ**	**MDP**	**3σ**
Opti. ON region cone [°]	4.8	5.0	4.6	5.0	7.4	5.0	10.0	5.0
Opti. BDT score	1.86	2.52	2.36	2.90	2.56	2.28	2.64	1.94
$\mathrm{N_{ON}}$	0	0	0	0	0	0	0	0
$\mathrm{N_{OFF}}$	6458	1857	13476	4500	2458	4392	888	3336
$\mathrm{N_{BG}}$	8.68e-3	2.71e-3	6.91e-3	2.72e-3	3.37e-3	2.75e-3	2.84e-3	2.67e-3

Table 1: Optimization and pre-blinding results for a subset of the studied FRBs (chosen in order to be representative of the full selection). The coordinates (local and equatorial) and the repeating source (if any) are displayed. For the two optimization metrics, the optimized cuts are shown (the ON zone size is fixed to 5° for the case of the '3σ' metric). The number of events in the ON (with scrambled data) and in the OFF zones are shown as well. Finally, the expected background rate is displayed, from N_{OFF} rescaled to the time window and to the ON cone size.

a classifier (*Boosted Decision Tree*) score, is the second.

The studied models used to optimize the two cuts in this low-signal environment are the following:

- The Model Rejection Factor (MRF) [21]. A certain value of the factor is computed from the Feldman-Cousins average upper limit [22], using the classifier score and ON region size pair, and by scanning over this two-parameter space the optimal parameter pair is found where the factor is minimized. This method maximizes the chances of rejecting a background hypothesis only, if some signal event is found in the data.
- The Model Discovery Potential (MDP): the background and signal are optimized such that one extra event added to the expected background is a discovery, or statistically speaking has a 5σ significance. This method chooses cuts such that a fluctuation of a background is highly improbable, and that any signal would lead to a strong correlation (5σ correlation).
- Another method (that could be called "1 event = 3 sigmas") could be to fix one parameter and choose the value of the other so that an extra event added to the background has a determined significance. In this case, the ON region size is fixed to 5° and the BDT score is optimized for a 3σ significance. This method is quite similar to the MDP with a different significance level.

After trying all three, the *MRF* metric was rejected. Indeed, it optimizes the cuts for a loose significance, offering less stringent cuts. It yields search cones of about 20° in size, which is too large to efficiently correlate spatially neutrinos and FRBs. As a result, the two metrics considered for the rest of this optimization study are the last two denoted 'MDP' and '3σ'.

Optimization Results

The analysis is prepared in blinded mode, using simulated data for the signal rather than real data, as well as real KM3NeT data for the background, but from runs different than the run of interest when some FRB was observed. In this way, it is ensured that no signal is present in the data used for estimating the background. Finally, after having performed the selection optimization (with both metrics described earlier) the real data from the run is used but scrambled in time, thus the arrival direction is fake as well so we are still using blinded data. The estimation of the OFF zone background is done using several days of data, and when rescaled to the ON zone size and time window duration we obtain the ON zone background estimation. This is to be compared with the number of events found in the ON zone with scrambled data, and eventually with the events of the un-blinded data. For simplicity, instead of showing the results of all studied bursts, 4 of them were chosen at different altitudes, and the corresponding results are shown in Table 1. The radii range from 4° to 10°, which can be considered large. These large radii are explained by the lack of statistics in this region of the sky and in such a small time window. No events are found in the ON zone when studying scrambled data, in accordance with the low expected background $\mathrm{N_{BG}}$ around 10^{-3} event.

Conclusion

After a brief description of the experiment KM3NeT, the analysis strategy for the neutrino-FRB correlated observations has been presented, leading to an optimized set of selection cuts for each source. The unblinding of the data will be realized soon to obtain the result of the analysis. Eventually, the analysis will complement those of IceCube [23, 24] and ANTARES [25], searching in several years of neutrino data and finding no significant coincidence with FRB observations. In the future, the analysis will be enhanced, on one hand by the increase of statistics and size of KM3NeT and on the other hand by the increase of the FRB detection rate. There is an estimate of about 5000 FRB per sky per day [26], with only a fraction of them detected by radiotelescopes today. The arrival of the Square Kilometer Array (SKA) in the scope of the radio experiments will allow for the detection of an even bigger part of this large population of FRBs.

References

[1] Abbott, B. P., Abbott, R., Abbott, T. D., et al. 2017, The Astrophysical Journal Letters, 848, L12

[2] Greus, F. S. & Losa, A. S. 2021, Universe, 7, 397

[3] Zhang, B. 2022, The Physics of Fast Radio Bursts

[4] Andersen, B. C., Bandura, K. M., Bhardwaj, M., et al. Nature 587, 54-58 (2020). https://doi.org/10.1038/s41586-020-2863-y

[5] Aiello, S., Albert, A., Garre, S. A., et al. 2023, Contributions of KM3NeT to ICRC2023

[6] Adrián-Martínez, S., Ageron, M., Aharonian, F., et al. 2016, Journal of Physics G, 43, 084001

[7] Gupta, A., Majumdar, D., & Halder, A. 2022, Modern Physics Letters A, 37

[8] Kurahashi, N., Murase, K., & Santander, M. 2022, Annual Review of Nuclear and Particle Science, 72, 365

[9] Sclafani, S. & Huennefeld, M. 2023, Observation of high-energy neutrinos from the Galactic plane

[10] Aiello, S., Albert, A., Garre, S. A., et al. 2021, The European Physical Journal C, 81

[11] Aiello, S., Albert, A., Garre, S. A., et al. 2022, The European Physical Journal C, 82

[12] Lorimer DR, Bailes M, McLaughlin MA, Narkevic DJ, Crawford F (2007) A bright millisecond radio burst of extragalactic origin. Science 318:777

[13] Metzger, B. D., Fang, K., & Margalit, B. 2020, The Astrophysical Journal Letters, 902, L22

[14] E. Petroff et al. Monthly Notices of the Royal Astronomical Society, Volume 451, Issue 4, 21 August 2015, Pages 3933-3940, https://doi.org/10.1093/mnras/stv1242

[15] Keane, E., Johnston, S., Bhandari, S. et al. The host galaxy of a fast radio burst. Nature 530, 453-456 (2016). https://doi.org/10.1038/nature17140

[16] Marcote, B., Nimmo, K., Hessels, J.W.T. et al. A repeating fast radio burst source localized to a nearby spiral galaxy. Nature 577, 190-194 (2020). https://doi.org/10.1038/s41586-019-1866-z

[17] Marcote, B. & Kirsten, Franz & Hessels, J. & Nimmo, K. & Paragi, Zsolt. (2022). PRECISE localizations of repeating Fast Radio Bursts.

[18] L. G. Spitler et al. Fast Radio Burst Discovered in the Arecibo Pulsar ALFA Survey. ApJ 790 101 (2014).

[19] Spitler, L., Scholz, P., Hessels, J. et al. A repeating fast radio burst. Nature 531, 202-205 (2016). https://doi.org/10.1038/nature17168

[20] Qu, Yuanhong & Zhang, Bing. (2022). Monthly Notices of the Royal Astronomical Society. 511. 10.1093/mnras/stac117.

[21] Hill, G. C. & Rawlins, K. 2003, Astroparticle Physics, 19, 393

[22] Feldman, G. J. & Cousins, R. D. 1997, Physical Review D, 57, 3873

[23] Aartsen, M. G., Ackermann, M., Adams, J., et al. 2018, Science, 361, eaat1378

[24] Abbasi, R., Ackermann, M., Adams, J., et al. 2023, The Astrophysical Journal, 946, 80

[25] Albert, A., André , M., Anghinolfi, M., et al. 2018, Monthly Notices of the Royal Astronomical Society, 482, 184

[26] Connor, L., Lin, H.-H., Masui, K., et al. 2016, Monthly Notices of the Royal Astronomical Society, 460, 1054